Steel fiber reinforced concrete for tunnel linings

MSc Thesis

Daniel Kallan

Delft University of Technology

TU Delft

Witteveen + Bos

Steel fiber reinforced concrete for tunnel linings

MSc Thesis

by

Daniel Kallan

to obtain the degree of Master of Science
at the Delft University of Technology,

Student number	4572858
University:	Delft University of Technology
Faculty:	Civil Engineering and Geosciences
Master track:	Structural Engineering
Specialization:	Concrete Structures

Supervisory committee

Dr. Ir. Yuguang Yang	Chair of committee	Delft University of Technology
Dr. Ir. Mauro Poliotti	Daily supervisor	Delft University of Technology
Dr. Ir. Manimaran Pari	External supervisor	Delft University of Technology
Ir. Nikolaas van Empel	Company supervisor	Witteveen+Bos

An electronic version of this thesis is available at `http://repository.tudelft.nl/`.

TU Delft

Witteveen+Bos

Preface

In front of you lies the master thesis 'Steel Fiber Reinforced Concrete for Tunnel Linings' which has been written in fulfilment of the Master of Science degree in Civil Engineering at the Delft University of Technology. The work of this thesis has been carried out under the Concrete Structures section of the Engineering Structures department, in collaboration with Witteveen+Bos. Both the relevance and nature of the topic spiked my interest, and after completing the thesis I can say I am pleased with the result.

I would like to thank all members of my graduation committee for their help and patience during the realization of this thesis. First of all I want to thank Mauro Poliotti, who provided me with guidance and feedback during our biweekly meetings. He helped me get the ball rolling and provided me with useful insights until the very end. I also want to thank Yuguang Yang for his critical yet helpful comments during our committee meetings, pointing me in the right direction. Both Anjali Mehrotra and Manimaran Pari I would like to thank for their specific knowledge on numerical modelling. Furthermore I would like to thank Nikolaas van Empel for giving me the opportunity to carry out my graduate internship at Witteveen+Bos and for engaging in various interesting discussions. I want to give a special thank you to Zhekang Huang for taking the time to help me overcome many challenges. His expertise and willingness to help played a big part in the completion of this thesis.

I want to thank my colleagues at Witteveen+Bos for welcoming me and helping me take my mind off things with light-hearted conversations at the coffee machine. In addition, I am grateful for the support of my friends, with whom I've shared many long study days. Last but not least, I am extremely thankful to my family and girlfriend for their continuous support throughout this intensive but valuable process.

Daniel Kallan
Delft, March 2023

Abstract

The use of precast Reinforced Concrete has been the norm for the construction of tunnel linings for decades. However, the use of Steel Fiber Reinforced Concrete is gaining popularity due to its beneficial mechanical properties, improved sustainability, improved durability, and lowered costs compared to traditional Reinforced Concrete (RC). The amount of reinforcing steel can be reduced significantly, lowering the costs and carbon footprint of a project making it an appealing alternative. One application of SFRC is found in tunnels making use of precasted concrete segments, typically built with a Tunnel Boring Machine (TBM). This type of tunnel is found in Amsterdam, namely the Noord/Zuidlijn: a metro line linking the north and south of the city. This project is used as a reference to perform a feasibility study on the use of SFRC and investigate its benefits.

The research involves a structural analysis of an SFRC design considering the loads and boundary conditions of the original Noord/Zuidlijn. The loads occur at different phases in the realization of the tunnel: transient, construction, and service phase. These loads can lead to various failure mechanisms, with the primary concern being tensile splitting of the concrete. Each phase is defined by a dominant component that governs its behaviour. During the transient stage, involving demoulding, stacking, and handling of the segments, the bending stresses inside the segment need to be checked. During the construction stage, the ring joints of the segments presents a weakness and need to be checked for spalling and/or splitting of the concrete. During the service stage, the longitudinal joint needs to be checked for splitting of the concrete and the global cross sectional stresses of the lining need to be examined.

Numerical models are created to assess SFRC's performance in the governing parts of the tunnel during the three phases, with the addition of identical RC models as a basis for comparison. The general bending and shear stresses, as well as localised splitting and spalling stresses, are investigated in both the Serviceability Limit State and Ultimate Limit State. The structural behaviour of SFRC corresponded with the characteristics found in literature, with a higher initial cracking load than RC and a more stable crack propagation due to its residual tensile strength. The peak strength of SFRC is found to be lower, but still passes all the checks. The results show that an SFRC design with the minimum fiber content of 30 kg/m^3 is sufficient for the transient and construction phases, but 40 kg/m^3 is needed for the service phase. The benefits of implementing SFRC in the Noord/Zuidlijn can be quantified in a steel reduction of 60%, which would mean a decrease in steel consumption of 3050 tons. The CO_2 emissions would decrease with 5500 tons, equivalent to the amount absorbed by 220.000 trees over the course of one year.

The concluding results can be used as guidance when opting for SFRC in a new bored tunnel project. The performed design checks show a governing load situation in both the construction phase and the service phase. The sufficiency of SFRC for the ring joint check during construction is governed by the splitting force between the loading shoes of the TBM. The magnitude of this splitting force depends on the size of the TBM, the characteristics of the soil, and the depth of the tunnel. A large diameter tunnel, high-friction soil, or deep tunnel will decrease the likelihood of a design with solely fibers. The same unfavorable conditions cause large internal bending moments which could pose problems for the longitudinal joint and global cross section check. A small diameter tunnel and a tunnel constructed in stiffer soil will increase the feasibility of a design making use of solely fibers.

Contents

List of Figures

List of Tables

1 Introduction

1.1. Background

The use of precast Reinforced Concrete (RC) segments has been the norm for the construction of tunnel linings for decades. However, the use of Steel Fiber Reinforced Concrete (SFRC) is gaining popularity due to its beneficial mechanical properties, improved sustainability, improved durability, and lowered costs compared to the traditional Reinforced Concrete (RC) segments. The beneficial mechanical properties of SFRC include improved ductility, toughness, flexural strength, and shear strength [1]. Additionally, SFRC is a good fit when opting for a sustainable and durable design. The amount of steel can be reduced significantly, lowering the carbon footprint of a project making it a more sustainable material than RC. The improved durability of SFRC arises from the reduction in crack width and porosity which is achieved through the use of a low water/cement ratio and the incorporation of diffused reinforcement [2]. The production of SFRC segments is also more straightforward and cost-effective compared to RC segments [3] [4].

A specific application of SFRC can be seen in tunnels constructed using a Tunnel Boring Machine (TBM). The research of this report will be applied to the Noord/Zuidlijn (North/South line). The Noord/Zuidlijn is a metro line crossing Amsterdam, partly constructed with the use of a TBM to preserve the historical city center. The tunnel is constructed in a region characterized by soft soil layers and a high ground water table. The part of the route which is constructed using the TBM and precast tunnel linings is shown in Figure 1.1. The metro line consists of two tunnel tubes that run horizontally or vertically, depending on their location along the route, and ranges in depth from -15 to 30 meters.

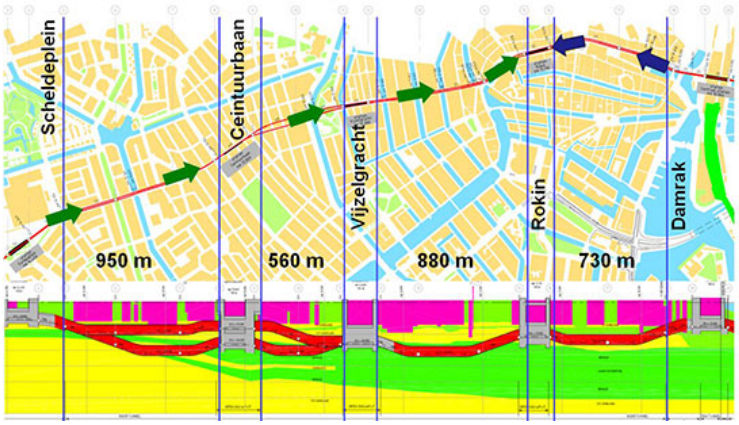

Figure 1.1: Plan and cross section of Noord/Zuidlijn drilling route [5]

1.2. Problem statement

The Noord/Zuidlijn has been constructed using a Tunnel Boring Machine and precast RC segments. The production of these RC segments is costly and time consuming due to the various types of reinforcement which are incorporated in a complex reinforcement cage. The reinforcement cage consists of large amounts of steel and has to be manufactured with high precision. Furthermore, the use of RC segments can face difficulties as a result of transport, installation, or unforeseen circumstances during their service life. There is a susceptibility to cracks and possibility of brittle failure [1]. Another issue that arises is the corrosion of rebars, which could lead to concrete spalling [6]. This problem is especially serious in The Netherlands, where the high water table makes the concrete more susceptible to water infiltration, which in turn can lead to corrosion of the reinforcement.

During construction of RC tunnel segments, the Tunnel Boring Machine (TBM) generates significant forces that require a large amount of splitting reinforcement to prevent concrete cracking and crushing. SFRC could present a solution to these problems due to its improved mechanical properties. In addition to the mechanical benefits, the production of SFRC segments is simpler and more cost-effective than RC segments. The complex reinforcement cage including the various reinforcement types can be replaced with fibers, reducing material costs, labor costs, and production time. Moreover, the production of RC segments negatively influences the total CO_2 emission of a project. Besides the well-known polluter of regular cement, high amounts of steel are used, of which the production emits tons of CO_2.

The application of SFRC has been used in several metro tunnels worldwide. These implementations were successful and will be elaborated on in Chapter 4. However, these projects differ in two ways to the Noord/Zuidlijn. Firstly, the designs used a combination of SFRC and RC due to the lack of experience in working with SFRC. The structural contribution of fibers was often not accounted for and not experimented on extensively. Secondly, the soil type in these areas differs from the soft soil of the Netherlands. For these reasons, it is interesting to research the feasibility of using SFRC in tunnel linings of the Noord/Zuidlijn.

1.3. Objective

The objective of this thesis is to explore the possibility of using SFRC in tunnel linings of the Noord/Zuidlijn. By doing so, a comparison between the behaviour of SFRC and RC can be made. The main research question is as follows:

What are the potential benefits in terms of mechanical properties, sustainability, and cost efficiency if traditional Reinforced Concrete is replaced with Steel Fiber Reinforced Concrete in tunnel linings of the Noord/Zuidlijn?

A new SFRC design will undergo the necessary structural checks in both the Ultimate and Serviceability Limit State to determine the least amount of fibers needed. This will be done using a numerical analysis, verified with analytically calculated results. A comparison between the original RC design and the new SFRC design will follow where different aspects will be evaluated such as structural performance, costs, sustainability, and durability.

The goal will be reached by first analysing the current Noord/Zuidlijn design to obtain requirement, boundary conditions, and loads. These will be used as input for both the analytical and numerical checks. Next, the available literature regarding the use of SFRC in tunnel lining will be analysed to find knowledge gaps and previous applications of the material. The relevant literature consists of research papers on the subject, as well as various design codes of SFRC. From the literature, constitutive laws of SFRC and requirements such as crack width are used for the analytical and numerical analysis. The obtained information will be applied to several models representing the different aspects of tunnel design. This will be done by performing checks on the structural integrity by analytical and numerical methods, considering a governing cross section of the tunnel. The goal is to investigate the plausibility of using SFRC in tunnel linings of the Noord/Zuidlijn and to see what possible benefits there are compared to the original design.

2

Bored segmented tunnel

This chapter provides the basic aspects of a tunnel design, complemented with information from the Noord/Zuidlijn. The goal is to provide requirements, loads, structural layout, failure mechanisms and desired structural checks for the concept of an SFRC tunnel in general, and subsequently the Noord/Zuidlijn. This is done by listing general functional and spatial requirements of a tunnel, providing all relevant loads acting in different phases of tunnel design, ranging from demoulding of a segment till the service phase of the structure. Furthermore, the most important failure mechanisms in a general tunnel design are broken down. Lastly, the consequent structural checks based on these failure mechanism are provided.

2.1. Requirements

Tunnels serve a variety of purposes, with the two main categories being traffic and conveyance. Traffic tunnels are used for roads, railways, and metro tracks, while conveyance tunnels are used to transport materials and infrastructure, such as water, gas, cables, pipes, and oil. The function and purpose of a tunnel determines the specific requirements and dimensions that must be met. A traffic tunnel for a three-lane highway tunnel will require a significantly larger diameter than a single metro track tunnel.

Each type of tunnel has specific requirements that must be met, and even within a specific project, there may be additional unique requirements. These requirements can be divided into two categories: functional and structural. Functional requirements for a traffic tunnel include ensuring that the tunnel has sufficient capacity, a large enough cross section for the type of traffic, and sufficient utilities such as lighting, ventilation, traffic control, and IT facilities. Safety must also be guaranteed through emergency exits, fire protection, a pumping system, and structural safety. Structural requirements for a traffic tunnel include ensuring the stability of the structure for every phase of construction, the ability to withstand internal and external forces, minimizing surface settlements, making the structure constructible and maintainable, and future-proofing the structure to account for potential future developments.

2.2. Specification

The type of tunnel of interest for this research is the bored tunnel. Bored tunnels are used in densely populated areas where the disturbance at ground level needs to be minimized. Bored tunnels are supported using tunnel linings, which are created by a Tunnel Boring Machine (TBM) that bores the tunnel and simultaneously places precast concrete segments to form a ring. After installing one ring, the TBM moves forward and installs the next ring ultimately forming a sequential tunnel able to withstand the weight of the soil. Tunnel rings can be single or double layered, with single layered being most common in the Netherlands. The structural design of the tunnel linings is determined by the loads the tunnel needs to withstand, including soil and water pressures, and production and construction loads. The design includes the thickness of segments, number of segments per ring, and the amount of reinforcement.

2.2.1. Cross section

The cross section of a tunnel is determined by the requirements of the tunnel. The most important factor for a tunnel is the clearance envelop of the traffic type. Due to the round shape of the tunnel, utilities and facilities can be facilitated at the sides, top, and bottom of the tunnel. An indication of the layout as a result of the clearance envelop is shown in Figure 2.1.

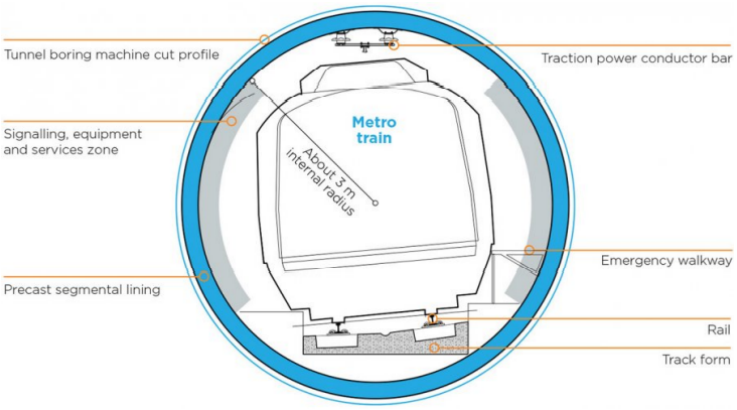

Figure 2.1: Cross section metro tunnel [7]

Reinders [7] provides an overview where indications of internal tunnel diameters are given per profile use. Profile uses range from a single lane guided bus to a double track train line. The profile of interest, single track metro line, gives an internal diameter of 5.95 meters. This indication comes very close to the actual internal diameter of the Noord/Zuidlijn, which is 5.82 meters.

The cross section of the tunnel determines the size of the TBM. The diameter of the TBM will be slightly bigger than the (external) diameter of the tunnel.

2.2.2. Segments and joints

A tunnel lining is composed of several segments, the number of which depends on the size of the cross-section. One of these segments is crucial in completing the ring and is called the key segment. It is smaller and wedge-shaped, making it easier to fit into place. To ensure quality and consistency, the segments are manufactured in a controlled environment, typically made of reinforced concrete. Once the segments have been assembled into rings, they are positioned in a sequence to form the tunnel. In cases where the tunnel route includes a bend, the rings can be cone-shaped to accommodate this curve. This means that the front and back faces of the ring will not be parallel.

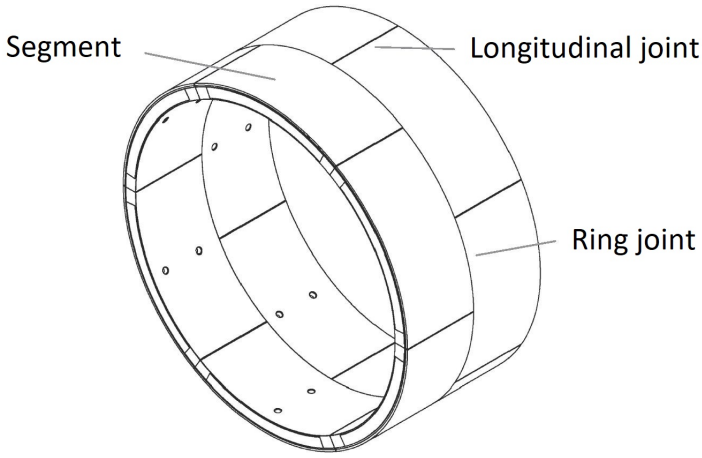

Figure 2.2: Joints in tunnel linings [7]

Each segment has rubber gaskets to ensure water tightness and guiding slots for easy assembly. Two types of joints can be distinguished in a sequence of tunnel linings: ring joints and longitudinal joints. These are shown in Figure 2.2. The longitudinal joint (or radial joint) is located between two segments in the same ring. The ring joint (or circumferential joint) is located between segments of adjacent rings. The rings are placed in a masonry layout to make sure longitudinal joints are not continuous for the best force transfer.

The joint connections can be done in various ways, which are listed below and visualised in Figure 2.3.

- Flat joint
- Tongue and groove joint
- Hinge joint
- Cam and pocket joint

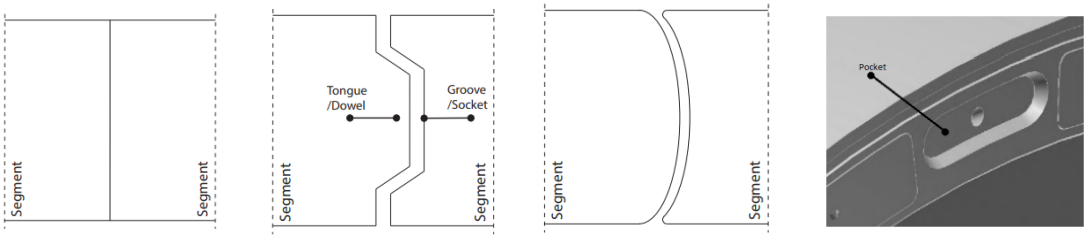

(a) Flat **(b)** Tongue and groove **(c)** Hinge **(d)** Cam and pocket

Figure 2.3: Different type of joints [8]

The flat joint is the most simple one and is characterised by coupling solely through friction. This type of joint is considered state of the art and most commonly used for longitudinal and ring joints. However, assembly of rings is quite hard with flat joints. For that reason, plastic dowels can be used to make the connection of the ring joint easier by guiding the dowel of one segment into the opening of another segment. The load transfer of a flat joint is very efficient and can result in less end reinforcement. With this type of joint, the connection between rings is either concrete to concrete or with a packing material in between so loads can be transferred better. Materials which can be used are: fiberboard, plywood, and kaubit (a bituminous material with very low stiffness). If segments are not

installed precisely, the thrust force of the TBM can cause high stress localisations when segments are connected concrete to concrete.

The tongue and groove joint is a geometric way to connect rings by having a groove in one ring and a tongue in the other sliding into each other. This way of coupling provides a solid connection if done correctly. However, there is a risk of high localised stresses if the connection is not done perfectly. For this reason, the tongue and groove method is less common.

The hinge joint can be done for the longitudinal joint and is the only joint which allows rotation, with one convex side and one hollow side. This type of connection cannot take up moments but dissipates it instead. Mainly two-layered lining systems have hinge joints, which is not common in the Netherlands. This is also due to the issue of water leakage which can occur with a hinged connection.

The cam and pocket joint is similar to the tongue and groove joint as it connects the ring joint through geometry. This type of joint has not one continuous, but several intermittent grooves which are called pockets. The cam (or pin) slides into the pocket in a similar manner as the tongue and groove. There is a chance of localised stresses making it a less commonly used method.

2.2.3. Longitudinal joint

An important aspect in tunnel design is the longitudinal joint. Understanding the behaviour of this joint under different loading conditions is vital for a safe design. Longitudinal joints provide a weak link during the service life of a structure in two ways: strength wise and serviceability wise. A joint has lower stiffness, strength, and bending capacity compared to the main segment, and can experience leaking when large rotations are applied [6]. Because of this, longitudinal joint failure can be a governing failure mechanism in tunnels. The driving forces are the normal force and bending moment generated by the ground and water pressure.

The most common type of longitudinal joint, flat joint, is characterised by concrete to concrete contact. The soil and water pressure acting on a tunnel cause a normal force in the lining which is transferred by this concrete to concrete contact. Compressive stresses arise, which are generally far below the capacity of the concrete. However, when a bending moment is introduced, the stress distribution changes over the height of the joint and the joint has the possibility of opening up. This happens when the stress approaches zero at one end and increase at the other end. Whether a joint opens up or not, and the magnitude of the accompanied stresses, are dependent on the magnitude of both normal force and bending moment. The height of the joint and the thickness of the segments also play a role.

Janssen theory

The relationship between moment and rotation of a joint is described by Janssen [9] with a nonlinear model. Janssen proposed the modelling of an equivalent concrete beam, which captures the rotation between two segments. This equivalent beam is not able to transfer tensile forces and the height is taken as equal to the joint height, as seen in Figure 2.4.

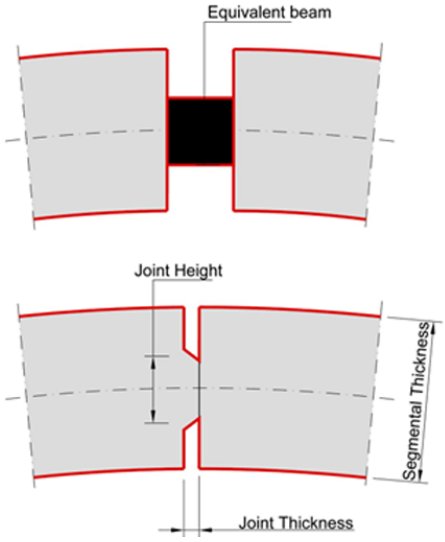

Figure 2.4: Longitudinal joint (bottom) modelled as an equivalent beam (top)

The proposed model distinguishes two stages in the bending moment-rotation relationship: a linear and nonlinear stage. The two stages are described by Equation 2.1, where the first equation describes the linear part and the second equation describes the nonlinear part.

$$\phi = \begin{cases} \dfrac{12M}{Eh^2b}, & \text{for } M < \dfrac{1}{6}Nh \\ \dfrac{8N}{Ehb9(\frac{M}{M_{max}} - 1)^2}, & \text{for } M \geq \dfrac{1}{6}Nh \end{cases} \tag{2.1}$$

Here M is the bending moment in the joint [Nmm], E is the Young's Modulus of the concrete [N/mm^2], h is the joint height [mm], b is the joint thickness [mm], and M_{max} is the maximum moment the joint can take [Nmm]. This maximum moment is calculated with:

$$M_{max} = \frac{1}{2} \cdot N \cdot h \tag{2.2}$$

These equations provide an moment-rotation relationship for a given normal force N. The outcome changes with different compressive normal forces present in the lining.

Figure 2.5 shows the moment-rotation behaviour of a longitudinal joint with dimensions and material characteristics as in the Noord/Zuidlijn design. The height of the joint is 160 mm and a normal force of -1000 kN/m is used. The moment-rotation curve can be seen to approach M_{max}, denoted with Capacity in the figure. However, the capacity acts as an asymptote and will never be reached.

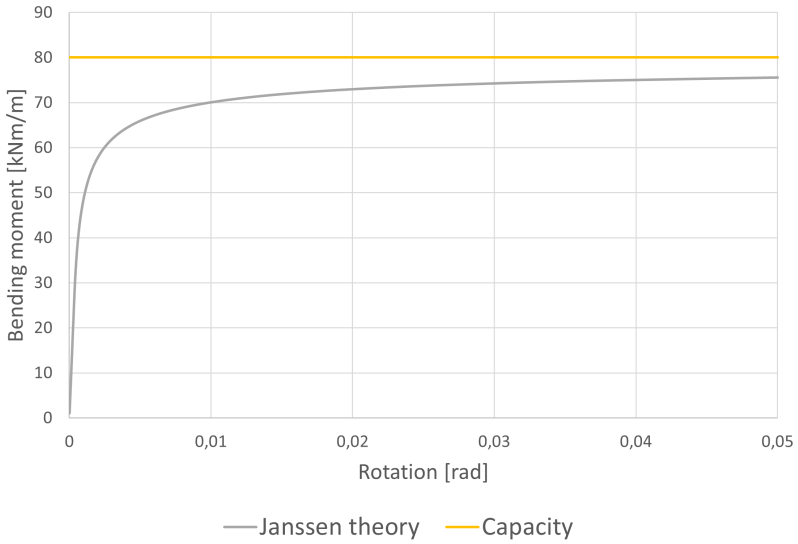

Figure 2.5: Longitudinal joint behaviour using Janssen theory

2.2.4. Ring joint

The ring joints play a significant role in transferring loads in longitudinal direction, i.e. the direction in which the tunnel propagates. Only the loading induced by the TBM will have an effect on the loads and stresses in the ring joint. The contact between segments is commonly done with packing material to spread the forces and avoid peak stresses in case of an eccentric loading from the TBM. Hardboard plates are often used as packing material and provide radial and tangential stiffness due to friction. This friction ultimately stiffens the tunnel structure. One condition for this stiffness to be present is the axial prestress in the tunnel, caused by the TBM loading. Concrete relaxation or deterioration of the hardboard plates can cause this prestress to decrease, causing a decreased stiffness of the tunnel. A solution to this problem is the use of couplers which allow for a radial coupling of the segment. This ensures a minimum amount of coupling between the rings.

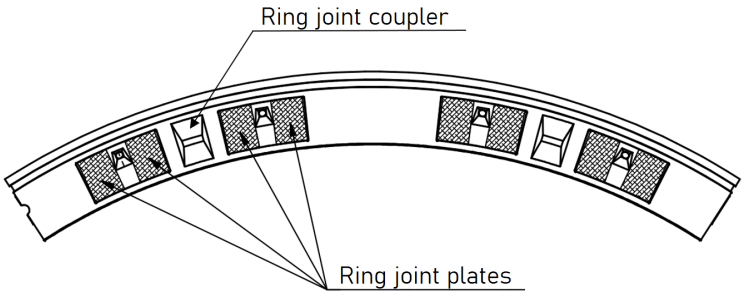

Figure 2.6: Ring joint layout

Figure 2.6 shows this common layout of a ring joint, taken from the Noord/Zuidlijn design. The segments transfer loads through the hardboard plates at four points along the segment, and are coupled with couplers at two points along the segment.

2.3. Loads

This section will provide the numerous loads acting on a single segment and the tunnel lining as a whole. The loads are divided in three phases: transient phase, construction phase, and service phase.

2.3.1. Transient phase

The transient phase is characterised by production, storage, handling, and transport of individual segments which make up a tunnel lining.

Demoulding

The first loading condition of a segment occurs during the production process. A precasted SFRC segment is manufactured under controlled conditions in a manufacturing plant. The desired mixture is poured into a mould, with or without a reinforcement cage, and cured for a certain amount of time. This can be done with heat treatment to speed up the process. After reaching a certain strength, segments can be demoulded and subsequently stacked.

Demoulding takes place in one of two ways: mechanically or with vacuum lifting pads, as shown in Figure 2.7. For fiber reinforced concrete, it is advised to demould using vacuum pads to reduce stresses by means of a greater supporting area [10].

(a) Vacuum lifting pads [11]

(b) Mechanically [12]

Figure 2.7: Two ways of demoulding a precast tunnel lining segment

A segment is lifted with the vacuum pads and placed upside down for segment stacking. The loading during this demoulding process comes only from the self weight. The effect of the self weight depends on the support conditions and obtained strength after a certain amount of curing. The shear force and bending moment due to the self weight have to be checked against the capacity of the fiber reinforced concrete. The self weight is calculated with:

$$g_k = \gamma_c \cdot t \cdot b \tag{2.3}$$

Where g is the self-weight [kN/m], γ_c is the density of the concrete [kN/m^3], t is the thickness of the segment [m], and b is the width of the segment [m]. The self-weight is calculated as a line load along the curved side of the segment. The structural scheme depends on the spacing of the vacuum pads and is depicted in Figure 2.8. The self weight provides a distributed line load and the vacuum pads act as supports.

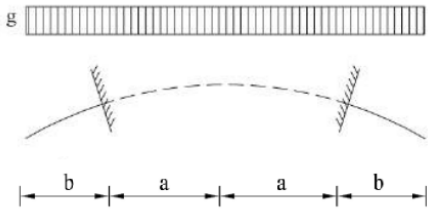

Figure 2.8: Structural scheme demoulding load [7]

The maximum bending moment can occur in the middle of the segment or at the location of the supports and is equal to:

$$M_k = max \begin{cases} \frac{1}{2} \cdot q_k \cdot b^2 \\ \frac{1}{8} \cdot q_k \cdot (2a)^2 \end{cases} \tag{2.4}$$

Stacking

The second loading condition of the transient phase occurs when segments are stacked. The segments of one tunnel lining ring are stacked on top of each other separated by wooden blocks. Loading is caused by the self weight of the segments, as well as eccentrically stacking, which is shown in Figure 2.9.

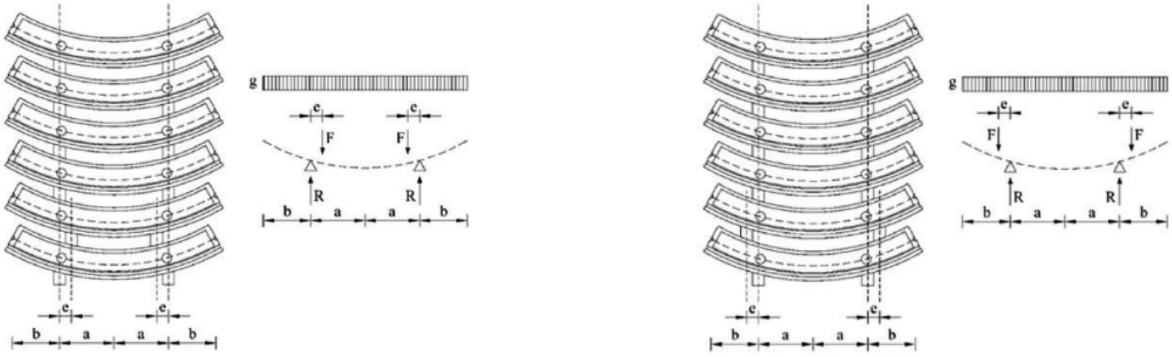

(a) Inward load eccentricity

(b) Outward load eccentricity

Figure 2.9: Loading condition and structural scheme for segment stacking for bottom segment [13]

The subsequent loading is schematized for the bottom segment which is governing. The maximum bending moment can either occur at the cantilevering part of the segment when there is a outward eccentricity, or in the middle when there is an inward eccentricity. Therefore the governing moment is the maximum of the two and is calculated to be:

$$M_k = max \begin{cases} \frac{1}{8} \cdot q_k \cdot (2a)^2 - \frac{1}{2} \cdot q_k \cdot b^2 + F_k \cdot e \\ \frac{1}{2} \cdot q_k \cdot b^2 + F_k \cdot e \end{cases} \tag{2.5}$$

Handling

Handling of segments in the factory, onto the transport, and inside the construction site needs to be accounted for. When handling a segment, only the middle is supported. This creates two cantilever sides which give rise to a bending moment. The maximum bending moment is equal to:

$$M_k = \frac{1}{2} \cdot q_k \cdot (\frac{l}{2})^2 \tag{2.6}$$

2.3.2. Construction phase

During the construction phase, the tunnel segments are placed to form linings which are placed sequentially by use of the TBM.

Thrust force

The most significant loading during construction is the thrust force of the TBM. As briefly mentioned in the introduction, the TBM pushes itself forward using already installed tunnel linings with the use of hydraulic jacks. These hydraulic jacks have a relatively small contact area giving rise to high stresses. The applied loading on one segment depends on the weight of the TBM, the friction which is encountered, and the amount of jacks used. A partial loading factor can be used for the load.

Grout pressure

The diameter of the TBM is slightly bigger than the outer diameter of the tunnel lining, which creates a gap giving rise to possible settlements at the surface. For this reason grout is injected to fill the gap and prevent settlements. The grout pressure has to be bigger than or equal to the total soil pressure and will provide loading to the tunnel linings. The exact magnitude of this load is difficult to calculate due to the uncertain distribution of the grout. The load will be similar to the ground pressure and is hard to include separately in a three dimensional numerical model. For that reason it is not included in the analyses.

2.3.3. Service phase

The final loading condition is during the service life of the structure. Concrete has reached it's desired strength and transient and construction loads are no longer present. There are several loads which are present in this final phase. The most important ones are listed below.

Tunnel self-weight

The self-weight of the tunnel depends on the volume and density of the concrete. The volume can be estimated by multiplying the cross sectional area with the width of a ring. The area of a cross section can be estimated with the inner and outer diameter as follows:

$$A = \frac{1}{4} \cdot \pi \cdot (D_o^2 - D_i^2) \tag{2.7}$$

where A is the concrete area of the cross section of the tunnel lining [m^2], D_o is the outer diameter [m], and D_i is the inner diameter [m]. The self weight of one ring can then be calculated with:

$$g = A \cdot b \cdot \gamma_c \tag{2.8}$$

where g is the self-weight of one tunnel lining ring [kN], b is the width of the ring [m], and γ_c is the unit weight of concrete.

Surface load

Surface load is defined as the load at ground level, which is transferred through the soil onto the underground structure. This can consist of vehicles and buildings for example. The surface load add to the soil pressure which acts deep in the soil onto the tunnel.

Ground and water pressure

The loading due to the soil depends on the type of soil and the depth of the structure. The combination of water pressure and ground pressure gives the total soil loading. Total ground pressure can either be

modelled as radial or split up into vertical and horizontal pressure. The latter is chosen. The following formulas apply:

$$\sigma_v = u + \sigma'_v = \gamma_{wat} \cdot H + \gamma' \cdot H \tag{2.9}$$

$$\sigma_h = u + K_0 \cdot \sigma'_v \tag{2.10}$$

where σ_v is the vertical soil pressure [kN/m^2], u is the water pressure [kN/m^2], σ'_v is the effective vertical soil pressure [kN/m^2], γ_{wat} is unit weight of water [kN/m^3], γ' is the effective soil unit weight [kN/m^3], σ_h is the horizontal soil pressure [kN/m^2], H is the depth [m], and K_0 is the coefficient of neutral horizontal soil stress [-]. There are several methods for schematizing the horizontal soil pressure. The most accurate being the one shown in Figure 2.10 where the pressure varies over the height.

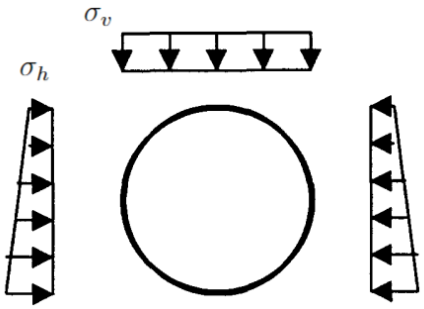

Figure 2.10: Soil pressure

In reality there are multiple soil layers with different characteristics. This will result is a more complicated calculation which will be done in Chapter 3.

Other mentionable loads

Besides the main loading aspects mentioned above, there are some less governing loads that can be taken into account. This includes: temperature loads, traffic load, loads of installations, and special loads such as a fire or explosion.

2.4. Structural checks

Section 2.3 stated the loading situations which occur when building a tunnel. These loads will be used to perform a numerical analysis, which will partly be verified with analytical calculations. The loads were presented in three phases. During every phase, stability and strength of global and local elements needs to be ensured.

This thesis will not focus on the stability of the tunnel and soil during and after construction. Aspects like face stability and induced settlements fall out of the scope of this research. What will be focused on is the behaviour of segments during production, construction, and service life. Table 2.1 provides an overview of the structural checks which are of importance for this research.

Table 2.1: Structural checks for different components

Phase	Component	Structural checks
Transient phase	Segment cross section	Bending stresses
Construction phase	Ring joint	Compressive stresses at shoe
		Spalling stresses between shoe
		Tangential splitting stresses under shoe
		Radial splitting stresses under shoe
Service phase	Longitudinal joint	Compressive stresses at contact area
		Splitting stresses under contact area
	Global cross section	Bending stresses
		Shear stresses

The table is divided in the aforementioned phases, with the relevant components per phase and several structural checks per component. The segment cross section refers to the bending stresses in one segment induced by its own or weight and the weight of others, while the global refers to the stresses inside all segments induced by ground and soil loading. Both refer to general bending and/or or shear stresses, not taking into account localised stresses. The two remaining components, ring joint and longitudinal joint, both give rise to localised stresses.

The checks highlighted in gray are of importance in general tunnel design, but will not be checked. This is due to fact that the failure mechanism is based on compressive stresses and SFRC does not influence the compressive behaviour significantly. All available structural codes and guidelines regarding designing with SFRC advise to use the same compressive behaviour as RC [14] [15] [16]. Because the compressive behaviour is assumed equal to that of RC, the outcome of the relevant checks will not differ from the original design of the Noord/Zuidlijn and are therefore redundant.

2.4.1. Segment cross section

The structural check of segments during the transient phase is very straightforward. The three loading stages - demoulding, stacking, and handling - give rise to bending stresses in the segments that could cause cracking or failure. The governing bending moment during each of these stages is calculated and compared with the capacity of the section will be calculated in section 4.1.3.

2.4.2. Ring joint

During construction of the tunnel linings, the TBM generates significant forces with its hydraulic jacks. The load of the jacks is transferred with so-called 'shoes' onto the segments, where two shoes per segment is the standard. The loading is captured by the ring joint and transferred to consecutive rings via the hardboard plates. The segment is checked for both spalling between the shoes and splitting underneath each shoe. A distinction is made between tangential and radial stresses. Tangential stresses

in are in the direction of the length of the segment, while radial stresses are in the direction of the thickness of the segment. In other words, tangential stresses can be seen when looking at the front of a segment, and radial stresses when looking at the side of a segment.

Tangential spalling stresses between shoes
The loading by the two shoes generates tensile stresses between the shoes which can lead to concrete spalling. The internal forces can be schematized using a strut-and-tie model. Figure 2.11 shows the tensile strut which forms at the surface, between the shoes.

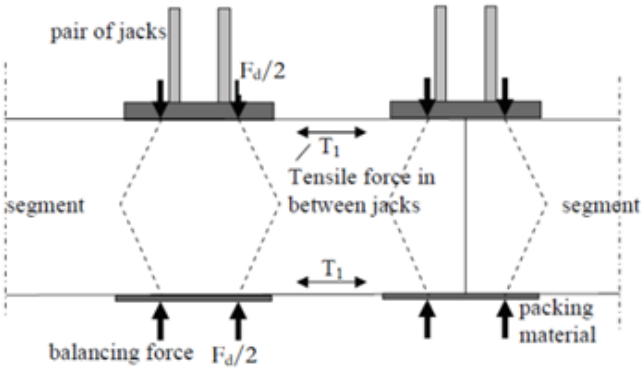

Figure 2.11: Spalling stresses between shoes [7]

This tensile force is normally taken up by splitting reinforcement which can be calculated by dividing the splitting force by the yield stress of steel.

Tangential splitting stresses under shoes
The loading by the two shoes also generates tensile stresses underneath each shoe. A tensile strut occurs in tangential direction, as shown in Figure 2.12.

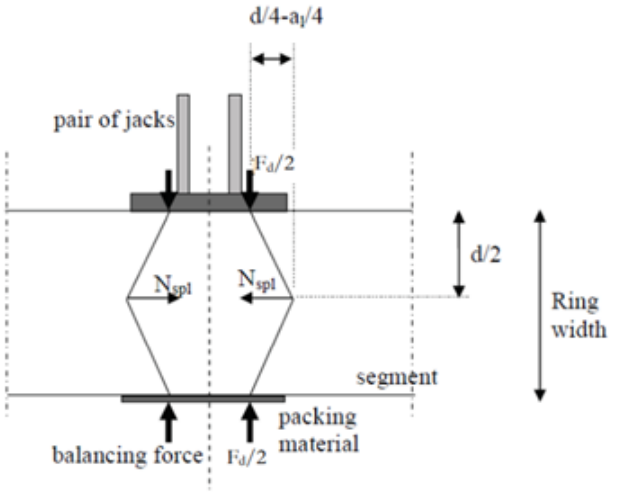

Figure 2.12: Tangential splitting stresses under shoe [7]

This tangential splitting force is also taken up by splitting reinforcement in RC structures.

Radial splitting stresses under shoes

The show of the TBM does not span over the entire thickness of the segment. This gives rise to a tensile strut in radial direction, which can be seen when looking at the side of a segment as shown in Figure 2.13.

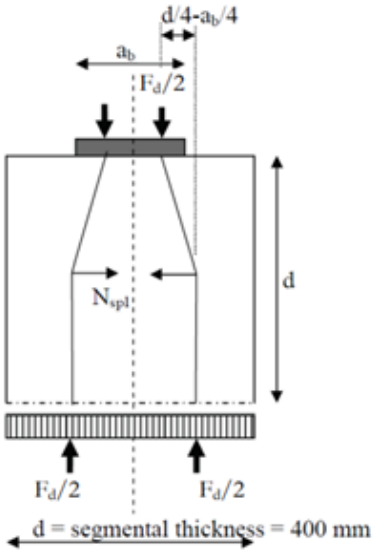

Figure 2.13: Radial splitting stresses under shoe [7]

This radial splitting force is also taken up by splitting reinforcement in RC structures.

2.4.3. Longitudinal joint

The cross sectional forces mentioned in 2.4.4 introduce stresses in the longitudinal joint. The combination of normal force and bending moment cause both compressive stresses at the surface, as tensile splitting stresses under the surface. The latter will be checked.

Splitting stresses under contact area

The normal force generates a tensile strut in the concrete, as in shown in Figure 2.14. The addition of a bending moment can shift and increase this tensile stress.

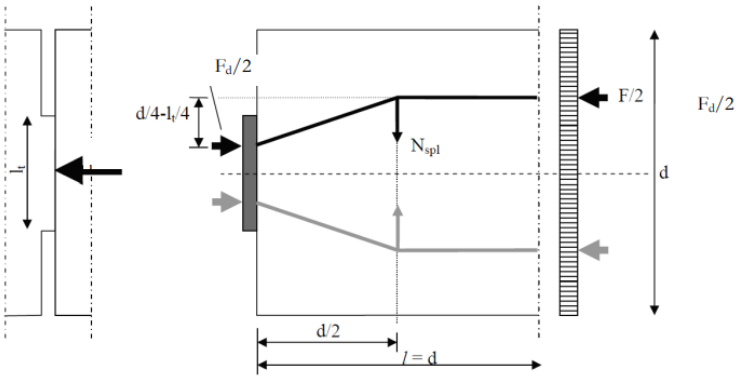

Figure 2.14: Splitting stresses under contact area [7]

These tensile stresses are also taken up by splitting reinforcement in RC structures.

2.4.4. Global cross section

During service life, the ground and soil pressure causes a normal force, bending moment and shear force into the lining. The acting bending moment may not exceed the moment capacity of the material in all parts of the tunnel lining. Similarly, the shear stress may not exceed the shear capacity of the material. Both the moment and shear capacity are increased to a certain extent by the compressive normal force in the lining. Figure 2.15 shows a simple sketch of the forces in the lining.

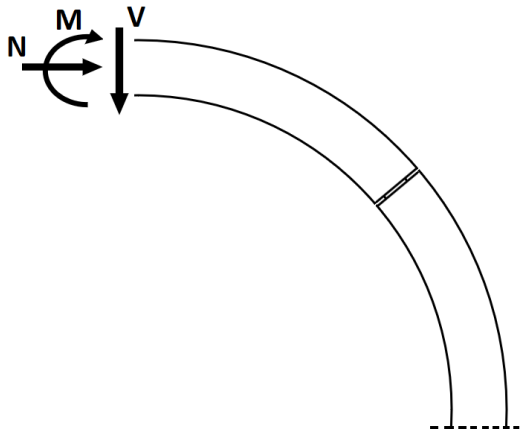

Figure 2.15: Internal forces due to soil and water pressure

3

Noord/Zuidlijn design

The previous chapter provided an overview of the key aspects of general tunnel design. This chapter will provide detailed information about the tunnel of interest: the Noord/Zuidlijn. This information will be implemented in the feasibility study of using SFRC in the configuration of the Noord/Zuidlijn.

3.1. Boundary conditions

The Noord/Zuidlijn is a metro line in Amsterdam that connects the northern and southern part of the city. It runs through eight stations in total, six of which were newly constructed for the line. Only a part of the route is underground and constructed using a Tunnel Boring Machine, as mentioned in the introduction. Figure 3.1 highlights the part which is constructed with a TBM in black, with green markers for every station.

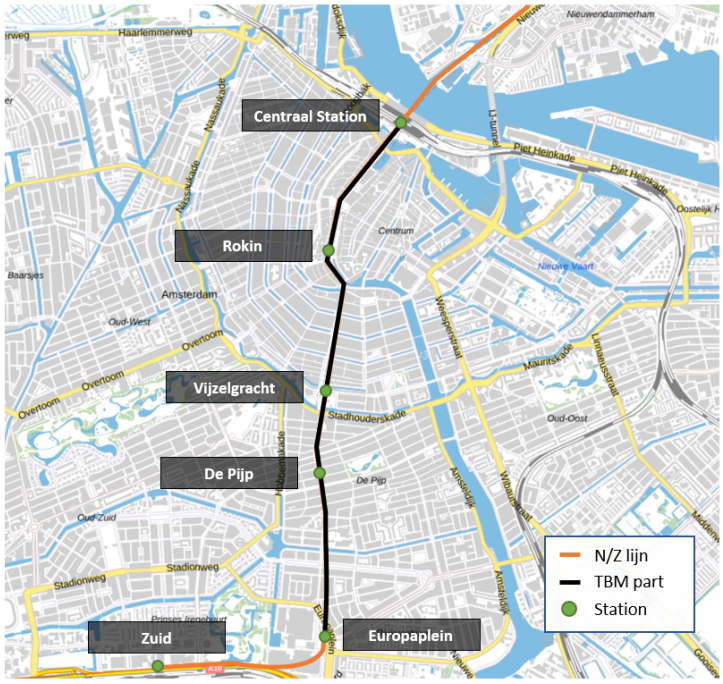

Figure 3.1: Noord/Zuidlijn route through city center

The orientation of the tunnels varies along the route of the Noord/Zuidlijn. The tunnels are aligned horizontally as a default, but are aligned vertically between station Vijzelgracht and Europaplein as a consequence of limited space.

3.2. Soil conditions

This section provides the soil conditions of Amsterdam. These are characterised by soft layers such as sand, clay, and peat, which made the construction of the Noord/Zuidlijn quite challenging. The original design worked with the soil profile as shown in Figure 3.2, which is typical for the Amsterdam soil. he tunnels are located at a depth of 30 meters beneath ground level.

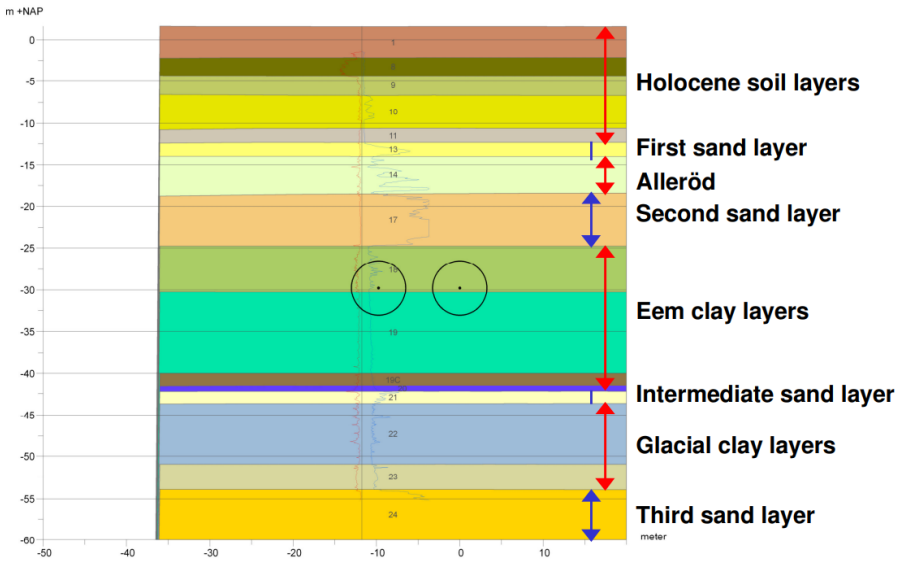

Figure 3.2: Typical soil profile Amsterdam [17]

There are a total of sixteen layers to be distinguished and each layer has its own mechanical properties. These properties will be used for the numerical model and can be seen in Appendix A. In general, the Amsterdam soil consists of several permeable sand layers with clay layers in between. The tunnels are mainly located in the Eem clay layers and second sand layer. Only the eastern tunnel stretch between station Vijzelgracht and Europaplein are located above the second sand layer [17].

3.3. Dimensions of tunnel

Figure 3.3 shows the original design of the tunnel ring which was used for the Noord/Zuidlijn. The ring consists of five normal sized segments and one smaller key segment. As explained in section 2.2.2, tunnel rings are placed in a staggered way to prevent continuous joints. This can be seen in Figure 3.3 by looking at the key segment 'K'. Two segments with the letter K can be seen, which represent two consecutive rings with the key segment of the second ring rotated clockwise.

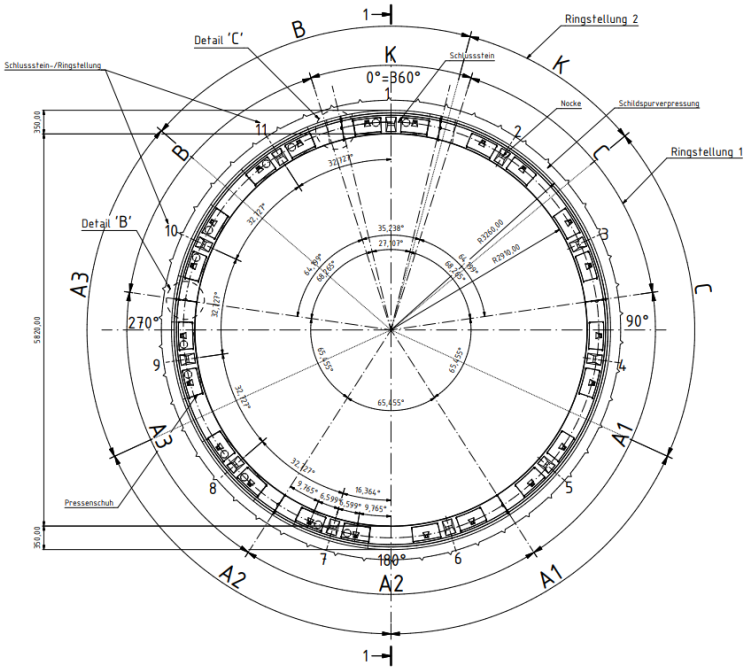

Figure 3.3: Original tunnel cross section [17]

Dimensions	
Number of segments:	5
Number of key segments:	1
External diameter:	6520 mm
Internal diameter:	5820 mm
Segment thickness:	350 mm
Segment width:	1500 mm
Concrete cover:	40 mm
Reinforcement	
Type 1 bending reinforcement:	⌀10 - 115 mm
Type 2 bending reinforcement:	⌀14 - 100 mm
Longitudinal reinforcement:	⌀10 - 135 mm
Bursting reinforcement long. joint:	$2 \cdot 13$ ⌀10 mm
Bursting reinforcement ring joint:	4 ⌀12 mm
Materials	
Concrete class:	C45/55
Steel class:	FeB 500

The dimensions, concrete material parameters, and reinforcement configuration are listed above. The reinforcement configuration consists of bending, longitudinal, and bursting reinforcement. The bending reinforcement has two types for different cross sections. The standard cross sections are designed with type 1, which is shown in Figure 3.4a, and the heavily loaded cross sections are designed with linings consisting of type 2 reinforcement. The longitudinal reinforcement is similar for all segments and cross sections and is shown in Figure 3.4b . The bursting reinforcement is different at ring joints and longitudinal joints, which are shown in Figure 3.4c and Figure 3.4d respectively.

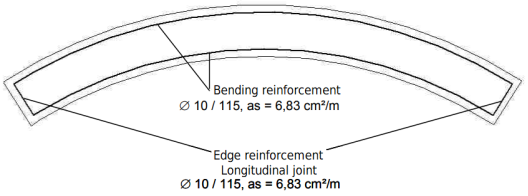

(a) Bending reinforcement

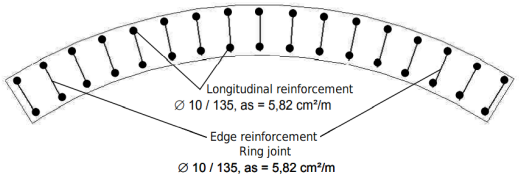

(b) Longitudinal reinforcement

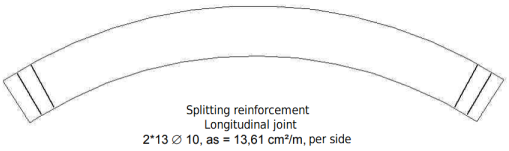

(c) Bursting reinforcement longitudinal joint

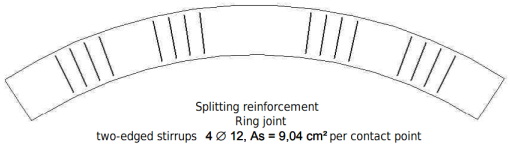

(d) Bursting reinforcement ring joint

Figure 3.4: All reinforcement configurations [18]

Figure 3.4 provides a basic overview of the reinforcement configuration. A more detailed reinforcement configuration can be seen in Appendix B.

3.4. Loads on tunnel

The formulas for calculating the loads during each phase have been given in section 2.3. This section will provide a quantification of these load to be used in the coming analyses.

Demoulding

In the case of the Noord/Zuidlijn, the segments dimensions are known. The dimensions concern the original RC design which is taken as a reference to the future SFRC design. The unit weight of SFRC is estimated lower than RC but higher than plain concrete, resulting in 2450 kN/m^3. The thickness of a segment is 350 mm and the segment is 1500 mm wide. Using these parameters in the equation for determining the self-weight during demoulding gives a characteristic self-weight of:

$$g_{segm,k} = 24.5 \cdot 0.35 \cdot 1.5 = 12.86 \text{ kN/m}$$

The maximum bending moment could occur either at the intermediate supports or at the middle of the segment. The governing bending moment is:

$$M_k = max \begin{cases} \frac{1}{2} \cdot 12.86 \cdot 0.9^2 = 5.20 \text{ kNm} \\ \frac{1}{8} \cdot 12.86 \cdot (1.77)^2 = 5.04 \text{ kNm} \end{cases}$$

So the maximum bending moment due to demoulding is 5.20 kNm.

Segment stacking

The Noord/Zuidlijn uses tunnel lining rings of six segments. This is the maximum amount of segments stacked on top of each other. The load on the bottom segment can be calculated by taking the distributed load $q_{segm,k}$ and multiplying with the length of the five segments on top. The load of the stacked segments is transferred through the two wooden blocks onto the 6^{th} segment. The concentrated loads transferred through these wooden blocks are:

$$F_k = \frac{5 \cdot 12.86 \cdot 3.57}{2} = 114.78 \text{ kN}$$

The bottom segment is thus loaded with two concentrated forces and its own self-weight. If stacking is done eccentrically, moments and shear forces due to the point loads F are generated. A maximum eccentricity of 100 mm is considered, following ACI Report on Design and Construction of Fiber Reinforced Precast Concrete Tunnel Segments [19].

Eccentric loading can be either outward or inward, as explained in section 2.3. The case which presents the largest bending moment is governing and is calculated to be:

$$M_k = max \begin{cases} \frac{1}{8} \cdot 12.86 \cdot 3.57^2 - \frac{1}{2} \cdot 12.86 \cdot 0.9^2 + 114.78 \cdot 0.1 = 11.31 \text{ kNm} \\ \frac{1}{2} \cdot 12.86 \cdot 0.9^2 + 114.78 \cdot 0.1 = 16.69 \text{ kNm} \end{cases}$$

So the maximum bending moment due to segment stacking is 16.69 kNm.

Handling

The bending moment due to handling is easily calculated as:

$$M_k = \tfrac{1}{2} \cdot 12.86 \cdot (\tfrac{3.57}{2})^2 = 20.49 \text{ kNm}$$

Thrust force
The actual thrust loading is taken from the original design of the Noord/Zuidlijn. The TBM had a maximum pressing force of 44209 kN. This force was exerted by the entire TBM and can be divided by the amount of jacks, which is 11. This way, the following force per jack is obtained:

$$F_{TBM} = \frac{44209}{11} = 4019 \text{ kN}$$

Tunnel self-weight
The area of a cross section can be estimated with the inner and outer diameter. These are 5.82 m and 6.52 meter respectively, giving an area of:

$$A = \frac{1}{4} \cdot \pi \cdot (6.52^2 - 5.82^2) = 6.784 \text{ m}^2$$

The width of one ring is 1.5 meters and the unit weight of SFRC is assumed at 2450 kg/m^3 or 24.5 kN/m^3. This gives a self-weight per ring of:

$$g_{ring,k} = 6.784 \cdot 1.5 \cdot 24.5 = 249.3 \text{ kN}$$

Surface load
A surface load of 20 kN/m^2 is used as input for design calculations of the Noord/Zuidlijn [17]. This loading increases the soil pressure at the depth of the tunnel.

Ground + water pressure
The previous section provided the general soil profile of Amsterdam. The soil consists of numerous layers with different mechanical parameters. The soil characteristics needed to calculate the total soil pressure are the wet unit weight of a soil type γ_{wet}, the thickness of different layers H, and the coefficient of neutral horizontal soil stress K_0. The ground water table is assumed to be at ground level. The ground pressure on the tunnel will be calculated using these parameters and split up into vertical and horizontal pressure. For the numerical analysis, the characteristics of all soil layers are implemented in a 3D model. The pressure around the lining is calculated accurately by the software and differs around the lining. For the analytical verification, a simplification will be made by considering the soil pressure at the axis of the tunnel.

First the total vertical soil pressure is calculated by considering the thickness and wet unit weight of all layers up until the axis of the tunnel. The depth of the Noord/Zuidlijn is 30 meters below ground level and the water table is assumed equal to ground level. The corresponding total vertical soil pressure is then calculated to be:

$$\sigma_v = u + \sigma'_v = \gamma_{wet} \cdot H = 535 \text{ MPa}$$

Secondly the total horizontal soil pressure is calculated, by considering the total vertical soil pressure, which is divided into water pressure and effective soil pressure, and applying a lateral earth coefficient K_0. The total horizontal earth pressure is then calculated to be:

$$\sigma_h = u + K_0\sigma'_v = 403 \text{ MPa}$$

Code used for calculations can be seen in Appendix C.2

4

Literature study on SFRC

This chapter provides an overview of the material Steel Fiber Reinforced Concrete (SFRC). This is done by outlining the mix design, its material characteristics, its structural capacity, and its use in tunnel linings. Furthermore, the current state of research will be given by analysing the available literature on relevant projects where SFRC is implemented successfully.

4.1. Steel fiber reinforced concrete

SFRC differs from regular RC is several ways. SFRC is a composite material consisting of regular concrete mixed with small steel fibers. These fibers can replace normal reinforcement bars and act as minuscule reinforcement bars to improve the tensile strength and bridge cracks. As described in the introduction, SFRC has many beneficial mechanical properties in comparison with RC, providing a promising alternative. The beneficial properties are, among other things: improved ductility, improved toughness, improved flexural strength, and improved shear strength [1]. On top of that, the production of SFRC segments is simpler and cheaper compared to RC segments. Figure 4.1 shows the inside of SFRC and a close-up of the wet mixture.

(a) Close-up SFRC mix [20]

(b) SFRC [21]

Figure 4.1: Steel Fiber Reinforced Concrete

4.1.1. Mix design

SFRC is produced like conventional concrete, but leaving out the reinforcement bars and adding steel fibers into the fresh concrete mixture. The use of steel instead of other alternatives like polymers, glass, and natural provides certain benefits: economy, manufacture facilities, reinforcing effects and resistance to the environment aggressiveness [22]. The most important aspect of producing SFRC is finding a good balance between workability and mechanical behaviour. This is influenced by both the aspect ratio of the fibers as the fiber content. Both parameters will be explained in the following subsections. One of the main difficulties with producing SFRC is possible clumping of fibers. This can be caused by several factors [23]:

i The fibers may already be clumped together before they are added to the mix; normal mixing action will not break down these clumps
ii Fibers may be added too quickly to allow them to disperse in the mixer
iii Too high a volume of fibers may be added
iv The mixer itself may be too worn or inefficient to disperse the fibers
v Introducing the fibers to the mixer before the other concrete ingredients will cause them to clump together

To prevent this, the mixing procedure should be executed thoughtfully. There are several aspects which should be kept in mind:

- The fibers should be added last to the wet concrete
- Fibers should be added free of clumps, e.g. by passing them through a screen
- The concrete alone should have a slump of 50-75 mm bigger than the desired SFRC slump

The orientation of fibers is generally random. However, the direction of flow during casting can influence the orientation, as fibers tend to align with the direction of flow [24]. This can be taken as an advantage when orientation of the forces consequent stresses are known. The alignment of fibers has a significant influence on the load carrying capacity. Fibers aligned parallel with a tensile force will provide better resistance that fibers aligned perpendicular. Graybeal [24] found that the flexural tensile strength could be decreased significantly due to perpendicular alignment. The compressive strength on the other hand is not influenced by fiber alignment.

Fiber aspect ratio

An important parameter regarding steel fibers is the aspect ratio. This ratio is defined as the length of a fiber divided by the diameter (l/D). The aspect ratio plays a big role in the mechanical properties of the SFRC, as well as the workability of the concrete. The latter is depicted in Figure 4.2, where the effect of different aspect ratios is shown on the workability of concrete. This is measured with a compacting factor, where a higher factor means better workability. As can be seen, the same fiber content for every aspect ratio content gives different compacting factors. A higher aspect ratio decreases the workability.

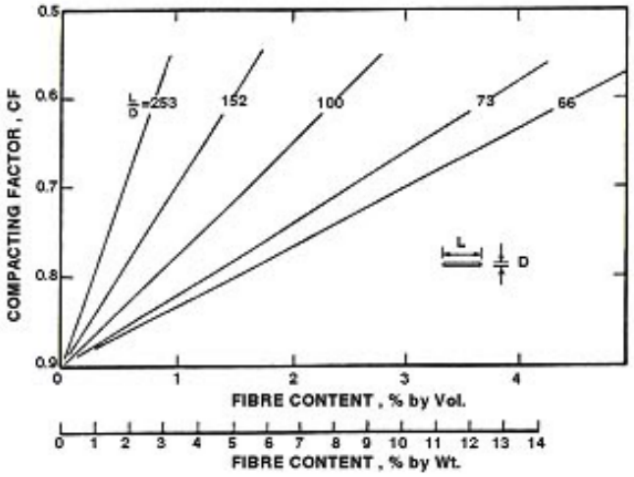

Figure 4.2: Effect of fiber aspect ratio on the workability of concrete [23]

The aspect ratio also has an effect on the tensile, compressive, and flexural strength of concrete. A higher aspect ratio shows a more pronounced increase in tensile strength than lower aspect ratios according to Abbass, Khan, and Mourad [25]. The compressive and flexural strength of SFRC is also proven to increase with an increasing aspect ratio. Yazıcı, Inan, and Tabak [26] tested specimens with aspect ratios ranging from 45 to 80 and found that a l/D ratio of 80 gave the highest compressive, tensile splitting, and flexural strength. Also here, a decreased workability was noticeable with increasing aspect ratio.

Fiber content

Fiber content plays a significant role in the mechanical properties of SFRC. Just with RC, more reinforcement generally means higher resistance to occurring loads. Same as with high aspect ratios, too much reinforcement can however work negatively as the workability decreases. A balanced consideration has to be made here.

A review of the literature on SFRC and its properties gave a preliminary insight into the beneficial properties and in what way these can be maximized. Abbass, Khan, and Mourad [25] and Song and Hwang [27] both state that when comparing different fiber contents, a higher fiber content gives higher tensile and compressive strength. Song and Hwang [27] also shares findings with Thomas and Ramaswamy [28] when considering the increase in split tensile strength and modulus of rupture due to the addition of fibers. The optimal fiber content is found to be 1.5% according to most tests. This means a higher fiber content generally means an increase in strength, but only up to a certain percentage. Only Song and Hwang [27] state that a fiber content of 2.0% gives the highest splitting tensile strength and modulus of rupture.

Similarly to RC, SFRC has a minimum amount of reinforcement to prevent brittle failure. For RC this standard is set by the Eurocode, which is widely accepted. For SFRC, there are multiple codes and guidelines produced in different years and different countries. Technical advisory committee CNR DT-204 [14] provides a minimum fiber percentage for structural applications. This volumetric percentage is set at 0.3% which is equal to 25 kg/m^3. Steel manufacturer Bekaert [29] provides a minimum fiber dosage depending on the fiber aspect ratio (fiber length / fiber diameter). With a fiber aspect ratio of 80, which will be used in this research, the minimum fiber content when using solely SFRC is given as 30 kg/m^3. As different codes have varying amounts of minimum fiber requirements, the strictest standard, 30 kg/m^3, will be worked with.

4.1.2. Material characteristics

Steel Fiber Reinforced Concrete behaves differently when loaded than Reinforced Concrete. A good way to compare different materials is through their load-displacement behaviour following a three point bending test. The general load-displacement curve for RC and SFRC differs mostly in the magnitude of the peak force and the post-peak behaviour. RC is able to handle loads of a higher magnitude, but fails relatively brittle. In contrast, SFRC handles loads of a lesser magnitude but has a ductile failure mechanism, which can be seen in Figure 4.3.

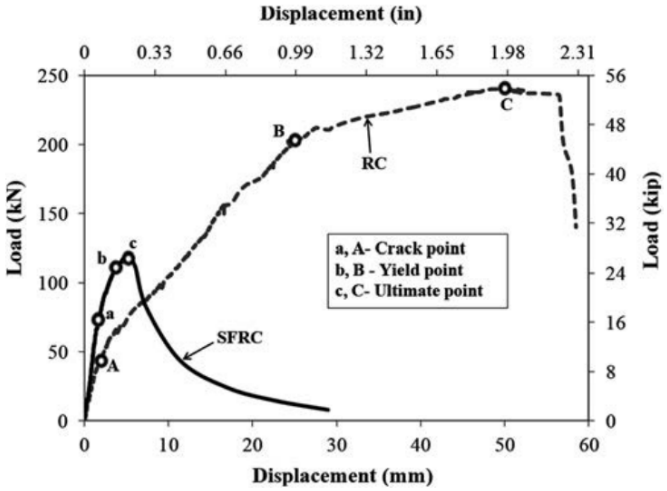

Figure 4.3: General load-displacement behaviour; SFRC and RC [30]

The main benefit of SFRC is its post-peak residual strength. It is important to understand and recognize the behaviour of SFRC in different loading stages, focusing on this post-peak behaviour. When looking at the general load-deflection curve of SFRC, four stages can be identified. Figure 4.4 shows these four stages, and the stress distribution over the height of the cross section for each stage. Figure 4.5 shows the crack propagation and fiber action in each of these four phases.

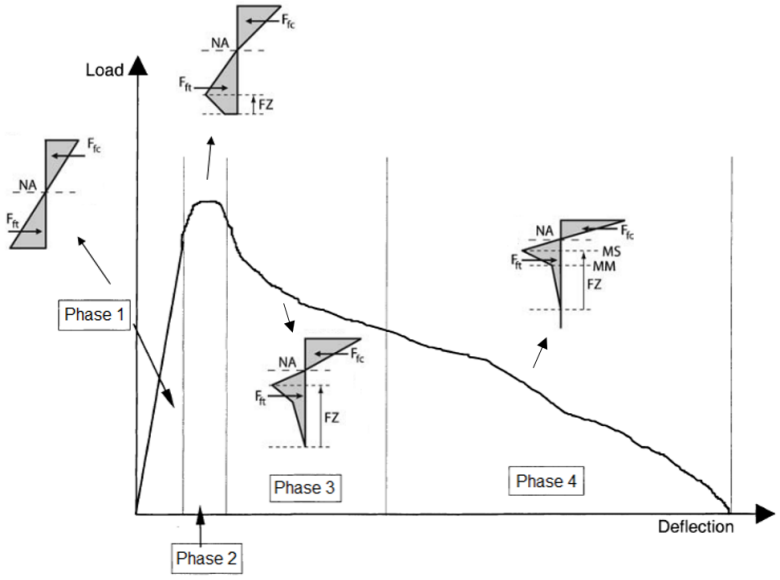

Figure 4.4: Load-deflection curve with corresponding stress distribution [31]

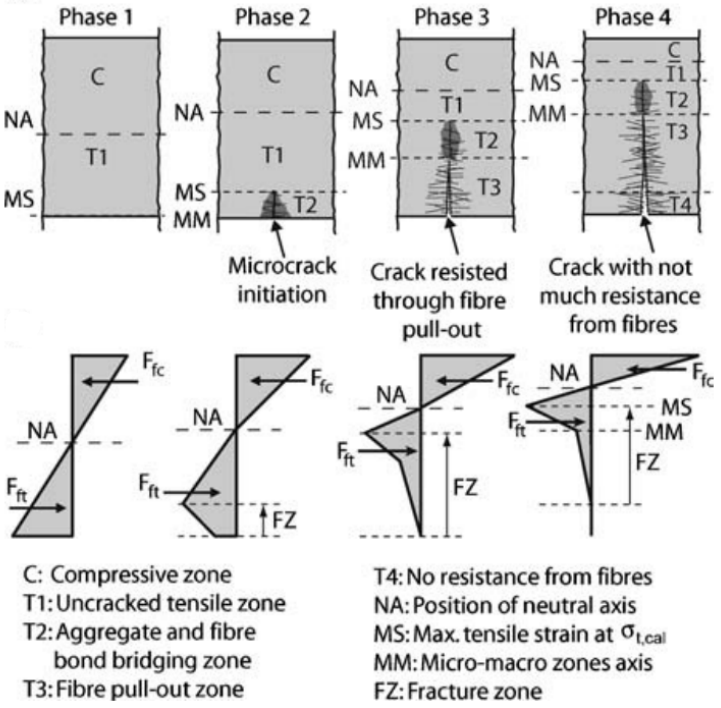

Figure 4.5: Visualisation of crack propagation and corresponding stress distribution [31]

Phase 1 is characterised by linear elastic behaviour of the concrete. The stress distribution is linear over the height and the peak tensile strength is not yet reached, meaning there is no cracking. The fibers do not contribute in this loading stage.

Phase 2 starts at the onset of non-linear behaviour, after the first linear part of the load-defection diagram as seen in Figure 4.4. The tensile strength of the concrete has been reached and microcracks start to form, causing a drop in the tensile stress. The first fibers begin to slip and their bond strength is activated. Fibers with short embedment lengths start to pull out while fibers with longer embedment lengths are still capable of carrying the load with increasing slip. At the end of Phase 2, the crack is noticeable and most fibers are beginning to slip at a constant load.

Phase 3 start when the crack is formed and is resisted through fiber pullout. The tensile stress decreases gradually due to misaligned and inactive fibers and the load is primarily carried by well-anchored fibers. As the crack opening increases, the fibers are pulled out the concrete causing a decrease in stress. At the end of Phase 3, most fibers are pulled out leaving no residual force.

Phase 4 starts when the concrete at the bottom of the crack carries no tensile stress, which is noticeable in Figure 4.5. The load is carried by the fibers with the best anchorage which are still engaged. The neutral axis has shifted upward leaving a small concentrated compressive zone, which can also cause concrete crushing.

Stress - strain relationship
SFRC behaves different under tension compared to regular RC. Fibers improve the tensile behaviour, which is depicted by either softening or hardening behaviour. Hardening makes for a increased tensile strength after cracking and softening allows for ductile behaviour post-cracking. In general, the fiber content determines which post cracking behaviour is expected. According to CNR DT-204 [14], a low fiber content ($< 2\%$) gives a softening behaviour while a high fiber content ($> 2\%$) gives a hardening behaviour. Blanco et al. [32] states that a material is considered as strain hardening when it shown hardening behaviour up to an ultimate tensile strain of 1%. If not, the material is considered as strain softening.

Two types of stress-strain relationships are distinguished in the Model Code 2010: a detailed one and a simplified one. Both stress-strain relationships have the same basis: bending tests performed on an SFRC specimen. A three point bending test is performed on a notched SFRC beam to obtain a load-CMOD (Crack Mouth Opening Displacement) curve, as seen in Figure 4.6.

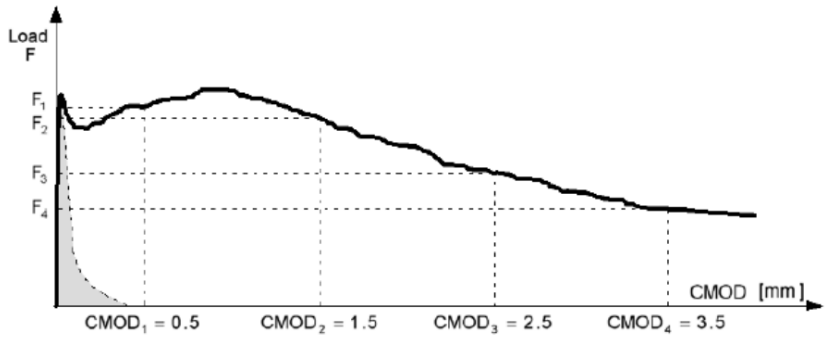

Figure 4.6: General F-CMOD curve [15]

Four predetermined CMOD values, depicted with CMOD_j, are linked to a force F_j. This force is used to calculate the residual flexural tensile strength at the corresponding CMOD value with the following formula:

$$f_{R,j} = \frac{3F_j l}{2bh_{sp}^2} \tag{4.1}$$

where $f_{R,j}$ is the residual flexural tensile strength corresponding with CMOD_j [N/mm^2], F_j is the load corresponding to CMOD_j [N], l is the span length [mm], b is the width of the specimen [mm], and h_{sp} is the distance between the notch tip and the top of the specimen [mm].

The values of $f_{R,j}$ are used to construct the stress-crack width relationship of the material. There are two stress-crack width relationships which can be constructed: simplified or advanced. The simplified stress-crack width diagrams are depicted in Figure 4.7, where the graph on the left gives a linear-elastic behaviour and the graph on the right gives a rigid plastic behaviour.

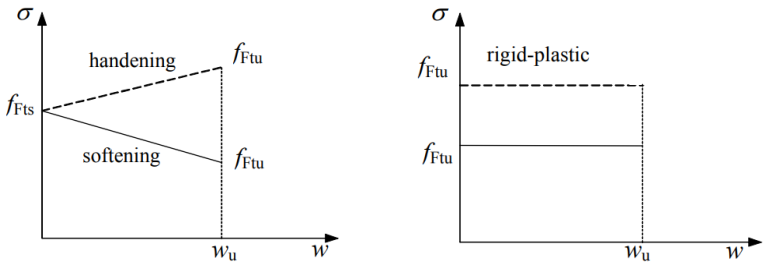

(a) Linear elastic **(b)** Rigid plastic

Figure 4.7: Simplified stress-crack opening law [14]

Here f_{Fts} represents the serviceability residual strength, and f_{Ftu} represents the ultimate residual strength. These differ for a linear elastic and rigid plastic analysis.

Linear elastic:

$$f_{Fts} = 0.45 f_{R1} \tag{4.2}$$

$$f_{Ftu} = 0.5 f_{R3} - 0.2 f_{R1} \geq 0 \tag{4.3}$$

Rigid plastic:

$$f_{Ftu} = \frac{f_{R3}}{3} \tag{4.4}$$

w_u represents the maximum crack opening which depends on design requirements.

The stress-crack opening diagram can be converted to a stress-strain diagram using Equation 4.5.

$$\varepsilon = w / l_{cs} \tag{4.5}$$

Here w is the crack opening and l_{cs} is the characteristic length. This characteristic length is taken as the height of the cross section by default. By converting crack opening to strain, a stress-strain diagram can be obtained as shown in Figure 4.8. The cracking strain is calculated by taking into account the tensile strength and pre-cracking modulus of elasticity. It is important to note that the ultimate strain ε_{Ftu} **is limited to 2%**.

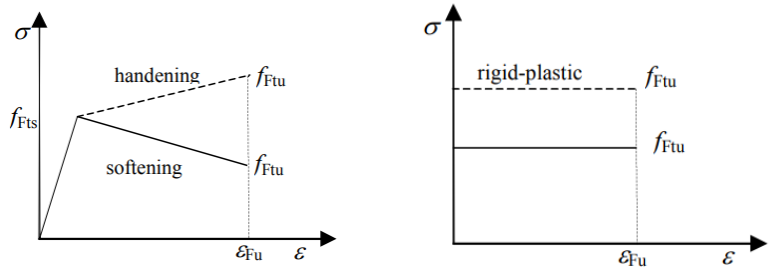

(a) Linear elastic **(b)** Rigid plastic

Figure 4.8: Simplified stress-strain law [14]

This constitutive law is generally used for ULS design and hand calculation.

The advanced stress-strain relationship is also given in the Model Code 2010. Figure 4.9 shows this detailed relationship where several points are highlighted. The diagram is constructed by taking the stress-strain relationship of plain concrete and combining it with the stress-strain relation of SFRC. The latter consists of two points, D and E, which are extrapolated to the plain concrete diagram.

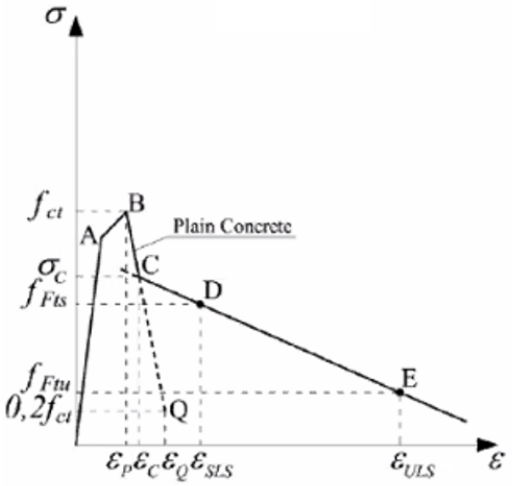

Figure 4.9: Stress-strain diagram for SFRC [15]

The different stress values can be obtained in the same way as with the basic constitutive law. The strains of points D and E correspond to CMOD's of 0.5 mm and 2.5 mm respectively.

This constitutive law is generally used for SLS design and numerical modelling.

FRC can be classified using the characteristic residual strengths according to the Model Code 2010. The material is classified using two parameters, namely f_{R1k} and the ratio between f_{R3k} and f_{R1k} represented by a letter between a and e. The first parameter, f_{R1k}, is rounded up to the nearest integer from 1 till 8 MPa. The ratio f_{R3k}/f_{R1k} correspond to one of the following letters:

'*a*' if $0.5 \leq f_{R3k}/f_{R1k} \leq 0.7$
'*b*' if $0.7 \leq f_{R3k}/f_{R1k} \leq 0.9$
'*c*' if $0.9 \leq f_{R3k}/f_{R1k} \leq 1.1$
'*d*' if $1.1 \leq f_{R3k}/f_{R1k} \leq 1.3$
'*e*' if $1.3 \leq f_{R3k}/f_{R1k}$

For example, a specimen with an f_{R1k} of 4.6 MPa and a ratio f_{R3k}/f_{R1k} of 0.8 will be denoted as '5b'.

Elastic modulus

The modulus of elasticity is generally not influenced by the addition of fibers to the concrete [14]. For that reason, the elastic modulus can be calculated with the formula provided by the Eurocode for concrete structures:

$$E_c = 22000\,(f_{cm}/10)^{0.3} \tag{4.6}$$

Where E_c is the modulus of elasticity [MPa] and f_{cm} is the mean compressive strength [MPa].

Fracture energy

The fracture energy G_F of concrete is defined as the amount of energy required to initiate a first crack of unit area [15]. It can be derived by taking the area of the stress-strain from cracking till failure. Tests have to be performed to determine this diagram and investigate how much the addition of fibers influences the fracture energy. In Figure 4.10 the difference between plain concrete and SFRC is shown. The ductile behaviour of SFRC gives an increased fracture energy G_{fFRC}.

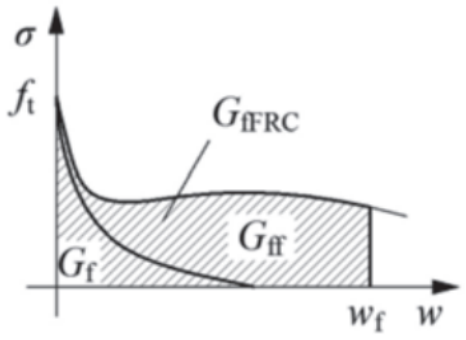

Figure 4.10: Fracture energy of plain concrete G_f, fiber reinforced concrete G_{fFRC}, and the added fracture energy G_{ff} [16]

4.1.3. Moment and shear capacity

The moment capacity of an SFRC member can be determined in a similar manner as the capacity of an RC member. Force and moment equilibrium is considered between external forces and internal forces following the internal stress distribution. This way the maximum allowable bending moment can be calculated, i.e. the moment resistance. This can be with or without reinforcement. The calculation procedure is described below and the outcome has been compared with results from the *fib* Bulletin 83: Precast Tunnel Segments in Fibre-Reinforced Concrete. This document provides a definition of the moment capacity of SFRC in SLS and ULS, which is in good agreement with the outcome of the hand calculations done in the following section.

The shear capacity of RC members is calculated in a certain order. First the capacity without shear reinforcement is calculated and compared with the acting shear force. If this capacity is found to be insufficient, the amount of shear reinforcement is calculated to take up the shear force. For SFRC this procedure does not apply. Structures using solely SFRC have a capacity which is not comparable with both plain concrete and shear-reinforced concrete. For that reason, an experimental study by Coccia, Meda, and Rinaldi [33] based on the Model Code 2010 is used to estimate the shear capacity.

Moment capacity in ULS

The moment capacity of an SFRC cross section is calculated by taking all possible strain and stress distributions over the height of the cross section. An arbitrary strain distribution gives a certain stress distribution following the stress-strain relationship of the material. The moment capacity and corresponding normal force can be calculated by taking into account a force equilibrium between internal and external forces, as well as a moment equilibrium between internal and external moments. By doing this for multiple strain combinations, several combinations of normal force and moment are obtained. These point can be plotted in a moment-normal force diagram to form an envelope. The strain combinations involving the ultimate strain at either compression or tension side will result in the outer points of the envelope: the ultimate capacity. This envelope will give insight in the capacity of a cross section with a given normal force. The calculation procedure is as follows:

- A strain distribution is chosen
- The height of the concrete compressive zone, x_u is calculated
- The force increments at the compressive and tensile side, N_c and N_t, are calculated
- The lever arms between the force increments and half of the cross section, z_c and z_t, are calculated
- By taking into account horizontal force equilibrium, N_{Ed} is calculated
- By taking into account moment equilibrium, M_{Rd} is calculated
- The process is repeated with all strain combinations leading to failure. The compressive strain is set to ε_{cu3} with alternating tensile strain, and the tensile strain is set to ε_{Ftu} with alternating compressive strain

Figure 4.11 gives a visualisation of the calculation method with one of the many possible strain combinations. Please note that the figure stresses are not to scale.

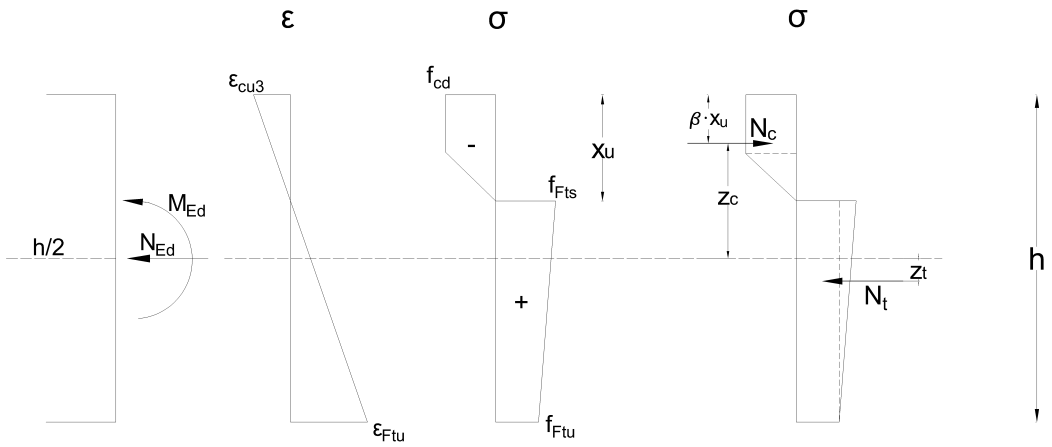

Figure 4.11: Cross sectional forces derived from strain and stress distribution in ULS

The stress-strain relationship as seen in the figure is derived from the simplified ULS stress-strain relationship. In the iterative calculation procedure, ε_{cu3} and ε_{Ftu} are used as the ultimate strains. For simplicity, the tensile side consist of one block starting with what seems a zero initial stiffness. This relationship is only used for these hand calculations to make the calculation easier, and having close to zero impact on the results. Both the tension side and the compression side can be split up in two stress increments. The forces N_c and N_t are calculated by taking the total area of the stress increments. The lever arms z_c and z_t are calculated by taking into account the size of the separate increments and their individual lever arms. An example calculation is given in Appendix C.1.

The final moment-normal force envelope is shown in Figure 4.12. The fiber content used in the calculation is 30 kg/m^3. Different dimensions and material characteristics would result in a different M-N envelope.

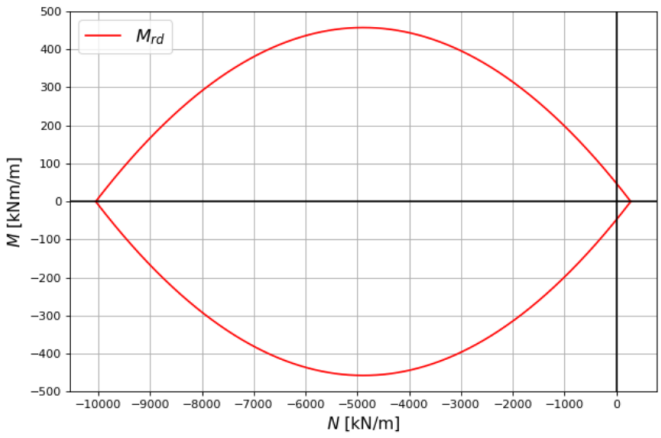

Figure 4.12: Moment-normal force envelope in ULS

Moment capacity in SLS

The moment capacity in SLS is calculated in a similar manner as the moment capacity in ULS. The calculation method is the same, but the material characteristics are different. The elaborate stress-strain relationship for SLS is used for this calculation. The concrete compressive stress is limited to 0.6 f_{ck}, as prescribed in the Model Code 2010 [15]. The crack width is limited to 0.15 mm. This crack width is translated to the strain ε_{max} by dividing the crack width by the height of the cross section. Figure 4.13 gives the scheme which is used for the calculation.

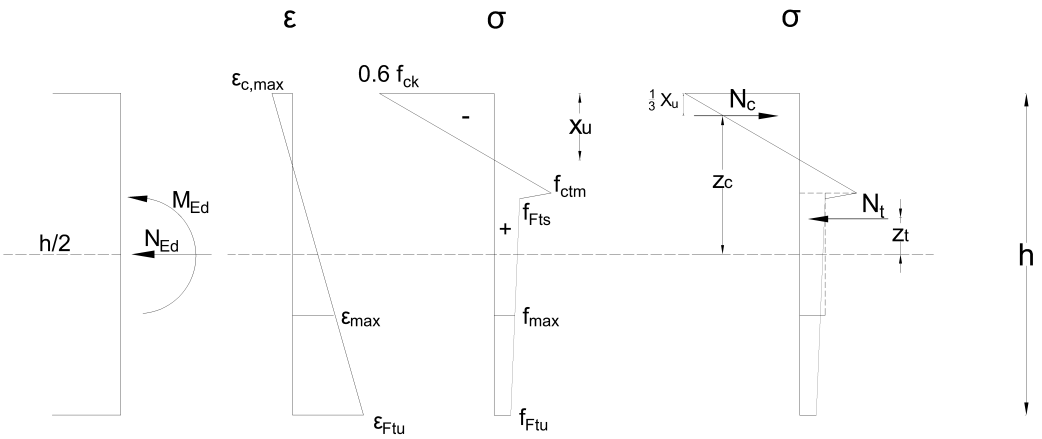

Figure 4.13: Cross sectional forces derived from strain and stress distribution in SLS

The forces N_c and N_t are derived from the stress increments as shown in the figure. By following the same calculation procedure as in the ULS, a moment-normal force envelope can be made. The moment-normal force envelope for a fiber content of 30 kg/m^3 is shown in Figure 4.14.

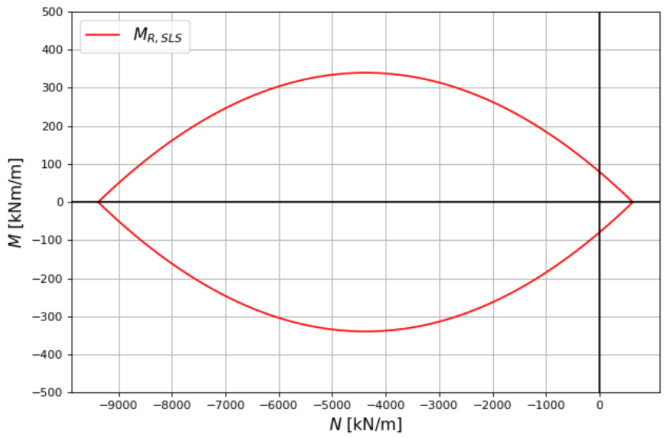

Figure 4.14: Moment-normal force envelope in SLS

Shear capacity in ULS

Similarly to the moment capacity envelope, an envelope can be constructed for the shear capacity of an SFRC member. Coccia, Meda, and Rinaldi [33] provide a formula derived from the Model Code 2010 to link the shear and normal force of an SFRC member.

$$\frac{V_{Rd}}{bhf_{Ftu}} = 0.311 + 0.145 \left(\frac{N}{bhf_{Ftu}} \right)^{0.8} \tag{4.7}$$

Here V_{Rd} is the shear capacity [N], b is the width of the cross section [mm], h is the height of the cross section [mm], f_{Ftu} is the design ultimate residual strength [N/mm^2], and N is the acting normal force [N].

The equation showed to be effective with a mean error of 1.48% compared to experimental results. Using this equation provides a shear-normal force diagram as shown in Figure 4.15.

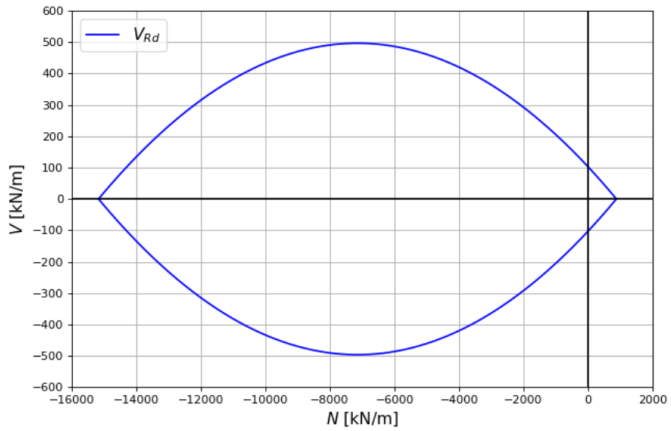

Figure 4.15: Shear-normal force envelope in ULS according to Coccia, Meda, and Rinaldi [33]

The fiber content used in the calculation is 30 kg/m^3.

4.1.4. SFRC in tunnel linings

The use of a tunnel boring machine to construct a tunnel has become quite popular in the last decades. As explained in section 2.2, this method is coupled with tunnel segments, originally made from regular reinforced concrete. However, the application of steel fibers instead of regular reinforcement bars has become an attractive alternative. Railway, metro, traffic, and water tunnels can all be constructed with steel fiber concrete, which has been done in numerous countries around the world, all with different working conditions. This worldwide implementation originates from a set of benefits which SFRC provides.

Structural benefits

One of the biggest problems occurring with RC is the corrosion of reinforcement bars with spalling of the concrete as a consequence. This happens when cracks are present and chloride infiltrates the concrete and affects the steel. This risk can be avoided by using SFRC due to its ability to control cracks. The substitution of reinforcement bars with fibers can not only improve crack control, but also increase the toughness and increase the ductility [6].

A tunnel segments goes through several phases in the construction process. These phases are transient phase, construction phase, and service phase with multiple loading situations per phase. These loading situations are provided with detail in section 2.3. A segment has to sustain every loading situation in order to fulfill the structural criteria. Before substituting RC with SFRC, insight has to be gained in the behaviour of SFRC in each of these loading situations.

The transient phase is split up into demoulding, stacking, and transport of segments. During these stages, the loading comes solely from the self-weight of the segments. The ability of SFRC to absorb tensile stresses in every direction and every part of the concrete ensures that no cracking will occur during these processes. The self-weight does not provide substantial forces so SFRC can suffice the ULS with ease. Special attention needs to be made to eccentric loading, as this can cause increased moments and shear forces.

The main loading during construction is that of the TBMs hydraulic jacks. The magnitude of which is calculated in section 3.4 and amounts to roughly 4 MN per jack. The stresses that occur during this phase are significant in comparison with the transient and service life phase and often a design is made with the construction phase being governing. As explained in section 2.4, joint bursting and concrete splitting are possible failure mechanisms during the TBM operation. High stresses are located under and around the jacks which ask for large amounts of splitting reinforcement. The use of SFRC brings the biggest benefit in this phase, as splitting of concrete is an often occurring and costly problem. Due to the fibers being distributed in the entire section, SFRC can take up the distributed tensile stresses.

The service phase of a structure is characterised by predominantly soil and water pressure. Besides these two, surface loads and loads inside the tunnel itself present loads to account for. The sum of these loads will present significant radial forces onto the tunnel linings with compression in the segments as a results. This compression is coupled with bending moments and shear forces, where the normal force works in favor of the structure by counteracting the tensile forces which cause cracks. This service phase is generally not governing and needs minimal reinforcement. One phenomena to account for, as mentioned in section 2.4, is opening of longitudinal joints with joint bursting as a possible outcome. SFRC works similar to RC in compression and will provide beneficial behaviour in the tensile regions which occur close to the joints.

Cost savings
A main benefit when using SFRC segments is the simple production compared to RC segments. RC segments are manufactured with the use of a complex reinforcement cage which is placed in a mould, as shown in Figure 4.16. SFRC on the other hand only has steel fibers being distributed in the concrete mix, after which it can be poured into a mould. This saves time, material costs, and man hours.

Figure 4.16: RC reinforcement cage [34]

Bin et al. [35] studied the difference in the manufacturing process of SFRC segments compared to RC segments. The manufacturing of an ordinary RC segment takes place in several steps, from preparing the mould till segment delivery. An important and time consuming step of the process is the assembly and installation of the reinforcement framework. This step can be left out when opting for solely SFRC, or it can be simplified when opting for less regular reinforcement. The research investigated the latter option, where reinforcement content was reduced drastically and fibers were added. The cost reduction in two Chinese tunneling projects was investigated.

1. The first one reduced reinforcement bar content from 98 kg/m^3 to 5 kg/m^3 and added 40 kg/m^3 of fibers. This alteration caused a reduction in total manufacturing costs of 15%.

2. The second one reduced reinforcement bar content from 167 kg/m^3 to 86 kg/m^3 and added 30 kg/m^3 of fibers. This alteration caused a reduction in total manufacturing costs of 10%.

Sustainability
The use of SFRC is very beneficial in terms of sustainability. The amount of steel is reduced and the service life of a structure is extended due to lower susceptibility to weathering of the concrete. The first component, reduced steel, is beneficial for lowering the carbon footprint of the structure. Less steel equals less omitted CO_2 from production of the steel. The second component, extending the service life, is sustainable due to the reduced need of repair/replacement and thus needing less new material. To get an idea of the magnitude of these benefits, a simple hand calculation is made. Only the effect of the reduced steel is examined.

For every ton of steel which is produced, 1.83 tons of CO_2 are emitted [36]. The segments of the original design of the Noord/Zuidlijn have steel contents of around 112 kg/m^3. The amount of steel of a new design with SFRC is not yet determined, so will be taken as high as possible for the most unfavorable outcome. A steel content of 60 kg/m^3 is found as the maximum in many papers testing SFRC segments so this will be used. The concrete volume over the total tunnel length is taken as a hollow cylinder, where joints/gaps are not taken into account. The length of the tunnel is only from the bored part, excluding the stations as seen in Figure 1.1. The total volume of concrete then becomes:

$$V_{concrete} = L \cdot (\tfrac{1}{4}\pi(D_{ex}^2 - D_{in}^2)) = 3120 \cdot (\tfrac{1}{4}\pi(6.52^2 - 5.82^2)) = 21166.9 \text{ m}^3$$

The total amount of steel for the old design using reinforcement bars and improved design using fibers can now be calculated. The main interest lies in the difference fibers can make, so the difference in total amount of steel is:

$$\Delta V_{steel} = 21166.9 \cdot (112 - 60) = 1100679.9 \text{ kg} = 1100 \text{ tons}$$

This amount is directly correlated to the emitted CO_2. The total amount of saved CO_2 is:

$$CO_2 \text{ saved} = 1100 \cdot 1.83 = 2013 \text{ tons}$$

Durability
One important characteristic of SFRC is the ability to mitigate crack widths and reduces the amount of cracks [6]. This quality of SFRC is linked to another quality of SFRC which is a high durability of the material. Due to the material having smaller and less cracks than RC, weathering of an SFRC segment is less likely to happen. In fact, SFRC segments are considered to have a 20% longer durability than RC [3]. The durability of concrete is mainly affected by three deterioration hazards:

- Chloride and sulfate corrosion
- Freeze-thaw cycle
- Carbonation

Chloride and sulfate infiltration with the consequence of corrosion is a often occurring problem with RC. Corrosion can lead to concrete spalling which can compromise the integrity of a structure. This asks for costly repairs and reduces the durability of the structure. SFRC works beneficial by its crack control characteristic to mitigate chemical infiltration into the cracks.

Freeze and thaw cycles can cause concrete cracks to increase in size. Water infiltrates cracks and freezes, causing the water to expand and the cracks to widen. The fibers in SFRC work against this phenomena by bridging all cracks and providing resistance to the tensile forces. However, freeze and thaw is unlikely to happen at the depth in which the Noord/Zuidlijn is located.

Carbonation can also lead to corrosion of reinforcement bars by decreasing the alkalinity of concrete. This can result in expansion of the concrete and the forming of cracks. The porosity and permeability of segments is altered reducing the durability. Fibers are found to work beneficial by compacting concrete and counteracting the process of carbonation [1]. Increasing fiber content was shown to increase resistance, up to a fiber content of 1.5%.

4.2. Reference projects

This section provides state of the art research on SFRC using past and ongoing projects worldwide. These projects gave rise to many researches on the topic and will provide a good understanding of the current state of literature and how it is applied in practice. Useful knowledge will be used and gaps in knowledge will provide room for research. Project that will be discussed are Metro Line 9 in Barcelona, the Toronto-York Spadina Subway Extension Project, and Metro Line A in Prague. All of these tunnels were made with the use of SFRC and extensive testing has been done on the structural integrity of such SFRC segments.

4.2.1. Metro Line 9 Barcelona

One of the most researched applications of precast SFRC segments is the case of Metro Line 9 in Barcelona. General information regarding the tunnel is given in Table 4.1, with the Noord/Zuidlijn as comparison. The metro tunnel is constructed using a TBM to avoid surface work in a high density populated area. The soil is characterized by low alteration granodiorite rock, which has a relatively high modulus of elasticity of 11,225 N/mm^2 and a groundwater table which is located around 15 meters below ground level [37]. This hard rock and low water table will present lower loads on the lining in comparison with the Dutch soil. The Barcelona tunnel is designed with precast SFRC segments using 30 kg/m^3 fibers and 97 kg/m^3 of traditional reinforcement [38]. A small part of the line consisting of 15 rings has been made with segments using solely fiber reinforcement of 60 kg/m^3. Multiple studies have been done on the feasibility of using solely SFRC and on hybrid compositions and will be analysed in this section.

Table 4.1: General dimensions Metro Line 9 Barcelona and Noord/Zuidlijn

	Metro Line 9 Barcelona	**Noord/Zuidlijn Amsterdam**
Length	41 km	3.8 km
Depth	30 - 70 m	20 - 30 m
External diameter	11.96 m	6.5 m
Internal diameter	10.9 m	5.9 m
Segments per ring	7 + 1 key	5 + 1 key
Segments thickness	0.35 m	0.35 m
Segments aspect ratio	13.9	9.8
Lining aspect ratio	31.1	16.9

A research conducted by Gettu et al. [38] concerned the same Barcelona Metro tunnel and the impact of different fiber contents on the performance of the structure. Fiber contents of 45 and 60 kg/m^3 were used, as well as a hybrid form of 30 kg/m^3 fibers coupled with conventional reinforcement, and solely conventional reinforcement. The most important parameters being tested were load-crack opening and load-deflection.

Flexural testing

A segment is expected to experience only circumferential compression and not flexure during service life in Barcelona's hard soil. However, inadequate grouting behind the lining can lead to local flexure of a segment. Therefore a flexural test was performed on a key segment using a three point bending test. A key segment was chosen due to practical limitations with transport and loading equipment. The test was performed using two continuous metal supports and a Temposonics transducer to apply loading, as shown in Figure 4.17.

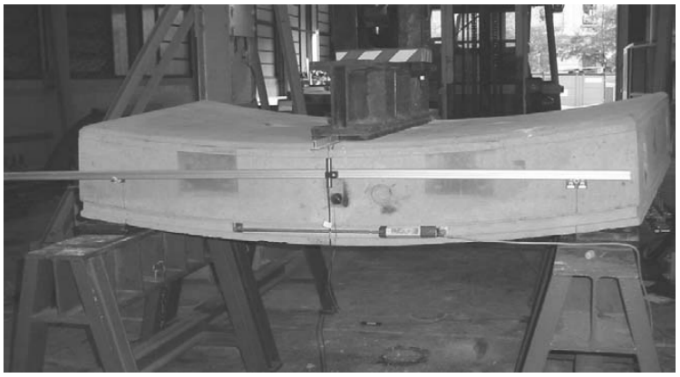

Figure 4.17: Test setup flexural loading of a key segment[38]

Each of the before mentioned four variants had two specimens, giving eight test results in total. A distinction was made between the complete response and the response up to a crack opening of 1.2 mm.

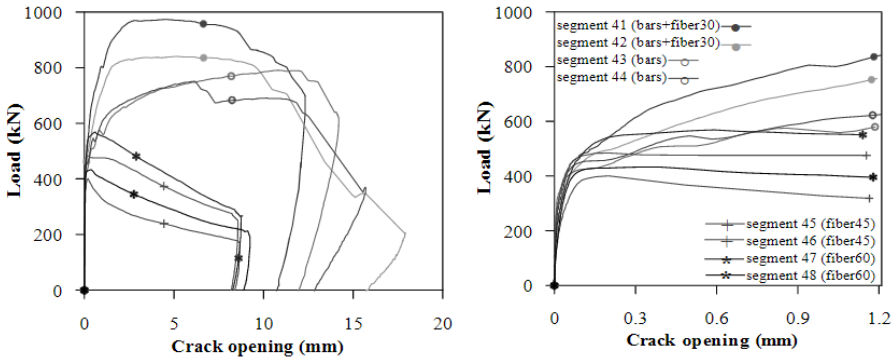

Figure 4.18: Load-crack opening response of all the segments: Complete (left) and initial (right) behaviour [38]

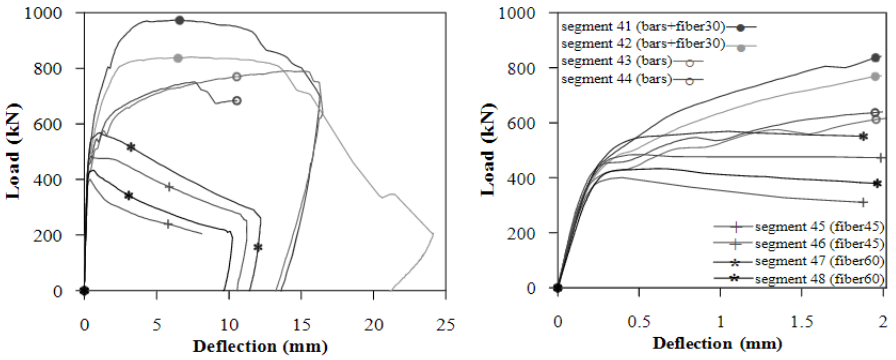

Figure 4.19: Load-deflection response of all the segments: Complete (left) and initial (right) behaviour [38]

As can be seen in Figures 4.18 and 4.19, the fiber variants show a qualitatively different pattern than the reinforcement bar and hybrid variants for both deflection and crack opening. All four of the fiber specimens show a relatively low load carrying capacity, which decreases heavily after a crack opening of 1 mm. The specimens with fiber content of 60 kg/m^3 performed better than the 45 kg/m^3 variant with respect to the load carrying capacity, but both are significantly lower than the segments with traditional and hybrid configurations. The hybrid segments showed a load carrying capacity approximately twice as high as the 60 kg/m^3 variant, and the rebar variant showed a capacity of 1.8 times higher than the

60 kg/m^3 variant. The (ultimate) crack opening of the hybrid and rebar segments was also 1.5 to 2 times higher than the fiber variants. However, the figures to the right indicating the initial response represent the service phase more closely. These figures show that the 60 kg/m^3 variant comes close to the traditional reinforcement bar variant up to crack openings of 1 mm.

Thrust loading
The effect of a single hydraulic jack was tested by Gettu et al. [38], on a half scale segment, using central and eccentric loading. The tests were done on panels with either conventional reinforcement coupled with 30 kg/m^3 fibers or panels with only 60 kg/m^3 of fibers. The same density was maintained. The results showed no failure of either configuration and concluded that the behaviour of the segment with only fibers would be similar as the hybrid option.

Summarizing
The Barcelona Metro Line 9 was an extensive project with a well researched application of the fairly new material SFRC. In designing the tunnel linings, ultimately a combination of SFRC and RC was used due to the lack of regulation regarding SFRC and its mechanical contribution. The fibers were only added to control cracks during handling and placing of segment. Only a small stretch of 15 linings was made with SFRC alone. Several studies have been done researching the feasibility of using segments with solely SFRC to withstand loading from all phases.

Gettu et al. [38] studied the structural integrity of SFRC segments with different fiber contents and concluded the following. Segments with 60 kg/m^3 of fibers have a similar response to flexural testing as hybrid segments with 30 kg/m^3 of fibers plus reinforcement bars. The load carrying capacity is lower, but looking at service life conditions the SFRC segments suffice. Both thrust loading and loads due to segment stacking proved SFRC segments with 60 kg/m^3 of fibers were strong enough.

Segments with 60 kg/m^3 of fibers were deemed feasible in the case of the Barcelona Metro Line 9. When comparing this reference project to the Noord/Zuidlijn there are several differences. The granodiorite rock beneath Barcelona provides a very stiff soil which places smaller loads on the tunnel lining, compared to the soft soil underneath Amsterdam consisting of sand, clay, and peat. On the other hand, it can be seen that the Noord/Zuidlijn has a smaller diameter tunnel than the Barcelona metro tunnel. Smaller diameter tunnels are more suitable being designed with just SFRC as stated by Lin et al. [12]. Lastly, the segments used in Barcelona have an aspect ratio of 13.88, compared to 9.8 for the Noord/Zuidlijn. This makes the Noord/Zuidlijn more favorable for using only fibers.

4.2.2. Toronto-York Spadina subway extension

SFRC tunnel linings have been tested and put into practice for a subway tunnel extension in Toronto. General information regarding the Toronto-York Spadina subway extension is given in Table 4.2, with the Noord/Zuidlijn as comparison. The soil in the area of Toronto is similar to Dutch soil with sand, loam, and clay being the main materials making up the soil. The tunnel is constructed with a TBM and implemented 100 rings of precasted SFRC segments after extensive lab testings. Each tunnel ring consists of 4 segments and 2 key segments [39]. The fiber dosage of the segments is 57 kg/m^3, or 2% volumetric percentage. Several testings have been done on similar SFRC segments and will be analysed.

Table 4.2: General dimensions Subway Tunnel Extension Toronto and Noord/Zuidlijn

	Subway tunnel Toronto	**Noord/Zuidlijn Amsterdam**
Length	8.6 km	3.8 km
Depth	15 - 20 m	20 - 30 m
External diameter	5.87 m	6.5 m
Internal diameter	5.4 m	5.9 m
Segments per ring	4 + 1 key	5 + 1 key
Segments thickness	0.235 m	0.35 m
Segments aspect ratio	13.5	9.8
Lining aspect ratio	23.0	16.9

Abbas, Soliman, and Nehdi [30] researched the behaviour of RC vs. SFRC segments for the Toronto Subway tunnel extension. Both the RC and SFRC segments used for testing had a length of 3180 mm, a width of 1500 mm, a thickness of 235 mm, and skewed edges. The concrete mixtures were identical apart from the addition of steel fibers for the SFRC segment. The SFRC segments had a fiber content of 1.5% and the amount of conventional reinforcement for the RC was not specified.

To determine the compressive and tensile strength, cylindrical cores were taken from the segments. It was found that the core compressive strength did not increase significantly by adding fibers, in contrast to the splitting tensile strength which increased by 20%. Following, the segments were subjected to monotonic and cyclic flexural load testing and thrust load testing, specifically monitoring the cracking behaviour.

Monotonic flexural loading

Monotonic flexural loading was done on the RC and SFRC segments using two steel I-beams as supports and a waffle tree loading frame. The schematized test setup is shown in Figure 4.20.

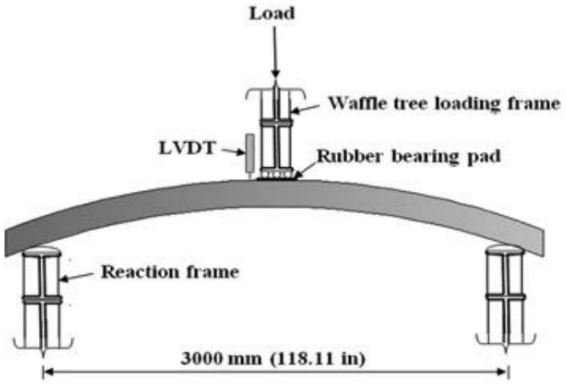

Figure 4.20: Test setup monotonic flexural loading [30]

The general behaviour of SFRC under a three point bending test is explained in section 4.1.2 and shown in Figure 4.3. For both RC and SFRC three main points can be identified: crack initiation, yielding, and ultimate loading. These are indicated by points A, B, and C respectively. The test results from Abbas, Soliman, and Nehdi [30] showed very similar behaviour, and can be seen in Table 4.3. The first major difference between RC and SFRC is the magnitude of the peak load and displacement, which are substantially higher for RC. In return, the failure mechanism of RC is found to be quite brittle with splitting off of a concrete cover and abrupt steel rupture. In comparison, SFRC showed ductile post-peak behaviour with fiber debonding and pullout of fibers causing failure. Secondly, the crack initiation load is higher for SFRC compared to RC with 71 kN and 45 kN respectively. This gives SFRC an advantage in transient phases such as fabrication, handling, delivery, and installation. Furthermore, smaller cracks widths were observed with SFRC satisfying SLS conditions. The crack width at ultimate load was 0.25 mm, which satisfies the limit of 0.30 mm.

Table 4.3: Flexural test results for RC and SFRC PCTL segments [30]

Parameters	RC	SFRC
First crack load, kN (kip)	45(10.11)	71(15.96)
Displacement at first crack, mm (in.)	1.80(0.070)	1.60(0.62)
Average crack width at first crack, mm (in.)	0.20(0.008)	$< 0.10(0.004)$
Peak load, kN (kip)	244(54.85)	119(26.75)
Peak load displacement, mm (in.)	50.26(1.97)	5.06(0.20)
Average crack width at peak load, mm (in.)	8.20(0.32)	0.25(0.0098)

Cyclic flexural loading

The load-displacement hysteresis curves of the cyclic thrust loading are shown in Figure 4.21. Again very different behaviour can be observed for RC and SFRC. The peak loading and corresponding peak displacements are of a higher magnitude for RC.

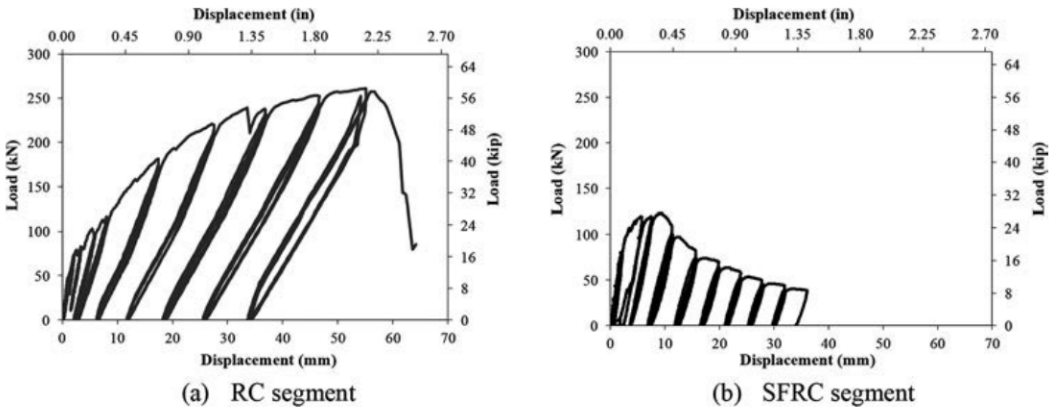

Figure 4.21: Load displacement hysteresis curves for segments under cyclic load [30]

From the envelop of the hysteresis curves from Figure 4.21, a so-called skeleton and energy dissipation curve can be drawn. These are shown in Figure 4.22 and visualize the maximum average load and corresponding displacement. The area under the envelope represents the energy dissipation capacity and is noticeably bigger for RC than SFRC, in fact three times bigger. However, the SFRC segment showed an energy dissipation 1.5 times larger than RC if initial cracking is the governing design criteria.

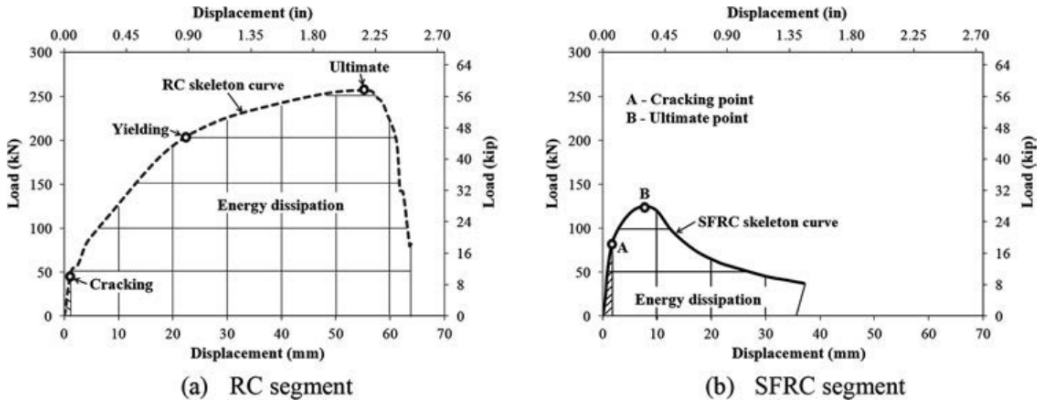

Figure 4.22: Skeleton and energy dissipation segments under cyclic load [30]

Summarizing

The Toronto-York Spadina subway extension implemented a stretch of 150 meters SFRC linings after extensive testing. The main reason for implementing SFRC was corrosion occurring for RC segments in the original subway line. This leaded to the use of SFRC segments with 57 kg/m^3 fiber content without the addition of reinforcement bars. Several testings have been done on similar segments, the most extensive study done by Abbas, Soliman, and Nehdi [30].

Abbas, Soliman, and Nehdi [30] studied SFRC segments of 1.5% fiber content in comparison with RC segments with same dimensions and material composition. Both monotonic and cyclic flexural loading were examined, as well as thrust loading. For monotonic flexural loading, the peak load of RC segments is approximately twice as high than for SFRC segments. However, the crack initiation load of SFRC is higher (71 kN) than for the RC variant (45 kN), with a corresponding displacement of 11% lower for SFRC. The failure mechanism of the SFRC segments was found to be more ductile than RC, with fiber debonding and fiber pullout causing failure, in contrast to splitting off of the concrete cover and abrupt steel rupture for RC. Cyclic flexural loading showed a higher energy dissipation capacity for RC segments. However, the SFRC segment showed an energy dissipation 1.5 times larger than RC if initial cracking is the governing design criteria.

The findings of this research can be seen as evidence for the use of SFRC to meet SLS requirements in Toronto. When comparing this subway extension to the Noord/Zuidlijn, the use of SFRC for the Noord/Zuidlijn seems achievable. The diameters of both tunnels are of similar order size, with different thicknesses. This gives the Toronto tunnel a segment aspect ratio of 13.5, compared to a more favorable 9.8 for the Noord/Zuidlijn. Also the lining aspect ratio differs, with 23 for the subway tunnel in Toronto vs. 17 for the Noord/Zuidlijn. Both the higher lining and segment aspect ratios are more favorable for using only fibers in the Noord/Zuidlijn. Only the lesser depth of the Toronto tunnel is more favorable. Lastly, the soil underneath Toronto is similar to the Amsterdam soil, being characterised as soft with low stiffness. This makes the Noord/Zuidlijn a viable candidate for using only fibers, just like in Toronto.

4.2.3. Metro Line A Prague

Metro Line A in Prague is constructed using RC tunnel linings, but with a small stretch of SFRC panels following extensive testing. The soil around Prague is quite diverse with limestone, clay, and shale. General information regarding the tunnel dimensions is given in Table 4.4. In total 10 rings of SFRC segments were assembled, amounting to 15 meters of tunnel. The segments had a dosage of 40 kg/m^3 of fibers without reinforcement bars. The testing prior to this practical application was done in Prague with segments manufactured in Slovakia. Two full rings were produced with contents of 40 kg/m^3 and 50 kg/m^3 fibers. Two governing load cases were imitated: loading by hydraulic jacks during construction and loading by ground-water pressure during service life [3].

Table 4.4: General dimensions Metro Line A Prague and Noord/Zuidlijn

	Metro Line A Prague	**Noord/Zuidlijn Amsterdam**
Length	17.1 km	3.8 km
Depth	11 - 21 m	20 - 30 m
External diameter	5.8 m	6.5 m
Internal diameter	5.3 m	5.9 m
Segments per ring	5 + 1 key	5 + 1 key
Segments thickness	0.25 m	0.35 m
Segments aspect ratio	12.0	9.8
Lining aspect ratio	21.2	16.9

Compression: thrust loading

The first test was done on an SFRC key segment which was loaded in compression in the longitudinal direction as seen in Figure 4.23a. Loading was increased by 300 kN per step and unloaded to 90 kN in between. First cracking occurred at 4200 kN and the peak load was 7250 kN. In comparison, an RC key segment had a first crack load of 3300 kN and ultimate load of 5870 kN. At this point separation of the concrete cover at the inner surface of the RC key segment occurred.

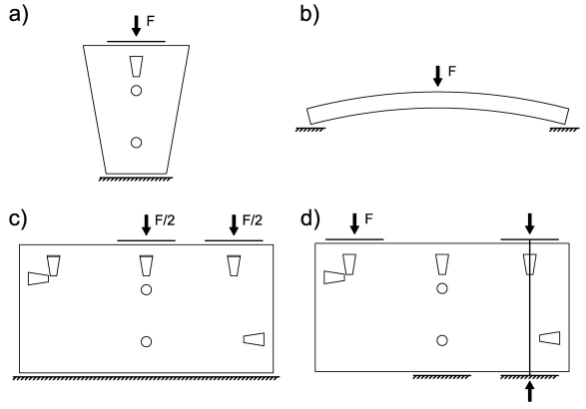

Figure 4.23: Tests performed on SFRC segments: (a) compressive strength of a key segment, (b) segment bending perpendicular to the segment plane, (c) compressive strength of the segment, (d) segment bending in the segment plane [3]

Bending: soil loading

To simulate soil loads, bending was investigated by applying a load perpendicular to the longitudinal axis as shown in Figure 4.23b. The loading was done in a displacement control manner. Four SFRC segments were tested. The general failure mechanism began with small cracks at the bottom under the applied load, resulting in one large crack and finally failure. The load capacity was measured to be between 100 kN and 150 kN.

Compression: uniformly and non-uniformly supported
The compressive load by hydraulic jacks on uniformly and non-uniformly supported segments is visualized in Figure 4.23c and 4.23d. The first one applied loads increasing in steps of 1200 kN and unloading to 400 kN after every step. Two SFRC segments were tested and found to have a first cracking load of 3600 kN. Large cracks running through the whole thickness were found from 6000 kN on wards and failure happened around 9000 kN.

The non-uniformly supported loading was meant to simulate inaccurate assembly or a non-uniform hydraulic jack loading. Loading was increased by steps of 100 kN with no unloading. Four SFRC segments were compared to RC segments. First cracking load occurred around 300 kN for the SFRC segments with a maximum force of 600 kN. A similar maximum force was found for the RC segments. However, cracking through the whole thickness of a segment happened later for SFRC than RC, with forces of 500 kN and 400 kN respectively.

Summarizing
Metro Line A in Prague implemented 15 meters of SFRC panels as a pilot in the tunnel design, due to water tightness issues occurring with RC segments. These segments have a fiber content of 40 kg/m^3 with no traditional reinforcement and were tested in several ways.

In compression, key segments consisting of SFRC had a higher first crack load and peak load compared to an RC key segment. A three point bending was done on SFRC panels which proved ductile behaviour with the initiation of numerous small cracks, and ultimately forming one large crack. Compressive loading on non-uniformly supported segments showed superior qualities for SFRC compared to RC segments. While the peak load was similar, significant cracking occurred at a load 20% higher for SFRC. This has a positive effect on SLS conditions, due to the fact that water infiltration happens earlier for RC than SFRC possibly leading to corrosion and spalling.

The outcome of the tests showed that SFRC is a good alternative to RC for the Prague Metro Line A. When comparing this implementation to a possible implementation in the Noord/Zuidlijn, there are a couple differences and similarities. Firstly the diameter of the Prague tunnel is substantially bigger than the Noord/Zuidlijn. Coupled with a smaller segment thickness in the Prague case, this makes for a bigger segment and lining aspect ratio making it less favorable for SFRC design than the Noord/Zuidlijn. Secondly, the soil in Prague is quite different than in Amsterdam. The Noord/Zuidlijn has to cope with softer soil, but the limestone in Prague also presents difficulties due to unknown geological conditions such as cavities and abundant rain/ground water [40]. The main reason for implementing SFRC in Prague was to ensure water tightness and counter possible corrosion and spalling as a result of cracks. The same benefit can be achieved in the Noord/Zuidlijn due to the high water table and possible cracking due to TBM loading. These similarities and differences give reason to believe the Noord/Zuidlijn can also be constructed using solely SFRC.

4.2.4. General tendencies reference projects

ITA Working Group 2 [41] provides a very useful overview of over 70 projects where SFRC has been (partly) implemented. From these projects, general data can be collected. First of all the popularity of using solely fibers or a hybrid solution of fibers + reinforcement bars. This is shown in Figure 4.24. As can be seen, the implementation of only fibers has been used more often.

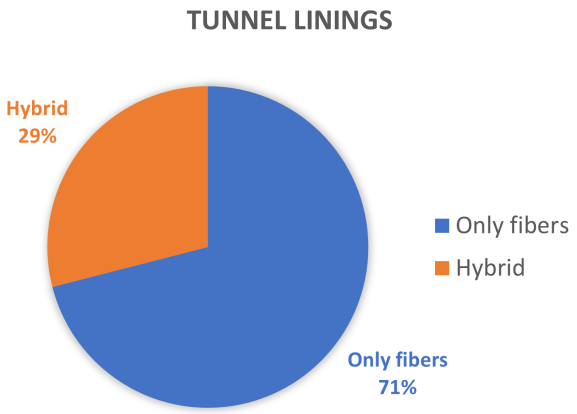

Figure 4.24: Distribution of reinforcement solution in the tunnel linings of 70 case studies

The most interesting statistic for this thesis is obtained when the use of only fibers or a hybrid form is linked to the diameter of the tunnel. This has been done for the list of reference projects, which resulted in the pie graphs shown in Figure 4.25. As can be seen in Figure 4.25a, smaller diameter tunnels are more favorable for using only fibers. Bigger diameter tunnels on the other hand, require the use of fibers + reinforcement bars as seen in Figure 4.25b. This data can be explained due to the fact that the diameter of a tunnel is linked to the stresses which occur in the tunnel linings. Bigger diameter tunnels experience higher bending moments and smaller normal forces. To be able to handle these forces, large amount of fibers are needed which leads to a very expensive solution.

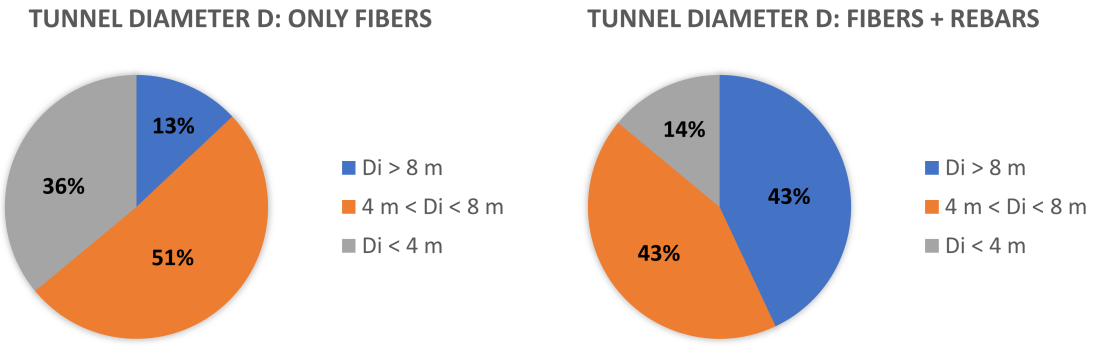

(a) Linings with only fibers

(b) Linings with fibers + reinforcement bars

Figure 4.25: Distribution of the internal diameter D_i in the tunnel linings of 70 case studies

The thickness of a segment also plays a role in the decision between only fibers or a hybrid variant. A lower thickness gives a higher segment aspect ratio (segment length / segment thickness) as well as lining aspect ratio (D_i / segment thickness). Both are more susceptible to bending loads. ITA Working Group 2 [41] found that projects using fibers + reinforcement bars generally had a aspect ratio of above 20. Only fiber projects had a 50/50 distribution between aspect ratios above 20 and under 20.

4.3. Concluding

The following conclusions can be drawn from the state of the art of SFRC in tunnel linings:

- The homogeneous fiber distribution of SFRC ensures it can absorb tensile stresses in any direction in every part of the concrete. This becomes advantageous especially when high stresses are expected in unpredictable locations during for example TBM thrust loading.
- SFRC performs excellent in terms of crack control. Several testings demonstrate that the initial cracking load of SFRC is higher compared to RC segments when loaded in flexure. The same is shown after compressive thrust loading. The crack openings that occur are generally smaller for SFRC compared to RC and fewer cracks arise.
- SFRC's ultimate load carrying capacity is lower than that of RC segments. This is true for both flexural and compressive (thrust) loading. However, the response up to a crack opening of 1 mm is almost identical, which means service life conditions can be met by SFRC.
- SFRC has a better post-cracking tensile behaviour compared to RC. Ductile behaviour of SFRC is in contrast with RC which can show brittle failure with splitting of concrete.
- Manufacturing costs are lower when (partly) substituting reinforcement bars for fibers in a segment. Manufacturing costs can be reduced by 10-15% due a lower amount of steel consumption and a lower amount of man hours needed for fabricating the reinforcement cage.
- SFRC is a more sustainable material than RC. CO_2 emissions are lowered due to the decreased steel consumption by replacing reinforcement bars by fibers. For the Noord/Zuidlijn this can mean a reduction of 2000 tons of CO_2 emitted.
- SFRC is a more durable material than RC, with SFRC segments generally having a 20% longer durability. Weathering of the material is lower due to fewer and smaller cracks which hinder chemical infiltration. Corrosion, to which RC is very susceptible, does not form a problem for SFRC. A possible consequence of corrosion is concrete spalling, which is avoided with SFRC lowering repair costs and extending the lifespan of a structure.

It can be concluded that SFRC presents better qualities for all discussed non-structural aspects than RC. Costs, sustainability, durability, and simplicity all favor SFRC. The only uncertainty is whether SFRC provides the same (or better) structural performance as RC. In the end, the structural integrity is the governing criteria in the design of a structure which makes this the deciding aspect. SFRC has both superior and inferior structural qualities, which are listed above. The main advantage being the enhanced post-cracking residual tensile strength which enables a better crack control and the main disadvantage being the lower ultimate capacity and ability to handle high localised stresses.

Reference projects showed that SFRC has been successfully implemented in projects around the world. These successful applications give room to believe the same can be done for the Noord/Zuidlijn. For this to be the case, the conditions and design must be similar. It was concluded that the three presented projects all had higher lining and segment aspect ratios than the Noord/Zuidlijn, which makes the Noord/Zuidlijn more suitable for using fibers. The main problem is the soft soil in the Netherlands giving rise to high loads onto the tunnel linings. Although the Noord/Zuidlijn has small aspect ratios compared the other projects, the significant radial loading onto the lining caused by the soft soil can still present a problem. However, the Toronto Subway Extension is built in similar grounds with an even more slender lining, making the implementation of SFRC for the Noord/Zuidlijn seem very feasible.

To prove SFRC is feasible for the Noord/Zuidlijn, the structural integrity has to be checked. The most important checks concern the TBM loading and the service loading, as stated in section 2.4. Significant forces from the hydraulic jacks need to be taken up by the segments, which can cause concrete spalling if no dedicated bursting reinforcement is present. Adding bursting reinforcement can solve the problem but is costly and needs an exact prediction of the location of stresses. SFRC can solve this problem due to the homogeneous fiber distribution which covers the entire cross section. The same goes for service conditions, where the ground pressure can cause localised splitting and compressive stresses. Both the ring joint and the longitudinal joint need to be checked for these tensile splitting forces. If these load cases together with the remaining load situations suffice in SLS and ULS, then SFRC can be deemed structurally feasible and advantageous with respect to costs, sustainability, and durability.

5

Methodology

The objective of this research, as stated in section 1.3, is to perform a feasibility study on using SFRC in tunnel linings of the Noord/Zuidlijn. To answer the research question, several steps will be taken. The literature study showed the challenging aspects of the design and provided insight in the material characteristics of SFRC. This forms the foundation to go over all relevant structural checks with the obtained material characteristics. The checks will partly be done with hand calculations and mostly with numerical analyses. These analyses will provide insight in the structural capabilities of an SFRC design and will be compared to the original RC design to give a clear overview of the possible benefits.

5.1. General approach

The following steps will be taken to answer the research question:

1. OBTAIN MATERIAL PARAMETERS SFRC FOR SLS AND ULS
   The method of obtaining the stress-strain diagram will be followed to get numerical input for the analyses. This will be done for different fiber contents in both SLS and ULS.
2. PERFORM NUMERICAL ANALYSIS ON SFRC MODELS
   The material properties of SFRC have been obtained and are used as input for both hand calculations and numerical analyses. The transient phases are checked with hand calculations and the construction and service phase with numerical models. This will be done with two types of models: a 3D model of the entire tunnel lining with soil-structure interaction and several 2D models of a single segment. The 3D model will be used to check cross-sectional forces in the lining, while the 2D models will be used to check for the localised failure mechanisms as highlighted in section 2.4.
3. PERFORM NUMERICAL ANALYSIS ON RC MODELS
   The original Noord/Zuidlijn design will be modelled and subjected to a numerical analysis to set a basis for comparison. This will be done for the 3D soil-structure interaction model, as well as the various 2D models. The effect of loading in the transient phases will not be compared.
4. COLLECT AND INTERPRET RESULTS
   The results of both SLS and ULS checks will be verified with the capacity of the material. A comparison between the original RC design and the new SFRC design will be made to highlight the benefits and downsides of the new design.
5. DRAW CONCLUSION
   The benefits of the new design compared the old case will be summarized. The impact with respect to structural integrity, costs, sustainability, and durability will be laid out.

5.2. Description loading and structural checks

The various loads and necessary structural checks are explained in Chapters 2 and 3 This section will show how these loads are implemented in the numerical analyses and how the structural checks will be performed.

5.2.1. Loading conditions

The 3D model includes the tunnel at a depth of 30 meters with the different soil layers as specified in 3.2. The material characteristics of each soil layer, as provided in Appendix A, are used as input in the numerical model. The numerical model will exert the loading caused by these soil layers onto the concrete tunnel and will give output results of the stresses generated in the concrete. This is all done automatically. However, to give an idea of the magnitude of loading onto the tunnel a simple hand calculation is made. Figure 5.1 provides an overview of the dimensions and the loading situation in the service phase. The 2D view shows the surface load and summation of soil and water pressure. The latter is shown on a single tunnel for simplicity, but acts on both.

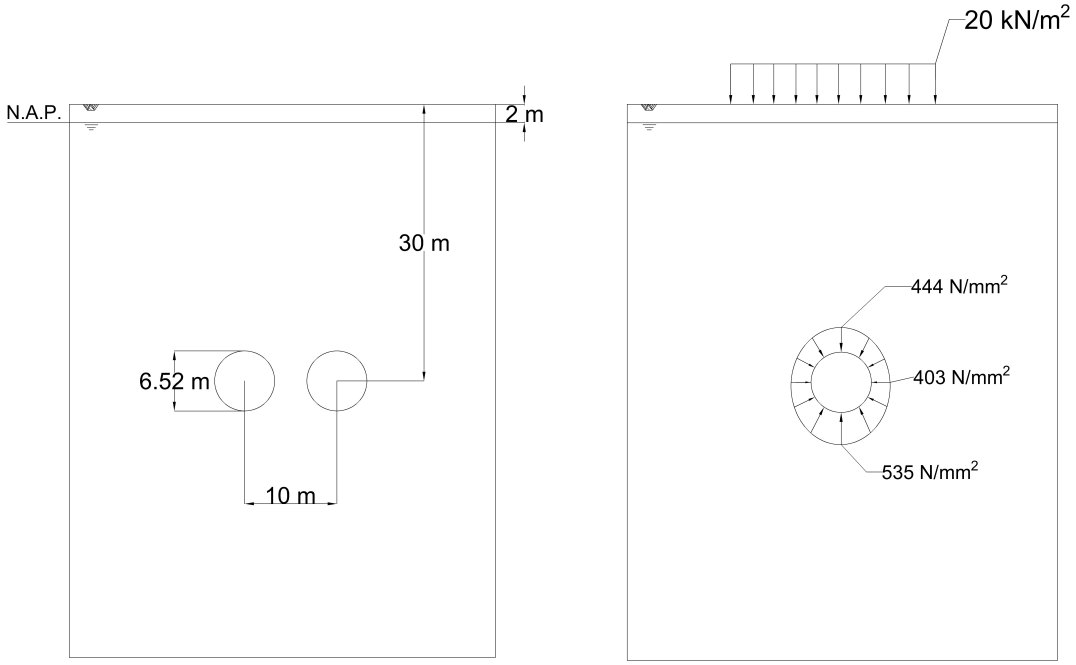

(a) Overview of dimensions

(b) Overview of normative loading

Figure 5.1: Position of tunnels and normative loading in service phase

The loading due to the soil and water pressure generates internal forces in the lining. The global cross section check is done with these forces. Furthermore, the normal force and bending moment provide loading to the longitudinal joint, which need to be checked. Figure 5.2a gives a general overview of the forces inside the tunnel ring. The actual forces are given in Figure 5.2b with the dimensions of the longitudinal joint as well. These forces are taken from the design report of the Noord/Zuidlijn and are in line with the results from the 3D model.

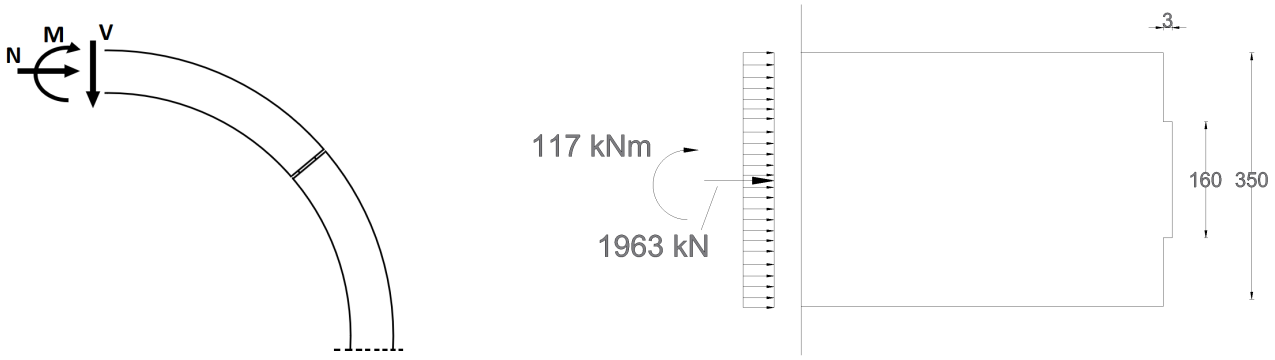

(a) Part of a tunnel ring showing internal forces

(b) Longitudinal joint loading configuration

Figure 5.2: Longitudinal joint loading due to soil and water pressure

Figure 5.3 gives an overview of the dimensions and the normative loading situations in the construction phase. These loads will be used for numerical modelling of a single segment. Figure 5.3b shows the load derived from the TBM. Each pair of hydraulic jacks has a maximum force of 4019 kN it can exert, which is spread out over the loading shoe as shown.

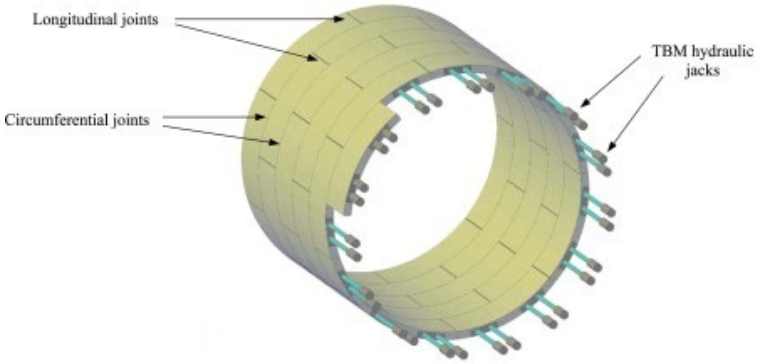

(a) 3D visualisation of loading by TBM hydraulic jacks in construction phase

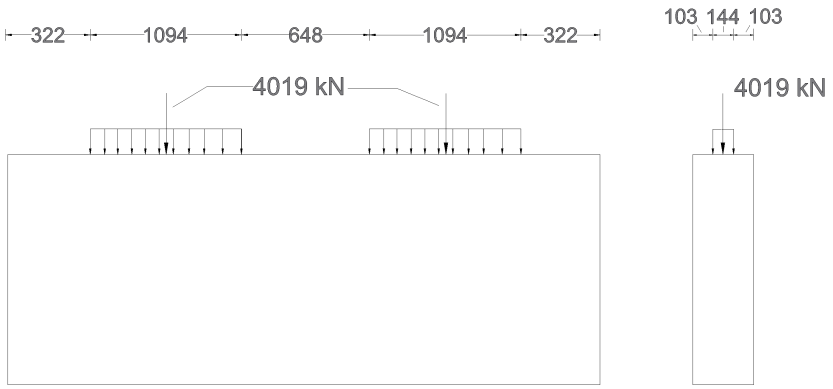

(b) Front and side view of loading configuration on a single segment; dimensions in mm

Figure 5.3: Loading by TBM pushing itself off of placed segments

5.2.2. Structural checks

The different failure mechanisms and corresponding structural checks can be divided into Serviceability Limit State (SLS) checks and Ultimate Limit State (ULS) checks. SLS verification is needed to verify whether a structure and it's parts can maintain it's function during the service life. Deflection should not harm the function and aesthetics of a structure, and cracks should not be big enough to cause durability problems. ULS verification is needed to verify whether structural failure occurs, i.e. stresses should not exceed the capacity of the structure. This includes bending, shear, pure compressive, and pure tensile stresses.

The most critical phases in the design are the construction and service phase. The ring joint plays a part in the construction phase and the cross sectional forces and longitudinal joint play a role in the service phase. Also the strength of the individual segment during the transient phase needs to be verified for their cross sectional forces. These three components need to be checked in both SLS and ULS. Table 5.1 shows an overview of the structural checks per phase per limit state.

Table 5.1: Structural checks for different phases in SLS and ULS

Component	Limit state	Structural checks
Cross sectional forces	ULS	Global bending stress Global shear stress
Ring joint	SLS	Crack width
	ULS	Localized compressive stress Localized tensile stress
Longitudinal joint	SLS	Crack width
	ULS	Localized tensile stress Localized compressive stress

It is important to define when a check is met or not, for both SLS and ULS. The requirements can differ per project and are highlighted below.

Serviceability Limit State

The main serviceability component that needs to be checked is crack width. Crack width induced by the loading, both in construction and service phase, cannot exceed the maximum allowable crack width. This allowable crack width depends on the exposure class. There are six main exposure classes:

1. No risk of corrosion or attack
2. Corrosion induced by carbonation
3. Corrosion induced by chlorides
4. Corrosion induced by chlorides from sea water
5. Freeze/Thaw Attack
6. Chemical attack

Tunnels fall inside Class 6, which is reserved for structures in natural soils beneath the ground water table. Chemicals in the soil and/or water can infiltrate small cracks in the concrete and deteriorate it. There are three levels inside the Chemical Attack class: XA1, XA2, and XA3. These stand for slightly, moderately, and highly aggressive chemical environment respectively. Class XA2 is chosen, seeing as there is no record of Dutch soils having extremely aggressive chemicals. For SFRC structures, the maximum crack design width is **0.15 mm** for class XA2 [41]. This maximum crack width is set to prevent fiber corrosion, ensure water tightness, and ensure a good concrete quality. AFTES [42] did

an examination of literature on this subject and found that for crack width smaller than 0.15 mm, steel fibers do not undergo corrosion causing a decrease in the mechanical abilities of the fibers.

This means that to comply with the SLS, the crack width should meet the following requirement:

$$w < 0.15 \text{ mm} \tag{5.1}$$

This requirement needs to be satisfied during all phases of construction and applies to all members.

Ultimate Limit State

The Ultimate Limit State for SFRC is checked in a similar manner as RC. The acting moment is compared with the moment capacity and the acting shear force is compared with the shear capacity. This method is for tunnel segments in their service phase, loaded in bending by the soil and water pressure. Additionally, a normal force is introduced in the lining which increases the moment and shear capacity. The moment and shear capacity are calculated in section 4.1 and used in the form of an envelope. To check the ULS, the acting bending moment and shear force of every part should remain inside the envelope. This means failure is reached when:

- Moment capacity M_{Rd} is exceeded
- Shear capacity V_{Rd} is exceeded

This method of checking the ULS is only valid for members loading in bending. Section 2.4 showed that there are multiple different loading configurations resulting in splitting stresses inside the concrete. The Model Code 2010 advises to verify the ULS by taking into account the strain in the material for these irregular cases. Failure is reached when one of the following conditions applies [15]:

- Attainment of the maximum compressive strain ε_{cu3}
- Attainment of the maximum tensile strain ε_{Ftu}

5.2.3. Safety methodology

To determine the feasibility of an SFRC design, the design checks have to incorporate a certain safety methodology. This research follows the recommendations of the Model Code 2010 and the *fib* Bulletin 83: Precast Tunnel Segments in Fibre-Reinforced Concrete. The latter presents guidance on the use of the Model Code 2010, based on successful projects where SFRC linings have been implemented.

The adopted safety methodology consists of two aspects:

- General partial safety factors on materials and loads
- Specific global safety factor on resistance

The design checks of the different stages in the transient phase are done in a conventional manner. Characteristic loads coming from the weight of the segments are multiplied with a factor of 1.35 to obtain the design loads [43]. The material is decreased to design values with a factor of 1.5, as prescribed in section 4.1.2.

The 2D models used for checking the ring and longitudinal joint also make use of the partial safety factors on the material (SFRC or RC) and load. Both of the joints are then checked for cracking in SLS and the longitudinal joint is checked for structural failure in ULS.

The 3D model of the tunnel makes use of a specific global safety factor, on top of a partial safety factors the material. This is done because in case of a tunnel, the loading mainly comes from the soil, which also provides support to the structure. Due to this nature, it is not simply possible to increase the relevant characteristics of the soil, since this can work beneficial to the structure. Instead, the resistance of the concrete is decreased in two steps. First, design values are used for the concrete properties to calculate the M-N envelope. Second, an additional global safety factor γ of 1.3 is used on the moment resistance envelope. This narrows the envelope to ensure a conservative approach, as seen in Figure 5.4.

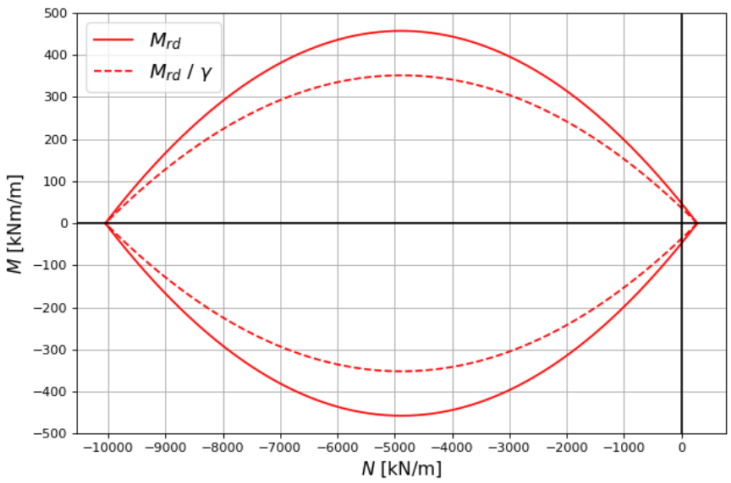

Figure 5.4: The effect of the global safety factor on the M-N envelope

The safety factor of 1.3 is based on uncertainties in both loading and modelling. The loading uncertainties arise from variations in building and surface loads, as well as from the load of constructing the second tunnel on top of the first tunnel. These three aspects have an effect on the cross section unity check. The deviations in unity check caused by these aspects are multiplied, resulting in a value just below 1.3. For that reason, a global safety factor of 1.3 is used to account for these uncertainties.

5.3. Description numerical analysis

Two types of models will be used in this research.

1. 3D model to model the full tunnel lining and surrounding soil
2. 2D models to model a single segment

Both the 3D and 2D models are made with DianaFEA, a Finite Element Analysis program. The geometry, element types, materials, and type of analysis will be elaborated in the following sections.

5.3.1. Geometry

The geometry of the 3D model is shown in Figure 5.5a. This model is made with the help of the TunnelTool2022 [44], a python tool which allows the user to easily setup the basic geometries, connections, and materials of a 3D tunnel with soil-structure interaction. The tool is used to setup the basics, and then further altered for use in this specific application.

A total depth of 60 meters is modelled, where each horizontal slice represents a soil layer with different properties. At a depth of 30 meters, the location of the two tunnels can be seen. The different components of these tunnels are shown in Figure 5.5b, where the components are taken apart for a better understanding. The to-be-excavated soil is located inside the tunnel linings, which are divided in several segment. The tunnel segments are modelled as curved shell elements which have no visible thickness. The fiber reinforcement is only modelled through the material characteristics of the concrete.

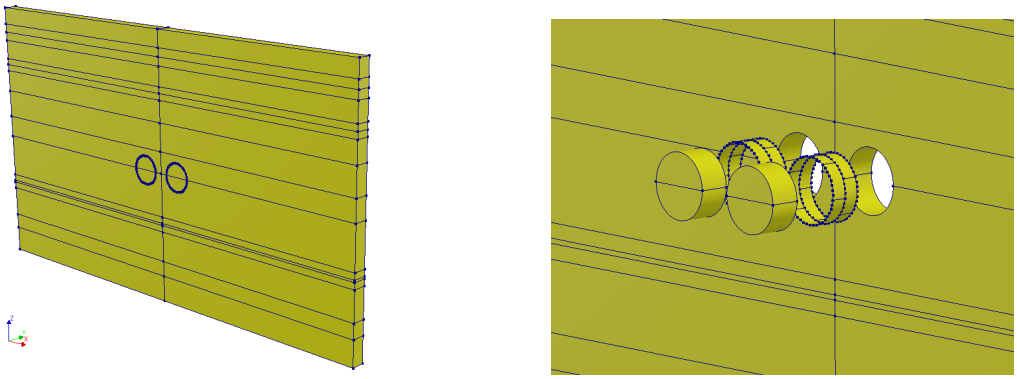

(a) Total geometry of 3D model

(b) Visualisation of excavated soil, tunnel linings, and remaining soil

Figure 5.5: Geometry of 3D model with soil-structure interaction

The model only includes two tunnel rings per tunnel, where the front is connected to the back to form a continuous loop. The couplers and plates of each segment, as well as the soil layers, are connected to create the illusion of an infinite tunnel. By doing so, any boundary influences are eliminated from the analysis. Furthermore, the face of each soil layer is supported in axial direction and the face of the bottom is supported in z direction. The soil is modelled with structural solids and has a coarse mesh of 1 m x 1 m x 1.5 m, with a finer mesh of a quarter of the size in and around the tunnel linings. The concrete tunnel segments are modelled with 2D shell elements and are 1.5 m x 0.5 m.

Several 2D models are made to check different local failure mechanism of the tunnel. The choice for multiple 2D representations of the segment instead of one 3D model is done to significantly reduce computational time. In order to account for cracking in all directions, two sides of a segment are modelled, one accounting for tangential splitting as observed from the front and one for radial splitting

as observed from the side. Because the splitting in radial direction is sensitive to the position of the jack shoe, a third model is needed to check whether the segment can withstand an eccentric loading of maximum 30 mm. All ring joint models are shown in Figure 5.6, where the denotations 'con' and 'ecc' stand for concentric and eccentric loading respectively.

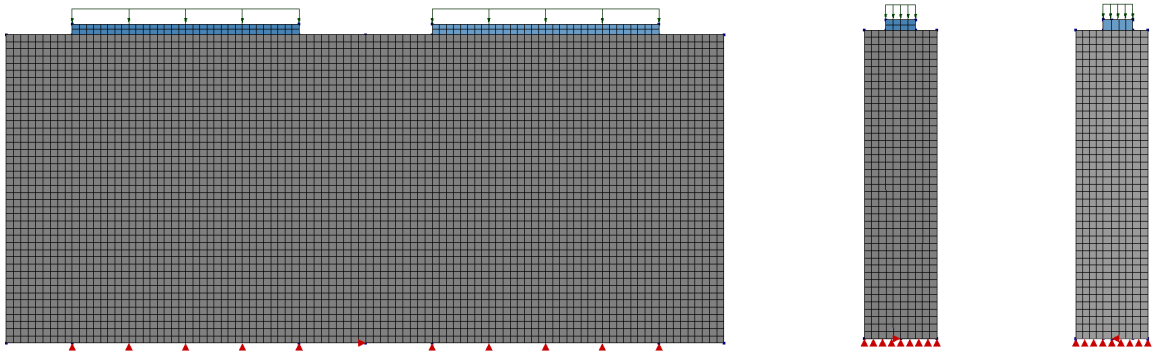

(a) Front view **(b)** Side view con **(c)** Side view ecc

Figure 5.6: Numerical models for ring joint

The hydraulic jacks produces line loads, transferred via loading plates. The support comes from contact with consecutive segments. The material characteristics of SFRC are used as input, as explained in subsection 4.1.2. A physically non-linear analysis is performed to analyse the post-peak cracking behaviour of the material. Because the accuracy of the results is highly important, different mesh sizes are taken into account. The results will be compared for the different mesh sizes to see if there is a noticeable mesh sensitivity towards the results.

The longitudinal joint is modelled using one 2D model, shown in Figure 5.7. The model simulates concrete to concrete contact at the right side by imposing a horizontal restriction and boundary interface with zero tensile stiffness. This allows for the joint to open up as a result of the bending moment in the lining. The top of the contact service is restricted in vertical direction, causing the point to act as a hinge.

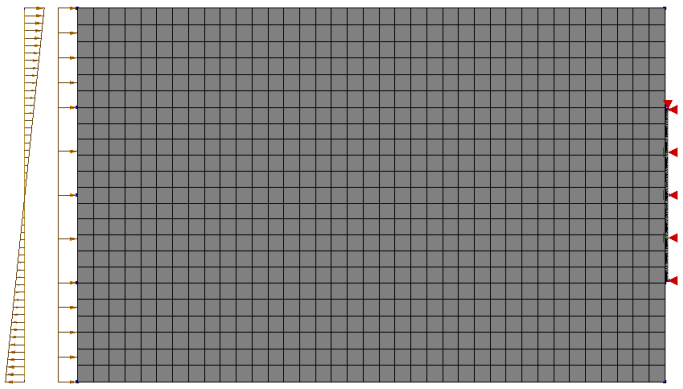

Figure 5.7: Numerical model for longitudinal joint

5.3.2. Elements

Several types of elements are used in the numerical models, each with its own characteristics.

3D model

- Solid elements
- Curved shell elements
- Reinforcement elements
- Interface elements
- Discrete spring elements

2D models

- Plane stress elements
- Reinforcement elements
- Interface elements

All elements are numerically integrated with a default integration scheme. The elements used in the 3D model are quadratic, and the elements used in the 2D models are linear. The reinforcement elements are only used in duplicate RC models which are compared to the SFRC models. The characteristics of the different elements are as follows:

Solid elements

Solid 8-noded elements are used to model all soil layers in the 3D model. These elements give the most accurate representation of stresses and strains in the soil. However, they produce large sets of equations resulting in large computational time.

Curved shell elements

Regular curved shell are used to model the concrete tunnel segments in the 3D model. The thickness of the elements count 9 integration layers. The output will include results, e.g. stresses, for every integration layer. Curved shell elements can take up forces in any direction, which is suitable for the application of a circular lining being radially loaded by soil.

Reinforcement elements

Embedded grid reinforcement is used to model the bending reinforcement in both the 3D model and the 2D models. These elements can be placed randomly within continuum elements without sharing nodes. This provides freedom in meshing because the mesh lines do not have to coincide with the positions of the reinforcements.

Interface elements

In the 3D model, shell line interfaces are used to model the ring joint and longitudinal joint, plane interfaces are used to model the soil-structure interaction, and point interfaces are used to model the friction pads in the ring joint. The 2D ring joint models make use of structural line interfaces to model the interface between the segment and the load plates, and a structural line (boundary) interface between the segment and the bottom supports, representing adjacent segments. The 2D longitudinal joint model makes use of a structural line (boundary) interface between the segment and the horizontal line support representing an adjacent segment.

Discrete spring elements

Translational springs are used in the 3D model to model the couplers in the ring joints. These couplers only provide stiffness in radial direction.

Plane stress elements

Plane stress elements are used to model the concrete segment in the 2D models. They are characterised by zero stress in the direction perpendicular to the plane, and non-zero strain perpendicular to the plane. This type of element can be used for structures with a relatively low thickness in comparison with the length and height which are not restricted in the out of plane direction [45].

5.3.3. Material characteristics

The numerical models make use of multiple materials, which are applied to either geometries or connections. A comparative RC model is created for each SFRC model using plain concrete and reinforcement bars.

3D model

- Steel fiber reinforced concrete
- Plain concrete
- Reinforcement steel
- Variety of soil layers
- Soil-structure interface
- Friction pad interface
- Coupler spring
- Longitudinal joint interface
- Ring joint interface

2D models

- Steel fiber reinforced concrete
- Plain concrete
- Reinforcement steel
- Load plate interface
- Boundary interface

Steel fiber reinforced concrete

The SFRC is modelled using a total strain based crack model. A Young's modulus of 36.000 N/mm^2, a Poisson ratio of 0.2, and a mass density of 2500 kg/m^3 is used. Furthermore, a rotating smeared crack model is used due to its flexible use. Rots and Blaauwendraad [46] found that fixed the fixed smeared crack model can produce overstiff results.

The stress-strain relationship of SFRC and how to obtain it is explained in section 4.1.2. The first step in obtaining the stress-strain relationship of a specimen is performing a three point bending test on a notched beam. The results can be used to calculate residual flexural tensile strengths $f_{R,j}$. This lab test is not possible with the time and resources of this research, so reference values will be used. These values are provided by Bekaert, an SFRC manufacturer, where the bending test has taken place for several concrete samples. The standardised results of these test are shown in Table 5.2.

Table 5.2: Residual flexural tensile strengths f_{Rj} for different fiber contents in MPa

(a) Mean values

	$f_{R1,m}$	$f_{R2,m}$	$f_{R3,m}$	$f_{R4,m}$
20 kg/m³	3,31	3,99	3,69	3,23
25 kg/m³	4,09	5,04	4,66	4,05
30 kg/m³	4,86	6,04	5,59	4,85
35 kg/m³	5,58	6,95	6,46	5,61
40 kg/m³	6,24	7,74	7,22	6,29

(b) Characteristic values

	$f_{R1,k}$	$f_{R2,k}$	$f_{R3,k}$	$f_{R4,k}$
20 kg/m³	2,32	2,79	2,58	2,26
25 kg/m³	2,86	3,52	3,26	2,83
30 kg/m³	3,40	4,22	3,91	3,39
35 kg/m³	3,91	4,86	4,52	3,92
40 kg/m³	4,37	5,41	5,05	4,40

Table 5.2a shows mean values of each residual flexural tensile strength. To calculate f_{Fts} and f_{Ftu}, characteristic values are needed. The characteristic values $f_{Rj,k}$ are calculated with:

$$f_{Rj,k} = K_{k,max} \cdot f_{Rj,m} \tag{5.2}$$

where $K_{k,max}$ is defined as the largest allowed value for the ratio between the characteristic lower limit value and the mean value of a post-crack tensile strength, and is taken as 0.7 [47]. This gives the characteristic residual flexural tensile strength values as shown in Table 5.2b.

Using these characteristic residual flexural tensile strengths, stress-crack width diagrams can be obtained for SLS and ULS design, following the steps explained in section 4.1.2. Subsequently, a characteristic length l_{cs} is needed to transform the stress-crack width relationship to a stress-strain relationship. The Model Code 2010 [15] proposes to use the height of the cross section as the characteristic length when no reinforcement is present. However, for numerical modelling this is not ideal and can present mesh-sensitive results. This is due to the fact that the same stress-strain relationship for different mesh sizes can give different results, as the crack width calculation in the program relies on the crack bandwidth which is linked to the element size. A larger element would result in a larger crack. The *fib* Bulletin 83 provides a solution to this problem. By taking the crack bandwidth of a model as the characteristic length, mesh sensitivity can be prevented. This method is implemented for all models, meaning the stress-strain relationship differs for all models having different mesh sizes.

Figure 5.8 shows the SLS stress-strain relationships when using the height of the cross section (350 mm) as characteristic length. Figure 5.8a shows the detailed stress-strain diagram with reference points A, B, C, D, and E. The explanation of each of these points is given in section 4.1.2, as well as an explanation of how to obtain the total diagram. Figure 5.8b shows the same graph for all different fiber contents. The fiber contents shown are not the same as in Table 5.2, but increase with 10 kg/m^3 increments up until 60 kg/m^3. This is done to give a larger range of available fiber contents, as in practice a common fiber content of 40-60 kg/m^3 is used. The values from the table are extrapolated, as a linear relation between fiber content and residual flexural strength could be seen.

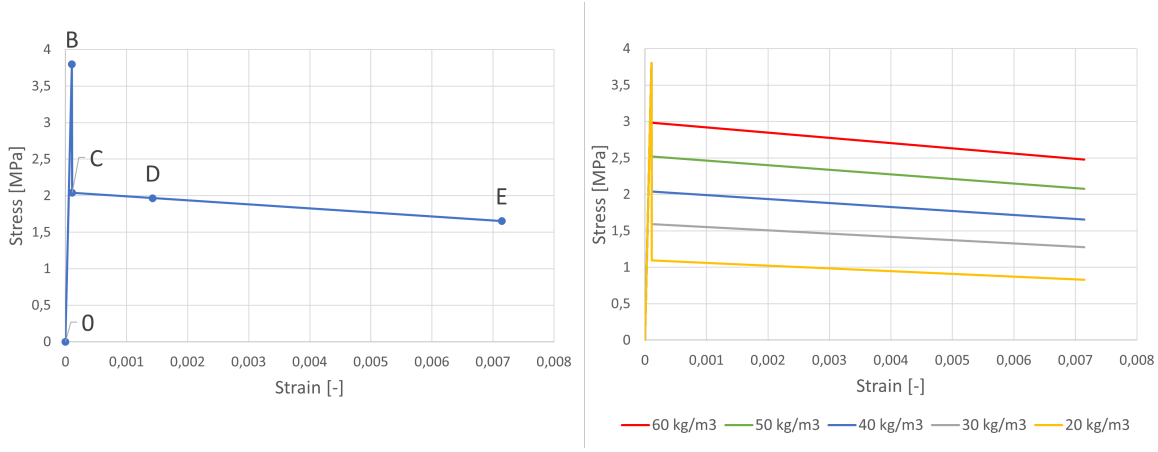

(a) Stress-strain relationship for SFRC 40 kg/m^3

(b) Stress-strain relationship for different fiber contents

Figure 5.8: Tensile stress-strain relationships SFRC used for SLS

The same can be done for ULS, where the simplified relationship as mentioned in section 4.1.2 is used. A partial safety factor of 1.5 is used when calculating f_{Fts} and f_{Ftu}. This value is used for FRC in tension [15]. The obtained stress-strain relationship consist of design values and is shown in Figure 5.9. The top figure shows the simplified stress-strain relationship for SFRC 40 kg/m^3, whereas the bottom figure shows the same simplified stress-strain relationship for different fiber contents.

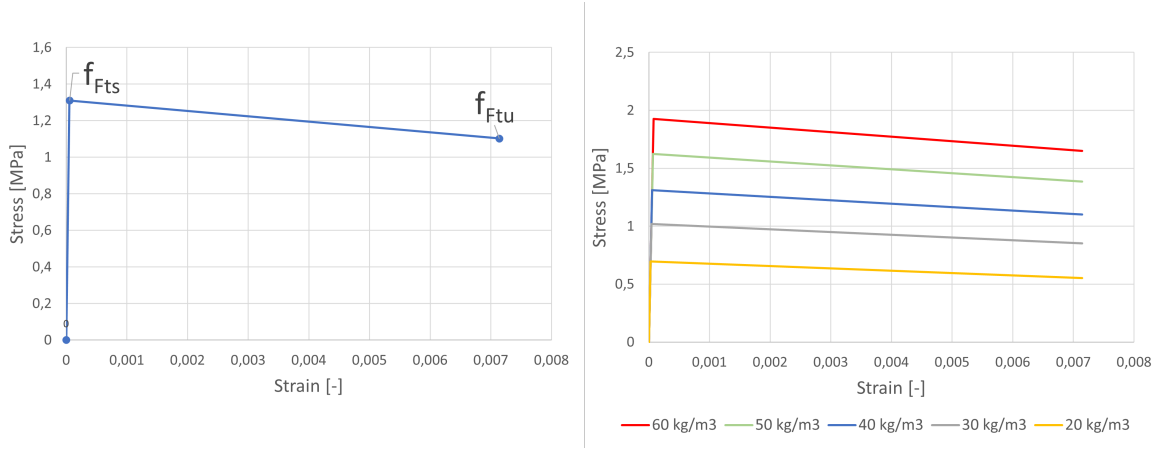

(a) Stress-strain relationship for SFRC 40 kg/m^3

(b) Stress-strain relationship for different fiber contents

Figure 5.9: Tensile stress-strain relationships SFRC used for ULS

The compressive behaviour of SFRC is said to change slightly by the addition of steel fibers. The phenomena of compressive softening behaviour is found and discussed in several research papers. Kytinou, Chalioris, and Karayannis [48] proposes a model based on Chalioris and Panagiotopoulos [49]. The model depends on the fiber volume fraction, aspect ratio and the concrete cylindrical compressive strength. Figure 5.10 shows the results of proposed model compared to the regular bi-linear stress-strain relationship of plain concrete.

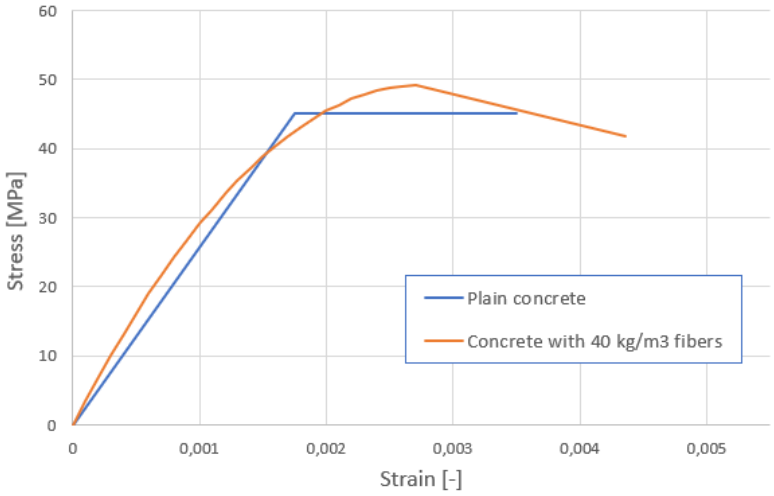

Figure 5.10: Compressive stress-strain relationship; plain concrete compared to SFRC

By adding fibers, the compressive strength increases slightly and softening occurs after the peak. However, the difference between the two graphs is small. The fiber content of 40 kg/m^3 is the highest which will be used. Lower contents are not shown in the figure, but will have a lower strength and shorter softening branch. The stress-strain relationship of plain concrete will be used for this reason. Another reason is to be more conservative and increase simplicity.

Plain concrete

The concrete grade which is used for all models is C45/55. The corresponding stress-strain relationship is modelled with a bi-linear compressive side and an exponential tensile side, as shown in Figure 5.11.

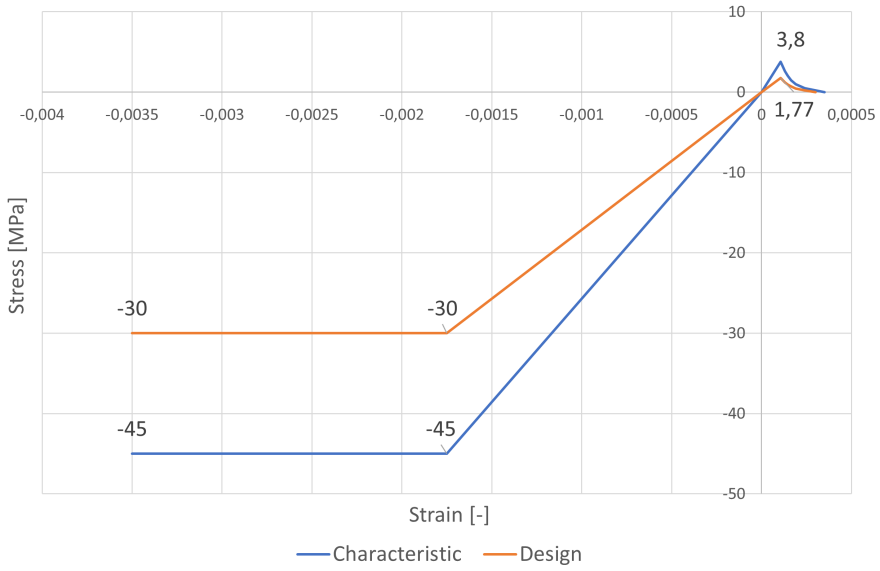

Figure 5.11: Stress-strain relationship C45/55

The plain concrete is modelled using a total strain based crack model. A Young's modulus of 36.000 N/mm^2, a Poisson ratio of 0.2, and a mass density of 2400 kg/m^3 is used. Furthermore, a rotating crack model is used.

Reinforcement steel

The reinforcement steel is of grade FEB 500 and is modelled with the Von Mises plasticity model. The design yield strength is 435 N/mm^2 and the Young's Modulus is 200.000 N/mm^2. The stress-stress relationship is shown in Figure 5.12.

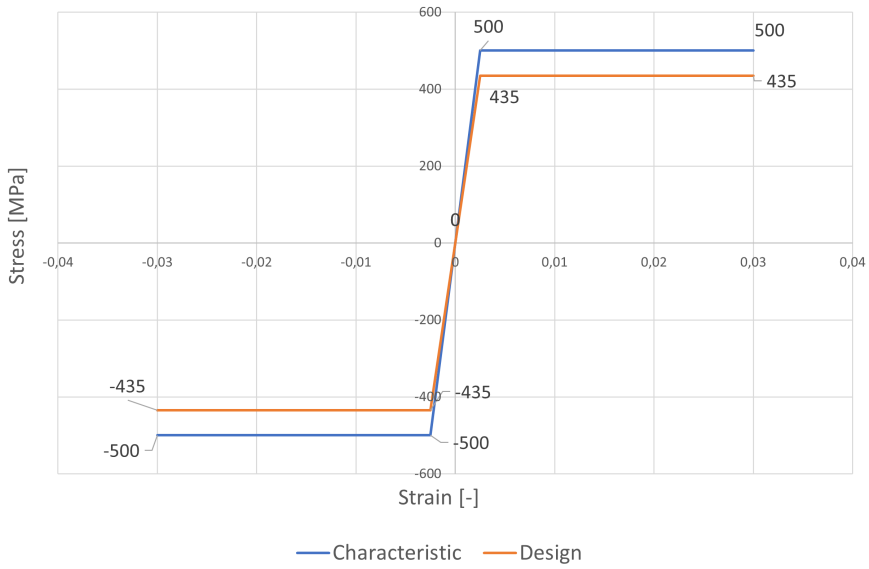

Figure 5.12: Stress-strain relationship FEB 500

Soil

The soil of the 3D model is modelled through the Hardening Soil Model / Modified Mohr-Coulomb engineering input. The soil consist of 16 different layers, as can be seen in Figure 3.2 of section 3.2.

All soil layers require the same material characteristics, which can be found in Appendix A in Figures A.1, A.2, and A.3.

Soil-structure interface
The soil-structure interface in the 3D model is represented using linear elastic properties. The interface has a normal stiffness of 20000 N/mm^3 and a shear stiffness close to zero.

Friction pad interface
Friction pads represent the hardboard plate which are the contact points between segments in the 3D model. Each friction pad is modelled with a 3D point interface. The interface has linear elastic material properties with a normal stiffness of 1 N/mm^3 and a shear stiffness of 8 N/mm^3 in both directions.

Coupler spring
The segment couplers are modelled through springs in the 3D model. A lateral spring is located at each coupler location, which acts laterally in radial direction. The springs behave linear elastic and have a stiffness of 50 kN/mm.

Longitudinal joint interface
The longitudinal joint interface of the 3D model is characterised by the Janssen model. The normal stiffness is 1000 N/mm^3 and the shear stiffness is close to zero. The bending stiffness is derived from the normal stiffness of the interface using Janssens theory [9].

Ring joint interface
The ring joint interface of the 3D model is used to model the continuous ring joint connection. A non-linear elasticity material model is used with a normal stiffness of 10000 N/mm^3 and a shear stiffness close to zero. The normal stiffness is reduced with a factor 1^{-9} when a critical interface opening of 1^{-4} mm is reached.

Load plate interface
A coulomb friction interface is used in the 2D models concerning the ring joint. The friction between the steel loading plate and concrete segment is captured with a normal stiffness, shear stiffness, and friction angle. The two stiffnesses are relative to the surrounding materials and element sizes, which means the characteristics differ per model and are calculated with:

$$k_n = 1000\frac{E}{l} \tag{5.3}$$

$$k_t = 0.001\frac{G}{l} \tag{5.4}$$

where:

$$G = \frac{E}{2(v+1)} \tag{5.5}$$

Here k_n is the normal stiffness [N/mm^3], k_t is the shear stiffness [N/mm^3], E is the elastic modulus of the adjacent elements [N/mm^2], l is the length of the adjacent elements [mm], G is the shear modulus [N/mm^2], and v is the Poisson ratio [-].

The friction angle of concrete to steel contact is assumed to be 57°[50].

Boundary interface
Boundary interfaces are used to model the concrete to concrete contact in both the 2D ring joint model and the 2D longitudinal joint model. The ring joint model makes use of a coulomb friction interface. The stiffness properties of the interfaces are dependent on the surrounding material stiffness and element size and are calculated with formulas 5.3 to 5.5. The friction angle of concrete to concrete contact is assumed to be 40°.

The longitudinal joint model makes use of a nonlinear elasticity interface. This interface represents the opening of the joint due to the applied bending moment. The normal and shear stiffness are initially calculated with formulas 5.3 to 5.5, and decreased with a factor 1^{-11} when the interface reaches an opening of 1^{-11} mm.

5.3.4. Analysis and output

Two types of analysis will be performed in total. The 3D model will be subjected to a phased analysis, while the 2D models will be subjected to a structural non-linear analysis.

3D model - Phased construction analysis

The phased construction analysis is divided in three phases.

1. Soil stress initiation
   During this phase the soil stress of each layer will be initialised. All soil is present and a linear distribution of stresses is seen downwards.
2. Excavation of soil and placement of tunnel 1
   The soil for tunnel 1 is excavated and the tunnel linings with corresponding reinforcement, connections, and interfaces are placed.
3. Excavation of soil and placement of tunnel 2
   The soil for tunnel 1 is excavated and the tunnel linings with corresponding reinforcement, connections, and interfaces are placed.

The analysis makes use of full Newton-Raphson solution procedure, with both displacement and force convergence norms with a convergence tolerance of 0.01.

The relevant output for this analysis consists of the internal principal stresses, bending moments, shear forces, crack widths, and displacements. This output is taken from the center of the elements in order to easily see if every element suffices the various checks. This way numerical irregularities of for example localised stresses will be averaged out over the element.

2D models - Structural non-linear analysis

The structural non-linear analysis is done taking into account the physical non-linear behaviour of the material. The analysis makes use of full Newton-Raphson solution procedure, with both displacement and force convergence norms with a convergence tolerance of 0.01. The loading is applied using displacement control to capture the complete behaviour. Step size differs per model in order to get the best convergence behaviour.

The relevant output for this analysis consists of the internal principal stresses, principal strains, principal crack width, and displacements. The principal stresses and strain are calculated in the integration points of every element to get the most accurate results. The crack width is computed by measuring the relative displacement at either sides of a crack. This is done to eliminate any influence of the calculation method on the crack width.

5.4. Numerical model verification

The models used in this research for checking the splitting and spalling phenomena during construction need to be verified and validated. This is done by replicating an experimental program with the proposed numerical model to see if real-world behaviour can be captured correctly. The numerical model is deemed accurate and credible if it can reproduce the results of the experimental study within a reasonable range. The goal is to calibrate the numerical model in such a way that the experiment can be reproduced, while basing the model parameters on relevant sources.

5.4.1. Material model

The material model as explained in section 4.1.2 is used to capture the tensile and compressive behaviour. The value of f_{Fts} happens to be smaller than f_{Ftu} for the experiments used for the verification.

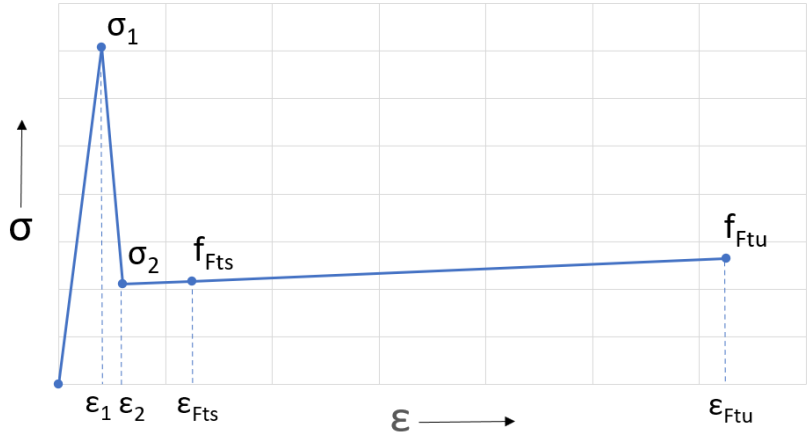

Figure 5.13: Tensile constitutive model: $\sigma - w$ relationship

$\sigma_1 = f_{ctm}$ $\quad$ $\varepsilon_1 = f_{ctm}/E_c$

$\sigma_2 = interpolated$ $\quad$ $\varepsilon_2 = interpolated$

$f_{Fts} = 0.45 f_{R1}$ $\quad$ $\varepsilon_{Fts} = 0.5 \,/\, l_{cs}$

$f_{Ftu} = 0.5 f_{R3} - 0.2 f_{R1}$ $\quad$ $\varepsilon_{Ftu} = 2.5 \,/\, l_{cs}$

An important aspect of this stress-strain relationship is the chosen characteristic length l_{cs}. The *fib* Bulletin 83, regarding SFRC in precast tunnel segments, recommends using the crack bandwidth of your numerical model as the characteristic length l_{cs}. Cracks are smeared over the crack bandwidth, so doing this will significantly reduce the mesh dependent influence on the crack width calculation. The stress-strain relationships used for the models is thus based on the mesh size.

5.4.2. Experimental program 1

The 2D models used for performing the ring joint check are verified using an experimental program by Conforti, Tiberti, and Plizzari [51]. The experiment compared segments with different reinforcement configurations subjected to thrust loading to evaluate the splitting and spalling behaviour. Rectangular blocks reinforced with either polypropylene fibers, polypropylene fibers and conventional reinforcement, or plain concrete were used. The specimens were non-curved and 1000 mm in length, 750 mm in height, and 150 mm in thickness. The thrust loading was applied symmetrically with two loading areas of 150 x 150 mm. To capture the spalling and splitting cracks, LVDTs (Linear Variable Differential Transformers) and PTs (Potentiometric Transducers) were installed. An overview of the

test setup is shown in Figure 5.14.

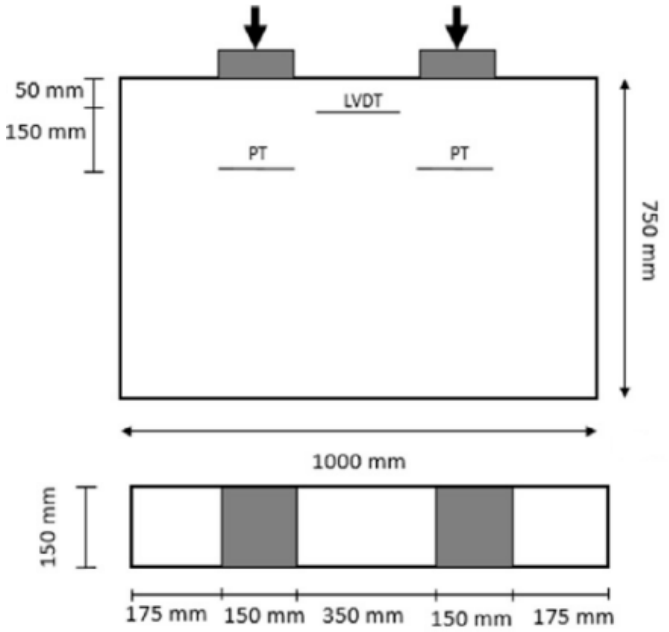

Figure 5.14: Test setup experimental program 1 [51]

The loading was applied in a load-controlled manner using hydraulic screw jacks with a total capacity of 2400 kN. A layer of polytetrafluoroethylene was used between the steel loading plates and the concrete to reduce friction. The specimens were placed on a steel plate, levelled with a high-strength mortar bed. Also here a layer of polytetrafluoroethylene was used to reduce friction.

The material properties used for the fiber reinforced segments are as follows. The mean cylindrical compressive strength f_{cm} is 48.5 MPa. The characteristic cylindrical compressive strength f_{ck} is calculated by subtracting 8 from f_{cm}. The mean tensile strength f_{ctm} is calculated using $f_{ctm} = 0.3\ f_{ck}^{0.66}$. Average values of residual flexural strength f_{R1} and f_{R3} are 2.40 MPa and 3.60 MPa respectively. The fracture energy G_f is calculated with $G_F = 73\ f_{cm}^{0.18}$.

Numerical model

The two dimensional numerical model is setup with the exact dimensions of the experimental program. Plane stress elements are used for the concrete segment. Two steel loading plates, modelled with plane stress elements, are introduced to model the hydraulic screw jacks with an interface layer between the concrete and steel. The shear stiffness of this interface layer is taken as relatively small (10^{-3} times shear stiffness surrounding elements) to mimic a frictionless surface, and the normal stiffness as sufficiently big such that the initial deformation is negligible compared to adjacent elements (10^3 times normal stiffness surrounding elements). The bottom of the segment is supported vertically along the edge, with a horizontal point support in the middle. A boundary interface is introduced to mimic the contact with the polytetrafluoroethylene layer. Also here a shear stiffness of 10^{-3} times the shear stiffness of the surrounding elements is used, and a normal stiffness of 10^3 times the normal stiffness of the surrounding elements. Two mesh sizes were used: 24 mm and 35 mm. These mesh sizes were chosen based on the guideline on minimum mesh size by Rijkswaterstaat [52], and the model dimensions. A mesh which is too coarse with respect to the model dimensions would not provide reliable results.

The loading is applied in displacement control to capture the full post-peak behaviour, focusing on crack control. By summing the reaction forces of all nodes where the displacement is applied, the applied force can be calculated. The crack width is measured by taking the relative displacement of nodes adjacent to the cracks, at the locations of the LVDTs and PTs.

Comparison results

The experimental program gathered results with respect to spalling cracks between the load pads and splitting cracks under the load pads. The load at which these cracks occurred, the maximum (failure) load, and the crack widths at this maximum load were collected. Figure 5.15 shows a comparison between the numerical model and the experiment with regard to the load-crack opening behaviour of the spalling crack.

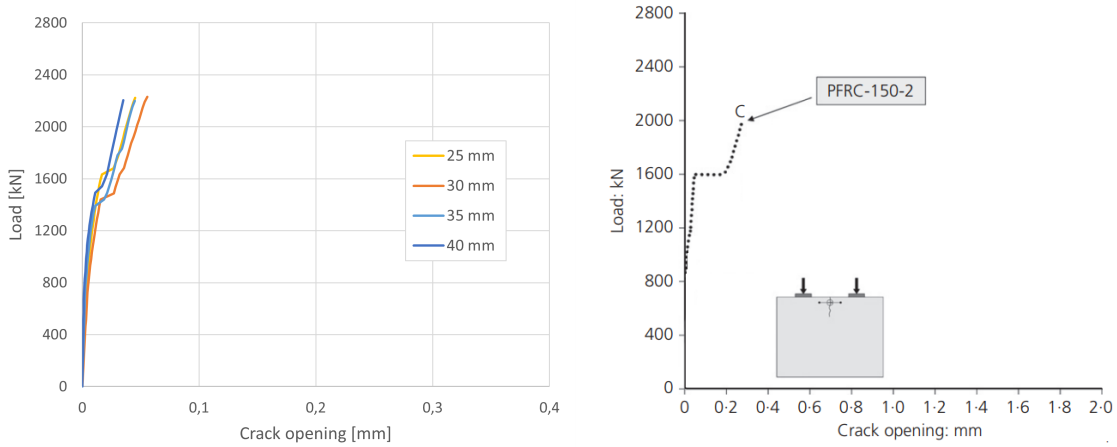

(a) Load-crack width behaviour of spalling crack in numerical model, for different mesh sizes **(b)** Load-crack width behaviour of spalling crack in experiment [51]

Figure 5.15: Load-crack opening comparison between numerical model and experimental program 1

Firstly it can be seen that different mesh sizes provide similar behaviour for the load-crack opening behaviour. Although there are minor variations in the force at which the crack localizes across different mesh sizes, the ultimate crack opening differs between mesh sizes. This can partly be explained due to the dependence of crack opening measurement height on the location of nodes. The experiment was conducted by measuring the crack width 50 mm from the top, which was only possible for the 25 mm mesh by counting two elements from the top. It was observed that a slight difference in measuring height could lead to quite a difference in crack width. Secondly it can be seen that the magnitude of the crack opening differs significantly between the numerical model and the experiment. This means the model does not represent the experimental crack width correctly. The reason for this can lie in the adopted material model, but can also be attributed to a measuring fault in the experiment itself. Even with the implementation of a notch in the numerical model at the crack location, the magnitude of the experimental crack width could still not be approached. This means that different material models would still not be possible to mimic the experimental behaviour. Lastly it can be seen that the load at which crack localisation happens in the the numerical models is similar to the experiment. The numerical models shows a slightly lower cracking load, making it more conservative. The ultimate load is slightly higher for the numerical models compared to the experiment. It can be concluded that the model does not represent this experiment in terms of crack width. The cracking behaviour however is represented accurately, with cracking load and ultimate load of similar magnitude.

5.4.3. Experimental program 2

A second experimental program is investigated to see if the quantitative behaviour can be matched with regard to splitting or spalling cracks. Tiberti, Conforti, and Plizzari [53] investigated the local splitting behaviour of FRC specimens under TBM loading. Tests were done on concrete prisms with either fiber reinforced concrete or plain concrete, loaded by a line load or point load. Specimens were casted either horizontally or vertically, to investigate the effect of fiber orientation on the performance of a specimen. Vertical casting ensures fibers to be orientated in a plane perpendicular to the crack orientation, while horizontal casting ensures fibers to be orientated in a plane parallel to the crack orientation. A perpendicular orientation is expected to be superior in terms of crack mitigation.

The tests of interest are the prisms loaded by a line load over the entire thickness. The prisms were 250 mm in length, 250 mm in width, 750 mm in height, and the loading was applied on a 100 mm wide strip. LVDTs (Linear Variable Differential Transformers) and PTs (Potentiometric Transducers) were used to measure the crack width at different locations over the height of the specimen. An overview of the test setup is given in Figure 5.16.

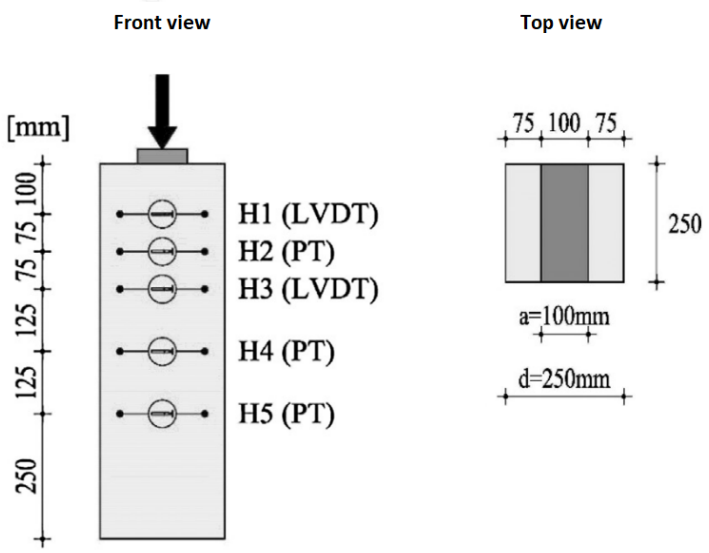

Figure 5.16: Test setup experimental program 2 [53]

The load was applied using a steel plate loaded by an electro-mechanical screw jack with a loading capacity of 1500 kN. Displacement control was adopted to capture the full post-peak behaviour and account for sudden load drops. A polytetrafluoroethylene (PTFE) layer was used between the specimen and the steel plate to reduce friction. Similarly, a polytetrafluoroethylene (PTFE) layer was used at the bottom of the specimen to reduce friction with a high strength mortar bed.

The material properties used for the fiber reinforced segments are the same as for experimental program 1. The mean cylindrical compressive strength f_{cm} is 48.5 MPa. The characteristic cylindrical compressive strength f_{ck} is calculated by subtracting 8 from f_{cm}. The mean tensile strength f_{ctm} is calculated using $f_{ctm} = 0.3\ f_{ck}^{0.66}$. Average values of residual flexural strength f_{R1} and f_{R3} are 2.40 MPa and 3.60 MPa respectively. The fracture energy G_f is calculated with $G_F = 73\ f_{cm}^{0.18}$.

Numerical model

The two dimensional numerical model is setup with the exact dimensions of the experimental program. Plane stress elements are used for the concrete segment. The steel loading plate, modelled with plane

stress elements, is introduced to model the electro-mechanical jack with an interface layer between the concrete and steel. The shear stiffness of this interface layer is taken as relatively low (10^{-3} times shear stiffness surrounding elements) to mimic a frictionless surface, and the normal stiffness as sufficiently big such that the initial deformation is negligible compared to adjacent elements (10^{3} times normal stiffness surrounding elements). The bottom of the segment is supported vertically along the edge, with a horizontal point support in the middle. A boundary interface is introduced to mimic the contact with the polytetrafluoroethylene layer. Also here a shear stiffness of 10^{-3} times the shear stiffness of the surrounding elements is used, and a normal stiffness of 10^{3} times the normal stiffness of the surrounding elements. Two mesh sizes were used: 25 mm and 33 mm. These mesh sizes were chosen based on the guideline on minimum mesh size by Rijkswaterstaat [52], and the model dimensions.

The loading is applied in displacement control to capture the full post-peak behaviour, focusing on crack control. By summing the reaction forces of all nodes where the displacement is applied, the applied force can be calculated. The crack width is measured by taking the relative displacement of nodes adjacent to the cracks, at the locations of the LVDTs and PTs along the height.

Comparison results

The experimental program collected results regarding the splitting crack opening underneath the loading pad. The crack opening measured by the LVDTs and PTs is plotted against the applied load. This is done for different locations along the height of the specimen, denoted with H1 to H5. Figure 5.17 shows the experimental results of specimens LL PFRC-V-3 and LL PFRC-H-2. LL stands for Line Load, PFRC stands for Polypropylene Fiber Reinforced Concrete, V or H denotes horizontally or vertically casted, and 2 or 3 denotes the specimen number.

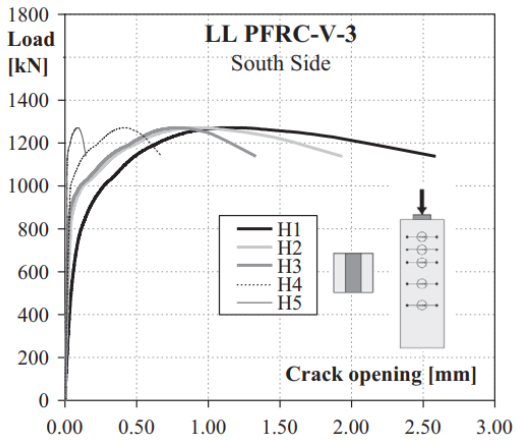

(a) Load-crack opening vertically casted specimens for five measuring locations

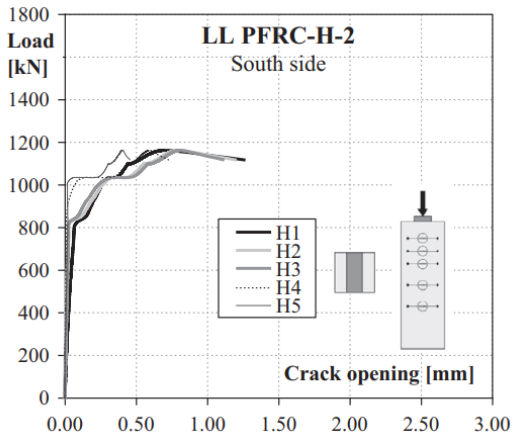

(b) Load-crack opening horizontally casted specimens for five measuring locations

Figure 5.17: Load-crack opening behaviour for vertically and horizontally casted segments of experimental program 2 [53]

The subfigures of Figure 5.17 show a difference in the load-crack opening behavior between vertically and horizontally casted specimens. The vertically casted specimen has smooth load-crack opening curves with clear distinctions in crack opening between measuring locations, reaching values of over 2 mm. In contrast, the horizontally casted specimen has an inconsistent behavior, with several loading plateaus and jumps in crack opening. There is no clear distinction in the ultimate crack opening of H1 to H3 and the maximum crack opening reaches values around 1.3 mm.

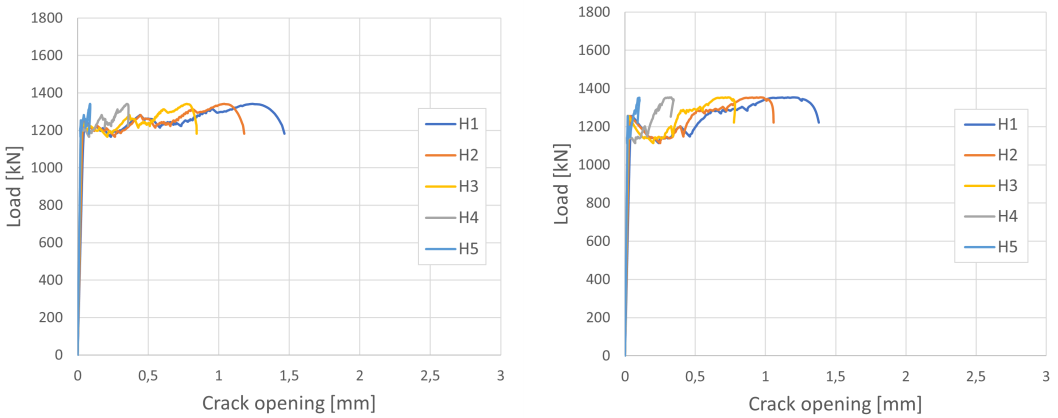

(a) Load-crack opening behaviour of splitting crack in numerical model for five measuring locations; 25 mm mesh

(b) Load-crack opening behaviour of splitting crack in numerical model for five measuring locations; 33 mm mesh

Figure 5.18: Load-crack opening behaviour of numerical model with different mesh sizes

Figure 5.18 shows the results of the numerical models, comparing the effect of mesh size on the splitting force and maximum force, as well as the crack opening of H1 to H5. Firstly, it is seen that the mesh size does not significantly affect the results since both the magnitude of the splitting force and maximum force are comparable. Similarly, the magnitude of the crack openings of H1 to H5 are comparable. Secondly, the numerical and experimental results show resemblance with regard to the crack opening and maximum load. The experimental results are divided in horizontal and vertically casted specimens. The numerical model does not make this distinction and assumes a homogeneous isotropic behaviour of the material. This means that the numerical results should lie somewhere in between the two experimental results. This is indeed what can be noticed. In the numerical results there is a clear distinction between H1 to H5 in terms of crack opening. The magnitude of the ultimate crack openings is slightly larger than what is found for horizontally casted specimens, however substantially smaller when compared to vertically casted specimens. The numerical results also show a rough behavior with several small load plateaus, similar to the horizontally casted experimental results but less severe.

Table 5.3 shows a comparison of the numerical model and the experiment using key values. The table compares the load at which the splitting crack occurs P_{split}, the crack opening at the splitting load w_{split}, the maximum load P_{max}, the crack opening at the maximum load w_{max}, and the ratio between P_{max} and P_{split}. The results for the experiment are given in ranges, since multiple specimens were used.

Table 5.3: Comparison results numerical models and experimental results

	Experiment		**Numerical**	
	Hor	Ver	25 mm mesh	33 mm mesh
P_{split} [kN]	836 - 985	840 - 1020	974	976
w_{split} [mm]	0.07 - 0.15	0.11 - 0.29	0.16	0.17
P_{max} [kN]	1022 - 1163	1160 - 1439	1340	1340
w_{max} [mm]	0.63 - 1.25	0.63 - 1.24	1.21	1.09
P_{max} / P_{split}	1.04 - 1.39	1.31 - 1.51	1.38	1.37

It can be seen that both the splitting force P_{split} and splitting crack width w_{split} taken from the numerical models fall inside the range of the experimental values for vertically casted specimens, and at the top of the range of the horizontally casted ones. The maximum force P_{max} of the numerical models falls inside

the range of the vertically casted specimen and is higher compared to the horizontally casted specimens. The maximum crack width w_{max} of the numerical models falls inside the ranges of both the horizontally and vertically casted specimens, which are very similar. Lastly, the ratio between P_{max} and P_{split} for the numerical models falls inside the range of the experimental values for vertically casted specimens, and at the top of the range of the horizontally casted ones.

5.4.4. Concluding

The numerical model has been demonstrated to be representative of reality to a certain extent. Experimental program 1 proved that the numerical model very accurately represents the different loading points, specifically the load at which the spalling crack localises. This characteristic is very important as it is vital to see if, and if yes at what load, a spalling crack localises which could exceed the serviceability criteria. The magnitude of the localised crack on the other hand is not captured correctly when compared with this experiment. Thus the reliability of the results can be questioned if the design checks of the new SFRC design for the Noord/Zuidlijn show a localised crack at the design load, because the magnitude of this crack is uncertain. If there is no localised crack at the design load, the results of the structural checks are more trustworthy. Experimental program 2 proved that the numerical and experimental results show resemblance with regard to both the splitting crack opening and the loading points. The experiment consisted of both horizontally and vertically casted specimens and the numerical models gave results in line with the middle ground. Theoretically this makes sense as the numerical model assumes a homogeneous isotropic behaviour of its material. The overall behaviour was correctly represented with a varying crack width over the height of the specimen. The magnitude of the maximum crack width is also close to the experiment. The only difference was seen in the beginning, where the numerical model showed stiffer behaviour with a late crack localisation. This outcome proves that the splitting crack opening can be represented to a certain extent, with similar values for ultimate loading and crack opening, but the initial behaviour is less stiff in practice.

5.5. Description analytical verification

The focus of this research lies on several numerical analyses to check different parts of the structure during different phases. While most of these checks are not possible to do by hand, some analytical formulas can be used to calculate the forces inside the tunnel lining due to the soil pressure. This approach allows for a comparison between the numerical and analytical results, making it possible to check whether there are any significant differences. If there are discrepancies, the hand calculations are performed incorrectly, or the numerical model is setup incorrectly.

During the service phase, the ground and water pressure acting radially on the tunnel linings causes a normal force, bending moment, and shear force in the lining. These forces are dependent on the angle θ, which represents the location around the tunnel. The angle θ is zero at the lowest part of the tunnel and increases counter-clockwise. When taking into account soil-structure interaction, the three main cross sectional forces are calculated with:

$$N(\theta) = C_{N_0} \frac{\sigma'_v + \sigma'_h}{2} \cdot r + u \cdot r - C_{N_2} \frac{\sigma'_v - \sigma'_h}{2} \cdot r \cdot \cos(2\theta) \tag{5.6}$$

$$M(\theta) = -C_m \frac{\sigma'_v - \sigma'_h}{4} \cdot r^2 \cdot \cos(2\theta) \tag{5.7}$$

$$V(\theta) = \frac{dM}{rd\theta} = -C_m \frac{\sigma_v - \sigma_h}{2} \cdot r \cdot \sin(2\theta) \tag{5.8}$$

The vertical and horizontal effective soil pressures σ'_v and σ'_h and the water pressure u are all taken at the centre line of the tunnel. Coefficients C_{N_0}, C_{N_2}, and C_m are used to take into account the soil-structure interaction. These depend on the characteristics of the tunnel lining and surrounding soil and are calculated with:

$$C_{N_0} \approx \frac{2}{2 + 1.54 \cdot \beta} \tag{5.9}$$

$$C_{N_2} \approx \frac{2 \cdot (1 + 0.064 \cdot \alpha)}{2 + 0.171 \cdot \alpha} \tag{5.10}$$

$$C_M \approx \frac{4}{4 + 0.342 \cdot \alpha} \tag{5.11}$$

Here α and β represent the flexibility and compressibility ratio of the soil and structure and are calculated with:

$$\alpha = \frac{E_s \cdot r^3}{E_t \cdot I_t} \tag{5.12}$$

$$\beta = \frac{E_s \cdot r}{E_t \cdot A_t} \tag{5.13}$$

where E_s is the constraint modulus of the soil [kN/m^2], r is the radius of the tunnel lining [m], E_t is the Young's modulus of the concrete including cracking behaviour [kN/m^2], I_t is the effective moment of inertia per unit length [m^4/m], and A_t is the cross sectional area of the lining per unit length of tunnel [m^2/m].

The input parameters for equations 5.6 till 5.13 for the case of the Noord/Zuidlijn are given and explained in Appendix D.

The cross sectional forces are not uniform around the tunnel lining. The normal force has its maxima at the sides of the tunnel and minima at the top and bottom. The bending moment has its positive maxima at the sides of the tunnel and it's negative maxima at the top and bottom. Using the simplified expressions, these values are the same but with a changed sign. The shear force has its maxima at four quarters of the lining, starting at $\phi = \frac{1}{4}\pi$. Figure 5.19 shows the general distributions of the cross sectional forces around the lining.

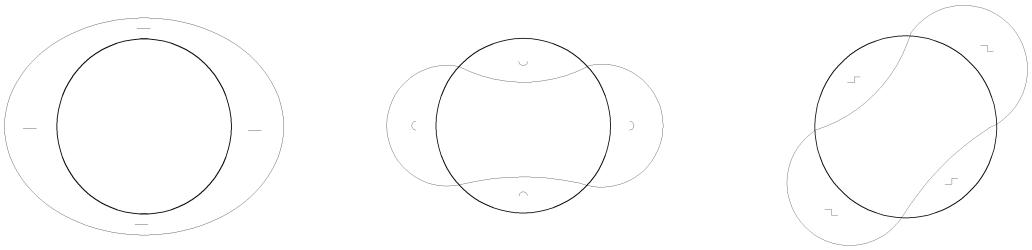

(a) Normal force distribution **(b)** Bending moment distribution **(c)** Shear force distribution

Figure 5.19: Cross sectional forces: general distribution over the tunnel lining

6

Results

6.1. Results SFRC

This section displays the results of the SFRC design, following all relevant structural checks. The transient phase can be checked with hand calculations, while for the construction and service phase the numerical models are used. These numerical models are used to check the ring joint during the construction phase, and the cross sectional forces and longitudinal joint during the service phase.

6.1.1. Transient phase

The different loading situations during the transient phase are highlighted in section 3.4. It can easily be seen whether the capacity is sufficient by comparing the acting bending moment with the moment envelope. The M-N envelopes in both SLS and ULS as calculated in section 4.1.3 are used. For the demoulding stage the material is assumed to have half of the final strength. The compressive and tensile strength are therefore halved to calculate the M-N envelope with the same method as described. Figure 6.1 shows the bending moment due to demoulding, plotted inside this reduced M-N envelope. It can be seen that both the SLS check shown in Figure 6.1a and ULS check shown in Figure 6.1b are met.

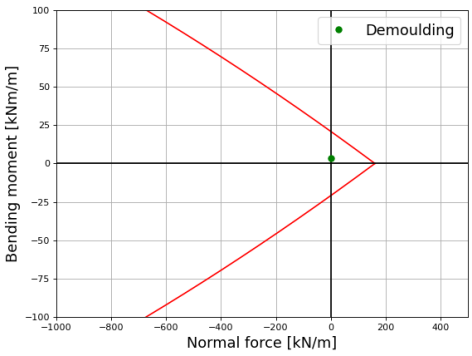

(a) Demoulding - SLS safety check

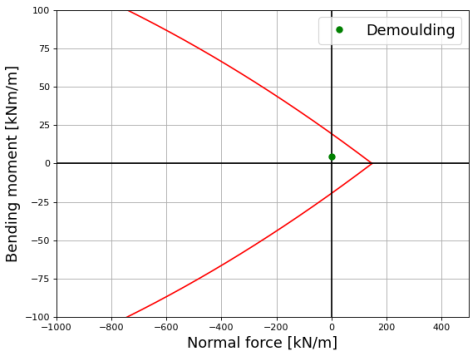

(b) Demoulding - ULS safety check

Figure 6.1: Safety checks of transient phase with reduced strength

Figure 6.2 shows the bending moments due to stacking, handling, and transport of segments plotted inside the full-strength M-N envelope. It can be seen that both the SLS check shown in Figure 6.2a and ULS check shown in Figure 6.2b are met.

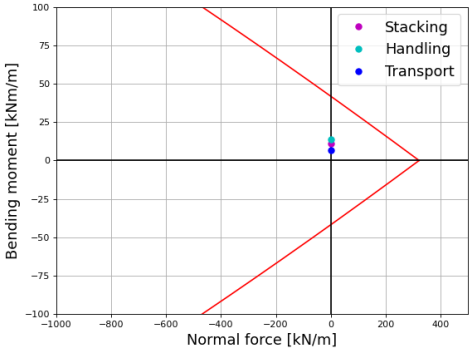

(a) Stacking, handling, and transport - SLS safety check

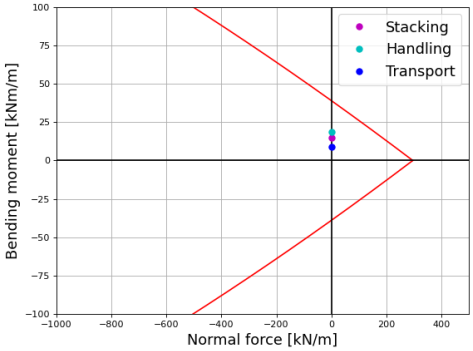

(b) Stacking, handling, and transport - ULS safety check

Figure 6.2: Safety checks of transient phases with full strength

6.1.2. Construction phase

Three models are used to check the ring joint: front view, side view with concentric loading, and side view with eccentric loading.

Front view - tangential splitting and spalling

The load-displacement behaviour of the front view model is shown in Figure 6.3. Four different mesh sizes were used to investigate the possibility of mesh sensitivity on the results. The four curves shown in the figure follow the same path but experience non-convergence at different points. This non-convergence is related to the convergence criteria and step size, and can be overcome by decreasing the step size and increasing the convergence tolerance. However, the focus lies on the loading up until and right after the failure criteria of interest: spalling and splitting. These failure mechanisms occur before non-convergence is reached, thus obtaining further convergence is not important.

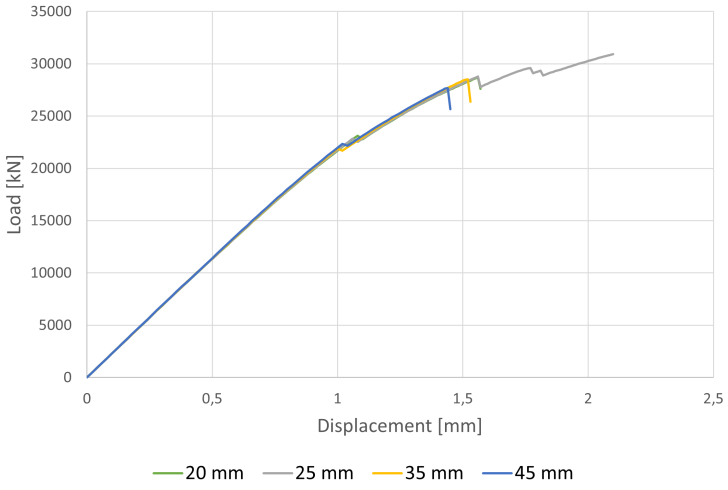

Figure 6.3: Ring joint load-displacement curve for different mesh sizes

Figure 6.4 shows the relationship between loading and crack width. This is done for the spalling crack between the loading plates and the splitting crack underneath the loading plates. Figure 6.4a shows the load-crack width relation for the spalling crack between the loading plates. The curves are plotted for four different mesh sizes, and can be seen to convergence to a solution with a decreasing mesh

size. Furthermore it can be seen that there is a stable increase in crack width, consisting of elastic deformation and micro cracking, until around 10 MN. After this loading point the crack localises and opens up, activating the fibers. The residual strength allows for a gradually increasing crack width until the segment fails due to the splitting crack underneath the loading plates. The design load during construction is 8038 kN, which is the sum of the two loading shoes per segment. It can be seen that at the design load, the spalling crack width is approximately 0.02 mm. The crack width limit of 0.15 mm is reached at approximately 1.75 times the design load.

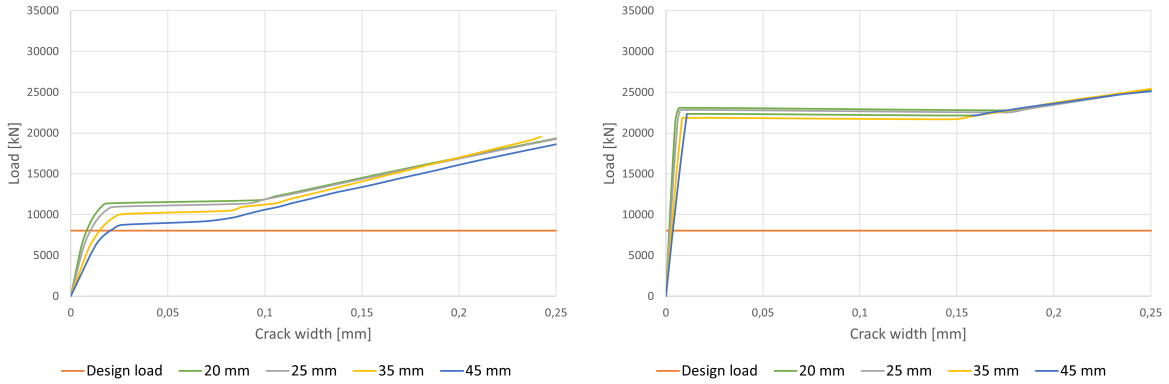

(a) Spalling crack

(b) Splitting crack

Figure 6.4: Load-crack width behaviour for different mesh sizes

Figure 6.4b shows the load-crack width relation for the splitting crack underneath the loading plates. This relationships is very different than the load-crack width relationship for the spalling crack. The first branch is characterised by elastic deformation with no cracking. When the loading reaches a certain point, around 22.5 MN, cracking occurs and localises immediately. After the splitting crack has formed, the crack width increases significantly with a marginally increasing load until the segment fails. The design load of 8038 kN is well below the point of splitting.

Figure 6.5 provides a visualization of the behaviour. When the load reaches the design load there is only microcracking and no localised crack, like the load-crack width graph showed. Spalling crack localisation happens at approximately 1.5 times the design load, and when the load reaches 2.8 times the design load, splitting occurs beneath the loading pad. Ultimately the segment fails at 3.2 times the design load due to cracking over the entire height of the segment splitting it in pieces.

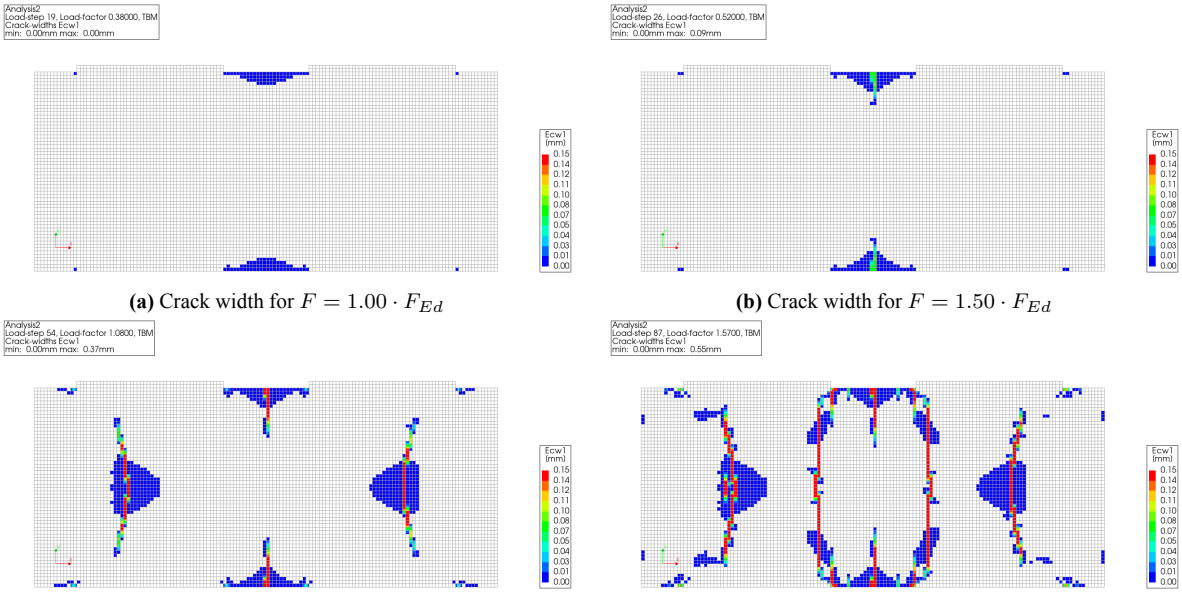

(a) Crack width for $F = 1.00 \cdot F_{Ed}$

(b) Crack width for $F = 1.50 \cdot F_{Ed}$

(c) Crack width for $F = 2.80 \cdot F_{Ed}$

(d) Crack width for $F = 3.20 \cdot F_{Ed}$

Figure 6.5: Crack development SFRC ring joint front view - 25 mm mesh

Appendix E.1 gives a visualization of the crack development with corresponding stress development for different mesh sizes: 25 mm, 35 mm, and 45 mm.

Side view - radial splitting

The load-displacement behaviour of the side view models is shown in Figure 6.6. Two different mesh sizes were used to investigate the possibility of mesh sensitivity on the results. The results from both the concentrically and eccentrically loaded models are shown in the same figure to show the effect of the placement of the loading shoe. The difference between mesh sizes for both cases is very small. It can be seen that the smaller mesh sizes reach non-convergence at an earlier stage. This can be resolved by decreasing the step size and increasing convergence tolerance, but is not relevant as mentioned before. Furthermore a difference in the peak load is noticeable between the concentric and eccentric case, with a slightly higher peak load for the concentric case.

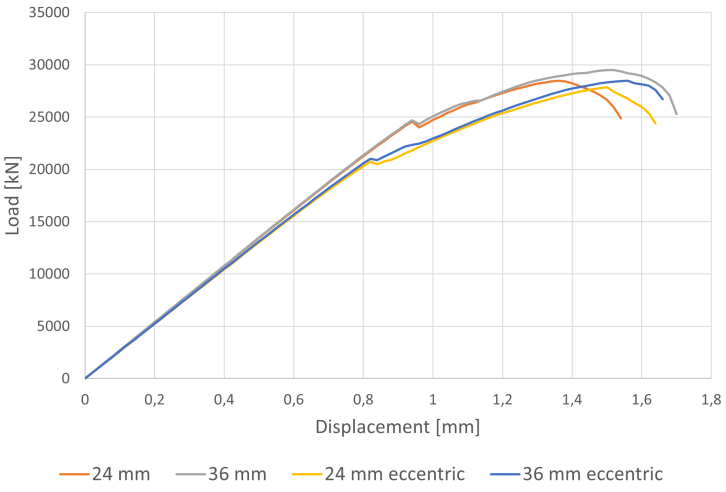

Figure 6.6: Radial ring joint load-displacement curve for concentric and eccentric loading for different mesh sizes

Figure 6.7 shows the load-crack width relation for the splitting crack underneath the loading plate. Similar to the splitting crack behaviour of the front view model, these results show a steep initial branch consisting solely of elastic deformation. Cracking occurs when the loading reaches a certain plateau, causing a localised crack. The magnitude of the crack width increases significantly with a marginally increasing load. The failure load is slightly higher than the splitting load and failure due to this splitting behaviour occurs shortly after the crack is formed.

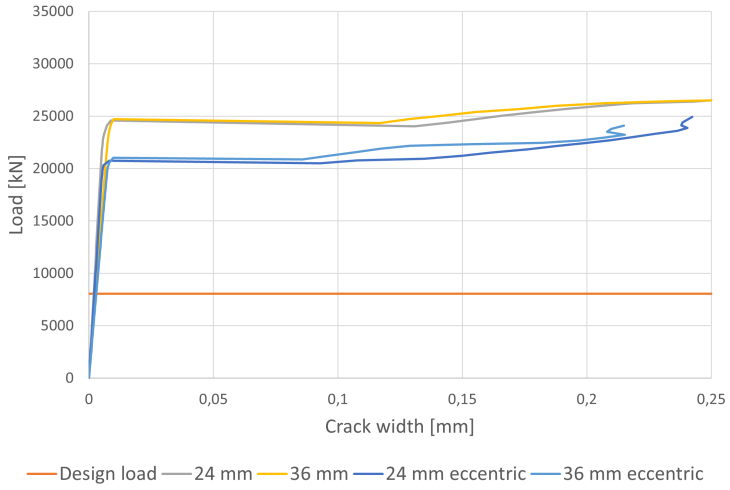

Figure 6.7: Radial ring joint load-crack width curve for concentric and eccentric loading for different mesh sizes

Figure 6.8 provides a visualization of the behaviour of the concentrically loaded segment. The first signs of microcracking can be seen at a very high load level, at approximately 2.9 times the service load. The localisation of the splitting crack happens quite fast after the first onset of microcracking, namely at 3 times the design load. This is in correspondence with what the load-crack width diagram showed. Ultimately the segment fails when the crack propagates upwards at both sides of the loading plate and the loading plate pierces the segment.

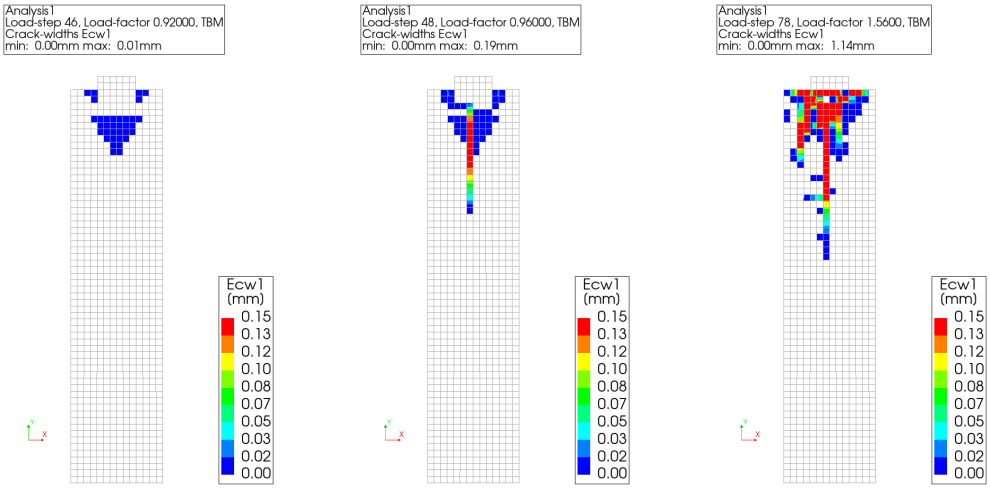

(a) Crack width for $F = 2.90 \cdot F_{Ed}$

(b) Crack width for $F = 3.00 \cdot F_{Ed}$

(c) Crack width for $F = 3.10 \cdot F_{Ed}$

Figure 6.8: Crack development concentrically loaded SFRC ring joint side view - 24 mm mesh

Figure 6.9 provides an visualization of the behaviour of the eccentrically loaded segment. Similar as with the concentrically loaded segment, the first signs of microcracking can be seen at a very high load

level. The difference the eccentricity makes can be seen in the fact that both microcracking and the crack localisation occur at a lower load level than for the concentrically loaded case. The failure mechanism is also changed by the eccentricity of the loading, causing the crack to propagate to only one side of the loading plate. The failure load is lower for the eccentrically loaded segment, which could also be seen in the load-crack width diagram in Figure 6.7.

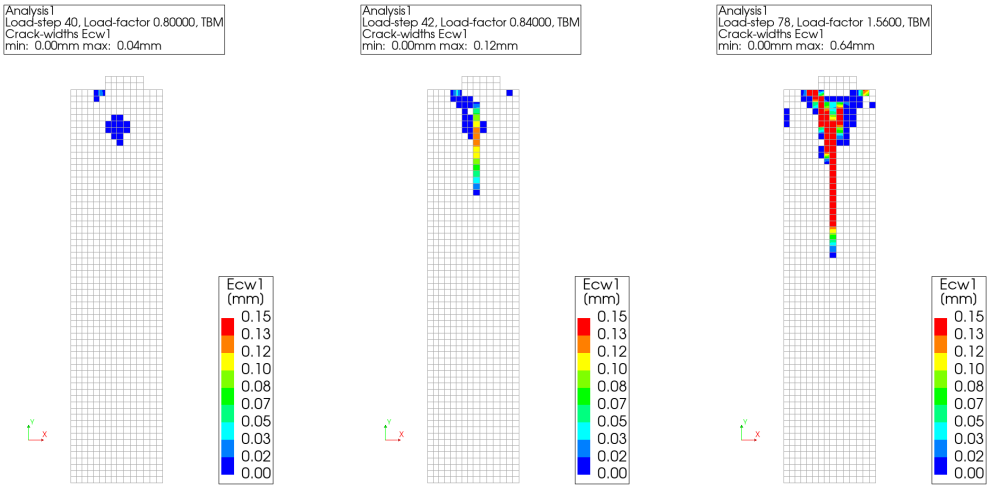

(a) Crack width for $F = 2.50 \cdot F_{Ed}$

(b) Crack width for $F = 2.60 \cdot F_{Ed}$

(c) Crack width for $F = 2.90 \cdot F_{Ed}$

Figure 6.9: Crack development eccentrically loaded SFRC ring joint side view - 24 mm mesh

Appendix E.1 gives an visualization of the crack and stress development for both the concentrically and eccentrically loaded case with different mesh sizes: 24 mm and 36 mm.

6.1.3. Service phase

Two models are used to check the service phase: a 3D model to check the global cross sectional forces caused by the soil loading and a 2D model to check the effect of the cross sectional forces on the longitudinal joint.

Global cross sectional forces

The cross sectional forces consisting of a normal force, shear force, and bending moment cause stresses in the tunnel linings which need to be checked. The structure is first checked for cracks to see if the Serviceability Limit State is passed, and then checked for failure in the Ultimate Limit State by using the moment and shear capacity envelopes as calculated in section 4.1.3.

The construction process is divided into three phases. Phase 1 is the original state of the soil before construction, phase 2 refers to the period following the completion of the first tunnel, and phase 3 refers to the period following the completion of the second tunnel. The circumferential bending moment in the lining after phase 2 and 3 is shown in Figure 6.10. The moment distribution around the lining corresponds with the theoretical expectation, which was shown in Figure 5.19 of section 5.5. The top and bottom of the ring experience the minimum bending moment, and the sides of the ring experience the maximum bending moment. The position of the maxima and minima differ slightly per ring due to the staggered position.

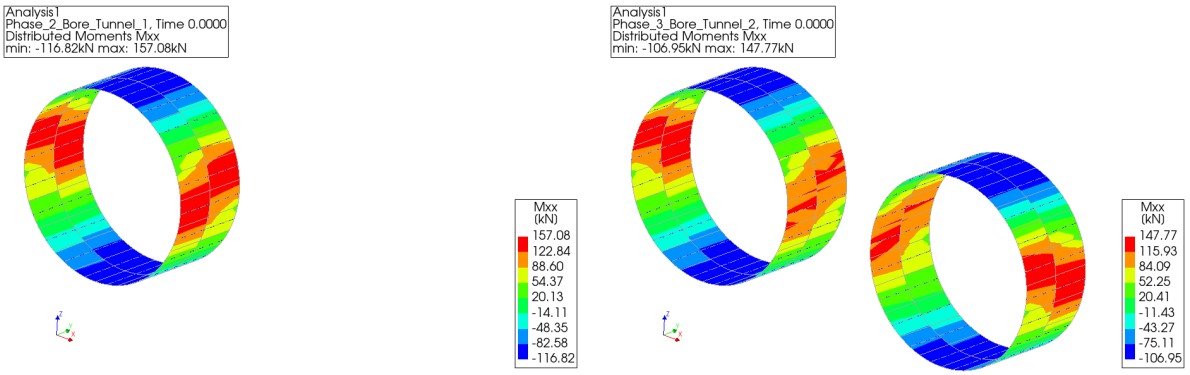

(a) M_{XX} - phase 2 **(b)** M_{XX} - phase 3

Figure 6.10: Bending moment M_{XX} distribution after phase 2 and phase 3

The bending moment, together with the normal force, induces stresses in the lining which are shown in Figure 6.11. The curved shell elements used for this model have 9 integration layers over the thickness of the element. Therefore different stresses are obtained for every integration layer. The figure shows the stress in the outer layer of every element, because this is where the maximum tensile stress occurs. It can be seen that during both phases, the maximum tensile stress does not exceed the characteristic tensile strength of the concrete, which is 3.8 N/mm^2. There are no signs of cracking, thus the structure suffices in the SLS.

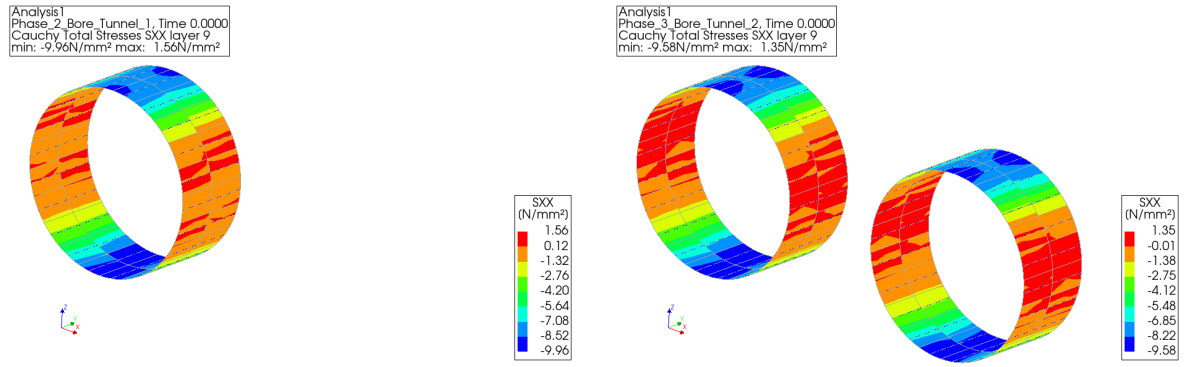

(a) S_{XX} - phase 2 **(b)** S_{XX} - phase 3

Figure 6.11: Stress S_{XX} after phase 2 and phase 3

Appendix E.3 provides additional plots of the bending moments and stresses. The bending moment M_{YY} and the torsional bending moment M_{XY} are given, as well as the stresses in the two remaining directions, i.e. S_{YY}, and S_{ZZ}. All stress levels are below the tensile strength of the concrete.

To check the Ultimate Limit State, the bending moment, normal force, and shear force of every element of the 3D model can be plotted in combination with the M-N (moment-normal force) and V-N (shear force-normal force) envelopes to see whether the capacity is sufficient. Figure 6.12 shows the acting bending moments and shear forces plotted in the ULS capacity envelopes. Both the M-N and the V-N envelope are plotted with design values (solid line) and design values divided by the global safety factor (dotted line). It can be seen that the bending moment and shear force of every element in the tunnel is within the capacity. Therefore the bending moment and shear force check are met in ULS.

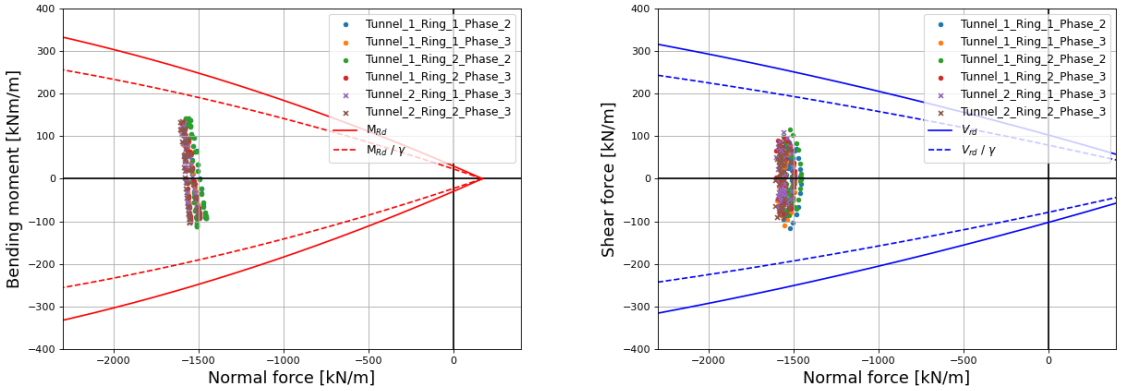

(a) Bending moment check in ULS

(b) Shear force check in ULS

Figure 6.12: Bending moment and shear force ULS safety check during service phase

The order of magnitude of the global cross sectional forces can be verified using the analytical formulas as presented in section 5.5. Here several formulas are provided to calculate the internal normal force, shear force, and bending moment. The calculated results using these formulas provide guidance to the numerical results. If the cross sectional forces calculated with these formulas are similar to the results of the numerical results it can be concluded that there are no major flaws in the modelling approach. The comparison can be found in Appendix D.2.

Longitudinal joint

The longitudinal joint is checked for splitting of the concrete due to the normal force and bending moment acting in the lining. This is done by showing the moment-rotation behaviour of the segment in both SLS and ULS. The design moment is compared with the moment at which failure occurs. For SLS failure is defined as exceeding the crack width criteria of 0.15 mm and for ULS failure is defined as exceeding the ultimate strain in either compression or tension.

Figure 6.13a shows the bending moment-rotation relationship obtained from the numerical model with SLS conditions. Characteristic values are used for the material input as well as the loading. The theoretical capacity according to Janssen is shown in red, the characteristic load in grey, and the load at which the crack width is exceeded in yellow. It can be seen that the load at which the SLS conditions are exceeded is close to the theoretical capacity and higher than the characteristic load. This means the SLS check for splitting has been met.

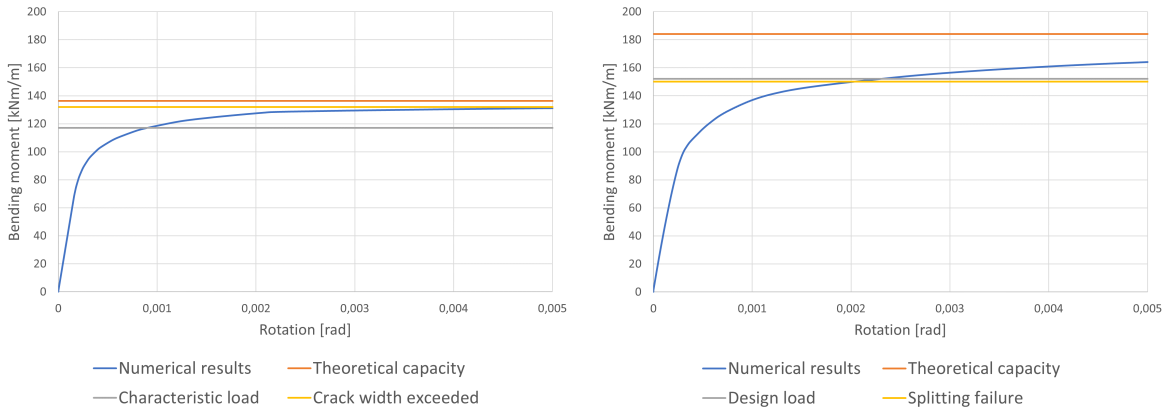

(a) SLS **(b)** ULS

Figure 6.13: Bending moment-rotation behaviour of SFRC longitudinal joint

Figure 6.13b shows the bending moment-rotation relationship obtained from the numerical model with ULS conditions. Design values are used for the material input as well as the loading. It can be seen that the failure load is slightly lower than the design load, meaning the ultimate strain is exceeded at the design load and the design **does not** meet the ULS check.

The ULS check shows that the minimum amount of fibers does not provide enough resistance against failure. Therefore the design needs to be altered by increasing the fiber content to increase the capacity. This gives the material a different stress-strain relationship according to section 4.1.2. The post-peak residual tensile strength is the parameter which is affected by the fiber content and will increase. The same design principles are used with a new design, meaning the new content is set at 40 kg/m^3, the new stress-strain relationship is used in the numerical model, and the same analysis is done. The results of the model using the increased fiber content are shown in Figure 6.14.

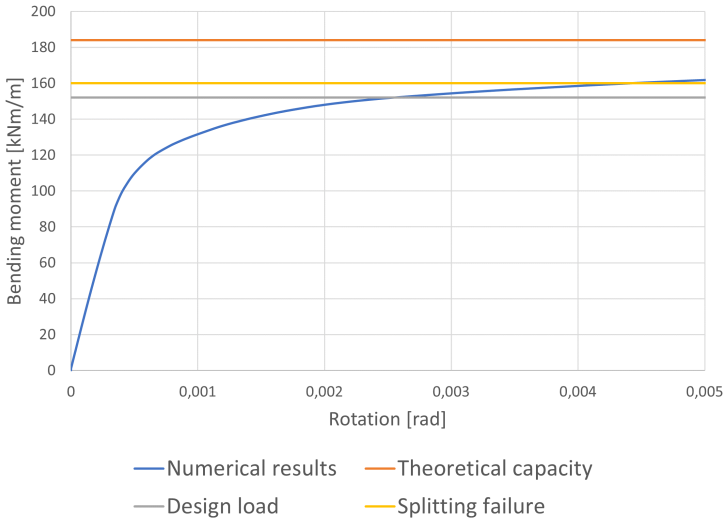

Figure 6.14: SFRC longitudinal joint bending moment-rotation for ULS with 40 kg/m^3

It can be seen that the behaviour is similar, only now the load at which the ultimate strain is reached has increased above the design load. This means the increased fiber content of 40 kg/m^3 provides enough capacity for the ULS check to be met.

Figure 6.15 gives a visualization on how the stress develops within the segment. The tensile stress shifts upward and increases in magnitude, due to the increasing moment with fixed normal force. The tensile stress nearly reaches the tensile strength at 1.15 times the characteristic bending moment. This is the loading point just before cracking, which happens abruptly. This is shown in Figure 6.16. Three loading point are shown: 1.15, 1.16, and 1.17 times the design loading. First there is microcracking, followed by a localised crack. This localised crack opens up and exceeds the crack width limit of 0.15 mm as can be seen in the most right subfigure.

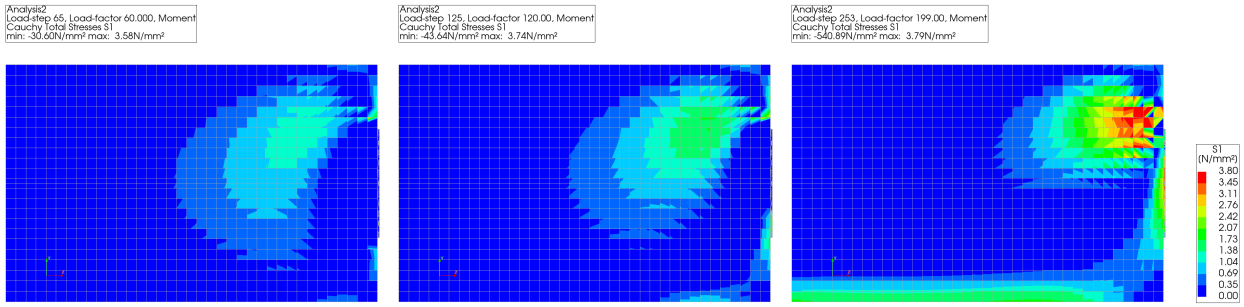

(a) Stress for $M = 0.35 \cdot M_{Ek}$ **(b)** Stress for $M = 0.70 \cdot M_{Ek}$ **(c)** Stress for $M = 1.15 \cdot M_{Ek}$

Figure 6.15: Stress development SFRC longitudinal joint - SLS

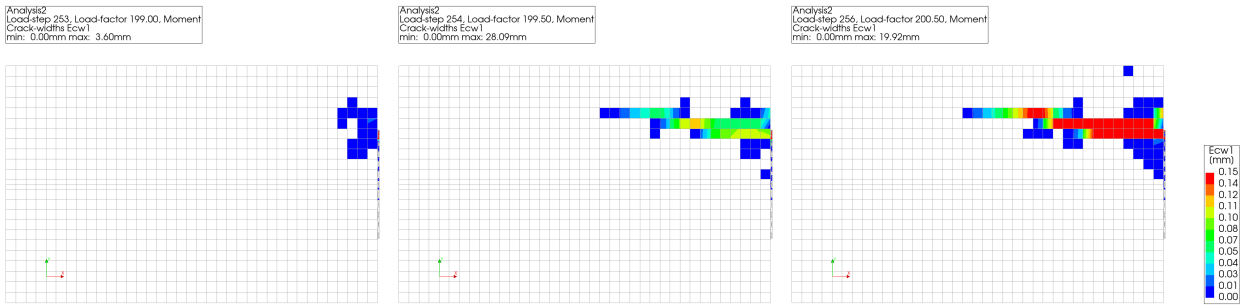

(a) Crack width for $M = 1.15 \cdot M_{Ek}$ **(b)** Crack width for $M = 1.16 \cdot M_{Ek}$ **(c)** Crack width for $M = 1.17 \cdot M_{Ek}$

Figure 6.16: Crack development SFRC longitudinal joint - SLS

In the Ultimate Limit State the focus lies on the internal stresses and strains. The failure criteria is not governed by cracking but by exceedance of the maximum strain, either in compression or tension. Figure 6.17 shows the stress development for three loading stages up until failure. Design values are used for both the loading and material. For this reason the legend is capped at the design tensile strength of this specific fiber content. It can be seen that the tensile stresses are relatively high and reach the design tensile strength quite early. In Figure 6.18 the tensile strains are shown for different load levels, closer to failure. The tensile strain increases at the cracking location and the segment ultimately fails at 0.98 times the design moment. As explained above the failure criteria is set for a tensile strain of 0.02. This means the segment does not suffice in the ULS, because the segment fails before the design loading is reached.

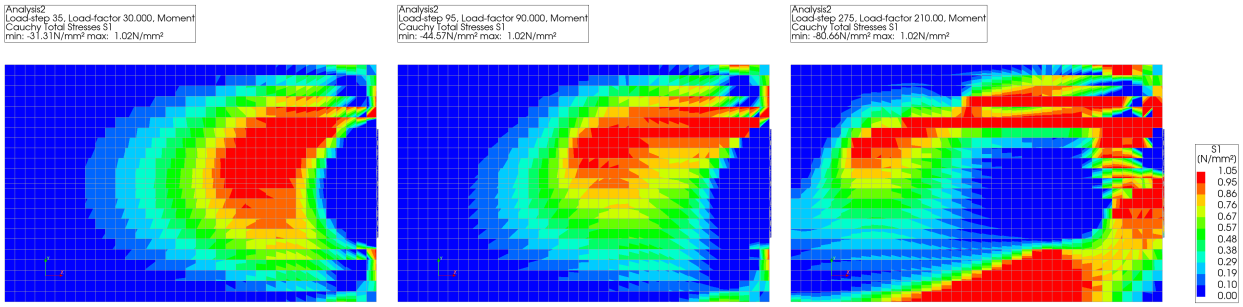

(a) Stress for $M = 0.13 \cdot M_{Ed}$ **(b)** Stress for $M = 0.67 \cdot M_{Ed}$ **(c)** Stress for $M = 0.98 \cdot M_{Ed}$

Figure 6.17: Stress development SFRC longitudinal joint - ULS

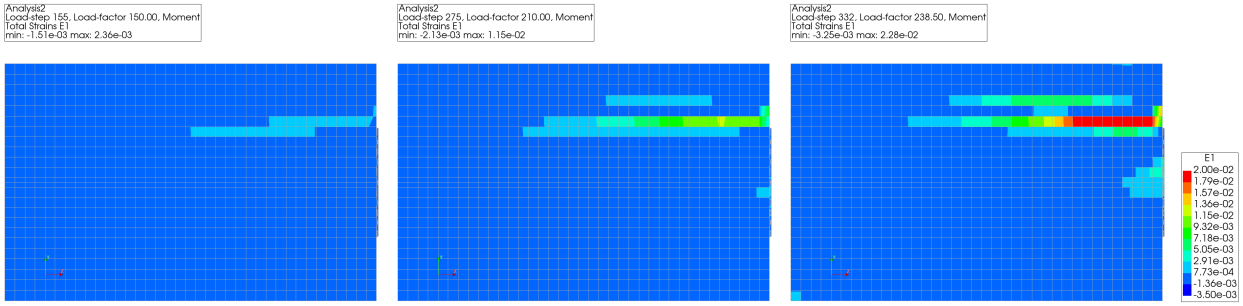

(a) Strain for $M = 0.67 \cdot M_{Ed}$ **(b)** Strain for $M = 0.94 \cdot M_{Ed}$ **(c)** Strain for $M = 1.07 \cdot M_{Ed}$

Figure 6.18: Strain development SFRC longitudinal joint - ULS

6.2. Comparison SFRC and RC

The original design of the Noord/Zuidlijn follows a certain design approach. The design of the segments for the service phase is done using a 3D FEM model, while the design for the transient phase and the construction phase is done with relatively simple calculations to determine the needed reinforcement. The different stages of the transient phase, demoulding, stacking, and handling, cause bending moments in the segments. The design bending moment is then used to calculate the amount of bending reinforcement to provide enough capacity. The construction stage follows a similar approach to calculate the needed amount of reinforcement. The construction stage has three main failure mechanisms: spalling, tangential splitting, and radial splitting. For each case, the splitting force acting in the segment is calculated using a strut-and-tie model. Then the amount of splitting reinforcement to take up this force is calculated by simply dividing the splitting force by the yield strength of the reinforcing steel. This is done for all checks, resulting in splitting reinforcement at different locations in the segment. Thus, the design has splitting reinforcement between the shoes, under the shoes in tangential direction, and under the shoes in radial direction.

This design approach is not applicable to an SFRC design, since it is not (yet) possible to calculate the needed amount of fiber reinforcement by simply considering the internal forces and moments. This research shows a different approach where the focus lies on numerical models. However, it is still interesting to investigate the difference in structural behaviour between an SFRC and RC design. For that reason, the SFRC models are also made with RC for a basis of comparison. The ring joint is modelled with reinforcement between the load pads at the location of the spalling stresses. Only the behaviour of the spalling crack is compared for the ring joint because this is undoubtedly the governing failure mechanism of the ring joint. The longitudinal joint is modelled with reinforcement at the location where splitting stresses arise. The reinforcement of both models is implemented following the original splitting reinforcement design of the Noord/Zuidlijn. Everything else has remained the same, including the dimensions, boundary conditions, loading, and analysis procedure. The two RC models are shown in Figure 6.19.

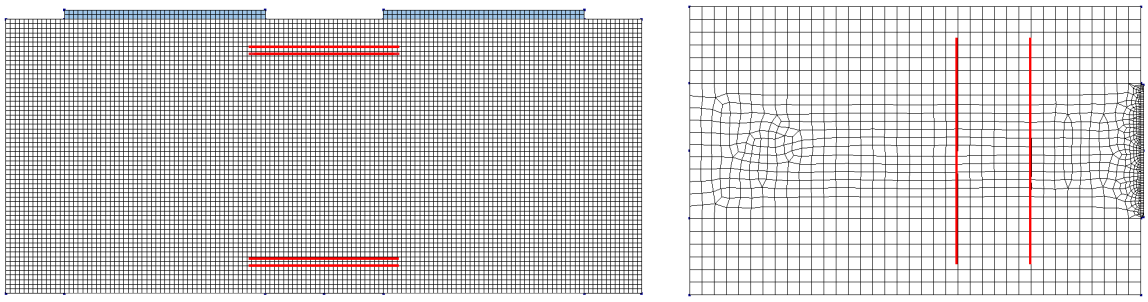

(a) Ring joint **(b)** Longitudinal joint

Figure 6.19: Numerical models with regular concrete and splitting reinforcement

6.2.1. Ring joint

The stress development in the ring joint is similar for SFRC and RC, as can be expected. First the stresses between the shoes rise and reach the tensile strength of the concrete, after which cracking occurs. This is followed by an increase in the tensile stress underneath each loading shoe, ultimately causing a significant splitting crack. The load increases further and the segment fails due to compressive crushing at the shoes or due to propagating splitting cracks.

The difference between SFRC and RC can be seen in the cracking behaviour. The comparison in crack propagation of the spalling crack can be seen in Figure 6.20. The development of the spalling

crack for the SFRC segment is known and described before. The RC segment shows a different cracking behaviour. Multiple cracks occur instead of one localised crack, at a lower load level than for SFRC. At the design load, several mid-sized cracks have formed and are held together by the splitting reinforcement. The crack width at the surface becomes larger with an increasing load level, but is controlled by the reinforcement. Ultimately the crack width limit is exceeded at the surface with possible spalling of the concrete as a consequence.

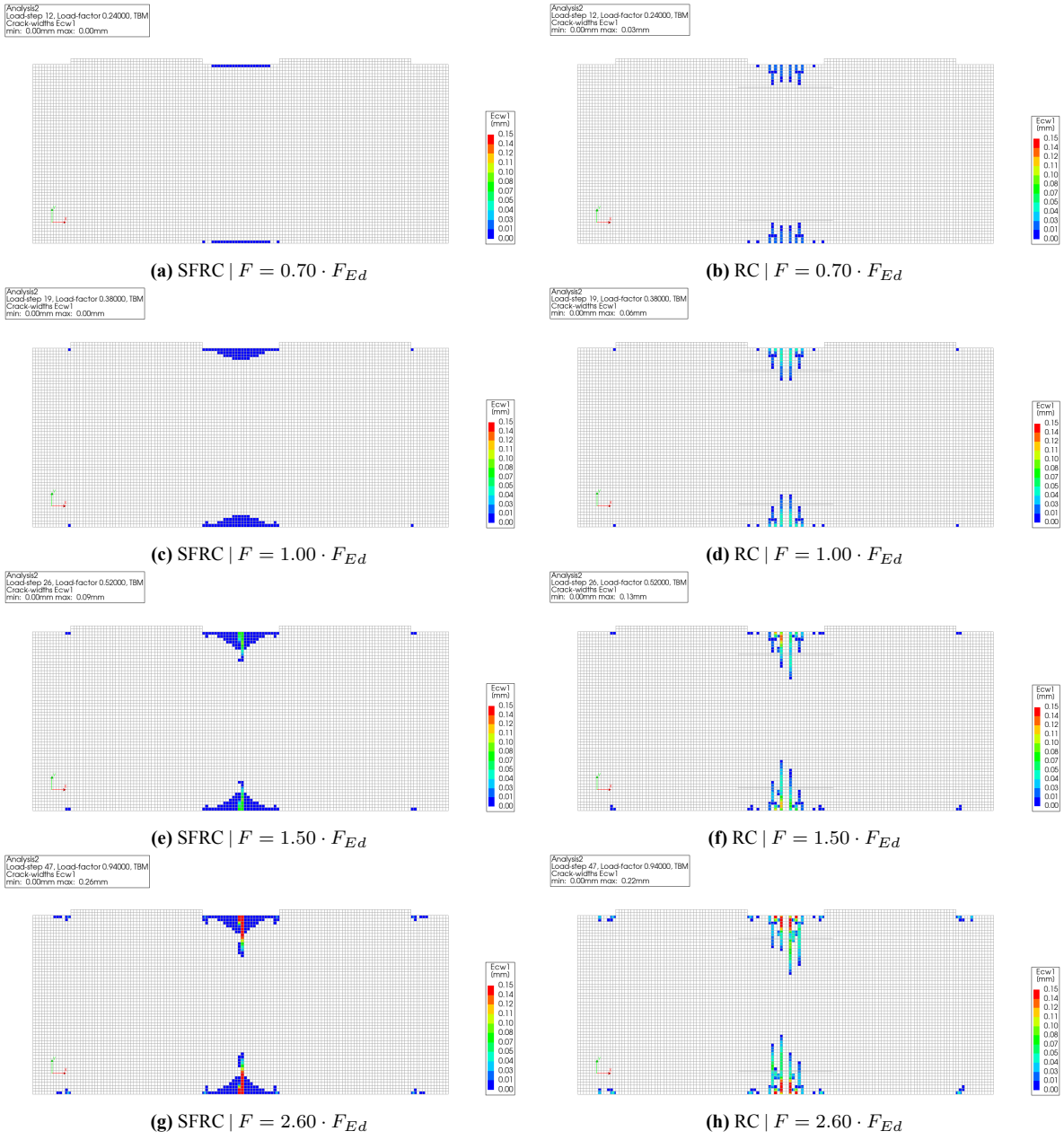

(a) SFRC | $F = 0.70 \cdot F_{Ed}$ **(b)** RC | $F = 0.70 \cdot F_{Ed}$

(c) SFRC | $F = 1.00 \cdot F_{Ed}$ **(d)** RC | $F = 1.00 \cdot F_{Ed}$

(e) SFRC | $F = 1.50 \cdot F_{Ed}$ **(f)** RC | $F = 1.50 \cdot F_{Ed}$

(g) SFRC | $F = 2.60 \cdot F_{Ed}$ **(h)** RC | $F = 2.60 \cdot F_{Ed}$

Figure 6.20: Comparison of crack development in the ring joint between SFRC and RC

Appendix E.1 provides plots of RC models with the stress, crack width, and reinforcement stress in the ring joint for different mesh sizes. It has to be kept in mind that these models only include splitting reinforcement at the top and bottom to take up the spalling cracks. The failure mechanism elsewhere in the segment will therefore be very brittle and not realistic.

Appendix E.1 also provides stress, crack width, and reinforcement stresses of the radial splitting models. Here, splitting reinforcement is provided underneath the loading pad. These figures are added for completeness but not used in a detailed comparison, since the the spalling crack in the ring joint is governing.

6.2.2. Longitudinal joint

The stress development in the longitudinal joint is also similar for the SFRC and RC models. Splitting stresses arise behind the contact surface following a strut-and-tie model and increase in magnitude while shifting upwards. A difference is noticeable in the cracking behaviour between the two and is shown in Figure 6.21. The cracking behaviour of the RC model is similar to the SFRC model with a slightly lower load. First microcracks start to form, and shortly after a localised crack occurs. After the crack has opened, the splitting reinforcement is activated and can be seen to reduce the crack width considerably. However, the crack width close to the surface exceeds the limit at a load level similar to the SFRC case.

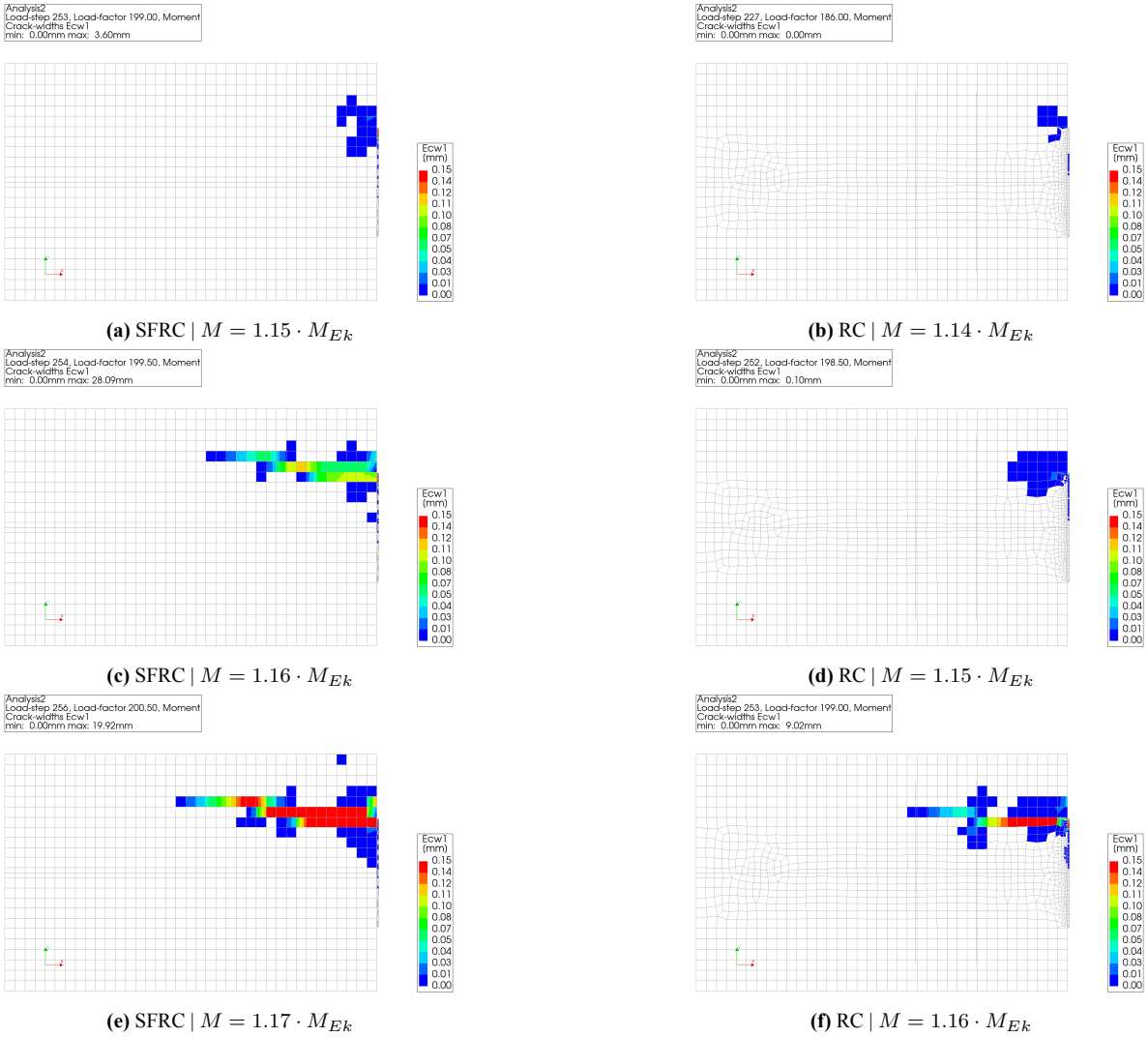

(a) SFRC | $M = 1.15 \cdot M_{Ek}$ **(b)** RC | $M = 1.14 \cdot M_{Ek}$

(c) SFRC | $M = 1.16 \cdot M_{Ek}$ **(d)** RC | $M = 1.15 \cdot M_{Ek}$

(e) SFRC | $M = 1.17 \cdot M_{Ek}$ **(f)** RC | $M = 1.16 \cdot M_{Ek}$

Figure 6.21: Comparison of crack development in the longitudinal joint between SFRC and RC

Appendix E.2 provides plots of RC models with the stress, crack width, and reinforcement stress in the longitudinal joint. It has to be kept in mind that these models only include splitting reinforcement to take up the splitting stresses. The reinforcement cage including bending and shear reinforcement is not

included for simplicity reasons, but in reality will contribute to take up stresses. The failure mechanism beyond the reinforcement will therefore be very brittle.

6.2.3. Global cross section check

The last comparison is made between the moment capacity of SFRC and RC. The same 3D model is used as displayed in section 5.3, but with the addition of bending reinforcement and the removal of SFRC properties. The original reinforcement design of the Noord/Zuidlijn is used and the same cross sectional check is executed. The bending moment of every element is plotted in the moment-normal force envelope of the reinforced section. Figure 6.22 shows the comparison of the bending moment check in ULS. The scattered points are approximately the same in both graphs as they represent the occurring bending moment in the elements, which is dependent on the loading and the stiffness of the material. The difference between the two models can be seen in the moment-normal force envelope. It is clearly visible that the minimum amount of bending reinforcement as implemented in the Noord/Zuidlijn design provides a higher moment capacity than the SFRC does.

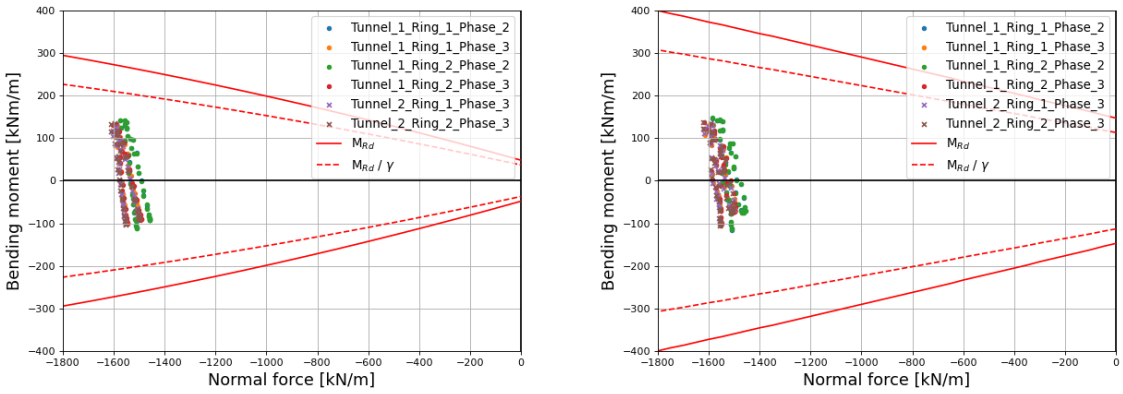

(a) SFRC with minimum fiber content

(b) RC with minimum reinforcement

Figure 6.22: Comparison between SFRC and RC bending moment check during service phase - ULS

6.3. Concluding

The design approach adopted in this research differs from the design approach used for the original Noord/Zuidlijn consisting of regular reinforced concrete. The original RC design is done with simple hand calculations to determine the amount of bending reinforcement needed for the transient phase and the amount of splitting reinforcement needed for the ring joint and the longitudinal joint. Only the soil-structure interaction during the service phase is checked with a numerical model. The SFRC design as proposed in this research also makes use of hand calculations for the transient stage and a numerical model for the service phase. However, several numerical models are needed to check the ring joint and longitudinal joint, in contrast to the hand calculations which are possible for the RC design.

The design checks of SFRC show that the minimum fiber content of 30 kg/m^3 is sufficient for the transient phase, the construction phase, and the global cross section check in the service phase. However, in the service phase the longitudinal joint fails in ULS conditions due to splitting stresses. By increasing the fiber content to 40 kg/m^3, the capacity of the material is increased slightly and the check can be met.

The difference in cracking behaviour between RC and SFRC models is shown for the spalling crack(s) in the ring joint and the splitting crack in the longitudinal joint. The cracking behaviour of the ring joint is seen to be quite different. Initial cracking occurs at a lower load in the RC model, and multiple cracks arise. In contrast, SFRC showed that initial cracking happens at a higher load level, and only one localised crack emerges. The longitudinal joint showed similar cracking behaviour, with one crack arising due to the splitting stresses. This crack is mitigated better with dedicated splitting reinforcement than fibers.

Lastly it is shown that the moment capacity of RC is higher than that of SFRC when comparing minimal reinforcement.

Benefits of SFRC design

The main benefits coming from a SFRC design lie in the costs and sustainability aspect of a project. The difference in costs and impact on sustainability as a consequence of using a verified SFRC design can be quantified to give an indication of the benefits.

The difference in costs between the new SFRC design and original RC design can be seen in multiple aspects. The biggest difference will be made in material savings, specifically the steel reinforcement. The concrete, cement, aggregates, and water content will stay the same, but reinforcement bars will be eliminated and replaced with steel fibers. On top of the material costs of the steel itself, the labour costs linked to production of the complex reinforcement cages are eliminated. Besides the material and labour costs, an important aspect is found in logistics. The traditional reinforcement bars have an irregular shape making them inconvenient to transport. To transfer the total amount of reinforcement to the production site takes significantly more trips with bars than with fibers, because fibers are transported in cube shaped bags which are very space-efficient. This lowers both the costs and environmental impact related to the transport of the reinforcement.

The difference in material costs are calculated by simply taking the difference in steel consumption between the old and new design. The total volume concrete of the segments in the tunnel lining is calculated by multiplying the total length of the two tunnels with the cross sectional area of the ring:

$$V_{concrete} = L \cdot \tfrac{1}{4} \cdot \pi \cdot (D_{ex}^2 - D_{in}^2) = (2 \cdot 3120) \cdot \tfrac{1}{4} \cdot \pi \cdot (6.52^2 - 5.82^2) = 42333 \text{ m}^3$$

The amount of steel saved with the new design becomes:

$$\Delta m_{steel} = 42333 \cdot (112 - 40) = 3047976 \text{ kg} \approx 3050 \text{ tons}$$

The reduction of steel in the new design also plays a big part in the total CO_2 emission of the project. On average, the production of one ton of steel results in the emission of 1.8 tons of CO_2 [36]. The total CO_2 savings resulting from a decrease in steel production is calculated to be:

$$\Delta m_{CO_2} = 3050 \cdot 1.8 = 5490 \text{ tons}$$

By using SFRC instead of RC 5490 tons of CO_2 emission related to the production of reinforcing steel can be saved. This number can be put into perspective by considering the amount of CO_2 a tree can take up. To produce oxygen, a tree takes up around 25 kg of CO_2 per year. This means an average of 40 trees are needed per year to convert 1 ton of CO_2 into oxygen. To take up 5490 tons of CO_2 in one year this would need 5490 · 40 = **220.000 trees**. On top of the decreased emissions due to material savings, the transport of these materials also leads to CO_2 emissions. Whether the material is transported by truck or by boat, air pollution will be high. The use of SFRC instead of RC leads to a decrease in the amount of transports which have to be done. This reduction of CO_2 is hard to quantify and therefore only mentioned as an indirect benefit.

7

Discussion, conclusions, and recommendations

7.1. Discussion

This research showed that the implementation of Steel Fiber Reinforced Concrete in tunnel linings of the Noord/Zuidlijn is feasible and provides several benefits. The structural behaviour is governed by failure mechanisms in the ring joint during construction, the longitudinal joint during service life, and the global cross section check during service life. In the ring joint, a localised crack appears between the loading shoes at approximately 1.5 times the maximum TBM load. This means that a design with the minimum fiber content of 30 kg/m^3 as starting point is sufficient for the ring joint. The longitudinal joint experiences a splitting crack at 1.15 times the characteristic load in SLS conditions, meaning it passes the check. However, it fails in ULS conditions due to exceedance of the maximum strain before the design load is reached. Increasing the fiber content to 40 kg/m^3 solves this problem and ensures that the ULS design check is met. Lastly, the global cross section check, which considers the bending moments and normal forces in the lining, is met with the minimum fiber content of 30 kg/m^3. Therefore, a design with a fiber content of 40 kg/m^3 meets all the checks. A hybrid design with 30 kg/m^3 of fibers and dedicated splitting reinforcement could also be an option, but this would require more steel, incur higher costs, and increase complexity due to the required reinforcement cage.

The difference in structural behaviour between SFRC and RC has been investigated and can be compared with the existing literature. The results of this research show that SFRC indeed has a higher initial cracking load than RC when subjected to tensile loading, which can be contributed to the presence of fibers in SFRC resisting the onset of microcracks. However, the peak load under flexural loading is higher for RC than for SFRC, as the presence of reinforcement bars increases the capacity of a segment. This is most noticeable when comparing the M-N capacity of SFRC and RC, taking into account minimum reinforcement. Another benefit of SFRC is its post-peak residual tensile strength, which allows for stable and ductile crack propagation. After a crack opens, stress gradually reduces as strain increases, and the fibers help to hold the crack together. The theory on the effect of fibers in crack mitigation shows that they are activated at the onset of microcracking, and ultimately pull out gradually at the mouth of the crack. This is well shown in the spalling crack propagation, where microcracking starts relatively early, but only results in a localised crack after a substantial increase in load. After the crack has localised, its width increases gradually until the segment fails elsewhere. In contrast, the tensile failure mechanism of RC is expected to be more brittle than that of SFRC. This is because concrete splitting and steel rupture happen abruptly at a high load for RC. This is noticeable in the 2D radial splitting model, where the segment fails abruptly as the reinforcement stress exceeds its capacity after crack localisation. In contrast, the SFRC model shows a localized splitting crack that

gradually increases until failure. Overall, the results of this research align with the expected structural behaviour of SFRC, demonstrating its benefits in crack mitigation.

Limitations of this research are found in the safety philosophy and the accuracy of the numerical models. The design methodology used in this research consists of multiple structural checks, which are done by hand and with numerical models. This makes it challenging to use one consistent safety methodology, especially when one of the numerical models involves soil-structure interaction where the loading of the soil also works as resistance. An effort is made to include partial safety factors where possible, and an additional global safety factor to account for uncertainty in the different load situations. The results obtained with this approach are therefore best used as an indication, not as a definitive design. Additionally, verification of the models with the use of experimental data was not entirely representative. The qualitative behaviour of cracking in the ring joint was captured correctly, but quantitatively this was hard to replicate. For this reason, it is crucial to ensure the loading does not reach the crack localization load, since only the magnitude of the load level was validated with an experiment, in contrast to the magnitude of the crack width. It is advised to conduct extensive laboratory testings in a new design process.

7.2. Conclusions

This research aimed to investigate the benefits of replacing traditional Reinforced Concrete (RC) with Steel Fiber Reinforced Concrete (SFRC) in tunnel linings of the Noord/Zuidlijn. The benefits in terms of mechanical properties include a higher initial cracking load in several loading situations, and a ductile failure mode which provides enough warning due to gradually opening cracks. An SFRC design of the bored Noord/Zuidlijn tunnel would reduce steel content by 60%, resulting in a total steel reduction of 3050 tons. This steel reduction consequently leads to a reduction in CO_2 emission of 5500 tons, equivalent to the amount 220.000 trees can take up in one year. Furthermore, costs are reduced due to reduced steel consumption, as well as in second order effects such as labor costs and the transport costs of reinforcement.

A new design methodology is provided which is different than the Reinforced Concrete (RC) design approach, where the emphasis is on calculating the amount of reinforcement. This research consisted of hand calculations and numerical models to check the key design aspects for cracking in SLS and failure in ULS. The governing failure mechanisms when opting for an SFRC design are found to be spalling of concrete in the ring joint in the construction phase, splitting of concrete in the longitudinal joint during the service phase, and bending failure of the global cross-section in the service phase.

The obtained results can serve as a guideline when opting for SFRC in a new bored tunnel. Special attention should be paid in the design checks to splitting of concrete between the loading shoes of the TBM during construction. This splitting force will depend on the size of the TBM and the characteristics of the soil. Furthermore, splitting of concrete in the longitudinal joint can pose an issue, when a large normal force and bending moment is present in the lining. These large internal forces can also cause a governing situation in the global cross section check. However, if a tunnel is constructed in stiffer soil such as rock, problems in the service phase are reduced and the global cross-section check as well as the longitudinal joint will be less significant. If there are any specific loading cases, such as existing buildings and foundations, fibers may not suffice. High localised loads resulting in large stresses are better taken up by dedicated reinforcement. However, it is possible to implement different reinforcement types in a tunnel. A hybrid form including SFRC and RC can be used for a specific stretch, while the rest of the route can be made of SFRC linings, still resulting in significant steel savings.

7.3. Recommendations

The discussion and conclusions of this research give room for recommendations for future research. These recommendations include aspects of this research that require further elaboration, as well as important design aspects that require attention as a result of this research.

Perform laboratory tests

It is recommended to perform several laboratory tests in the design process. Firstly, it is important to perform the standardized of determining the material characteristics of an SFRC mixture. This includes a 3-point bending test performed on a notched beam to obtain a load-crack mouth opening relationship. The results of this test can subsequently be used to follow the steps mentioned in section 4.1.2 to obtain the material characteristics used in the design process. Secondly it is recommended to conduct the same laboratory test on a full-scale section, as has been performed in the numerical models of this study. Doing this allows for a one-on-one comparison between the numerical model and experimental outcome.

Make use of 3D models

It is recommended to perform the numerical analyses of the ring joint as shown in this research using a 3D model. This research only used 2D models to significantly reduce computational time. With the help of powerful computers/servers and enough time, 3D simulations are doable and recommended for more certainty. 3D models could take into account the curvature of the segment and give a better overall cracking behaviour.

Pay attention to production aspects

The mechanical performance of SFRC is highly dependent on production aspects such as casting and compacting. Tiberti, Conforti, and Plizzari [53] showed that the casting direction has an effect of the orientation of the fibers, which has an effect on the structural behaviour. Therefore is it crucial when opting for a design with SFRC, that special attention is paid to the production of the segments. This requires a proper casting technique followed by extensive compacting to ensure a homogeneous fiber distribution and inhomogeneous orientation, to account for stresses in all parts of the concrete in every direction.

Investigate hardening behaviour

The research in this thesis is performed taking into account softening behaviour of SFRC. An SFRC mixture with hardening behaviour can be used to increase the moment capacity of SFRC and change the cracking behaviour. A high fiber content is needed for an SFRC mixture to experience hardening behaviour, but perhaps this is worthwhile for heavily loaded sections. The difference in cracking behavior is that SFRC with hardening behavior results in more small cracks, whereas a softening behavior results in a single, larger crack. A consideration has to be made between the increased costs of adding more fibers in order to gain a hardening behaviour, versus the improved mechanical behaviour. This would be an interesting topic for further research.

References

[1] Xiuling Wang et al. *Steel fiber reinforced concrete: A review of its material properties and usage in tunnel lining*. 2021.

[2] Giuseppe Tiberti, Fausto Minelli, and Giovanni Plizzari. *Reinforcement optimization of fiber reinforced concrete linings for conventional tunnels*. 2013.

[3] Jaroslav Beňo and Matouš Hilar. *Steel fibre reinforced concrete for tunnel lining – verification by extensive laboratory testing and numerical modelling*. 2013.

[4] Roger Paul Johnson, Sotiris Psomas, and Colin Michael Eddie. *Design of steel fibre reinforced concrete tunnel linings*. 2016.

[5] COB. *Amsterdam, Noord/Zuidlijn*. `https://www.cob.nl/over-ondergronds-bouwen/voorbeeldprojecten/amsterdam-noordzuidlijn/`. n.d.

[6] Chenjie Gong et al. *Comparison of the structural behavior of reinforced concrete and steel fiber reinforced concrete tunnel segmental joints*. 2017.

[7] Kristina Reinders. *Nieuwe dictaat tunnels*. 2019.

[8] D.J. Kunst. *Modelling construction phases of bored tunnels with respect to internal lining forces*. 2017.

[9] Janssen. *Tragverhalten von tunnelausbauten mit gelenktubbings*. 1983.

[10] ITAtech Activity Group Support. *Guideline For Good Practice Of Fibre Reinforced Precast Segment - Vol. 2 : Production Aspects*. 2018.

[11] M. Marek et al. *Steel fiber reinforced concrete precast tunnel segments: design using nonlinear analysis*. 2016.

[12] Liao Lin et al. *Design of FRC tunnel segments considering the ductility requirements of the Model Code 2010*. 2015.

[13] F. Di Carlo, A. Meda, and Z. Rinaldi. *Design procedure for precast fibre-reinforced concrete segments in tunnel lining construction*. 2016.

[14] CNR DT-204. *Guide for the Design and Construction of Fiber-Reinforced Concrete Structures*. 2006.

[15] *fib* Special Activity Group 5. *fib Model Code 2010 - First complete draft Volume 1 and 2*. 2010.

[16] ITAtech Activity Group Support. *ITAtech design guidance for precast fibre reinforced concrete segments – draft report*. 2015.

[17] Projectorganisatie Noord/Zuidlijn. *Design report concrete tunnel segments*. 2009.

[18] Saturn X. *Tübbingbemessung Bewehrungstyp I*. 2009.

[19] ACI Committee 544. *Report on Indirect Method to Obtain Stress-Strain Response of Fiber-Reinforced Concrete (FRC)*. 2016.

[20] Juan Rodriguez. *Uses and Applications for Steel Fiber Concrete*. 2019.

[21] Gopal Mishra. *Fiber Reinforced Concrete - Types, Properties and Advantages of Fiber Reinforced Concrete*. 2012.

[22] J.A.O. Barros and J. Sena Cruz. *Fracture energy of steel fibre reinforced concrete*. 2001.

[23] Nguyen van Chanh. *Steel Fiber Reinforced Concrete*. 2015.

[24] Benjamin Graybeal. *Material Property Characterization of Ultra-High Performance Concrete*. 2006.

[25] Wasim Abbass, Iqbal Khan, and Shehab Mourad. *Evaluation of mechanical properties of steel fiber reinforced concrete with different strengths of concrete*. 2018.

[26] Semsi Yazıcı, Gözde Inan, and Volkan Tabak. *Effect of aspect ratio and volume fraction of steel fiber on the mechanical properties of SFRC*. 2007.

[27] Peyshiuan Song and Shin Hwang. *Mechanical properties of high-strength steel fiber-reinforced concrete*. 2004.

[28] Job Thomas and Ananth Ramaswamy. *Mechanical Properties of Steel Fiber-Reinforced Concrete*. 2007.

[29] Bekaert. *Choosing the Right Fiber for Fiber Reinforced Concrete Precast Tunnel Segments*. 2020.

[30] Safeer Abbas, Ahmed Soliman, and Moncef Nehdi. *Mechanical Performance of Reinforced Concrete and Steel Fiber-Reinforced Concrete Precast Tunnel Lining Segments: A Case Study*. 2014.

[31] H. Tlemat, K. Pilakoutas, and K. Neocleous. *Modelling of SFRC using inverse finite element analysis*. 2005.

[32] Ana Blanco et al. *Application of constitutive models in European codes to RC-FRC*. 2013.

[33] Simona Coccia, Alberto Meda, and Zila Rinaldi. *On shear verification according to fib Model Code 2010 in FRC elements without traditional reinforcement*. 2015.

[34] A. de la Fuente et al. *Sustainability based-approach to determine the concrete type and reinforcement configuration of TBM tunnels linings. Case study: Extension line to Barcelona Airport T1*. 2016.

[35] Wang Bin et al. *Manufacturing technology and cost analysis of SFRC segment*. 2021.

[36] The World Counts. *Environmental impact of steel production*. 2022. URL: `https://www.theworldcounts.com/challenges/planet-earth/mining/environmental-impact-of-steel-production/story`.

[37] Climent Molins and Oriol Arnau. *Experimental and analytical study of the structural response of segmental tunnel linings based on an in situ loading test. Part 1: Test configuration and execution*. 2011.

[38] Ravindra Gettu et al. *Steel Fiber Reinforced Concrete for the Barcelona Metro Line 9 Tunnel Lining*. 2004.

[39] Martin Blazejowski. *Flexural behaviour of steel fibre reinforced concrete tunnel linings*. 2012.

[40] N. Zaki et al. *Geological Prediction Ahead of Tunnel Face in the Limestone Formation Tunnel using Multi-Modal Geophysical Surveys*. 2017.

[41] ITA Working Group 2. *Twenty Years of FRC Tunnel Segments Practice: Lessons Learnt and Proposed Design Principles*. 2016.

[42] AFTES. *Design, dimensioning and execution of precast steel fibre reinforced concrete arch segments*. 2013.

[43] European Committee for Standardization. *EN 1992-1-1: Eurocode 2: Design of concrete structures*. 2005.

[44] Zhekang Huang and Michele Longo. *TunnelTool2022*. 2022.

[45] DIANA FEA. *User's Manual - Release 10.5*. 2023.

[46] Jan Rots and Johan Blaauwendraad. *Crack Models for Concrete: Discrete or Smeared? Fixed, Multi-directional or Rotating?* 1989.

[47] Centraal Overleg Bouwconstructies. *Toetsingshulp voor Staalvezelbeton voor Funderingsconstructies*. 2018.

[48] Violetta Kytinou, Constantin Chalioris, and Chris Karayannis. *Analysis of Residual Flexural Stiffness of Steel Fiber-Reinforced Concrete Beams with Steel Reinforcement*. 2020.

[49] C. Chalioris and T.A. Panagiotopoulos. *Flexural analysis of steel fibre-reinforced concrete members*. 2018.

[50] B. Rabbat and H. Russell. *Friction Coefficient of Steel on Concrete or Grout*. 1985.

[51] Antonio Conforti, Giuseppe Tiberti, and Giovanni A. Plizzari. *Combined effect of high concentrated loads exerted by TBM hydraulic jacks*. 2016.

[52] Rijkswaterstaat. *Guidelines for Nonlinear Finite Element Analysis of Concrete Structures*. 2020.

[53] Giuseppe Tiberti, Antonio Conforti, and Giovanni Plizzari. *Precast segments under TBM hydraulic jacks: Experimental investigation on the local splitting behavior*. 2015.

[54] Cees Blom. *Design philosophy of concrete linings for tunnels in soft soils*. 2002.

A

Soil properties Amsterdam

Tracé	Noord tot en met Europaplein Parameters ten behoeve van Eindig Elementen Model berekeningen			Massa		Sterkte				Doorlatendheid	Additioneel				Hardening Soil model					
	nr.	grondlaag	Omschrijving	γ_m [-]	γ_{nat} [kN/m³]	γ_m [-]	c' [kPa]	φ' [°]	ψ [°]	k_v [m/s]	v [-]	K_0 [-]	POP [kPa]	OCR [-]	γ_m [-]	Pref [kPa]	E'50;ref [kPa]	Eoed;ref [kPa]	Eur;ref [kPa]	m
uiterste grens -				1.0	15.0	1.2		18		1.0E-05					1.3		6600	4600	19200	
ondergr. vervorming					15.0			22		1.0E-05							6567	6000	25000	
verwachting	01	Aanvulling	Aanvulmateriaal, puin, klei, veen en zand		15.0			25		1.0E-06	0.15					100	10000	8000	30000	0.8
bovengr. vervorming					15.0			28		1.0E-07							11433	10000	35000	
uiterste grens +				1.0	15.0	1.2		34		1.0E-07					1.3		14900	13000	45500	
uiterste grens -				1.0	18.4	1.2		23		1.0E-04					1.3		13200	11500	38500	
ondergr. vervorming					18.4			27		1.0E-04							17134	15000	50000	
verwachting	01A	Ophooglaag, zand	Ophoogmateriaal zand		18.4			30		1.0E-05	0.15					100	20000	20000	60000	0.8
bovengr. vervorming					18.4			32		1.0E-06							22866	30000	70000	
uiterste grens +				1.0	18.4	1.2		38		1.0E-06					1.3		29700	39000	91000	
uiterste grens -				1.0	12.1	1.2		15		1.0E-07			10		1.3		1300	600	2300	
ondergr. vervorming					12.1			18		1.0E-07			10				1713	800	3000	
verwachting	04	Geulopvulling veen met kleilagen			12.1		9	20		1.0E-08	0.15	0.60	10			100	2000	1000	5000	0.8
bovengr. vervorming					12.1			22		1.0E-09			10				2287	1200	9000	
uiterste grens +				1.0	12.1	1.2		26		1.0E-09			10		1.3		3000	1600	11700	
uiterste grens -				1.0	16.9	1.2		20		1.5E-08			10		1.3		6700	1900	11500	
ondergr. vervorming					16.9			24		1.5E-08			10				8700	2500	15000	
verwachting	07	Geulopvulling slappe klei	KLEI, met zandlaagjes		16.9		6	26		1.5E-09	0.15	0.50	10			100	10000	4000	25000	0.8
bovengr. vervorming					16.9			29		1.5E-10			10				11300	5500	35000	
uiterste grens +				1.0	16.9	1.2		35		1.5E-10			10		1.3		14700	7200	45500	
uiterste grens -				1.0	13.9	1.2		17		5.7E-09			10		1.3		3300	800	11500	
ondergr. vervorming					13.9			20		5.7E-09			10				4284	1000	15000	
verwachting	07A	Geulopvulling slappe humeuse			13.9		10	22		5.7E-10	0.15	0.55	10				5000	1500	20000	0.8
bovengr. vervorming					13.9			24		5.7E-11			10				5716	2000	25000	
uiterste grens +				1.0	13.9	1.2		29		5.7E-11			10		1.3		7400	2600	32500	
uiterste grens -				1.0	10.5	1.2		15		1.0E-07			10		1.3		1500	600	5400	
ondergr. vervorming					10.5			18		1.0E-07			10				2000	800	7000	
verwachting	08	Hollandveen	VEEN (bruin)		10.5		5	20		1.0E-08	0.15	0.65	10			100	2000	1000	10000	0.8
bovengr. vervorming					10.5			22		1.0E-09			10				2000	1200	13000	
uiterste grens +				1.0	10.5	1.2		26		1.0E-09			10		1.3		2600	1600	16900	
uiterste grens -				1.0	16.5	1.2		22		1.5E-08			10		1.3		5600	1500	15400	
ondergr. vervorming					16.5			26		1.5E-08			10				7500	2000	20000	
verwachting	09	Oude zeeklei	KLEI (matig vast), grijs		16.5		7	33		1.5E-09	0.15	0.50	10			100	9000	3000	25000	0.8
bovengr. vervorming					16.5			33		1.5E-10			10				10500	4000	30000	
uiterste grens +				1.0	16.5	1.2		40		1.5E-10			10		1.3		13700	5200	39000	
uiterste grens -				1.0	17.9	1.2		23		1.0E-06					1.3		7700	3100	19200	
ondergr. vervorming					17.9			27		1.0E-06							10000	4000	25000	
verwachting	10	Wadafzetting, zandhoudend	ZAND (matig fijn), sterk kleihoudend/ KLEI, grijs,		17.9		2	35		1.0E-07	0.20	0.40				100	12000	5000	33000	0.5
bovengr. vervorming	10B				17.9			38		1.0E-08							14000	6000	40000	
uiterste grens +				1.0	17.9	1.2		46		1.0E-08					1.3		18200	7800	52000	
uiterste grens -				1.0	15.2	1.2		23		1.0E-08			10		1.3		5800	1500	7700	
ondergr. vervorming					15.2			27		1.0E-08			10				7500	2000	10000	
verwachting	11	Wadafzetting, Hydrobia klei	KLEI (grijs), sterk zandig		15.2		8	34		1.0E-09	0.15	0.59	10			100	9000	3000	15000	0.8
bovengr. vervorming					15.2			34		1.0E-10			10				10500	4000	20000	
uiterste grens +				1.0	15.2	1.2		41		1.0E-10			10		1.3		13700	5200	26000	
uiterste grens -				1.0	11.7	1.2		15		1.0E-07			10		1.3		1500	600	5400	
ondergr. vervorming					11.7			18		1.0E-07			10				2000	800	7000	
verwachting	12	Basisveen	VEEN (bruin), met enkele kleilaagjes		11.7		6	21		1.0E-08	0.15	0.65	10			100	2000	1000	10000	0.8
bovengr. vervorming					11.7			23		1.0E-09			10				2000	1200	13000	
uiterste grens +				1.0	11.7	1.2		28		1.0E-09			10		1.3		2600	1600	16900	
uiterste grens -				1.0	19.8	1.2		28		1.5E-03					1.3		26900	15400	76900	
ondergr. vervorming					19.8			33	3	1.5E-03							35000	20000	100000	
verwachting	13	Eerste zandlaag	ZAND (grijs), matig fijn, zwak siltig		19.8			33	3	1.5E-04	0.20	0.40				100	40000	30000	200000	0.5
bovengr. vervorming					19.8			39	9	1.5E-05							45000	40000	280000	
uiterste grens +				1.0	19.8	1.2		47	17	1.5E-05					1.3		58500	52000	364000	

Figure A.1: Soil layer characteristics for layers 01 to 13

Tracé — *Noord tot en met Europaplein*

Parameters ten behoeve van Eindig Elementen Model berekeningen

	nr.	grondlaag	Omschrijving	Massa		Sterkte				Doorlatendheid	Additioneel			Hardening Soil model					
				γm [-]	γwet [kN/m³]	γm [-]	c' [kPa]	φ' [°]	ψ [°]	kv [m/s]	ν [-]	K0 [-]	POP [kPa]	OCR [-]	γm [-]	Pref [kPa]	E'50;ref [kPa]	Eoed;ref [kPa]	Eur;ref [kPa]	m
uiterste grens -				1.0	18.5	1.2		23		3.0E-04					1.3		11500	5400	23100	
ondergr. vervorming					18.5			28		3.0E-04							15000	7000	30000	
verwachting	14	Allerod	LEEM, sterk zandig		18.5			33		3.0E-05	0.20	0.40				100	17000	13000	45000	0.5
bovengr. vervorming					18.5			35		3.0E-06							19000	20000	60000	
uiterste grens +				1.0	18.5	1.2		42		3.0E-06					1.3		24700	26000	78000	
uiterste grens -				1.0	17.8	1.2		23		1.0E-08					1.3		6500	1900	19200	
ondergr. vervorming					17.8			27		1.0E-08							8400	2500	25500	
verwachting	15	Geulvulling Kiel met zandlagen	KLEI, matig zandig, matig humeus, kalkrijk		17.8			32		1.0E-09	0.15	0.50				100	8400	3500	35000	0.8
bovengr. vervorming					17.8			36		1.0E-10							8400	4500	42000	
uiterste grens +				1.0	17.8	1.2		43		1.0E-10					1.3		10900	5900	54600	
uiterste grens -				1.0	18.6	1.2		23		1.0E-04					1.3		6500	3100	19200	
ondergr. vervorming					18.6			27		1.0E-04							8400	4000	25000	
verwachting	16	Geulvulling zand met kleilagen	ZAND (matig fijn), met kleilaagjes, schelpen		18.6			33		1.0E-05	0.15	0.47				100	8400	5000	35000	0.8
bovengr. vervorming					18.6			38		1.0E-06							8400	6000	42000	
uiterste grens +				1.0	18.6	1.2		46		1.0E-06					1.3		10900	7800	54600	
uiterste grens -				1.0	19.0	1.2		28		1.0E-03					1.3		24600	19200	81500	
ondergr. vervorming					19.0			33	3	1.0E-03							32000	25000	80000	
verwachting	17	Tweede zandlaag	ZAND (grijs), matig fijn tot matig grof, kalkrijk		19.0			35	5	1.0E-04	0.20	0.40				100	35000	35000	190000	0.5
bovengr. vervorming					19.0			39	9	1.0E-05							36000	45000	260000	
uiterste grens +				1.0	19.0	1.2		47	17	1.0E-05					1.3		49400	58500	364000	
uiterste grens -				1.0	18.4	1.2		23		2.4E-05					1.3		20800	11500	46200	
ondergr. vervorming					18.4			27		2.4E-05							27000	15000	60000	
verwachting	17A	Marien siltig Eemzand	ZAND (fijn), grijs, met kleilaagjes		18.4			33	3	2.4E-06	0.20	0.40				100	30000	20000	120000	0.5
bovengr. vervorming					18.4			35	5	2.4E-07							33000	25000	150000	
uiterste grens +				1.0	18.4	1.2		42	12	2.4E-07					1.3		42900	32500	195000	
uiterste grens -				1.0	18.0	1.2		23		4.0E-07					1.3		5800	2300	26900	
ondergr. vervorming					18.0			27		4.0E-07							7500	3000	35000	
verwachting	18	Overgangslaag	KLEI, uitersl siltig, zwak humeus, kalkrijk		18.0		15	34		4.0E-08	0.15	0.49				100	9600	4000	64000	0.8
bovengr. vervorming					18.0			34		4.0E-09							11000	5000	80000	
uiterste grens +				1.0	18.0	1.2		41		4.0E-09					1.4		14300	6500	104000	
uiterste grens -				1.0	17.9	1.2	10	24		2.0E-08					1.5		6200	2300	23100	
ondergr. vervorming					17.9		10	29		2.0E-08					1.5		8000	3000	30000	
verwachting	19	Marlene Eemklei (zone 1)	KLEI (grijsgroen), zwak siltig tot zwak zandig		17.9		20	32		2.0E-09	0.15	0.68		2.0		100	11000	4000	50000	0.8
bovengr. vervorming					17.9		30	34		2.0E-10		0.76		2.5			14000	5000	65000	
uiterste grens +				1.0	17.9	1.2	15	41		2.0E-10		0.76		2.5	1.3		18200	6500	84500	
uiterste grens -				1.0	17.1	1.2	10	24		2.0E-08		0.55		1.5	1.3		6900	2700	26900	
ondergr. vervorming					17.1		10	29		2.0E-08		0.55		1.5			9000	3500	35000	
verwachting	19A	Marlene Eemklei (zone 2)			17.1		20	34		2.0E-09	0.15	0.65		2.0			12000	4500	55000	0.8
bovengr. vervorming					17.1		30	35		2.0E-10		0.74		2.5			15000	5500	70000	
uiterste grens +				1.0	17.1	1.2	15	42		2.0E-10		0.74		2.5	1.3		19500	7200	91000	
uiterste grens -				1.0	17.2	1.2	10	23		2.0E-08		0.61		1.5	1.3		5400	1900	21500	
ondergr. vervorming					17.2		10	28		2.0E-08		0.61		1.5			7000	2500	28000	
verwachting	19B	Marlene Eemklei (zone 3)			17.2		20	30		2.0E-09	0.15	0.71		2.0			9000	3000	45000	0.8
bovengr. vervorming					17.2		30	32		2.0E-10		0.79		2.5			11000	3500	60000	
uiterste grens +				1.0	17.2	1.2	15	38		2.0E-10		0.79		2.5	1.3		14300	4600	78000	
uiterste grens -				1.0	16.6	1.2	10	23		2.0E-08		0.61		1.5	1.3		4600	1900	21500	
ondergr. vervorming					16.6		10	26		2.0E-08		0.61		1.5			6000	2500	28000	
verwachting	19C	Marlene Eemklei (zone 4)			16.6		20	30		2.0E-09	0.15	0.71		2.0			8000	3000	40000	0.8
bovengr. vervorming					16.6		30	32		2.0E-10		0.79		2.5			10000	3500	55000	
uiterste grens +				1.0	16.6	1.2	15	38		2.0E-10		0.79		2.5	1.3		13000	4600	71500	
uiterste grens -				1.0	14.5	1.2		22		6.0E-08		0.58		1.2	1.3		5400	1200	19200	
ondergr. vervorming					14.5			26		6.0E-08		0.58		1.2			7000	1500	25000	
verwachting	20	Laag van Harting	KLEI, groengrijs, licht zandhoudend,		14.5		10	28		6.0E-09	0.15	0.64		1.5		100	10000	2000	46000	0.8
bovengr. vervorming					14.5			30		6.0E-10		0.73		2.0			13000	2500	60000	
uiterste grens +				1.0	14.5	1.2		36		6.0E-10		0.73		2.0	1.3		16900	3300	78000	

Figure A.2: Soil layer characteristics for layers 14 to 20

Tracé — Noord tot en met Europaplein

Parameters ten behoeve van Eindig Elementen Model berekeningen

nr.	grondlaag	Omschrijving	Massa		Sterkte				Doorlatendheid	Additioneel				Hardening Soil model				
			γ_m [-]	γ_{nat} [kN/m³]	γ_m [-]	c' [kPa]	φ' [°]	ψ [°]	k_v [m/s]	ν [-]	K_0 [-]	POP [kPa]	OCR [-]	γ_m [-]	Pref [kPa]	E50;ref [kPa]	Eoed;ref [kPa]	Eur;ref [kPa]	m
uiterste grens -			1.0	19.4	1.2		25		1.0E-04					1.3		15400	7700	38500	
ondergr. vervorming				19.4			30		1.0E-04							20000	10000	50000	
verwachting	21	Tussenlaag zand		19.4			33	3	1.0E-05	0.20	0.40				100	25000	15000	140000	0.5
bovengr. vervorming		ZAND, zeer fijn, zwak siltig		19.4			35	5	1.0E-06							30000	20000	175000	
uiterste grens +			1.0	19.4	1.2		42	12	1.0E-06					1.3		39000	26000	227500	
uiterste grens -			1.0	19.7	1.2		27		1.0E-08		0.49		1.2	1.3		9200	2300	38500	
ondergr. vervorming				19.7			32		1.0E-08		0.49		1.2			12000	3000	50000	
verwachting	22	Glaciale Drenthe klei		19.7		15	34		1.0E-09	0.15	0.55		1.5		100	15000	5000	75000	0.8
bovengr. vervorming		KLEI, zwak zandig		19.7			36		1.0E-10		0.65		2.0			18000	8000	90000	
uiterste grens +			1.0	19.7	1.2		43		1.0E-10		0.65		2.0	1.3		23400	10400	117000	
uiterste grens -			1.0	18.5	1.2		22		1.0E-06		0.52		1.2	1.3		9200	2300	30800	
ondergr. vervorming				18.5			28		1.0E-06		0.52		1.2			12000	3000	40000	
verwachting	23	Glaciale Warven klei		18.5		5	32		1.0E-07	0.15	0.58		1.5		100	15000	4000	58000	0.8
bovengr. vervorming		KLEI, zwak siltig met zandlaagjes		18.5			34		1.0E-08		0.66		2.0			18000	5000	70000	
uiterste grens +			1.0	18.5	1.2		41		1.0E-08		0.66		2.0	1.3		23400	6500	91000	
uiterste grens -			1.0	19.6	1.2		28		1.0E-03					1.3		23100	26900	54600	
ondergr. vervorming				19.6			33	3	1.0E-03							30000	35000	71000	
verwachting	24	Derde zandlaag		19.6			35	5	1.0E-04	0.20	0.40				100	35000	40000	200000	0.5
bovengr. vervorming		ZAND, matig fijn, zwak siltig tot zwak grindig		19.6			39	9	1.0E-05							45000	45000	300000	
uiterste grens +			1.0	19.6	1.2		47	17	1.0E-05					1.3		58500	58500	390000	

Figure A.3: Soil layer characteristics for layers 21 to 24

B

Noord/Zuidlijn reinforcement configuration

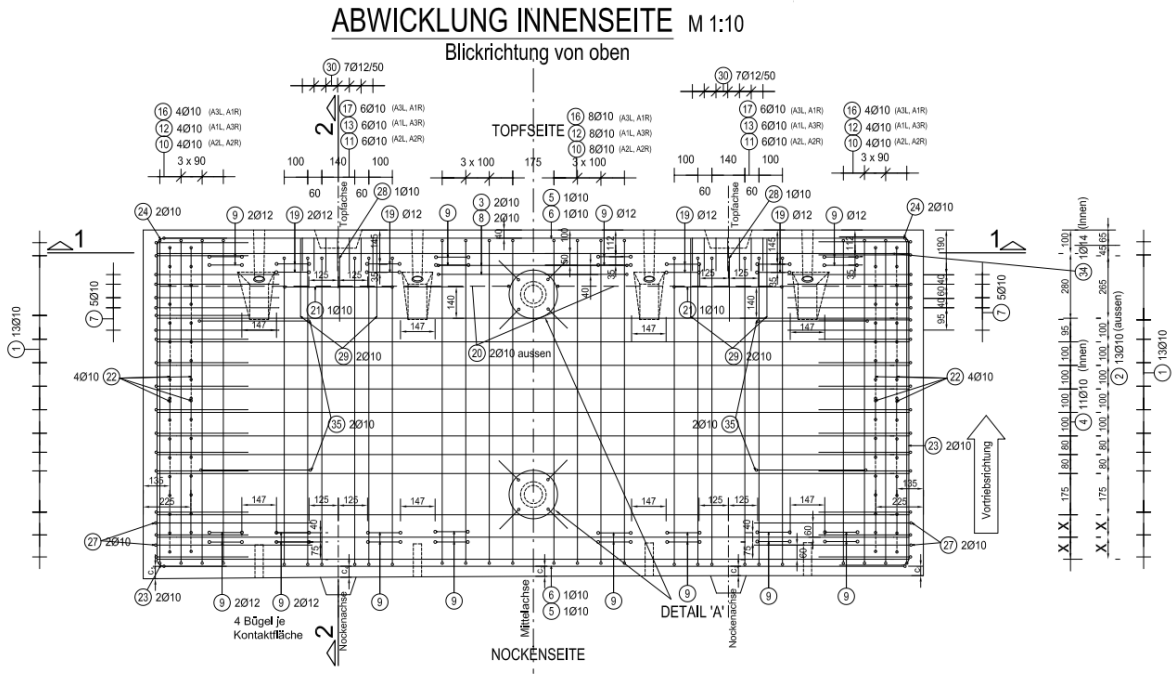

Figure B.1: Reinforcement detailing - front view

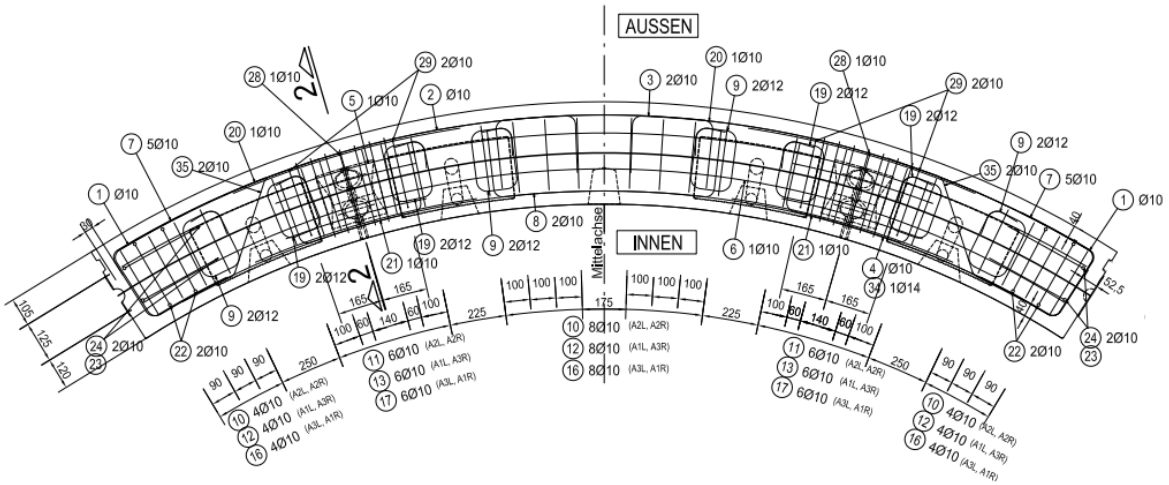

Figure B.2: Reinforcement detailing - top view

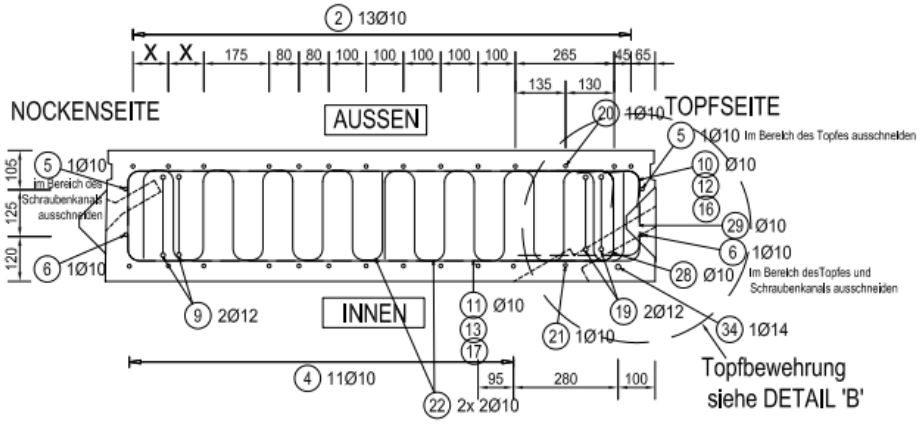

Figure B.3: Reinforcement detailing - side view

C

Calculations

C.1. Calculation of lever arm for capacity calculation

The tension side of the stress-strain diagram is divided into two stress increments, as shown in Figure C.1. Determining z_t of section 5.3.3 is done as follows:

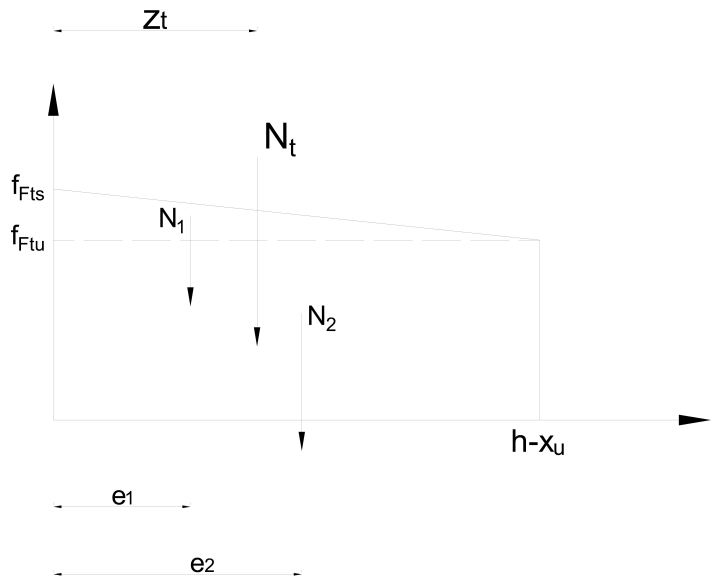

Figure C.1: Calculation method of lever arm z_t

The distance z_t is calculated by taking into account the area and distance of each increment as follows:

$$z_t = \frac{e_1 N_1 + e_2 N_2}{N_1 + N_2} = \frac{\frac{1}{3}(h - x_u) \cdot \frac{1}{2}(f_{Fts} - f_{Ftu})(h - x_u) + \frac{1}{2}(h - x_u) \cdot f_{Ftu}(h - x_u)}{\frac{1}{2}(f_{Fts} - f_{Ftu})(h - x_u) + f_{Ftu}(h - x_u)} \tag{C.1}$$

C.2. Calculation of soil pressure

```python
#general info
tunnel_depth = 30
gamma_water = 10

# wet unit weight, thickness and lateral earth coefficient for every of the 16 layers
gamma_wet = [15, 10.5, 16.5, 17.9, 15.2, 19.8, 18.5, 19, 18, 17.9, 16.6, 14.5, 19.4, 19.7, 18.5, 19.6]
H = [4, 2, 2, 4, 1.5, 1.5, 5, 6, 5, 10, 1.5, 0.5, 1, 6.5, 3, 6]
K0 = [.5, .55, .5, .4, .59, .4, .4, .4, .44, .68, .68, .57, .4, .54, .54, .4]


# the tunnel is located at the bottom of the 9th layer so first 9 values are needed
gamma_wet_new = y_wet[0:9]
H_new = H[0:9]

# calculate the total vertical soil pressure
sigma_v = 0
for i in range(len(H_new)):
    sigma_v += gamma_wet_new[i]*H_new[i]
print('The total vertical soil pressure at a depth of 30 meters is:', sigma_v, 'MPa')

# calculate the total horizontal soil pressure
sigma_eff = sigma_v - tunnel_depth * gamma_water
sigma_h = tunnel_depth * gamma_water + K0[8] * sigma_eff
print('The total horizontal soil pressure at a depth of 30 meters is:', sigma_h, 'MPa')
```

```
The total vertical soil pressure at a depth of 30 meters is: 534.5999999999999 MPa
The total horizontal soil pressure at a depth of 30 meters is: 403.22399999999993 MPa
```

Figure C.2: Calculations vertical and horizontal soil pressure

D

Analytical verification

D.1. Input parameters

The values of the parameters used in Equations 5.6 till 5.13 of section 5.5 are given below.

- $\boldsymbol{E_s = 10500 \text{ to } 24000 \text{ MPa}}$
  The soil stiffness E_s is given as a range, as the tunnel is located in two layers. This means the parameters dependent on E_s are given in a range.
- $\boldsymbol{r = \frac{1}{2} \cdot D = 3260 \text{ mm}}$
  The radius is half of the diameter.
- $\boldsymbol{E_t = \frac{1}{2} \cdot E_{cm} = 18000 \text{ MPa}}$
  The Young's Modulus of the concrete tunnel (including cracking behaviour) is half of the mean Young's Modulus of the concrete, which is 36000 MPa in this case.
- $\boldsymbol{I_t = 0.6 \cdot \frac{1}{12} \cdot h^3 = 2143750 \text{ mm}^4\text{/mm}}$
  The effective moment of inertia is calculated with the formula above according to Blom [54].
- $\boldsymbol{A_t = h = 350 \text{ mm}^2\text{/mm}}$
  The cross sectional area is taken as the height of the cross section since a unit length is used.
- $\boldsymbol{\alpha = 11.67 \text{ to } 26.67}$
- $\boldsymbol{\beta = 0.58 \text{ to } 1.33}$
- $\boldsymbol{C_{N0} = 0.69 \text{ to } 0.49}$
- $\boldsymbol{C_{N2} = 0.87 \text{ to } 0.82}$
- $\boldsymbol{C_M = 0.50 \text{ to } 0.30}$
- $\boldsymbol{\sigma'_v = 253 \text{ MPa}}$
  No distinction is made between the top and bottom of the tunnel in the calculation of the effective vertical soil pressure; the center point is taken as a reference depth.
- $\boldsymbol{\sigma'_h = 111 \text{ MPa}}$
  No distinction is made between the top and bottom of the tunnel in the calculation of the effective horizontal soil pressure; the center point is taken as a reference depth.
- $\boldsymbol{u = 30 * 10 = 300 \text{ MPa}}$
  The water pressure is calculated by multiplying the depth with the unit weight of water γ_w which is 10 kN/m^3.

D.2. Analytical verification

The cross sectional forces can be calculated using a simplified approach as seen in the equations of section 5.5. However, these cross sectional forces are not uniform around the tunnel lining. The normal force has its maxima at the sides of the tunnel and minima at the top and bottom. The bending moment has its positive maxima at the sides of the tunnel and it's negative maxima at the top and bottom. The shear force has its maxima at four quarters of the lining, starting at $\phi = \frac{1}{4}\pi$. Figure 5.19 of section 5.5 shows the general distributions of the cross sectional forces around the lining.

The input of soil stiffness E_s plays a significant role in the outcome of the cross sectional forces. This is because the force distribution is dependent on the relative stiffness of different components; stiffer parts attract more forces. It is to be expected that a stiffer soil results in lower forces in the lining. For that reason, the cross sectional forces are calculated using both lower and upper boundary of E_s and are shown in Table D.1.

	Normal force		**Bending moment**		**Shear force**
	Top and bottom [kN/m]	Sides [kN/m]	Top and bottom [kNm/m]	Sides [kNm/m]	Quarter [kN/m]
E_s = 10500	-1364	-1774	-208	208	$\pm$127
E_s = 23000	-1372	-1760	-136	136	$\pm$83

Table D.1: Cross sectional forces at different positions around the tunnel lining for the original Noord/Zuidlijn design for different soil stiffnesses

The normal force ranges from -1364 kN to -1774 kN, the bending moment ranges from -208 kNm to 208 kNm, and the shear force ranges from -127 kN to 127 kN. These values can be compared to the points plotted in Figure 6.12. The normal force of all element in all figures are near -1550 kN which is in line with the analytical results. The bending moment ranges from -120 kNm to 160 kNm which is slightly lower than the analytical results. The shear force ranges from -120 kN to 120 kN which is very similar to the analytical results. Even though the analytical formulas are a rough estimation of reality, it can be concluded that the numerical results are in line with what is expected from the available hand calculations.

E

Numerical results

E.1. Ring joint

Front view

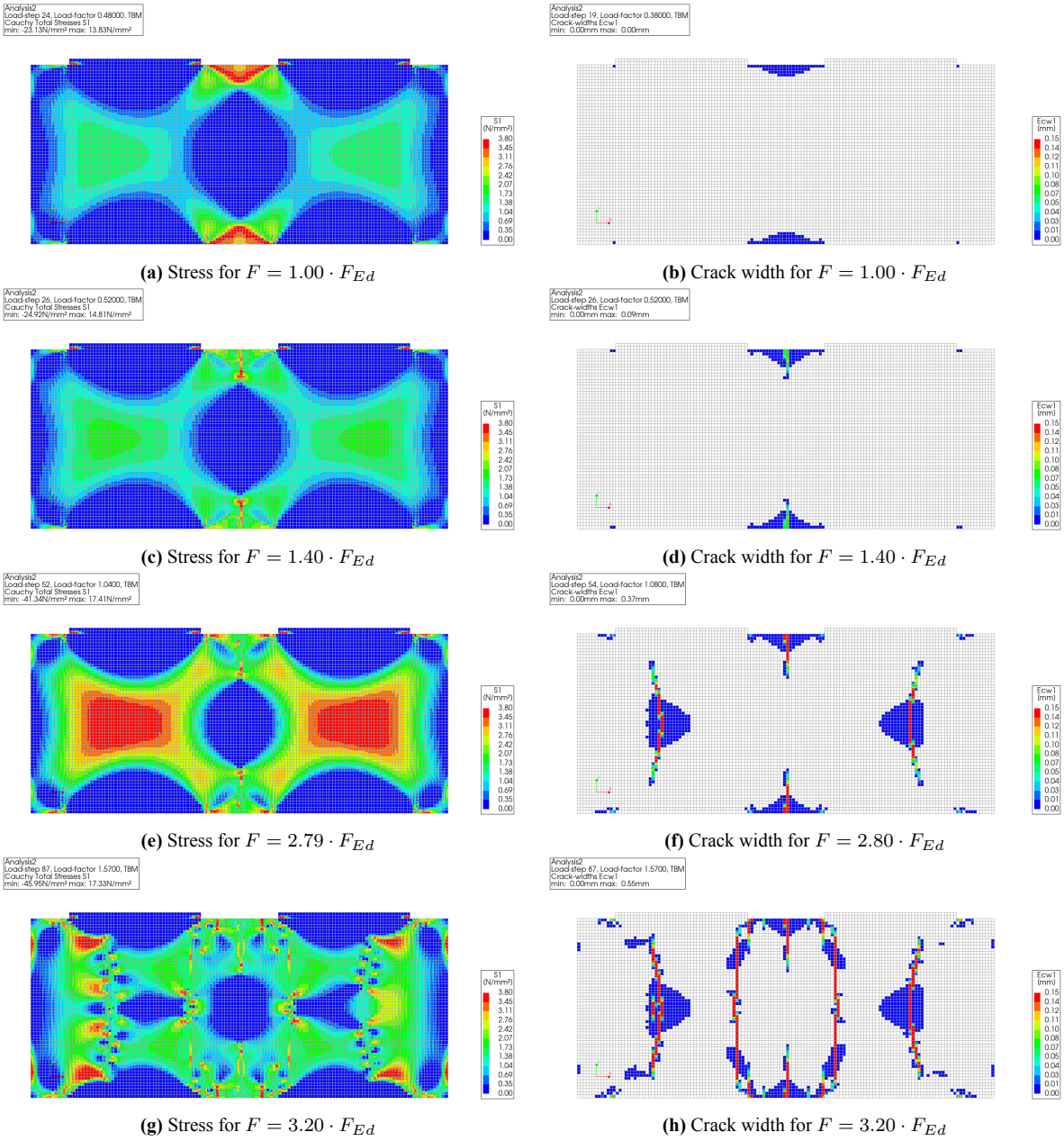

(a) Stress for $F = 1.00 \cdot F_{Ed}$

(b) Crack width for $F = 1.00 \cdot F_{Ed}$

(c) Stress for $F = 1.40 \cdot F_{Ed}$

(d) Crack width for $F = 1.40 \cdot F_{Ed}$

(e) Stress for $F = 2.79 \cdot F_{Ed}$

(f) Crack width for $F = 2.80 \cdot F_{Ed}$

(g) Stress for $F = 3.20 \cdot F_{Ed}$

(h) Crack width for $F = 3.20 \cdot F_{Ed}$

Figure E.1: Stress and crack development SFRC ring joint front view - 25 mm mesh

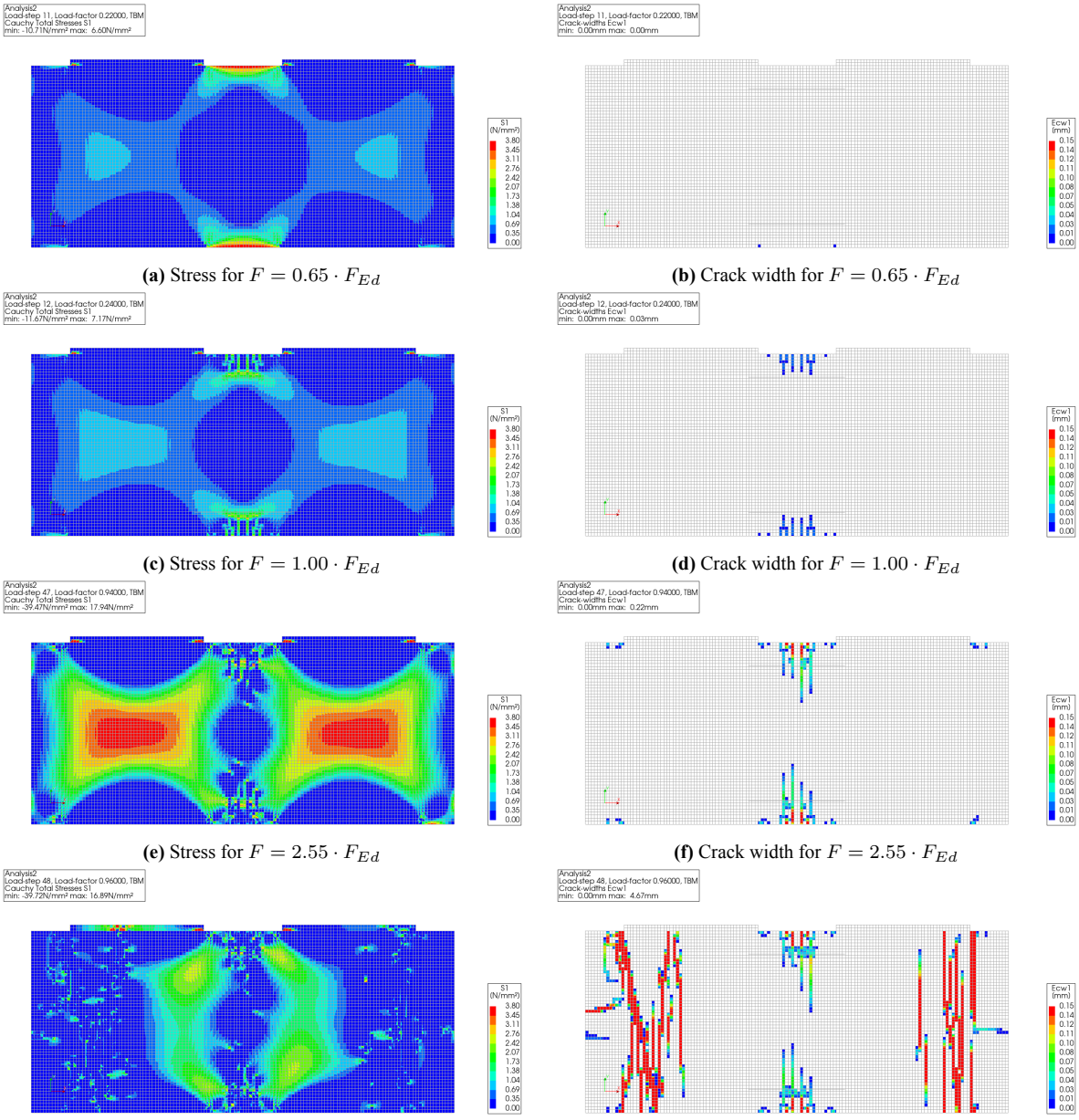

(a) Stress for $F = 0.65 \cdot F_{Ed}$

(b) Crack width for $F = 0.65 \cdot F_{Ed}$

(c) Stress for $F = 1.00 \cdot F_{Ed}$

(d) Crack width for $F = 1.00 \cdot F_{Ed}$

(e) Stress for $F = 2.55 \cdot F_{Ed}$

(f) Crack width for $F = 2.55 \cdot F_{Ed}$

(g) Stress for $F = 2.60 \cdot F_{Ed}$

(h) Crack width for $F = 2.60 \cdot F_{Ed}$

Figure E.2: Stress and crack development RC ring joint front view - 25 mm mesh

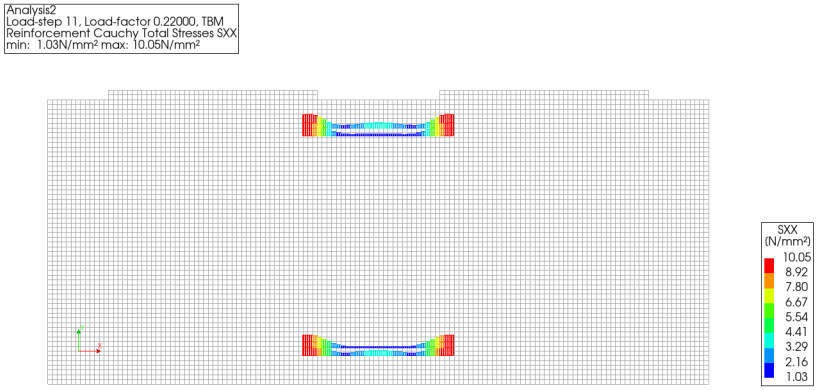

(a) Rebar stress for $F = 0.65 \cdot F_{Ed}$

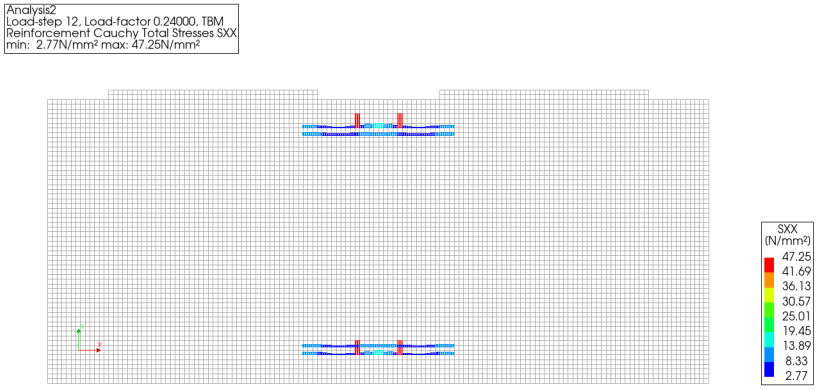

(b) Rebar stress for $F = 1.00 \cdot F_{Ed}$

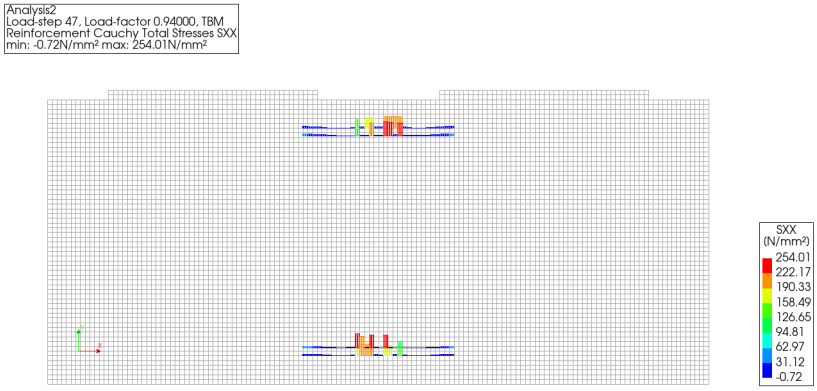

(c) Rebar stress for $F = 2.55 \cdot F_{Ed}$

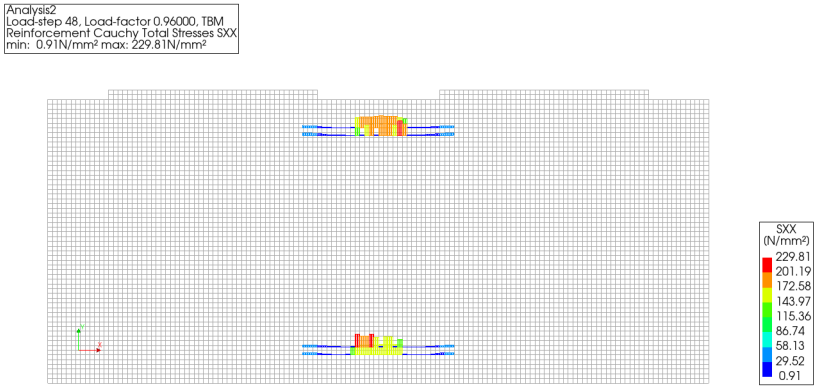

(d) Rebar stress for $F = 2.60 \cdot F_{Ed}$

Figure E.3: Rebar stress RC ring joint front view - 25 mm mesh

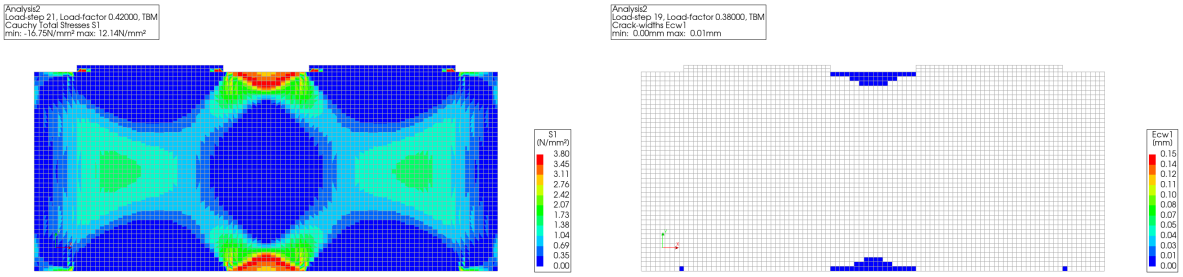

(a) Stress for $F = 1.00 \cdot F_{Ed}$

(b) Crack width for $F = 1.00 \cdot F_{Ed}$

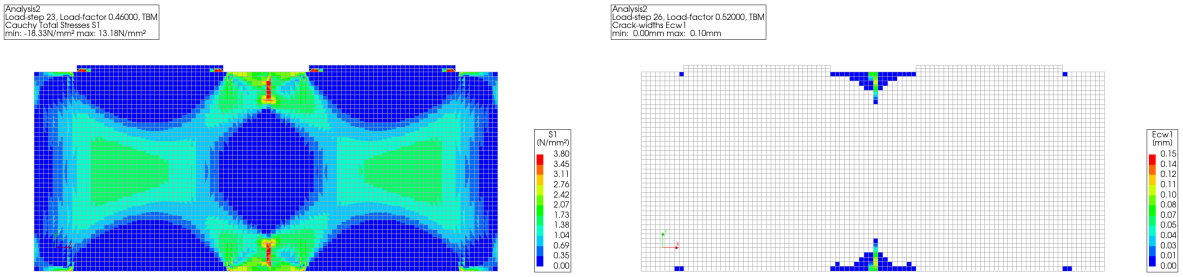

(c) Stress for $F = 1.35 \cdot F_{Ed}$

(d) Crack width for $F = 1.35 \cdot F_{Ed}$

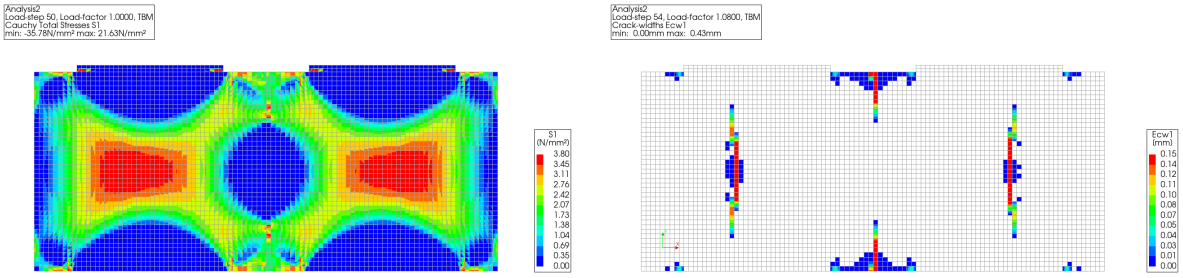

(e) Stress for $F = 2.69 \cdot F_{Ed}$

(f) Crack width for $F = 2.70 \cdot F_{Ed}$

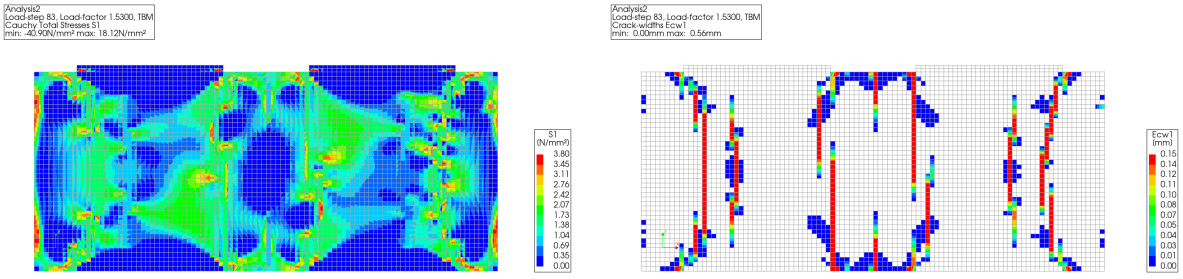

(g) Stress for $F = 3.25 \cdot F_{Ed}$

(h) Crack width for $F = 3.25 \cdot F_{Ed}$

Figure E.4: Stress and crack development SFRC ring joint front view - 35 mm mesh

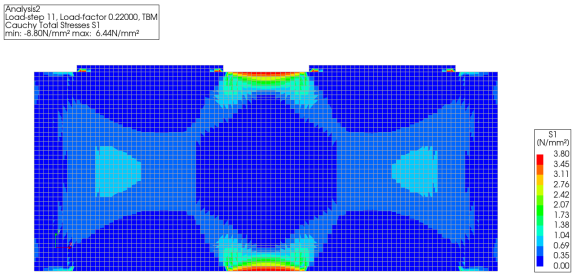

(a) Stress for $F = 0.65 \cdot F_{Ed}$

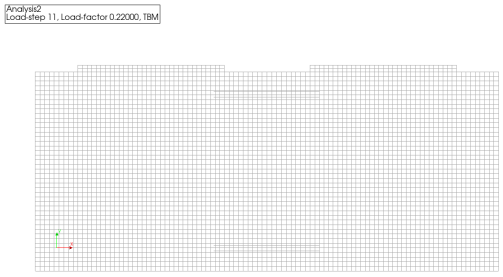

(b) Crack width for $F = 0.65 \cdot F_{Ed}$

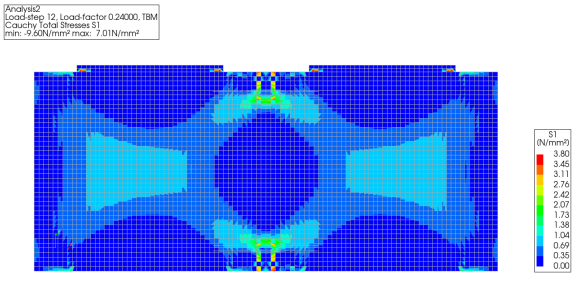

(c) Stress for $F = 1.00 \cdot F_{Ed}$

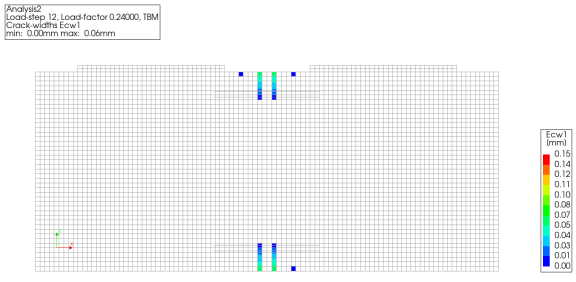

(d) Crack width for $F = 1.00 \cdot F_{Ed}$

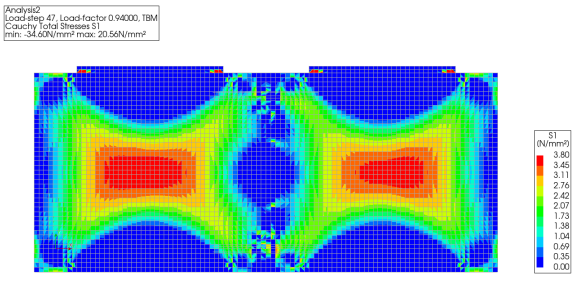

(e) Stress for $F = 2.60 \cdot F_{Ed}$

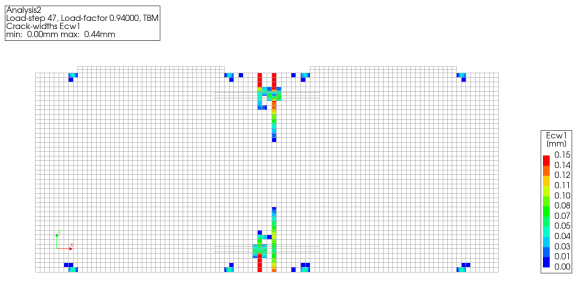

(f) Crack width for $F = 2.60 \cdot F_{Ed}$

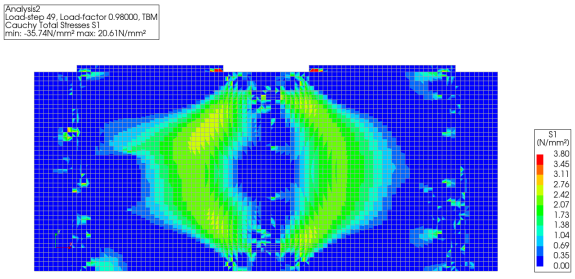

(g) Stress for $F = 2.65 \cdot F_{Ed}$

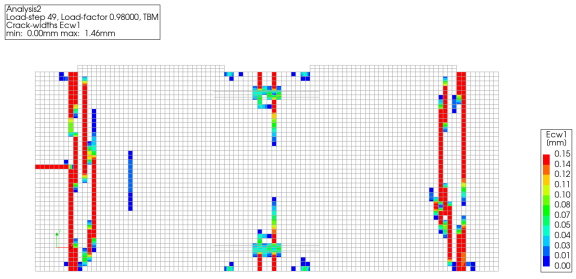

(h) Crack width for $F = 2.65 \cdot F_{Ed}$

Figure E.5: Stress and crack development RC ring joint front view - 35 mm mesh

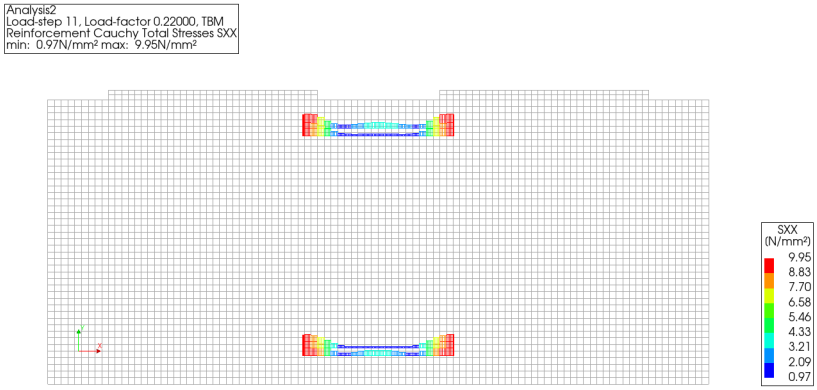

(a) Rebar stress for $F = 0.65 \cdot F_{Ed}$

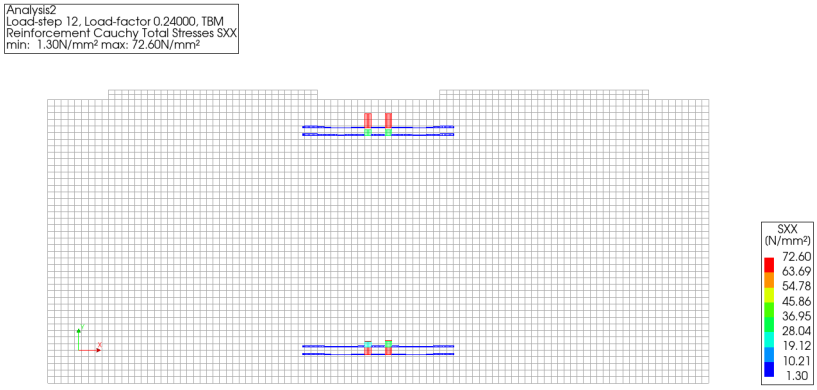

(b) Rebar stress for $F = 1.00 \cdot F_{Ed}$

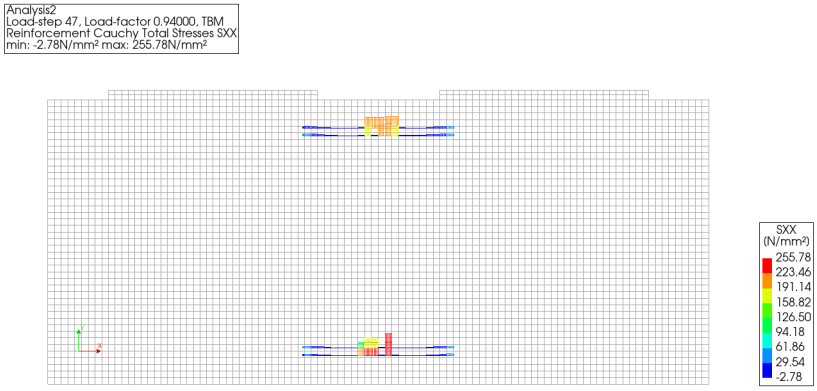

(c) Rebar stress for $F = 2.60 \cdot F_{Ed}$

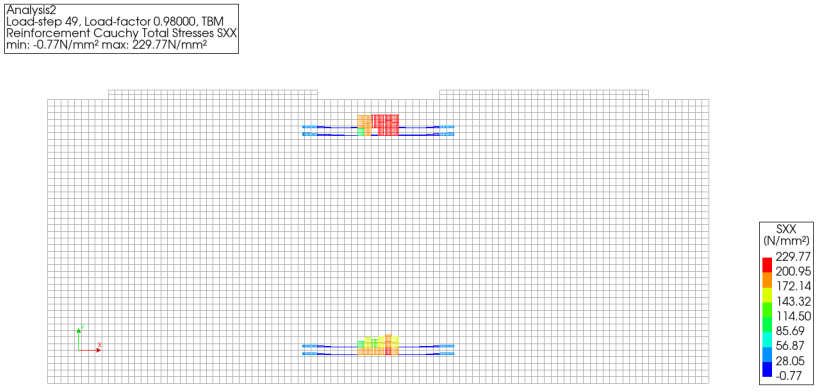

(d) Rebar stress for $F = 2.65 \cdot F_{Ed}$

Figure E.6: Rebar stress RC ring joint front view - 35 mm mesh

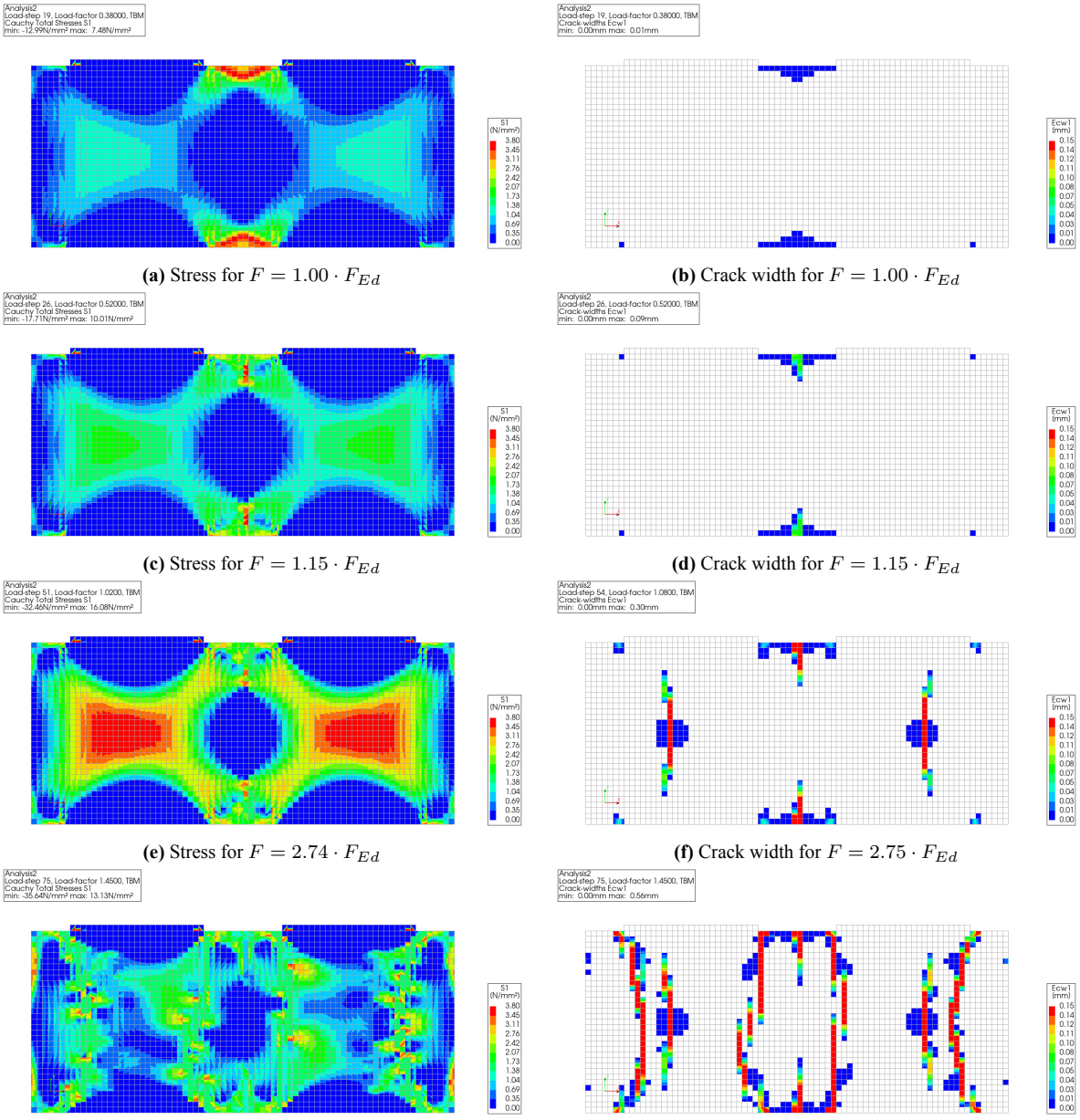

(a) Stress for $F = 1.00 \cdot F_{Ed}$

(b) Crack width for $F = 1.00 \cdot F_{Ed}$

(c) Stress for $F = 1.15 \cdot F_{Ed}$

(d) Crack width for $F = 1.15 \cdot F_{Ed}$

(e) Stress for $F = 2.74 \cdot F_{Ed}$

(f) Crack width for $F = 2.75 \cdot F_{Ed}$

(g) Stress for $F = 3.20 \cdot F_{Ed}$

(h) Crack width for $F = 3.20 \cdot F_{Ed}$

Figure E.7: Stress and crack development SFRC ring joint front view - 45 mm mesh

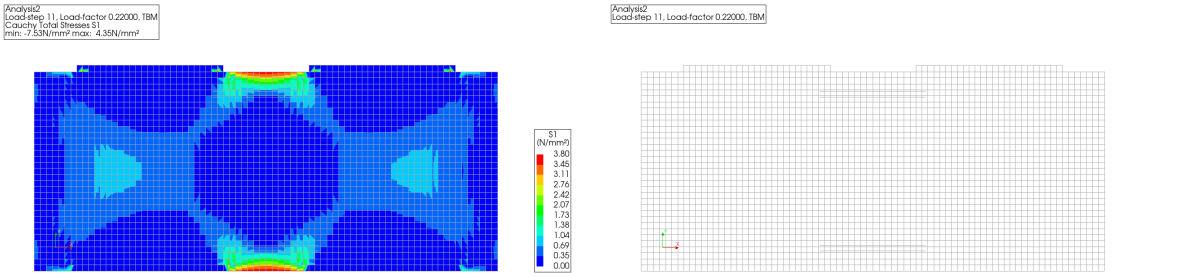

(a) Stress for $F = 0.60 \cdot F_{Ed}$ **(b)** Crack width for $F = 0.60 \cdot F_{Ed}$

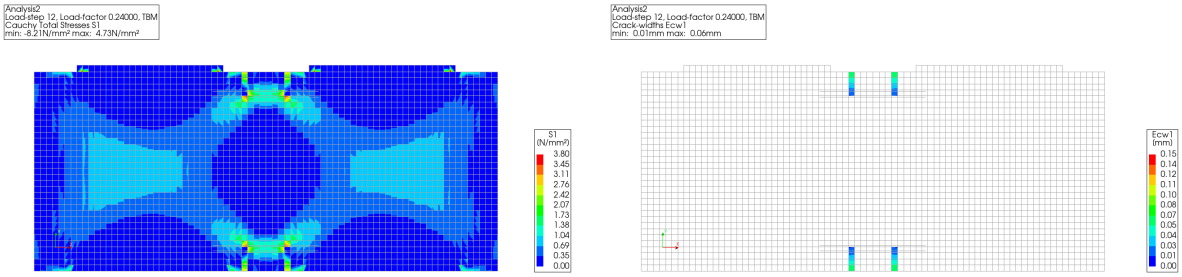

(c) Stress for $F = 1.00 \cdot F_{Ed}$ **(d)** Crack width for $F = 1.00 \cdot F_{Ed}$

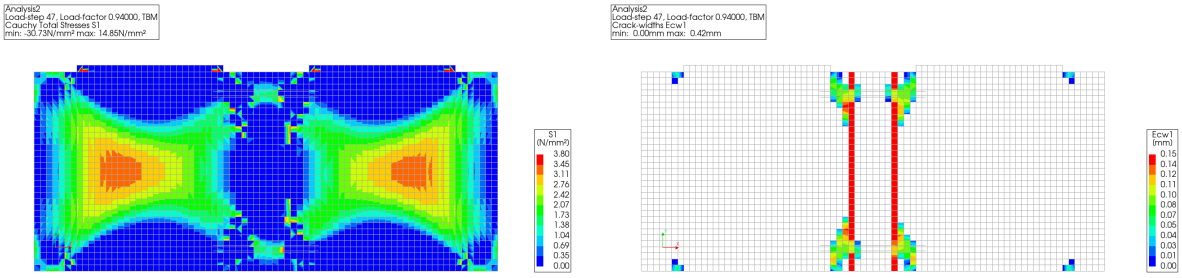

(e) Stress for $F = 2.55 \cdot F_{Ed}$ **(f)** Crack width for $F = 2.55 \cdot F_{Ed}$

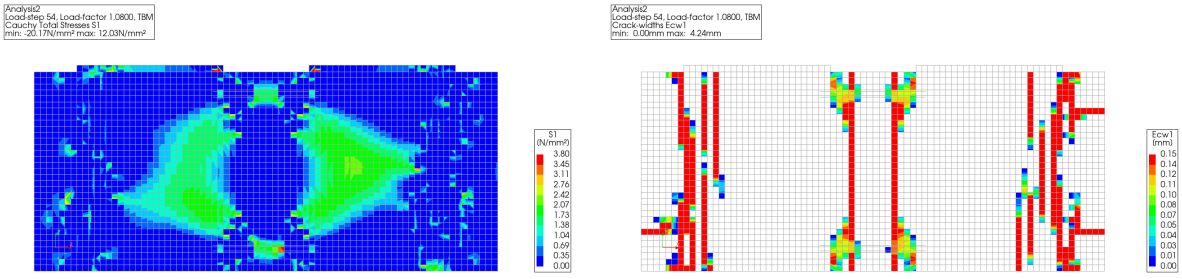

(g) Stress for $F = 2.65 \cdot F_{Ed}$ **(h)** Crack width for $F = 2.65 \cdot F_{Ed}$

Figure E.8: Stress and crack development RC ring joint front view - 45 mm mesh

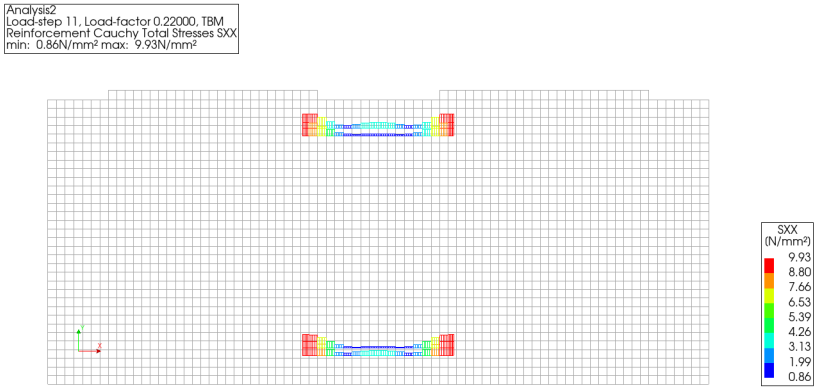

(a) Rebar stress for $F = 0.60 \cdot F_{Ed}$

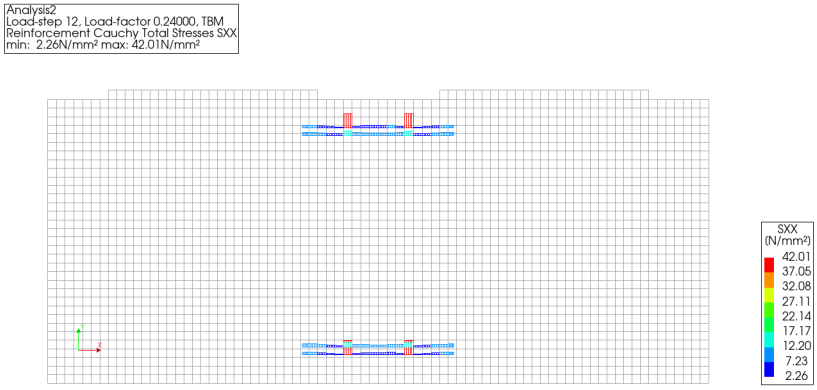

(b) Rebar stress for $F = 1.00 \cdot F_{Ed}$

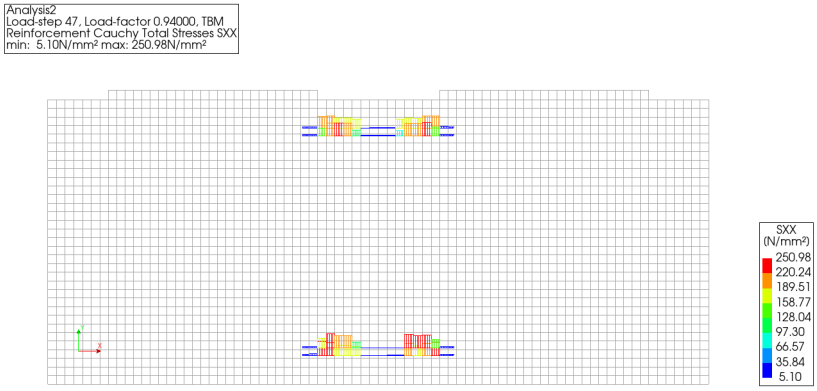

(c) Rebar stress for $F = 2.55 \cdot F_{Ed}$

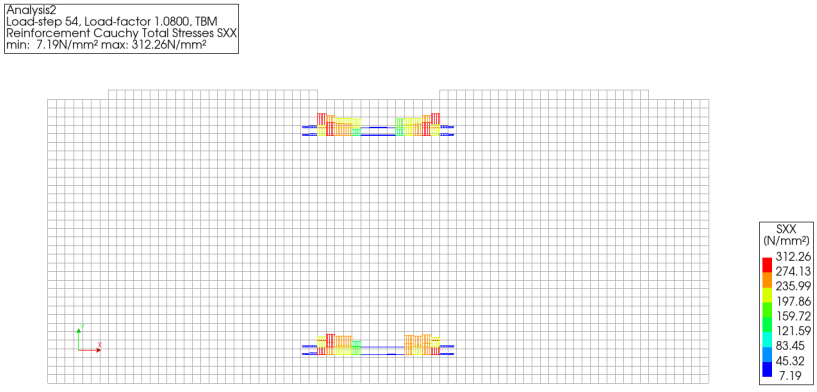

(d) Rebar stress for $F = 2.65 \cdot F_{Ed}$

Figure E.9: Rebar stress RC ring joint front view - 45 mm mesh

Side view - Concentrically loaded

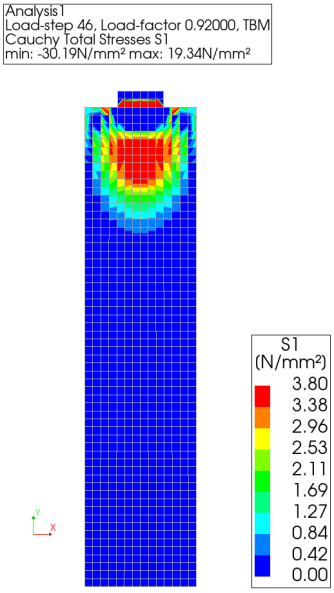

(a) Stress for $F = 2.90 \cdot F_{Ed}$

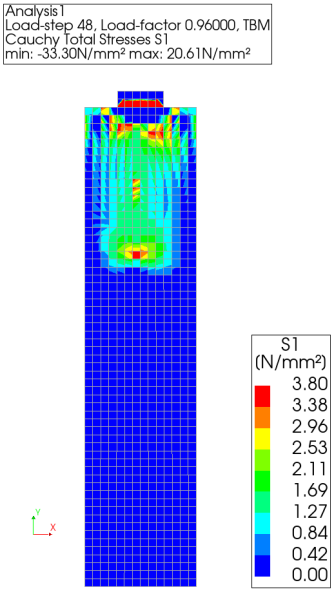

(b) Stress for $F = 3.00 \cdot F_{Ed}$

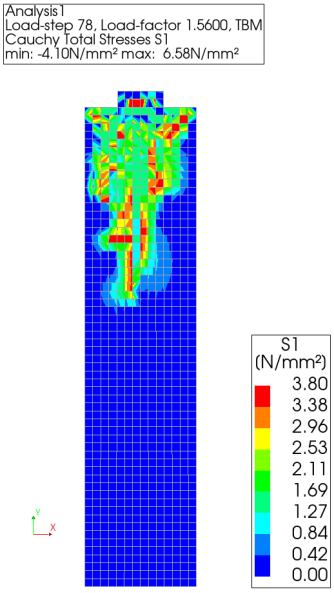

(c) Stress for $F = 3.10 \cdot F_{Ed}$

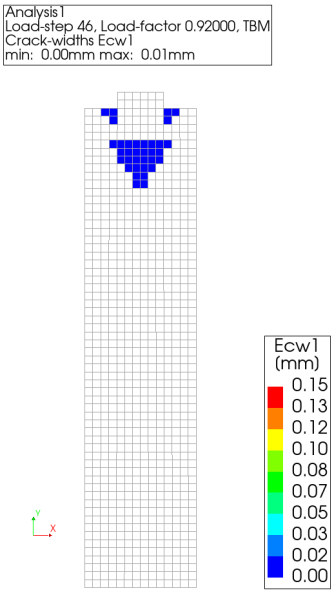

(d) Crack width for $F = 2.90 \cdot F_{Ed}$

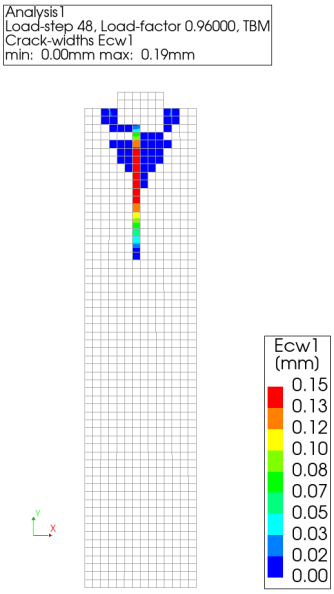

(e) Crack width for $F = 3.00 \cdot F_{Ed}$

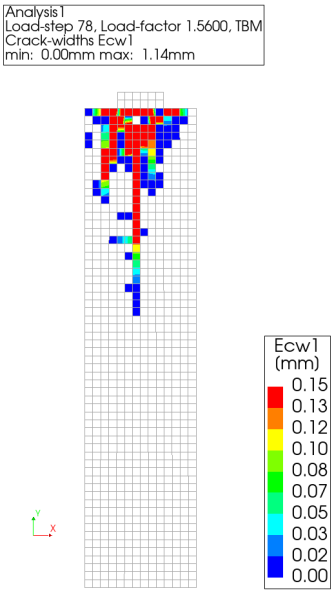

(f) Crack width for $F = 3.10 \cdot F_{Ed}$

Figure E.10: Stress and crack development concentrically loaded SFRC ring joint side view - 24 mm mesh

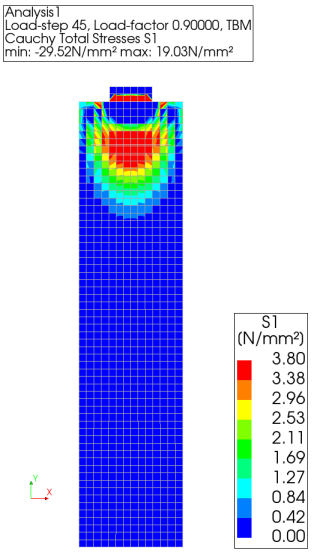

(a) Stress for $F = 2.95 \cdot F_{Ed}$

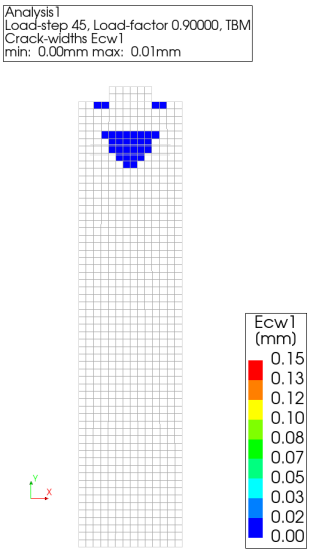

(b) Crack width for $F = 2.95 \cdot F_{Ed}$

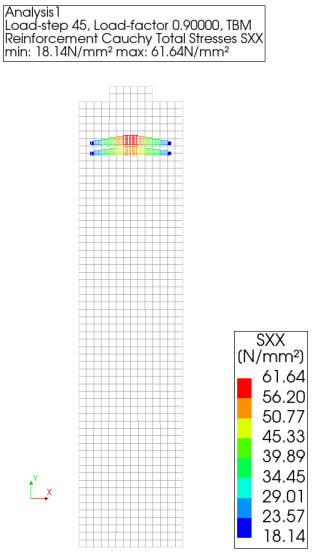

(c) Rebar stress for $F = 2.95 \cdot F_{Ed}$

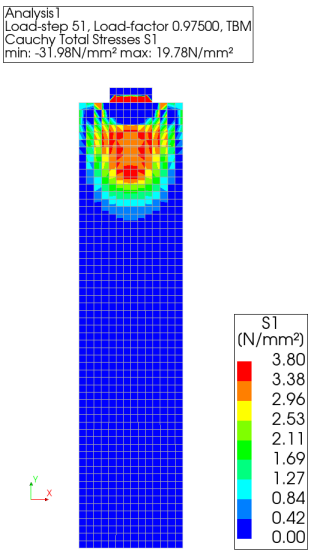

(d) Stress for $F = 3.15 \cdot F_{Ed}$

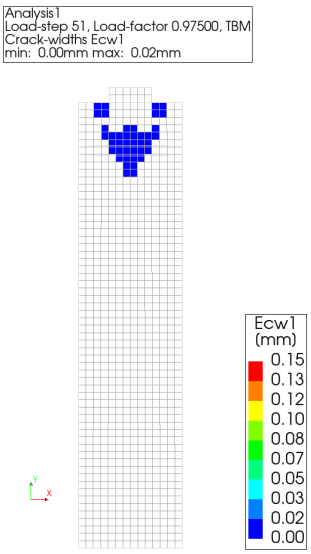

(e) Crack width for $F = 3.15 \cdot F_{Ed}$

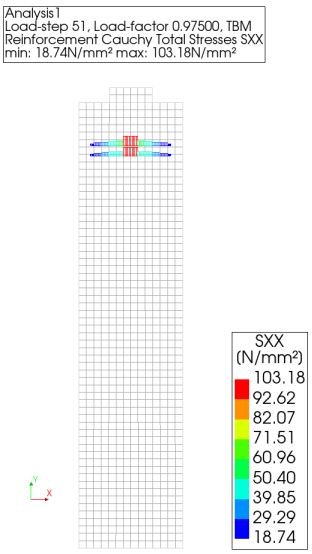

(f) Rebar stress for $F = 3.15 \cdot F_{Ed}$

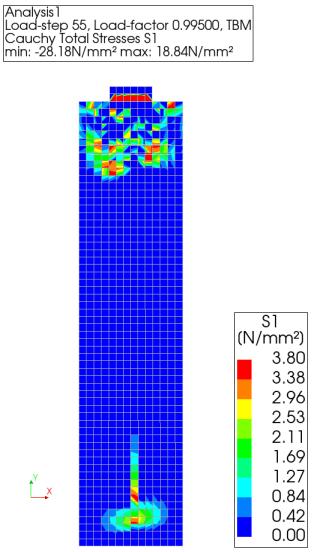

(g) Stress for $F = 3.20 \cdot F_{Ed}$

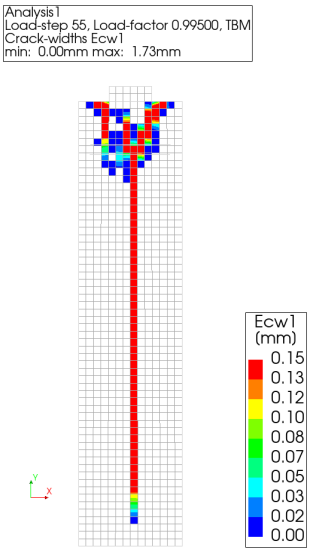

(h) Crack width for $F = 3.20 \cdot F_{Ed}$

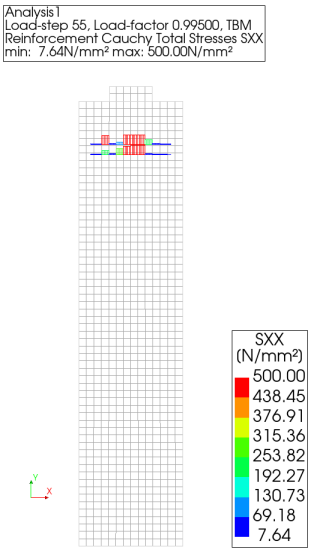

(i) Rebar stress for $F = 3.20 \cdot F_{Ed}$

Figure E.11: Stress, crack, and rebar stress development concentrically loaded RC ring joint side view - 24 mm mesh

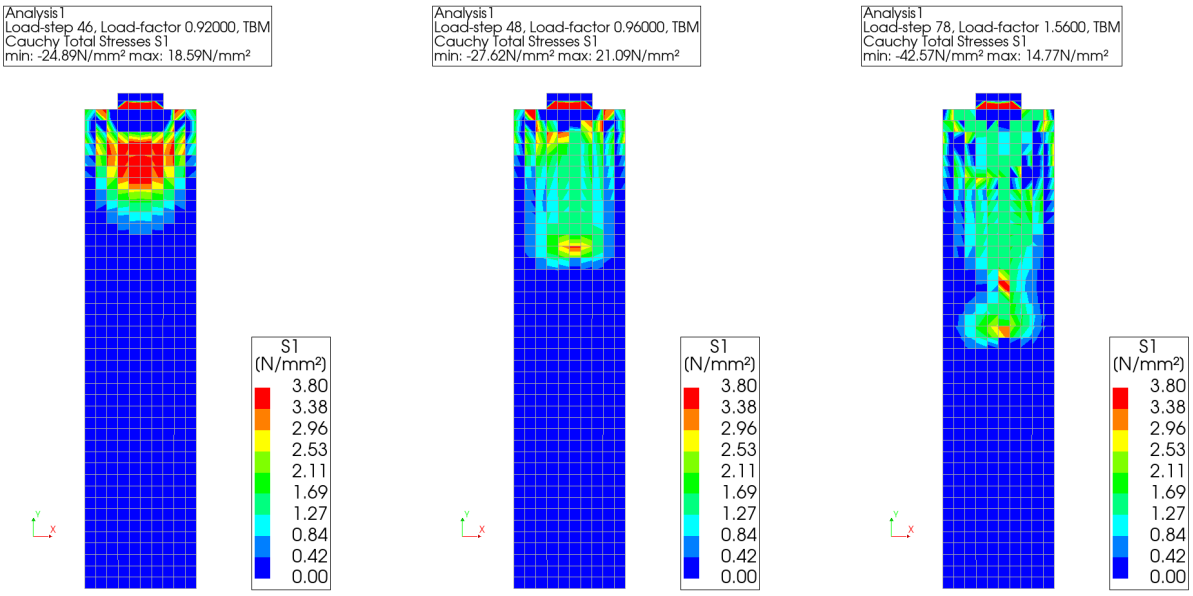

(a) Stress for $F = 2.95 \cdot F_{Ed}$ **(b)** Stress for $F = 3.00 \cdot F_{Ed}$ **(c)** Stress for $F = 3.10 \cdot F_{Ed}$

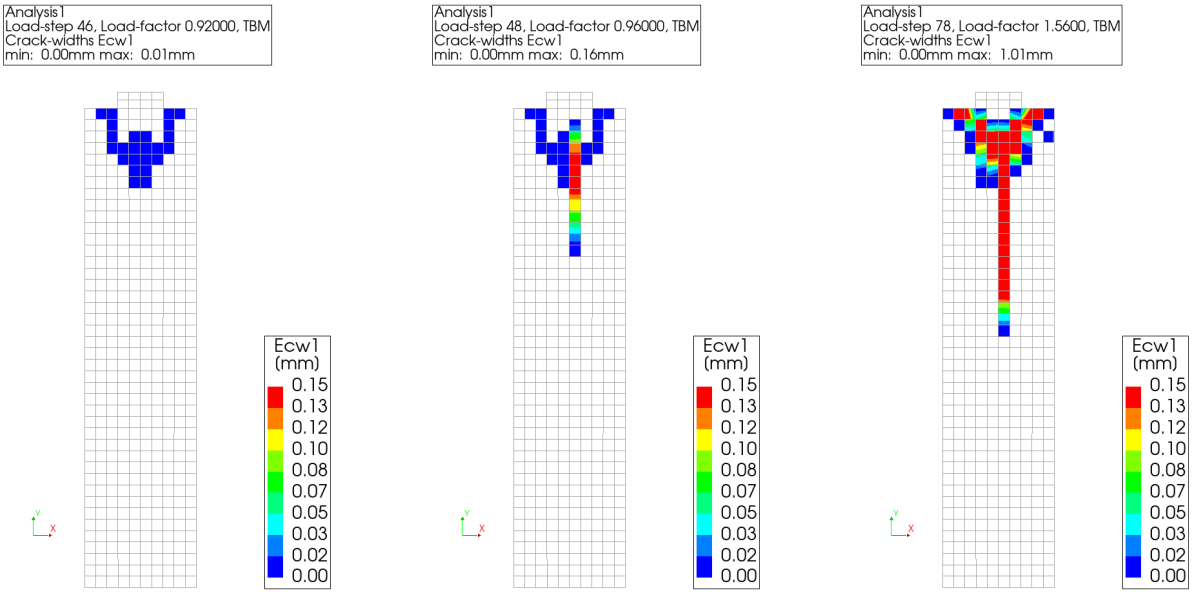

(d) Crack width for $F = 2.95 \cdot F_{Ed}$ **(e)** Crack width for $F = 3.00 \cdot F_{Ed}$ **(f)** Crack width for $F = 3.10 \cdot F_{Ed}$

Figure E.12: Stress and crack development concentrically loaded SFRC ring joint side view - 36 mm mesh

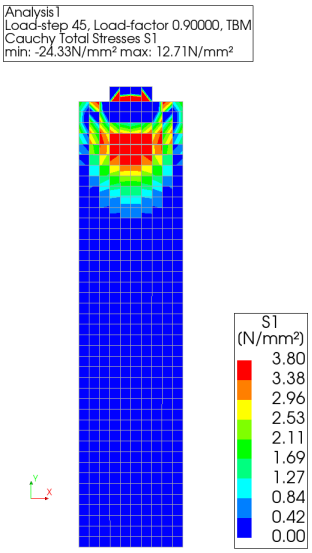

(a) Stress for $F = 2.95 \cdot F_{Ed}$

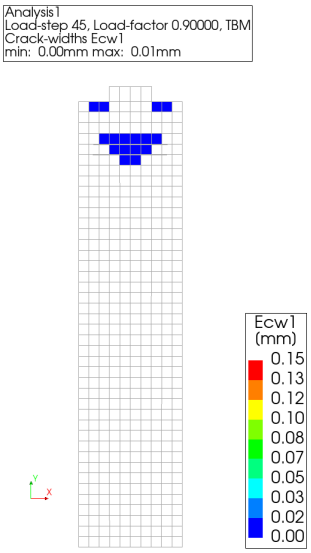

(b) Crack width for $F = 2.95 \cdot F_{Ed}$

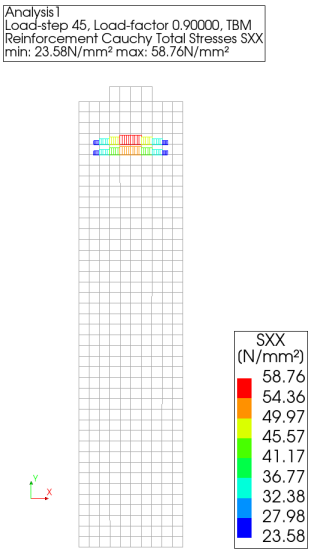

(c) Rebar stress for $F = 2.95 \cdot F_{Ed}$

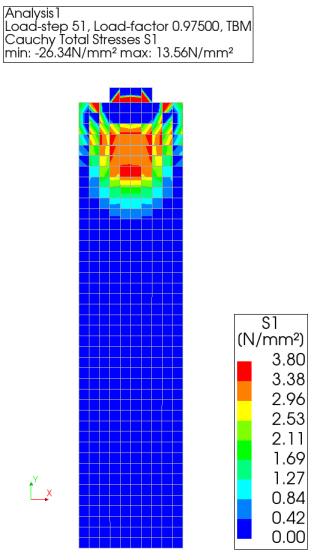

(d) Stress for $F = 3.15 \cdot F_{Ed}$

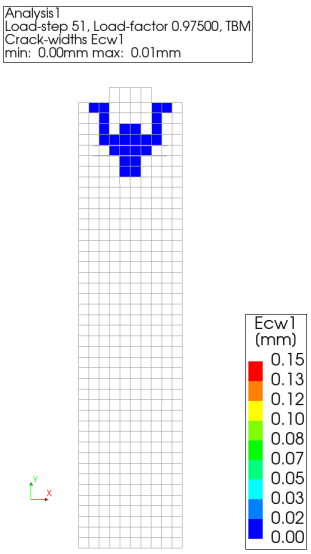

(e) Crack width for $F = 3.15 \cdot F_{Ed}$

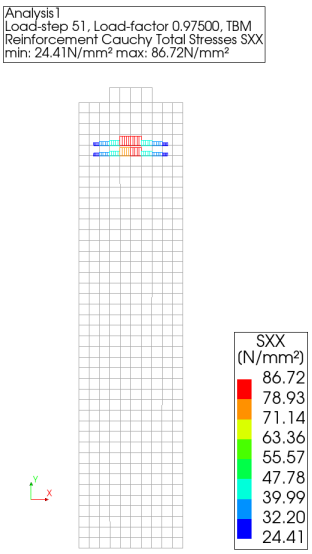

(f) Rebar stress for $F = 3.15 \cdot F_{Ed}$

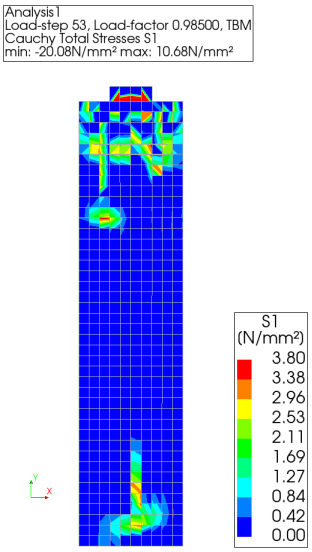

(g) Stress for $F = 3.20 \cdot F_{Ed}$

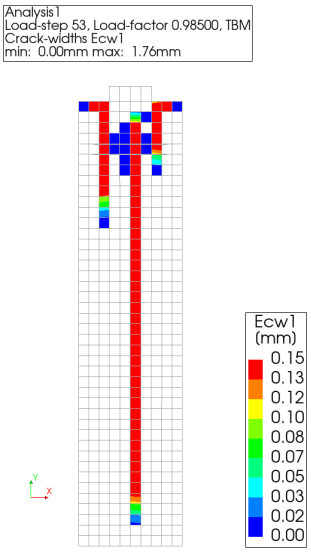

(h) Crack width for $F = 3.20 \cdot F_{Ed}$

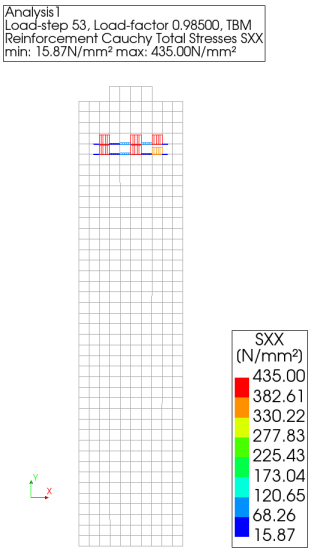

(i) Rebar stress for $F = 3.20 \cdot F_{Ed}$

Figure E.13: Stress, crack, and rebar stress development concentrically loaded RC ring joint side view - 36 mm mesh

Side view - Eccentrically loaded

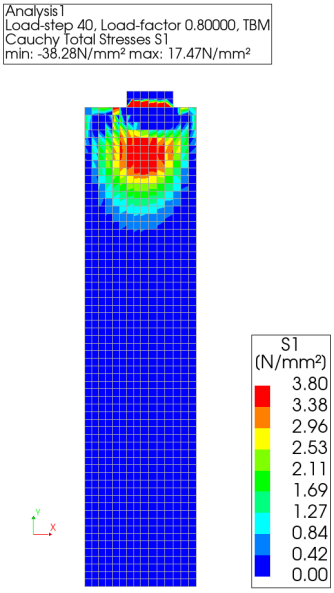

(a) Stress for $F = 2.50 \cdot F_{Ed}$

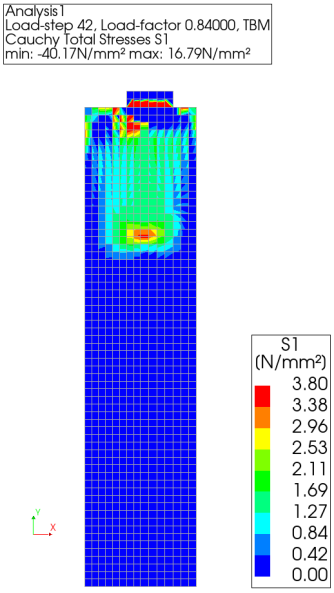

(b) Stress for $F = 2.60 \cdot F_{Ed}$

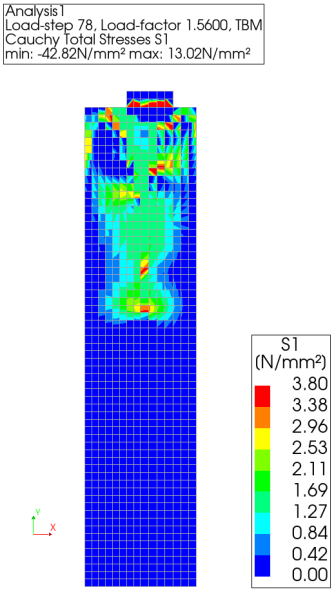

(c) Stress for $F = 2.90 \cdot F_{Ed}$

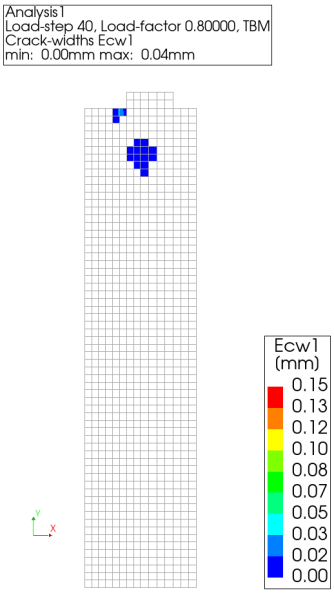

(d) Crack width for $F = 2.50 \cdot F_{Ed}$

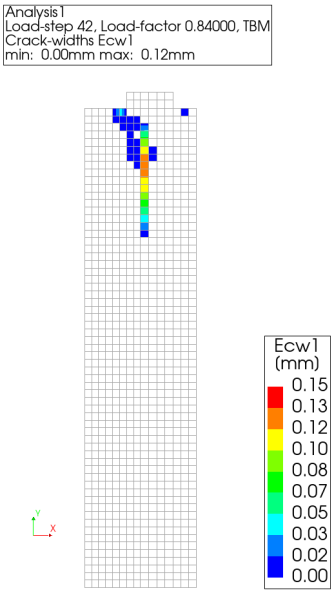

(e) Crack width for $F = 2.60 \cdot F_{Ed}$

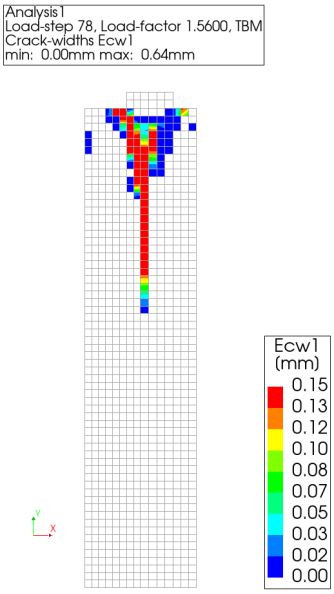

(f) Crack width for $F = 2.90 \cdot F_{Ed}$

Figure E.14: Stress and crack development eccentrically loaded SFRC ring joint side view - 24 mm mesh

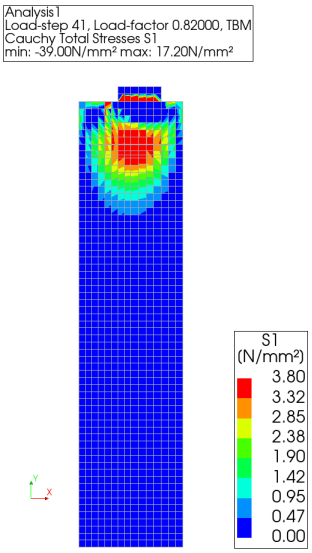

(a) Stress for $F = 2.55 \cdot F_{Ed}$

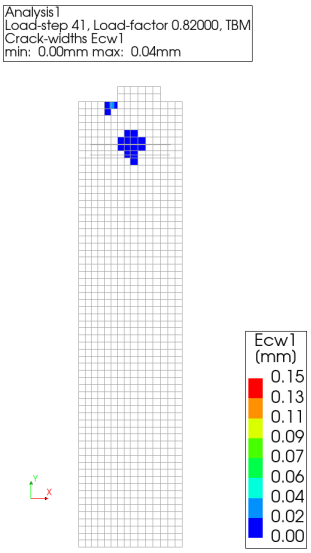

(b) Crack width for $F = 2.55 \cdot F_{Ed}$

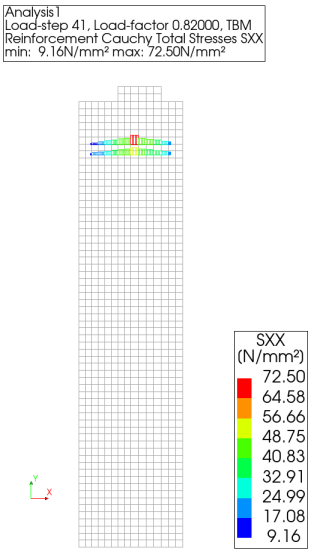

(c) Rebar stress for $F = 2.55 \cdot F_{Ed}$

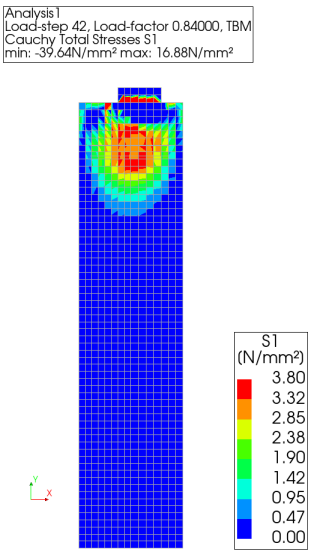

(d) Stress for $F = 2.60 \cdot F_{Ed}$

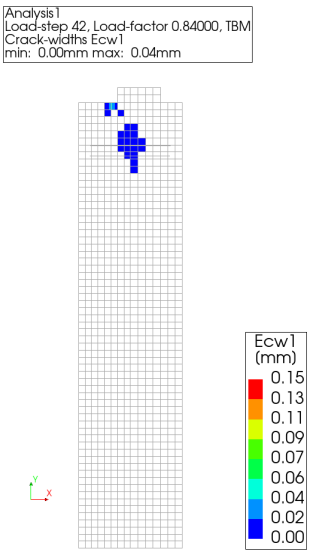

(e) Crack width for $F = 2.60 \cdot F_{Ed}$

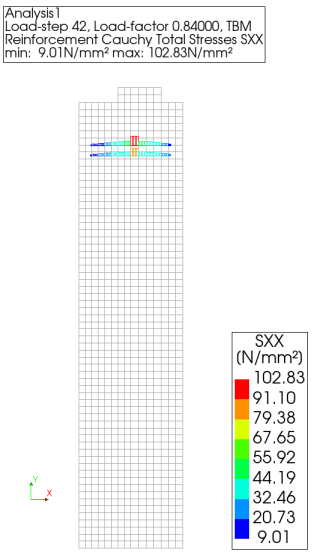

(f) Rebar stress for $F = 2.60 \cdot F_{Ed}$

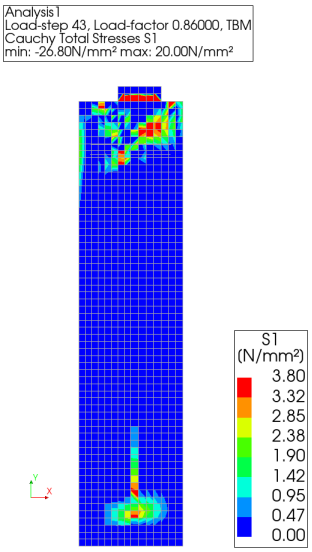

(g) Stress for $F = 2.65 \cdot F_{Ed}$

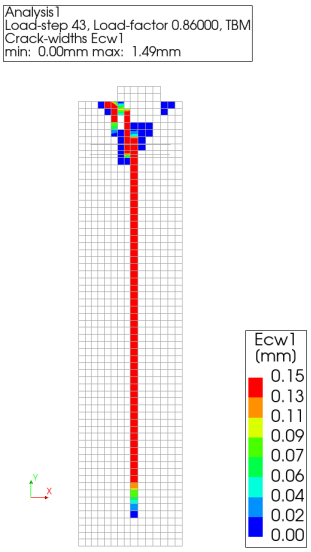

(h) Crack width for $F = 2.65 \cdot F_{Ed}$

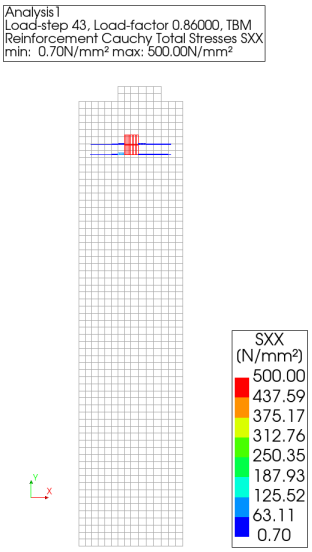

(i) Rebar stress for $F = 2.65 \cdot F_{Ed}$

Figure E.15: Stress, crack, and rebar stress development eccentrically loaded RC ring joint side view - 24 mm mesh

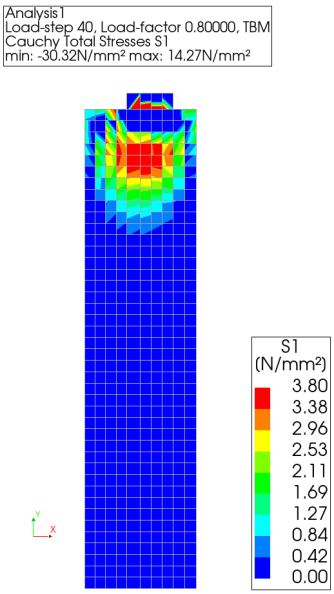

(a) Crack width for $F = 2.50 \cdot F_{Ed}$

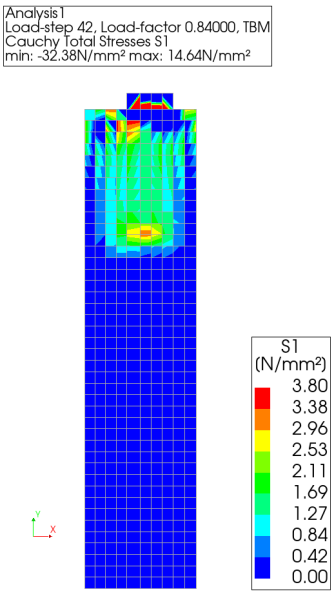

(b) Stress width for $F = 2.60 \cdot F_{Ed}$

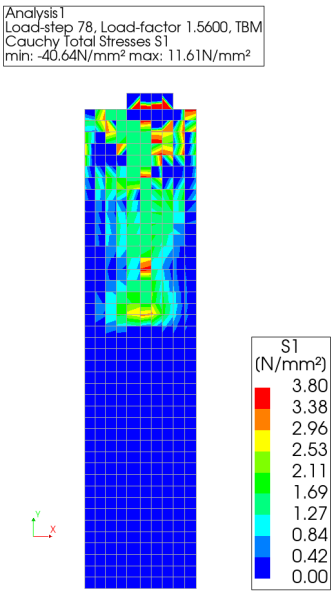

(c) Stress width for $F = 3.10 \cdot F_{Ed}$

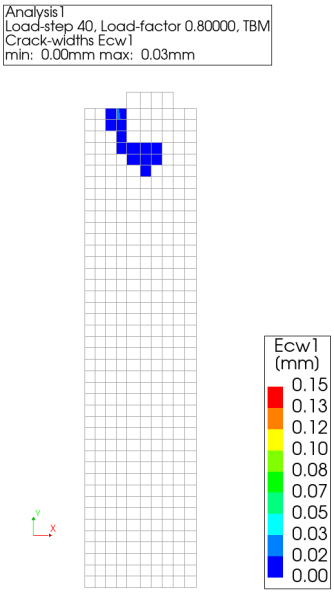

(d) Crack width for $F = 2.50 \cdot F_{Ed}$

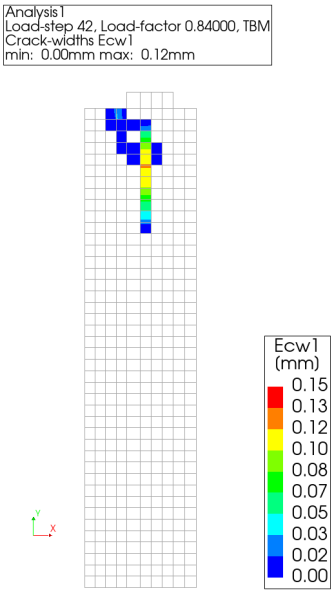

(e) Crack width for $F = 2.60 \cdot F_{Ed}$

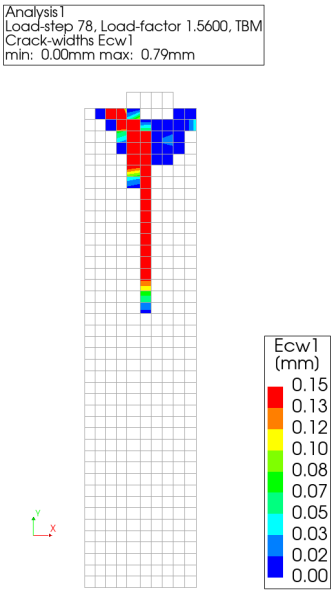

(f) Crack width for $F = 3.10 \cdot F_{Ed}$

Figure E.16: Stress and crack development eccentrically loaded SFRC ring joint side view - 36 mm mesh

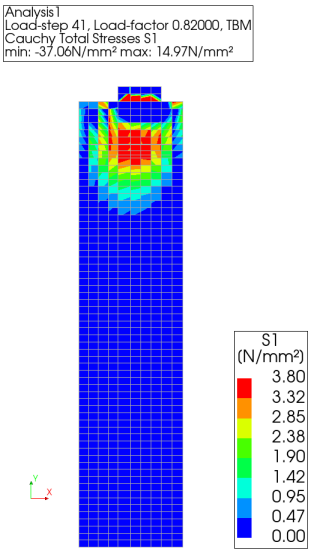

(a) Stress for $F = 2.55 \cdot F_{Ed}$

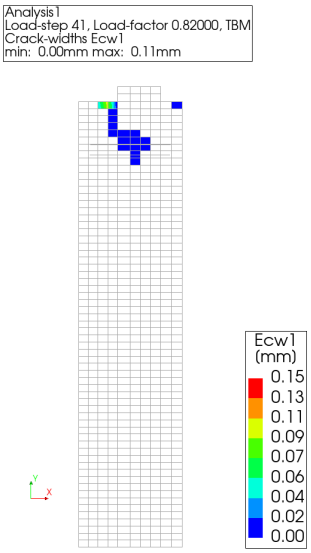

(b) Crack width for $F = 2.55 \cdot F_{Ed}$

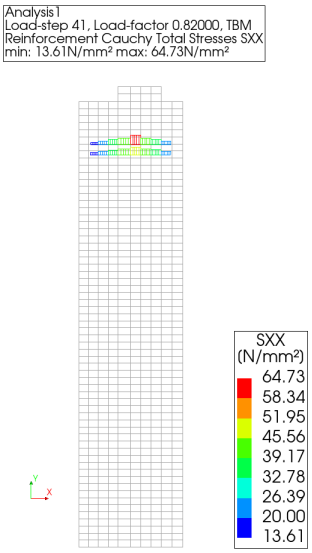

(c) Rebar stress for $F = 2.55 \cdot F_{Ed}$

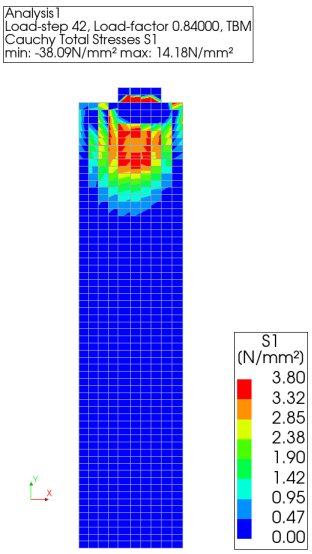

(d) Stress for $F = 2.60 \cdot F_{Ed}$

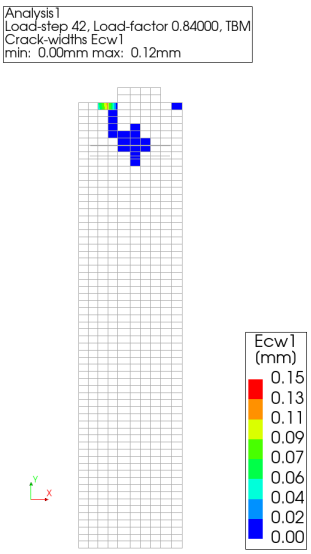

(e) Crack width for $F = 2.60 \cdot F_{Ed}$

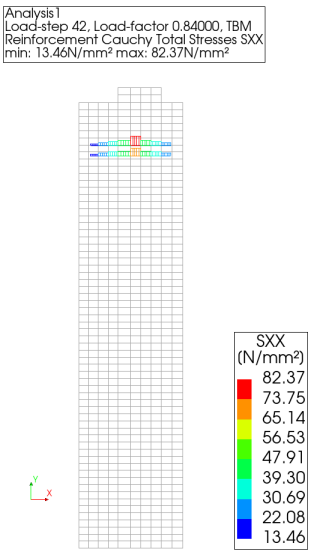

(f) Rebar stress for $F = 2.60 \cdot F_{Ed}$

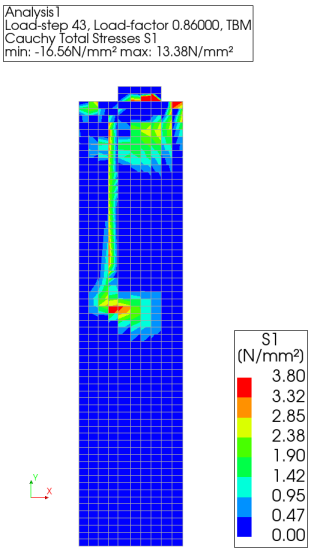

(g) Stress for $F = 2.65 \cdot F_{Ed}$

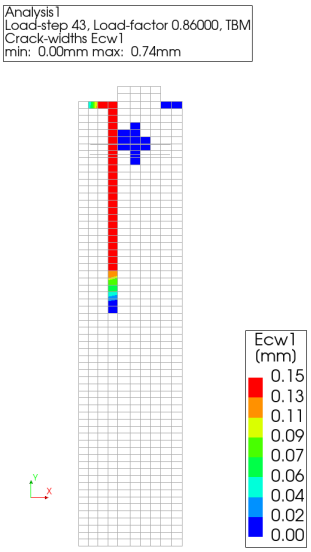

(h) Crack width for $F = 2.65 \cdot F_{Ed}$

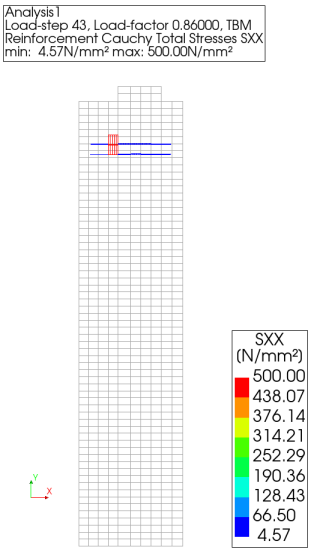

(i) Rebar stress for $F = 2.65 \cdot F_{Ed}$

Figure E.17: Stress, crack, and rebar stress development eccentrically loaded RC ring joint side view - 36 mm mesh

E.2. Longitudinal joint

SLS

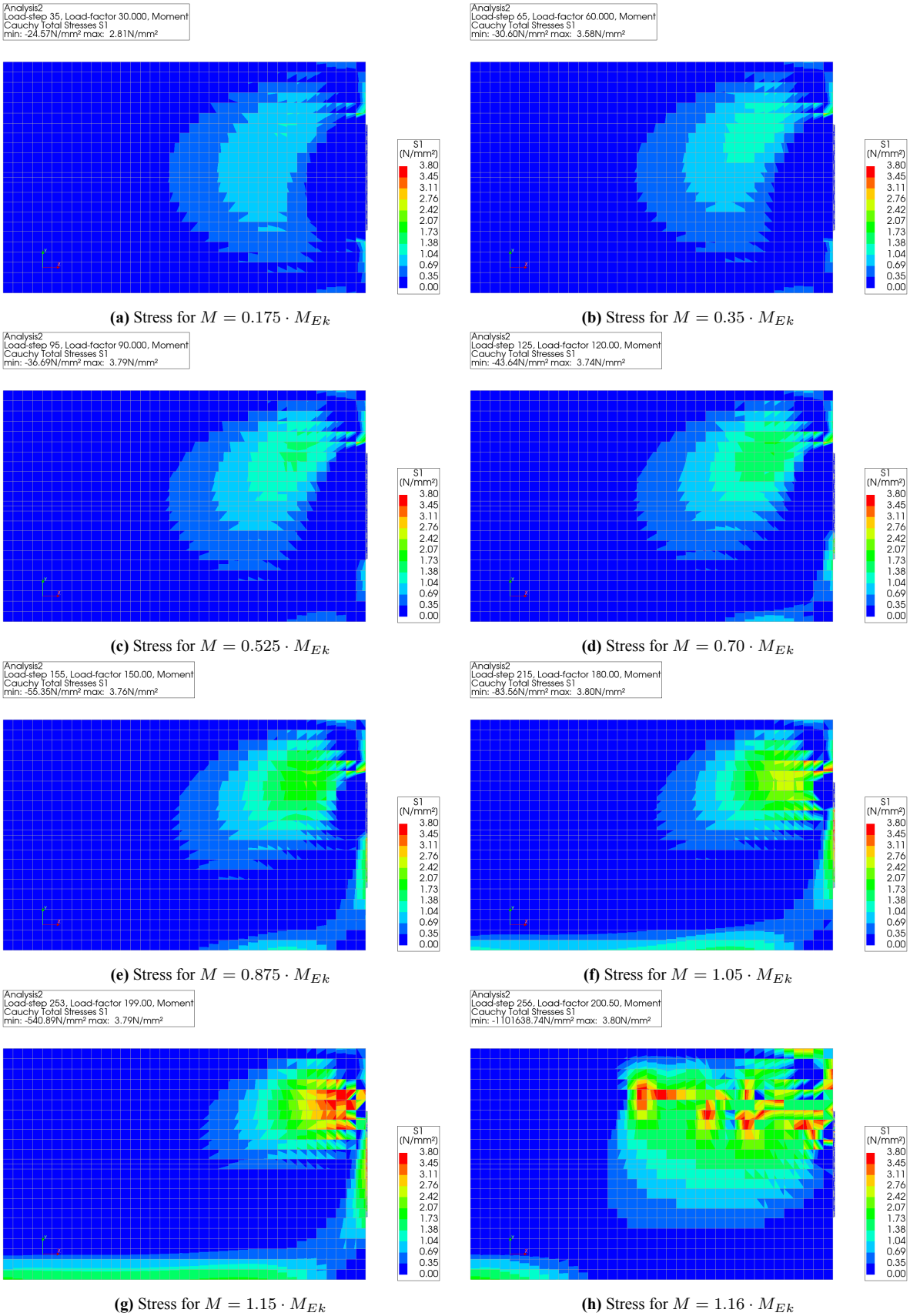

(a) Stress for $M = 0.175 \cdot M_{Ek}$

(b) Stress for $M = 0.35 \cdot M_{Ek}$

(c) Stress for $M = 0.525 \cdot M_{Ek}$

(d) Stress for $M = 0.70 \cdot M_{Ek}$

(e) Stress for $M = 0.875 \cdot M_{Ek}$

(f) Stress for $M = 1.05 \cdot M_{Ek}$

(g) Stress for $M = 1.15 \cdot M_{Ek}$

(h) Stress for $M = 1.16 \cdot M_{Ek}$

Figure E.18: Stress development SFRC longitudinal joint - SLS

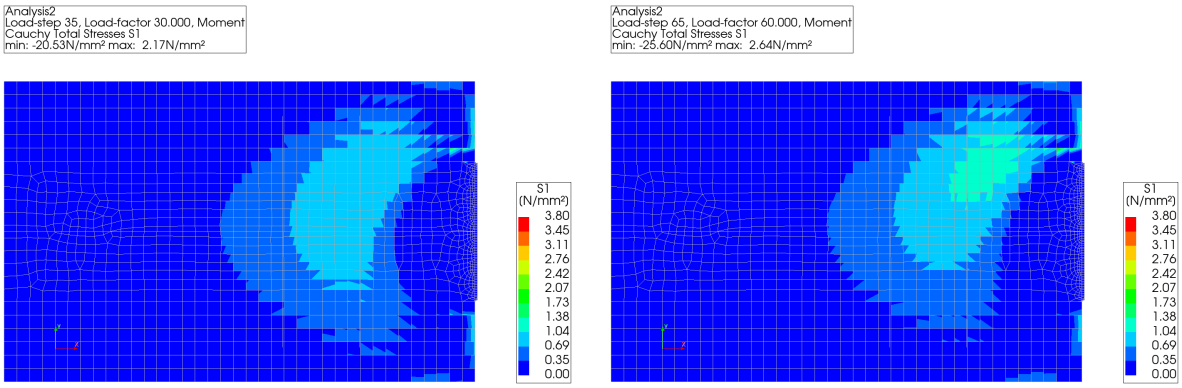

(a) Stress for $M = 0.175 \cdot M_{Ek}$

(b) Stress for $M = 0.35 \cdot M_{Ek}$

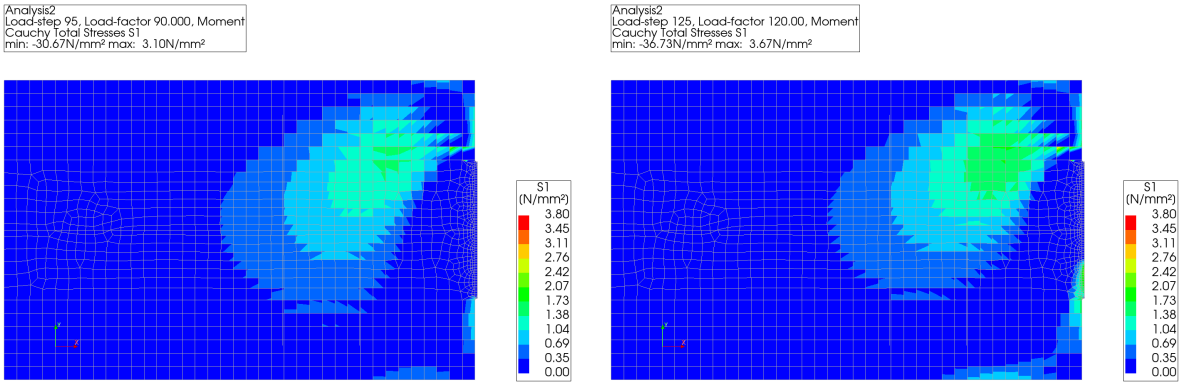

(c) Stress for $M = 0.525 \cdot M_{Ek}$

(d) Stress for $M = 0.70 \cdot M_{Ek}$

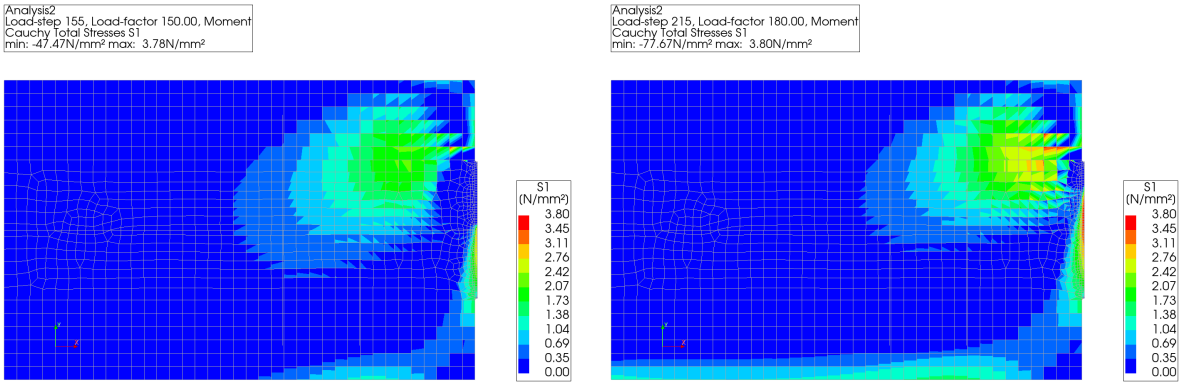

(e) Stress for $M = 0.875 \cdot M_{Ek}$

(f) Stress for $M = 1.05 \cdot M_{Ek}$

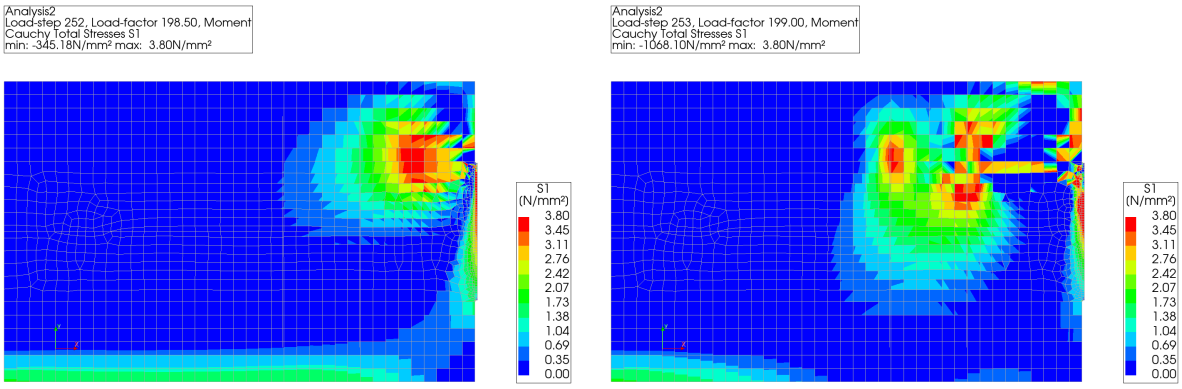

(g) Stress for $M = 1.14 \cdot M_{Ek}$

(h) Stress for $M = 1.15 \cdot M_{Ek}$

Figure E.19: Stress development RC longitudinal joint - SLS

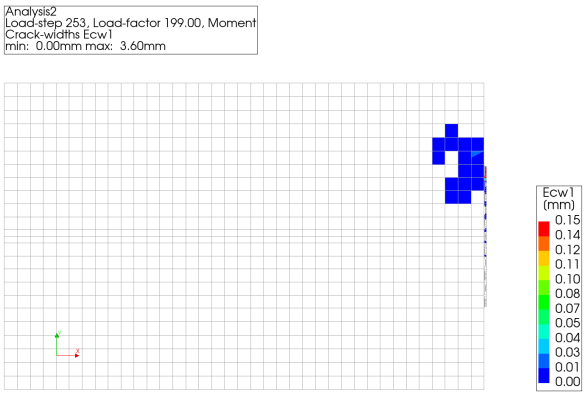

(a) Crack width for $M = 1.15 \cdot M_{Ek}$

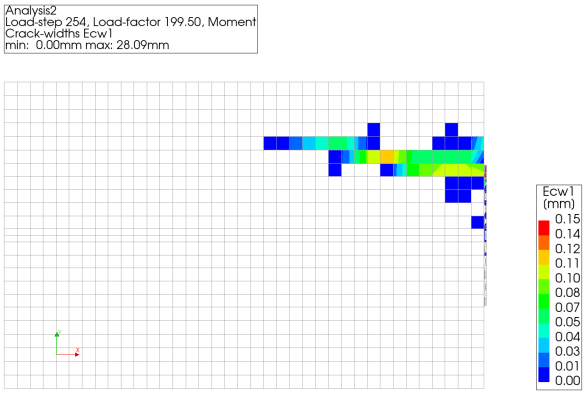

(b) Crack width for $M = 1.16 \cdot M_{Ek}$

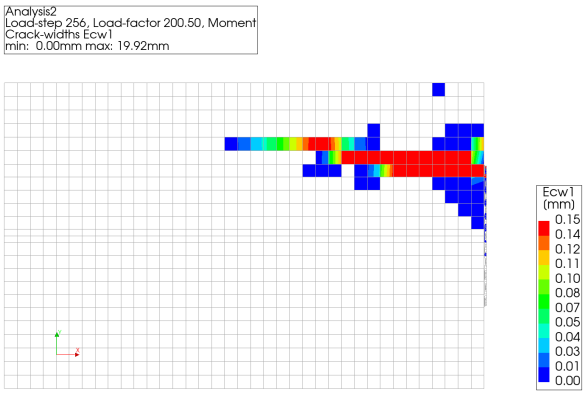

(c) Crack width for $M = 1.17 \cdot M_{Ek}$

Figure E.20: Crack development SFRC longitudinal joint - SLS

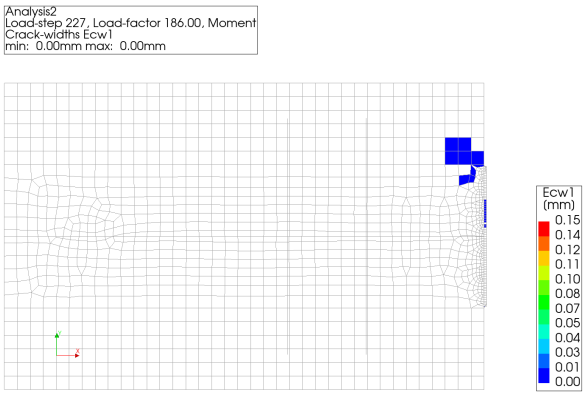

(a) Crack width for $M = 1.08 \cdot M_{Ek}$

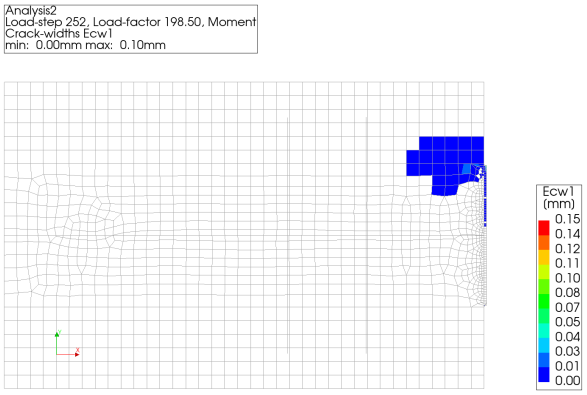

(b) Crack width for $M = 1.14 \cdot M_{Ek}$

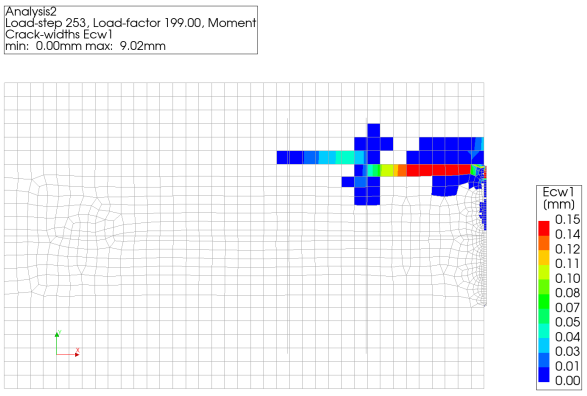

(c) Crack width for $M = 1.15 \cdot M_{Ek}$

Figure E.21: Crack development RC longitudinal joint - SLS

ULS

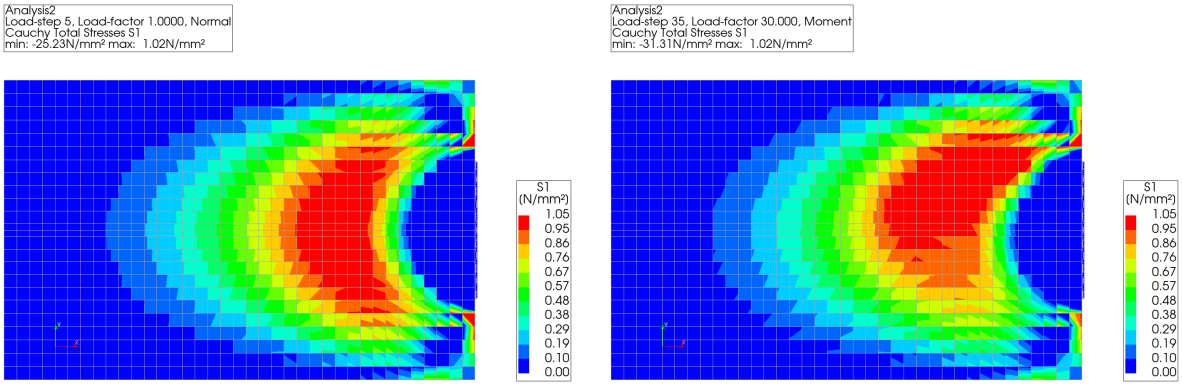

(a) Stress for $M = 0.01 \cdot M_{Ed}$

(b) Stress for $M = 0.13 \cdot M_{Ed}$

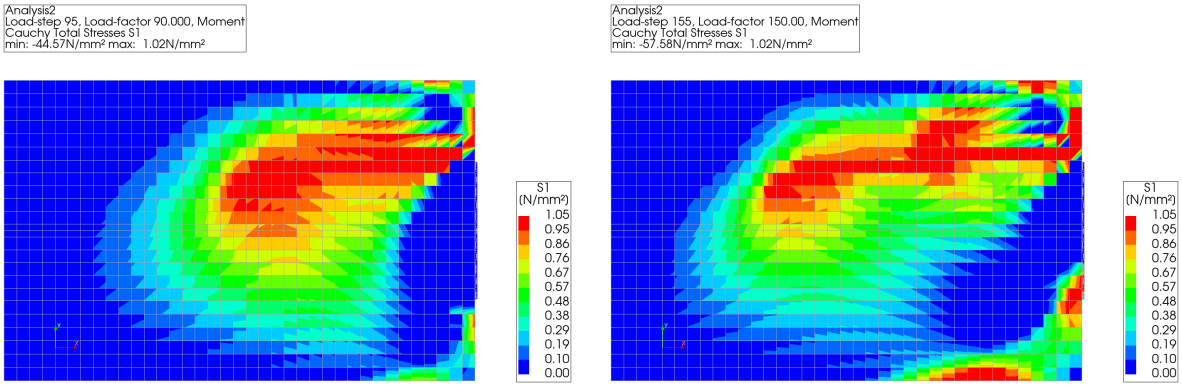

(c) Stress for $M = 0.40 \cdot M_{Ed}$

(d) Stress for $M = 0.67 \cdot M_{Ed}$

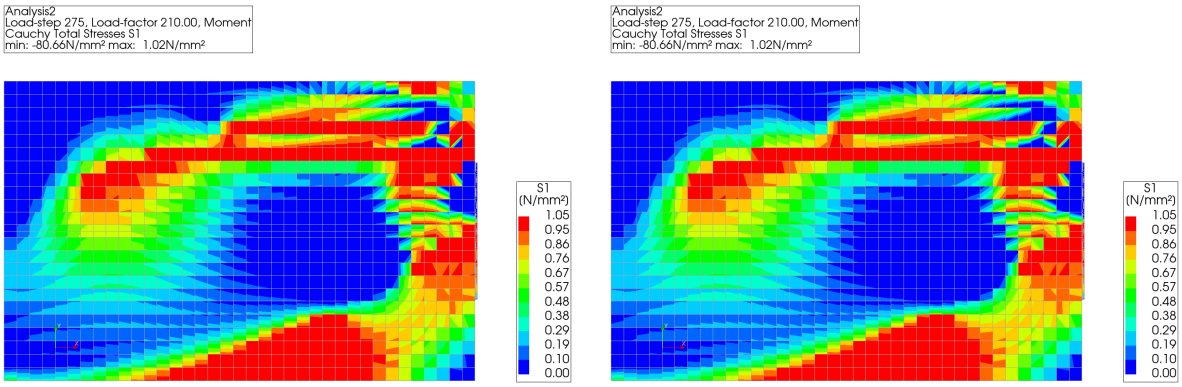

(e) Stress for $M = 0.94 \cdot M_{Ed}$

(f) Stress for $M = 0.98 \cdot M_{Ed}$

Figure E.22: Stress development SFRC longitudinal joint - ULS

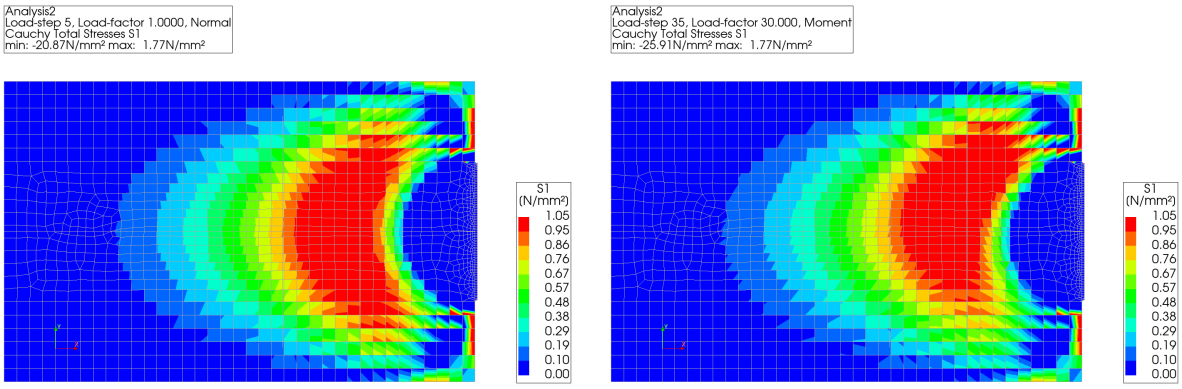

(a) Stress for $M = 0.01 \cdot M_{Ed}$

(b) Stress for $M = 0.13 \cdot M_{Ed}$

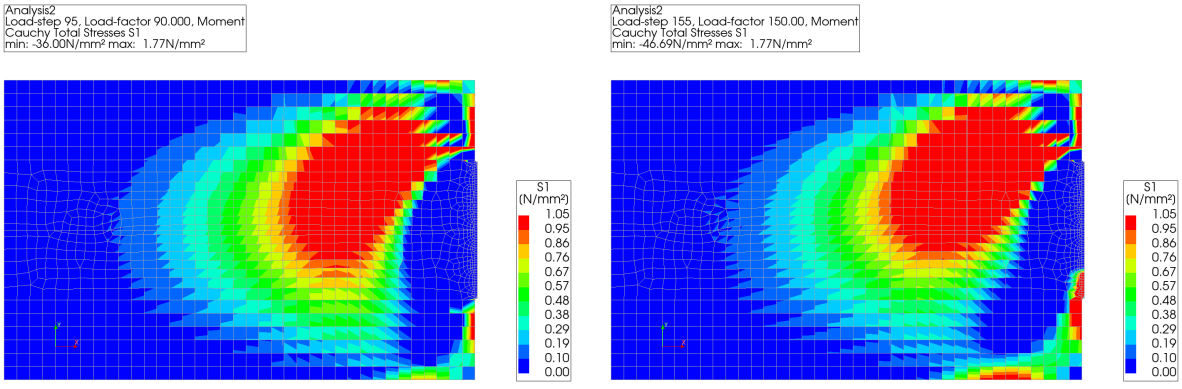

(c) Stress for $M = 0.40 \cdot M_{Ed}$

(d) Stress for $M = 0.67 \cdot M_{Ed}$

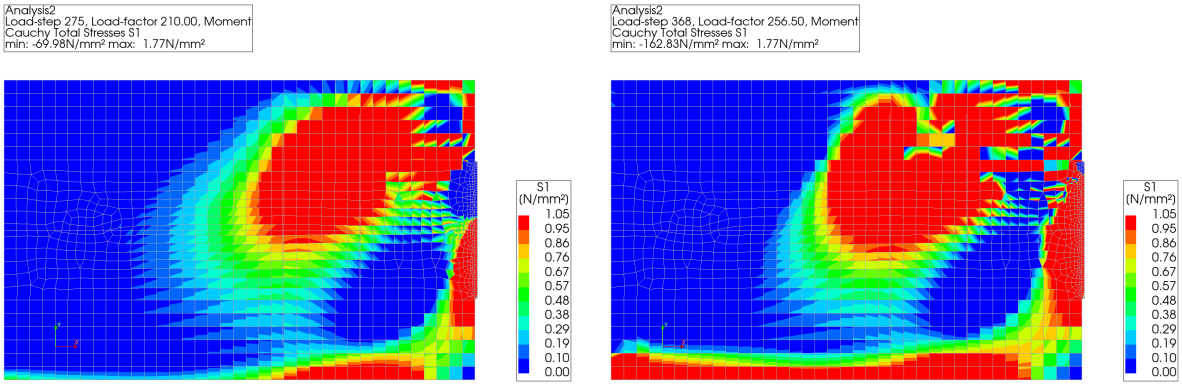

(e) Stress for $M = 0.94 \cdot M_{Ed}$

(f) Stress for $M = 1.15 \cdot M_{Ed}$

Figure E.23: Stress development RC longitudinal joint - ULS

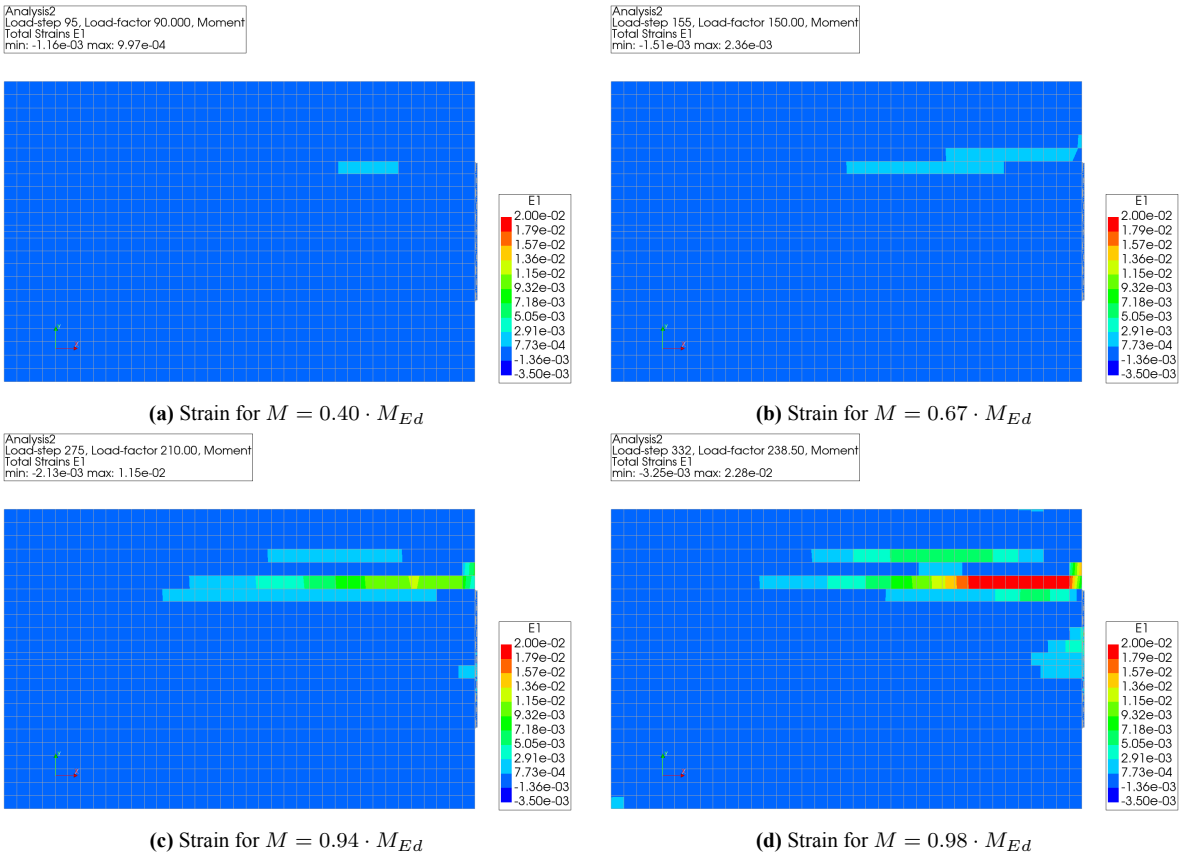

(a) Strain for $M = 0.40 \cdot M_{Ed}$

(b) Strain for $M = 0.67 \cdot M_{Ed}$

(c) Strain for $M = 0.94 \cdot M_{Ed}$

(d) Strain for $M = 0.98 \cdot M_{Ed}$

Figure E.24: Strain development SFRC longitudinal joint - ULS

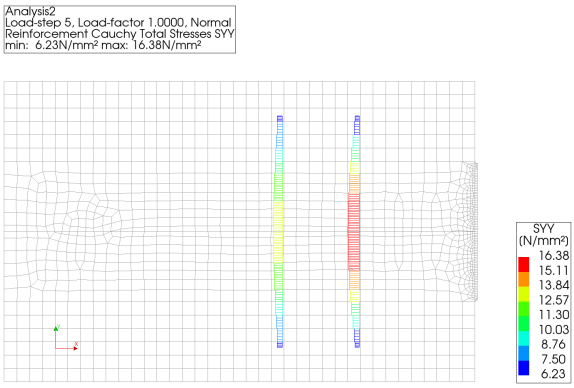

(a) Rebar stress for $M = 0.01 \cdot M_{Ed}$

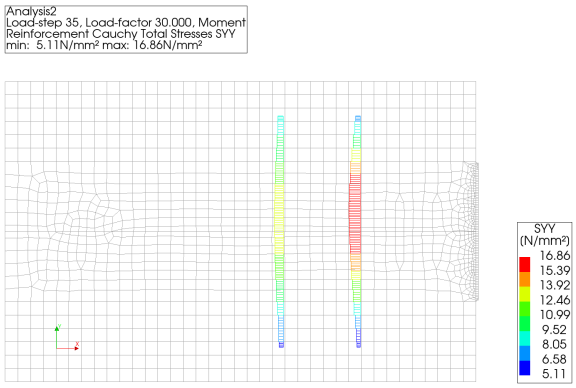

(b) Rebar stress for $M = 0.13 \cdot M_{Ed}$

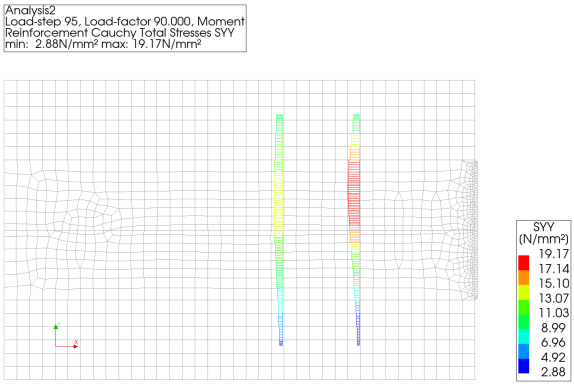

(c) Rebar stress for $M = 0.40 \cdot M_{Ed}$

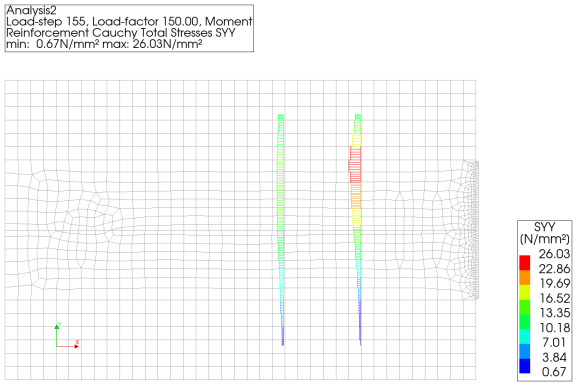

(d) Rebar stress for $M = 0.67 \cdot M_{Ed}$

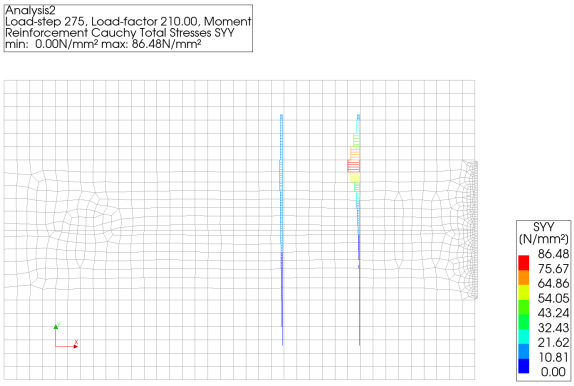

(e) Rebar stress for $M = 0.94 \cdot M_{Ed}$

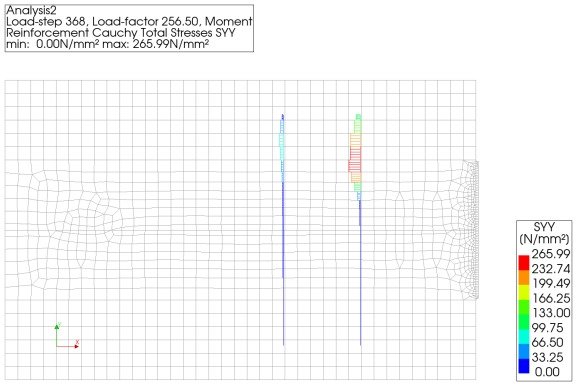

(f) Rebar stress for $M = 1.15 \cdot M_{Ed}$

Figure E.25: Rebar stress development RC longitudinal joint - ULS

E.3. Global cross section

Bending moments

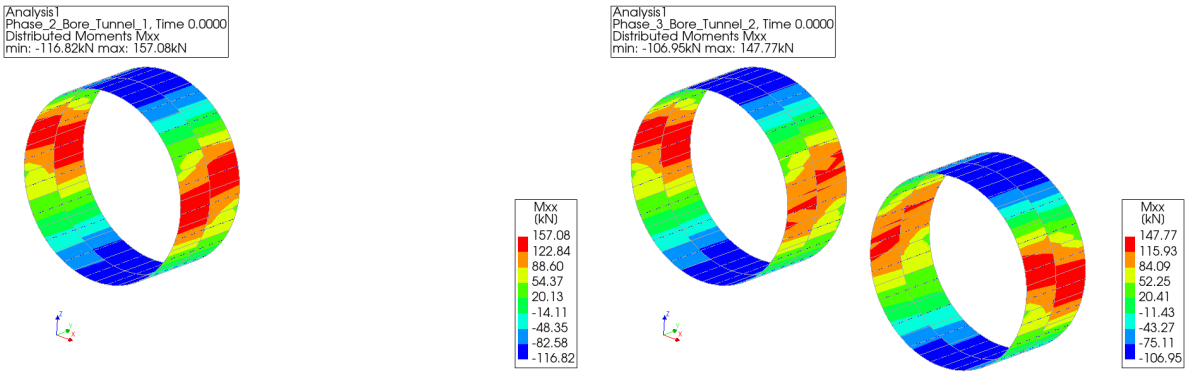

(a) M_{XX} - phase 2 **(b)** M_{XX} - phase 3

Figure E.26: Bending moment M_{XX} distribution after phase 2 and phase 3

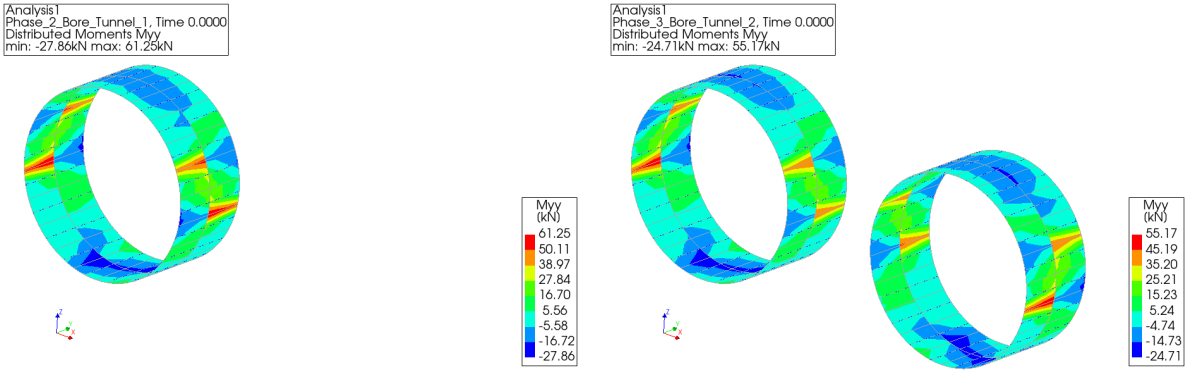

(a) M_{YY} - phase 2 **(b)** M_{YY} - phase 3

Figure E.27: Bending moment M_{YY} distribution after phase 2 and phase 3

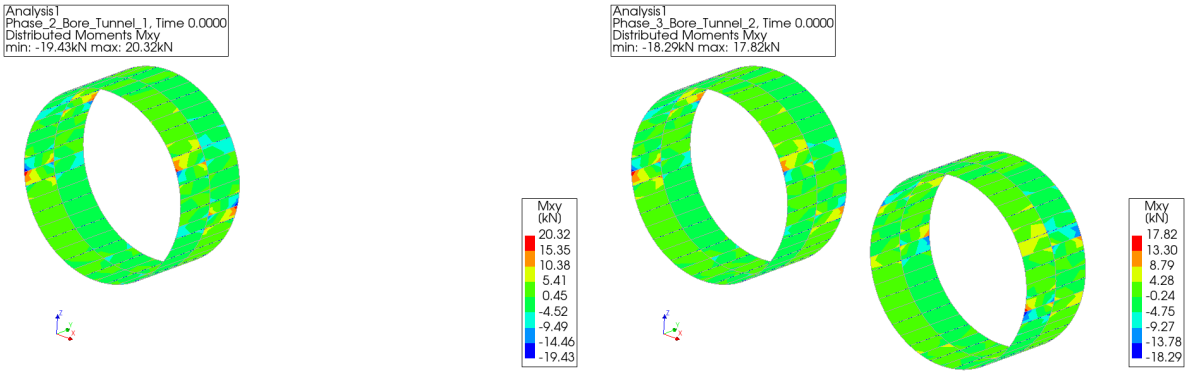

(a) M_{XY} - phase 2 **(b)** M_{XY} - phase 3

Figure E.28: Bending moment M_{XY} distribution after phase 2 and phase 3

Stresses

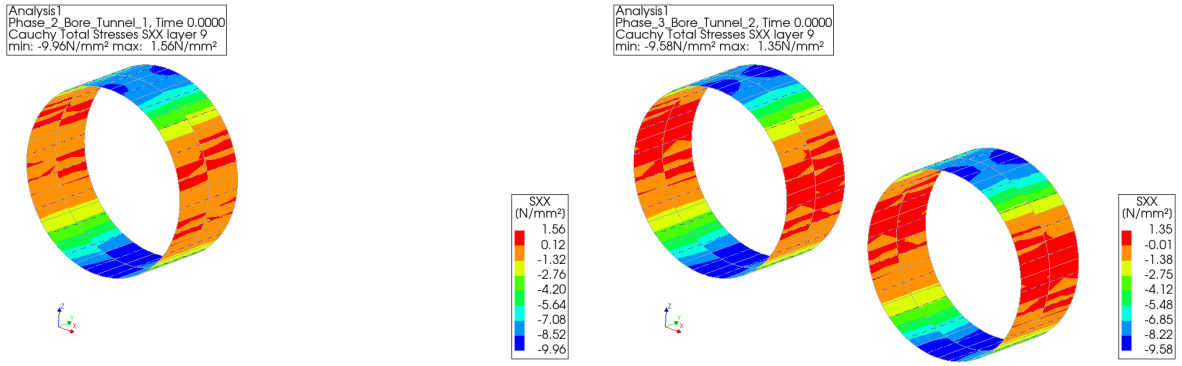

(a) S_{XX} - phase 2 **(b)** S_{XX} - phase 3

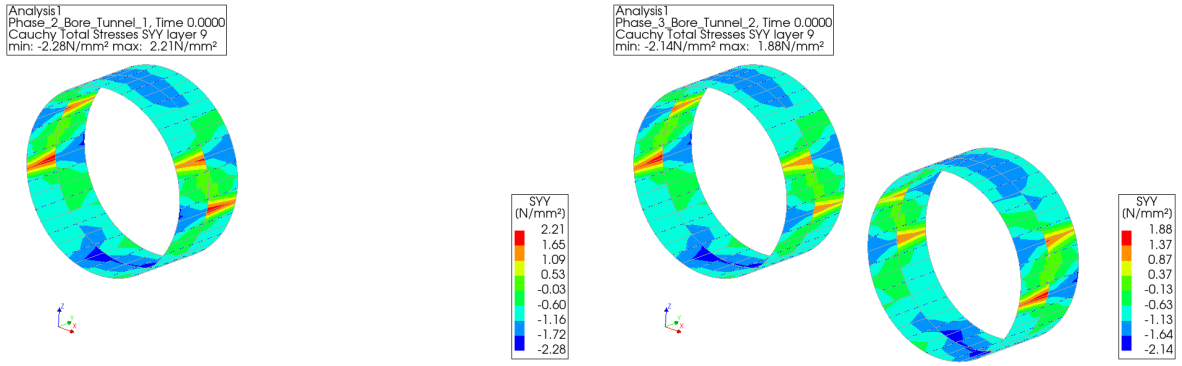

(c) S_{YY} - phase 2 **(d)** S_{YY} - phase 3

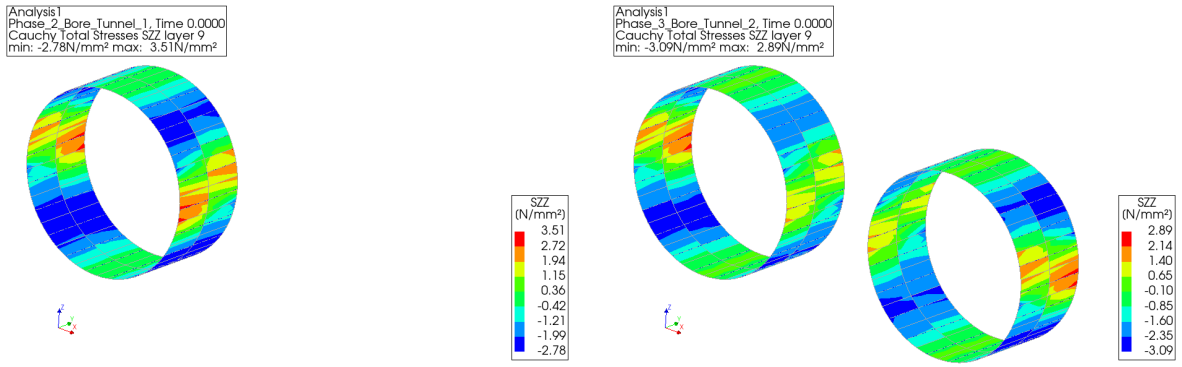

(e) S_{ZZ} - phase 2 **(f)** S_{ZZ} - phase 3

Figure E.29: Stresses S_{XX}, S_{YY}, and S_{ZZ} after phase 2 and phase3